Electron Spin Echo Envelope Modulation Spectroscopy of Radical Pairs in Photosynthetic Bacteria

A thesis submitted for the degree of
Doctor of Philosophy
by

Catherine E. Fursman

Christ Church
Oxford University

Hilary Term 2000

Electron Spin Echo Envelope Modulation Spectroscopy of Radical Pairs in Photosynthetic Bacteria

A thesis submitted for the degree of
Doctor of Philosophy
by

Catherine E. Fursman

Christ Church
Hilary Term 2000

Electron spin echo envelope modulation (ESEEM) spectroscopy is widely used to study the radical pairs created during the primary steps of photosynthesis. In this thesis the analysis of ESEEM spectra is improved, and some new applications and variations of this experiment suggested.

Experimental spectra from species such as $P^+Q_A^-$, the secondary radical pair formed in the reaction centre of the bacterium *Rhodobacter sphaeroides*, give information about the exchange and dipolar couplings between the radicals. The model used to analyse the data affects the results; this thesis suggests two improvements. First, the effect of anisotropic hyperfine couplings in the radicals is considered by the addition of a single spin-1/2 nucleus to the model. This approach suggests that previous models neglecting the effect of nuclei may have been slightly in error. Secondly, several model fittings are performed in the time domain. This approach avoids the Fourier transformation to the frequency domain so that experimental dead-time does not corrupt the data. An excellent fit to experimental data is found with a model containing one spin-1/2 nucleus on each radical. The hyperfine coupling parameters resulting from the fit are consistent with independent experimental results.

Use is made of the method of Cramér-Rao lower bounds to assess the precision to which experimental parameters are determined from a time domain curve fitting. It is shown that the lower bounds may also be used to determine the optimum sampling strategy for the experiment.

An example is given of the novel use of ESEEM to determine the distance between the radicals in the strongly coupled, uncorrelated radical pair $Q_A^-Q_B^-$. ESEEM has not yet been used for this purpose, and the simulated spectra produced here indicate that the experiment could be used to evaluate the dipolar coupling and hence the inter-radical distance.

This thesis considers the possibility of performing ESEEM at higher frequencies than are usually considered. Calculations show that the increased resolution of the g-tensors allow an experiment performed at the W-band frequency of 95 GHz to make a correlation between the relative orientations of the radicals and the dipolar axis, information which has previously been unavailable from a single experiment.

Acknowledgements

Principal thanks must go to my supervisor, Dr. Peter Hore, for his constant advice, support and patience whilst coaxing me gently through the work that has eventually become this thesis.

I am extremely grateful to both Pete Biggs and Jonathan Jones who have gallantly put up with all my computer-related whimperings and panics over the last three years. Your lives, and those of the computers, will doubtless be far more peaceful without me.

Thanks must also go to Prof. Richard Wayne, and to the powers-that-be at Christ Church for giving me so much money to go away to conferences. It was all well used, and very much appreciated.

I should like to thank Drs. Robert Bittl and Stephan Zech for some interesting discussions concerning the work in Chapters 3 and 5, and especially for letting me within 10 feet of their W-band machine. It was great to finally see what it looked like! Thanks also to Stephan for assistance with Figure 5.2. Special thanks go to Dr. Chris Timmel, not only for collaborations with the work in Chapter 2, but also for the enormous amount of advice and assistance she gave me at the start of, and all the way through, my research.

As a thesis writer, I am indebted to my proof readers. First, Peter and Chris for correcting my wonky science, and secondly RQ for correcting my wonky English. Hopefully your essays in red pen have taught me something for the future! Thanks also to Michael Fuhs for comments on Chapter 5, and to Ailsa.

Life in the PTCL would not have been the same without the other members of the PJH group. I thank Chris for being great fun and a good friend on top of everything else, Ulrike for teaching me how to shop properly, Jake for teaching me which end of a PC is which and for allowing me to chatter on during many a visit to "Friends", and Charlie for finishing first and making useful comments such as "thesis writing - the worst time of my life". I must not forget Ailsa. Thank you for introducing me to my newest, and healthiest vice, namely rowing, and for fixing my bike every time I broke a new bit. And of course for being a really good mate. To the other members of the PJH group past and present, especially Ian, who asked me questions I could answer and made me feel clever, and to Sharon, Tariq and Rob, it's been great fun working with you. My legs still ache just thinking about walking in the Lake District!

Away from the lab, big thank you's and sloppy kisses to my friends from Southampton; Becky, Lizzie, Marc, Mike, Greg, Kieran, Lou, Flic and Beth, for frequently disturbing the peace in Oxford whilst on a mission to remind me of the importance of beer. I shall always let you know where I am, and long may the tradition continue.

I also have to thank Rachel "Mum" Quarrell, Marcus "Überslapper" Munafó and Tig for being the best house-mates a girl could want, and for feeding me chocolate, wine and pancakes at just the right moments. I shall really miss living with you.

Thanks to the Notley Abbey Posse and Lucy, I hope we remain friends for another 15 years at least, to Paul for injecting something cultural into my life, and to Catherine for not sacking me as her bridesmaid when I broke my leg, I promise not to do it again!

I certainly couldn't have done this without the support of my family, and I thank Mum, Dad and Mary for being there for me all the way through. I love you all very much.

Publications arising directly from work described in this thesis

1. Spin-correlated radical pairs: microwave pulse effects on lifetimes, electron spin echo envelope modulations, and optimum conditions for detection by electron spin echo spectroscopy

   C. R. Timmel, C. E. Fursman, A. J. Hoff and P. J. Hore.

   Chem. Phys. **226** (1998) 271

2. The nuts and bolts of distance determination and zero- and double quantum coherence in photoinduced radical pairs

   A. J. Hoff, P. J. Gast, S. A. Dzuba, C. R. Timmel, C. E. Fursman and P. J. Hore.

   Spectrochimica Acta A **54** (1988) 2283

3. Reliability of distance determination in photosynthetic radical pairs using electron spin echo envelope modulation spectroscopy

   C. E. Fursman and P. J. Hore.

   Magnetic Resonance and Related Phenomena. Proceedings of the Joint 29th AMPERE - 13th ISMAR International Conference, Berlin, 2 - 7 August 1998, pp 943

4. Distance determination in spin-correlated radical pairs in photosynthetic reaction centres by electron spin echo envelope modulation

   C. E. Fursman and P. J. Hore.

   Chem. Phys. Lett. **303** (1999) 593

5. Electron spin echo envelope modulation of $P^+Q_A^-$ at W-band (95 GHz)

   C. E. Fursman and P. J. Hore.

   in preparation

Contents

Table of abbreviations

Abbreviation	full expression
BChl	bacteriochlorophyll
bRC	bacterial reaction centre
CIDNP	chemically induced dynamic nuclear polarisation
CRLB	Cramér-Rao lower bound
cw EPR	continuous wave electron paramagnetic resonance
emr	electromagnetic radiation
ENDOR	electron nuclear double resonance
EPR	electron paramagnetic resonance
ESEEM	electron spin echo envelope modulation
FT EPR	Fourier transform electron paramagnetic resonance
I	bacteriopheophytin
LH	light harvesting complex
mw	microwave
NMR	nuclear magnetic resonance
P	special pair of bacteriochlorophylls
$P^+Q_A^-$	secondary radical pair in *Rb. sphaeroides*
PS	plant photosystem
Q_A	quinone (A-branch in the RC of *Rb. sphaeroides*)
Q_B	quinone (B-branch in the RC of *Rb. sphaeroides*)
Rb. sphaeroides	*Rhodobacter sphaeroides*
Rps. viridis	*Rhodopseudomenas viridis*
RC	reaction centre
rf	radiofrequency
RP	radical pair
SCRP	spin-correlated radical pair
TREPR	time-resolved electron paramagnetic resonance
ZQC, SQC, DQC	zero, single and double quantum coherence

Chapter 1

Introduction

Photosynthesis, the conversion of sunlight into chemical energy, is essential to life on earth. This process has been the subject of many scientific studies, not only because of its biological importance, but also because, as a source of energy, it is almost one hundred percent efficient. Although it can be expressed as a simple chemical equation, photosynthesis is in fact a highly complex process which is not fully understood and has hitherto been impossible to reproduce. Current research investigates the primary steps of the process *in vivo* and attempts to mimic the system by the use of chemical models. These primary steps, which begin with the absorption of light, create a pair of radicals which lend themselves well to investigation by methods of electron paramagnetic resonance (EPR). This thesis is concerned with the study of photosynthetic radical pairs by one particular EPR technique: electron spin echo envelope modulation (ESEEM). This experiment can be used to shed light upon the environments in which photosynthesis takes place and is routinely used in the ongoing investigations into this fascinating phenomenon.

1.1 Photosynthesis

Photosynthesis occurs in green plants and in a small number of bacteria. Of the two main types of photosynthesis, aerobic and anaerobic, the former, which involves and evolves oxygen, is the most common. Anaerobic photosynthesis first occurred some three billion years ago, preceeding the involvement of oxygen in aerobic processes by around one billion years. Anaerobic photosynthesis occurs in single-celled bacteria such as the purple bacteria *Rhodobacter (Rb.) sphaeroides* and *Rhodopseudomonas (Rps.) viridis.* Both of these organisms are being used in current scientific studies into this process since, as the evolutionary precursors to better-known photosynthetic systems, they provide a useful starting point. Common (or aerobic) photosynthesis is performed by plants and cyanobacteria (blue-green algae) [1].

The chemical equation governing *all* photosynthesis takes the form

$$H_2A + D \rightarrow A + H_2D.$$

It is the nature of the substrate, H_2A, which determines the characteristics of the reaction. In the case where this substrate is water, the process is the familiar conversion of carbon dioxide and water into oxygen and stored chemical energy in the form of carbohydrate, as performed by plants. In purple bacteria, by contrast, the substrate is H_2S, and this anaerobic reaction is in fact inhibited by the presence of oxygen.

In this thesis, the primary steps of the photosynthetic reaction in the purple bacterium *Rb. sphaeroides* have been studied using simulated EPR data. These primary steps create a charge separation across the bacterial membrane, leading to the production of a radical pair. The spin chemistry involved in these investigations is discussed shortly, in the next section the photosynthetic processes themselves are introduced.

1.1.1 The Photosynthetic Pathway

In all photosynthetic organisms, the primary steps of photosynthesis occur in the reaction centre (RC). Here the absorption of light starts an electron transfer chain which creates a charge separation across the membrane, the first hurdle on the way to completion of the reaction. In multi-celled organisms, such as plants, these reaction centres are found in chloroplasts. The membranes within the chloroplast fold to create stacked thylakoid discs, and the reaction centre lies within the membrane space between the two walls of a disc [2]. Photosynthetic bacteria (including cyanobacteria) contain neither chloroplasts nor thylakoid discs. These single-celled organisms have reaction centres positioned within folds in the cell membrane [3].

Absorption of Light

Photosynthesis begins with the absorption of a photon by a chlorophyll molecule. In plants two different types of chlorophyll, *a* and *b*, are present. These two molecules absorb light in different regions of the visible part of the electromagnetic spectrum: with wavelengths of 620 – 670 nm and 350 – 500 nm for *a* and *b* respectively. Cyanobacteria, which only absorb light in the red region of the spectrum, contain chlorophyll *a* alone. Other photosynthetic bacteria, such as *Rb. sphaeroides*, absorb light using bacteriochlorophylls (BChl). These molecules differ from the chlorophylls found in plants by the conjugation of the cyclo-pentane ring. As with those in plants, there are two distinct types, both of which absorb in the red and infrared ($\lambda > 760$ nm) parts of the electromagnetic spectrum.

Light Harvesting Complexes

The primary steps of photosynthesis use the light absorbed by chlorophyll molecules extremely efficiently. That is to say, almost every photon absorbed by a chlorophyll or bacteriochlorophyll associated with a reaction centre will lead to a charge separation across the photosynthetic membrane. Therefore in the interest of maximising the photosynthetic output of the plant or bacterium, it is important that as many reaction centre chlorophylls as possible are exposed to the light source. To this end photosynthetic systems have developed light harvesting or antenna complexes to funnel the energy from incident light in towards the reaction centre.

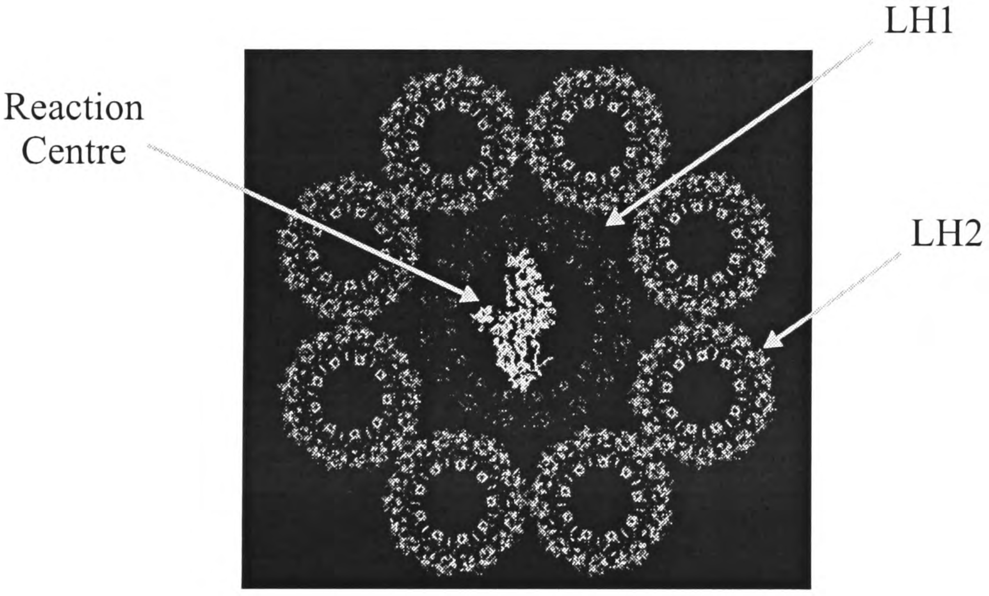

Figure 1.1: Proposed arrangement of the two light harvesting complexes found around the reaction centre of *Rb. sphaeroides* [4–6].

The exact structure of the light harvesting complexes found in bacteria and plants is the subject of a great deal of ongoing research [4–6]. *Rb. sphaeroides* has a strong reason to evolve such antenna complexes since its natural habitat is the water one metre below the surface in ponds and lakes, where it lies in layers. Here the bacteria are isolated from oxygen, which would inhibit photosynthesis in this species, but are also shielded from much of the sun's energy. However, the antenna complexes assist the bacteria in harnessing what little light is available. The proposed arrangement of the two different light harvesting complexes in *Rb. sphaeroides* is shown in Figure 1.1 [4, 7, 8]. The first, LH1, forms a circle of BChl*a*- and BChl*b*-containing species around the reaction centre. LH2 is thought to be a smaller ring, several of which are positioned in a peripheral ring around the LH1 unit. Whatever the exact structure of the antenna complexes, their purpose is clear; the channelling of energy from sunlight into the membrane and to the photosynthetic reaction centre.

1.1.2 The Structure and Function of Bacterial Reaction Centres

The reaction centre of *Rb. sphaeroides* was first isolated by Reed and Clayton in 1968 [9], nearly forty years after its existence was postulated [10]. From that time onwards, research has continuously been done to determine the exact structure and function of this reaction centre. Attention has also been focused on the RCs of the related bacteria *Rps. viridis*, and on the two photosystems forming the reaction centre in plants. The breakthrough in structural determination came with high resolution X-ray crystallography studies, which were used to determine the spatial arrangements in the reaction centre of the cofactors, the electron donors and acceptors, to a resolution of 2 – 3 Å [11]. The determination of the structure of *Rps. viridis* by this method in 1984 earned Deisenhofer and Michel the Nobel Prize [12].

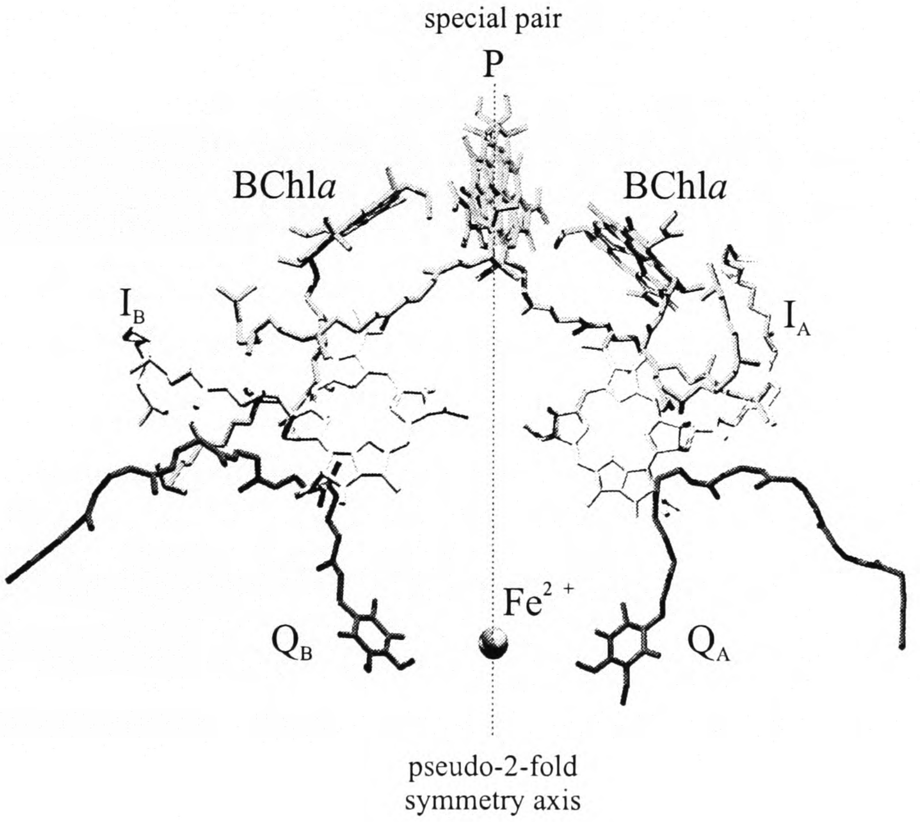

Figure 1.2: The structure of the reaction centre of *Rb. sphaeroides* showing the various cofactors and the pseudo-2-fold axis. P is the "special pair" of bacteriochlorophyll *a* molecules, I denotes the bacteriopheophytin, and Q_A and Q_B the ubi-quinones. The structure of this reaction centre was determined by Allen *et al.* in 1987 [11], and this particular diagram is drawn using the coordinates stored in the Protein Data Base, entry 2RCR [13].

The reaction centre in *Rb. sphaeroides* is attached to the cell membrane via three integral protein subunits known as L (light), M (medium) and H (heavy). The RC contains the following cofactors: four BChl*a* molecules, two of which form a dimer known as the "special pair", P, with the others acting as "voyeurs"; two bacteriopheophytins, I; two ubi-quinones, Q_A and Q_B; and a non-haem high-spin iron cation, Fe^{2+}. These cofactors are arranged, as shown in Figure 1.2 on the previous page, along the L and M subunits of the protein, giving the RC two branches, A and B, and a pseudo-2-fold symmetry axis.

The Reaction Centre in Plants

Photosynthesis in plants takes place in two photosystems known as PSI and PSII. Although each of these units contains the necessary equipment to create a charge separation similar to that in bacteria, in plants the photosystems work in tandem to produce a greater trans-membrane potential. Each of the photosystems has been studied by methods like those used to investigate bacterial reaction centres [14, 15], but both PSI and PSII were found to be far more complex than the bRCs of either *Rb. sphaeroides* or *Rps. viridis*: indeed the structure of PSII has yet to be reliably determined by X-ray crystallography. Plant photosynthesis is not the theme of this thesis and will not be discussed in detail.

1.1.3 Electron Transfer in *Rhodobacter sphaeroides* R26

The primary steps of photosynthesis in *Rb. sphaeroides* are initiated by the absorption of a photon, channelled by the antenna complexes to the special pair of bacteriochlorophylls, P [16]. The excited state P*, created by the addition of energy to the system, now releases an electron, beginning an electron transfer chain which eventually results in a trans-membrane charge separation. Despite the approximate C_2-symmetry present in the RC (Figure 1.2), in almost every case the electron moves down the A-branch of the reaction centre, reaching the acceptor quinone Q_A before crossing to the B-branch and Q_B. The reasons for this behaviour are not fully understood, but given the high symmetry in the RC itself, it is possible that subtle differences in the surrounding protein matrix make passage along the A-branch the more favourable pathway.

The steps of the electron transfer chain are shown schematically in Figure 1.3 overleaf. Assisted by the voyeur BChl*a*, P* donates an electron to the bacteriopheophytin, I, thus creating a charge separated state, the primary radical pair, $P^{+}I^{-}$. The formation of this radical pair occurs in a matter of picoseconds, and the pair is short lived, with I^- surrendering an electron to the quinone, Q_A, a fraction of a nanosecond later. This transfer creates the secondary radical pair, $P^+Q_A^-$. In the laboratory it is possible to halt the electron transfer process here, but under normal biological conditions the transfer can go one step further, with an electron crossing to the B-branch creating $P^+Q_B^-$. This final step takes longer, around 100 μs.

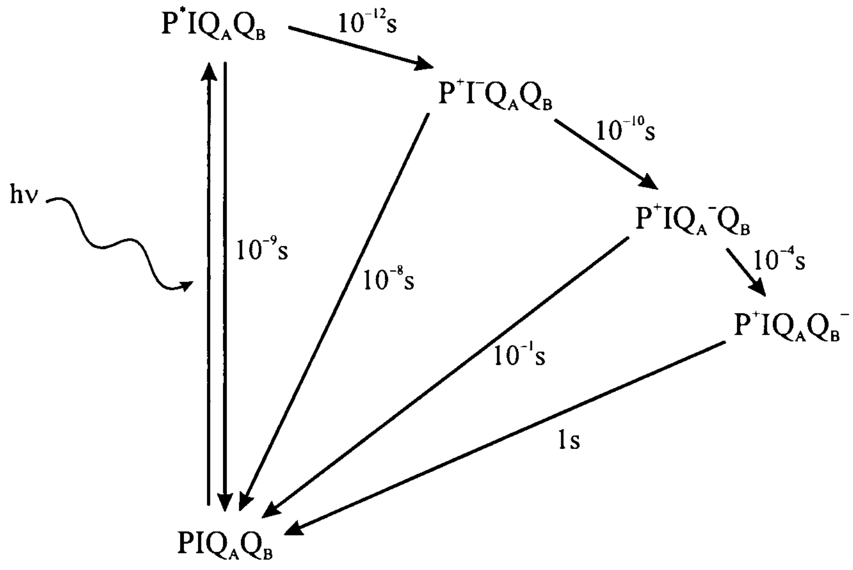

Figure 1.3: Schematic representation of the electron transfer chain in bacterial reaction centres [16]. The y-axis represents the energy of each species.

The beauty of this electron transfer process is its irreversibility. For every step, it is energetically favourable for the electron to move forward rather than backward, and each forward electron transfer happens in a shorter time than the pair would take to recombine. Under certain laboratory conditions, the radical pairs generated in this process can be sufficiently long lived to allow them to be studied by various EPR techniques. An introduction to EPR and its use in the study of photosynthesis follows.

1.2 Introducing the Study of Radical Pairs by EPR

1.2.1 Electron Spins in a Magnetic Field

The first indication of the quantum mechanical phenomenon later to become known as "spin" was given in an experiment performed by Stern and Gerlach in 1921 [17]. On shooting paramagnetic silver atoms through an inhomogeneous magnetic field they observed that the beam split into two bands, and thus concluded that the electron magnetic dipole moment must take discrete values. Four years later Uhlenbeck and Goudsmidt linked electron magnetic moment to the concept of spin angular momentum [18].

Particles are assigned a fixed spin quantum number, s, related to the magnitude of the spin angular momentum, S, by the equation

$$S = \sqrt{s(s+1)}\hbar. \tag{1.1}$$

s will always take integer values for bosons and half-integer values for fermions, and for the electron, $s = 1/2$. The component of S in an arbitrary direction, $m_s\hbar$, can take $2s+1$ values with $m_s = s, s-1, \ldots, -s$. When the electron is placed in a static magnetic field of strength B, the quantisation of S is along the field direction, usually defined as the z-axis in Euclidean space. For an electron m_s takes values of $\pm 1/2$, with these two states denoted α or spin-up ($m_s = +1/2$), and β or spin-down ($m_s = -1/2$) [19,20].

A particle spinning about an internal axis creates an electric current which in turn generates a magnetic dipole moment, $\boldsymbol{\mu_l}$, due to its orbital angular momentum, $\boldsymbol{L}$, also related to its mass, m, and charge, q:

$$\boldsymbol{\mu_l} = \frac{q}{2m}\boldsymbol{L}. \tag{1.2}$$

A particle with spin angular momentum, $\boldsymbol{S}$, creates a magnetic dipole moment, $\boldsymbol{\mu_s}$, where

$$\boldsymbol{\mu_s} = -\boldsymbol{g}\mu_B\boldsymbol{S}. \tag{1.3}$$

As a quantum mechanical particle, the electron will have both spin and orbital angular momenta, and their associated magnetic dipole moments. In equation 1.3 above, μ_B is the Bohr magneton; the electronic charge divided by twice its mass, so that $\mu_B = 9.27 \times 10^{-27}$ JT^{-1}. The $\boldsymbol{g}$-tensor contains information regarding the environment (*e.g.* the effect of spin-orbit coupling) in which the electron sits. If the electron were a point charge in free space, $\boldsymbol{g}$ would be replaced by the scalar quantity, $g_e = 2.0023$. For electrons in atoms and molecules where this is never the case, the g-value deviates slightly from this number and, in the case that the electronic environment is spatially anisotropic, becomes a tensor.

If a magnetic field $\boldsymbol{B}$ is applied, by definition along the z-axis, the component of $\boldsymbol{\mu_s}$ in that direction, $\mu_z = -g\mu_B m_s\hbar$, must be considered. The two possible values of m_s will necessarily give rise to two different dipole moments. Since the energy associated with the magnetic moment in the field is

$$E = -\mu_z B_z, \tag{1.4}$$

then clearly the different values of m_s cause two distinct energy levels, the energy gap between them being defined by

$$\Delta E = g\mu_B B_z. \tag{1.5}$$

This splitting between the two energy levels is known as the Zeeman energy, and is the amount of energy required to generate a transition between the two levels due to the two m_s values. In other words, the Zeeman energy is the amount of energy required to "flip" the electron spin from β to α. In an EPR experiment this energy is applied in the form of electromagnetic radiation (emr) obeying the Planck-Einstein formula: $\Delta E = h\nu$. *Resonance* occurs between the two energy levels in the case where the emr has a frequency ν which satisfies the resonance condition:

$$h\nu = g\mu_B B_z. \tag{1.6}$$

This is the basic principle of EPR: the application of magnetic fields and electromagnetic radiation to systems with unpaired electrons, *i.e.* radicals, in order to cause resonance between the electronic energy levels therein.

1.2.2 Radical Pairs and Magnetic Fields

The attention is now turned to the situation where a pair of coupled, unpaired electrons, a radical pair, interacts with a magnetic field. Section 1.1.3 (page 5) gave details of the formation of radical pairs in the photosynthetic reaction centre, and EPR techniques are widely used to study the nature of such radical pairs. Particular applications are discussed in detail later. First, the interactions occurring in radical pairs are introduced.

Singlet and Triplet States: The Vector Model

The two electrons making up a radical pair (RP) will have their spins aligned in either a parallel or an anti-parallel manner. The alignment of the spins describes the "spin-state" of the RP. If the spins are anti-parallel, the RP is in a singlet state, $|\mathrm{S}\rangle$. Here, both the magnitude of the spin angular momentum, S, and the spin quantum number, m_s, are zero. A triplet state arises if the electron spins are parallel, giving $s = 1$, with the three possible triplet states, $|\mathrm{T}_{-1}\rangle$, $|\mathrm{T}_0\rangle$ and $|\mathrm{T}_{+1}\rangle$, occurring for $m_s = -1, 0$ and $+1$ respectively. In terms of the product basis (the α and β spin states of the individual electrons) the four spins states of the radical pair

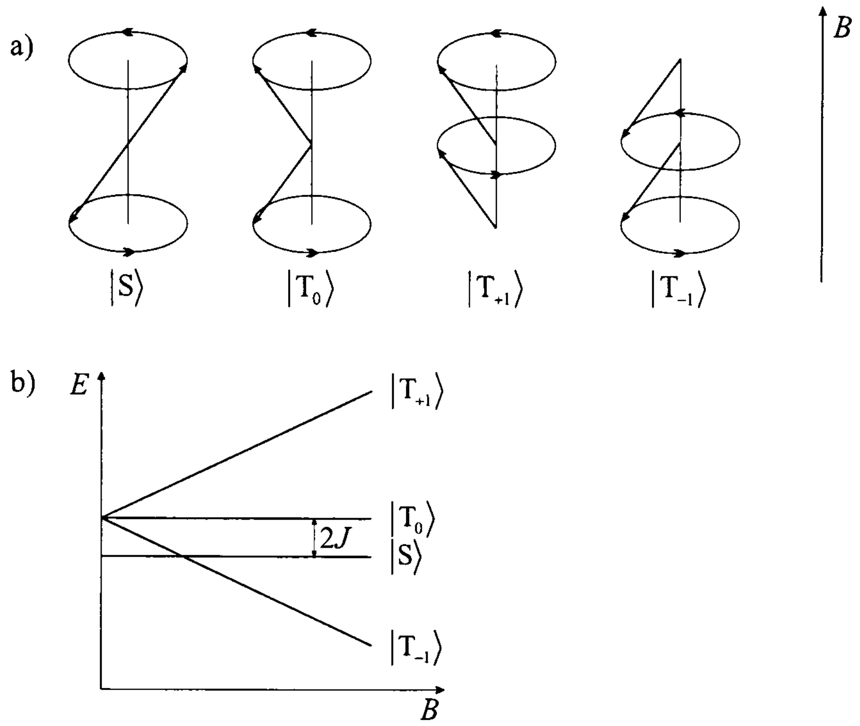

Figure 1.4: a) The Vector Model illustrating the singlet, $|\mathrm{S}\rangle$, and triplet, $|\mathrm{T_0}\rangle$, $|\mathrm{T_{+1}}\rangle$ and $|\mathrm{T_{-1}}\rangle$, states of a radical pair. b) The energies of $|\mathrm{T_{+1}}\rangle$ and $|\mathrm{T_{-1}}\rangle$ change as B increases, but those of $|\mathrm{S}\rangle$ and $|\mathrm{T_0}\rangle$ remain separated by the exchange interaction, J, (see Section 1.2.3). In this example, J is negative.

are:

$$\begin{aligned}
|\mathrm{T_{+1}}\rangle &= |\alpha\alpha\rangle \\
|\mathrm{T_0}\rangle &= \tfrac{1}{\sqrt{2}}(|\alpha\beta\rangle + |\beta\alpha\rangle) \\
|\mathrm{S}\rangle &= \tfrac{1}{\sqrt{2}}(|\alpha\beta\rangle - |\beta\alpha\rangle) \\
|\mathrm{T_{-1}}\rangle &= |\beta\beta\rangle
\end{aligned} \tag{1.7}$$

Figure 1.4a above, illustrates these states using the Vector Model [19–22]. This model, although a classical picture, is useful for describing the precession of spins in a radical pair. The electron spins are represented by arrows of length equal to the magnitude of their spin angular momenta. These spins precess about the field axis at the Larmor frequency of the electron: $\omega_L = g\mu_B B\hbar^{-1}$, tracing out a cone, each half of which has height m_s. Those states with $m_s = 0$, *i.e.* $|\mathrm{S}\rangle$ and $|\mathrm{T_0}\rangle$, clearly have no net contribution in the direction of the magnetic field, and are consequently unaffected by changes in the field strength, B. $|\mathrm{T_{+1}}\rangle$ and $|\mathrm{T_{-1}}\rangle$ however, have a net component of $\boldsymbol{S}$ in the field direction that is equal to $\pm\hbar$ and hence move away from $|\mathrm{S}\rangle$ and $|\mathrm{T_0}\rangle$ with increasing field, as indicated by Figure 1.4b.

Radical Pair Formation

A radical pair will either be spin-correlated or uncorrelated, depending upon its method of formation [23]. Radical pairs formed from a molecular precursor are always spin-correlated, inheriting the spin-state of that precursor. Both the primary and secondary radical pairs of *Rb. sphaeroides* formed by the electron transfer chain are spin-correlated radical pairs (SCRP) formed in the singlet state. Uncorrelated radical pairs arise when two radicals come together independently to form the pair, for example two radicals colliding in solution, or when an RP is formed as a result of two independent electron transfer processes, an example of which is described in Chapter 3.

In uncorrelated radical pairs, the populations of the four spins states are governed solely by the Boltzmann distribution, with one quarter of the pairs formed in singlet states, and the rest in triplet states. Figure 1.5a shows the populations of the states, and the EPR spectrum thus created. All four lines (corresponding to the four possible single quantum transitions between the states, i.e. $|1\rangle \leftrightarrow |2\rangle$, $|1\rangle \leftrightarrow |3\rangle$, $|2\rangle \leftrightarrow |4\rangle$ and $|3\rangle \leftrightarrow |4\rangle$) are in absorption, leading to the absorptive spectrum shown. In contrast to this, a singlet-born SCRP will only occupy those spin states with singlet character. In Figure 1.5b these are the states labelled $|2\rangle$ and $|3\rangle$ (Chapter 2 contains a detailed explanation). Hence both absorptive and emissive single quantum transitions occur in an SCRP, giving rise to an anti-phase EPR line-shape.

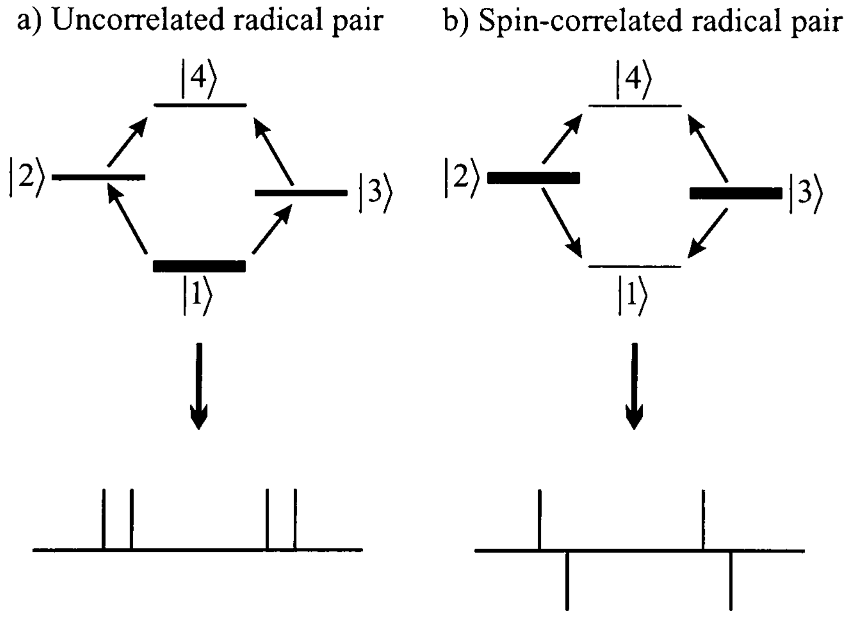

Figure 1.5: Populations of spin states for a) uncorrelated and b) spin-correlated radical pairs. The thickness of the bars indicates the population of each state. Transitions between spin states give rise to the EPR spectra shown.

1.2.3 Interactions in Radical Pairs

Spin-Spin Interactions

Between the two electrons in a radical pair, two types of "spin-spin" interaction are present. The first of these, the **exchange interaction**, J, is an electrostatic interaction arising from the Pauli Exclusion Principle, which is dependent upon the extent of overlap between the wavefunctions of the two electrons [24, 25]. It is this interaction which causes the splitting apart of the energies of the singlet and triplet states, shown in Figure 1.4b. The exchange interaction is described by the spin Hamiltonian

$$\hat{\mathrm{H}}_{\mathrm{ex}} = \hat{\boldsymbol{S}}_1{}^T \cdot \boldsymbol{J} \cdot \hat{\boldsymbol{S}}_2 + \hat{\boldsymbol{S}}_2{}^T \cdot \boldsymbol{J} \cdot \hat{\boldsymbol{S}}_1,$$

where $\hat{\boldsymbol{S}}_i$ is the spin angular momentum operator for electron i, and $\boldsymbol{J}$ is a tensor describing the coulombic interaction between the two electrons. When radicals tumbling randomly in solution are considered, $\boldsymbol{J}$ is isotropic, but in all other cases the exchange interaction does have some degree of anisotropy. However, when dealing with frozen solutions of photosynthetic radical pairs it is possible to consider the anisotropic part of $\boldsymbol{J}$ as indistinguishable from that part of the dipolar tensor, $\boldsymbol{D}$. Hence only the isotropic part of the exchange interaction, $\hat{\mathrm{H}}_J$, is used:

$$\hat{\mathrm{H}}_J = 2J\hat{\boldsymbol{S}}_1{}^T \cdot \hat{\boldsymbol{S}}_2, \tag{1.8}$$

where J is the isotropic part of $\boldsymbol{J}$. Since J is largely coulombic, its value is tied closely to the distance between the electrons. It is thought that J falls exponentially with the inter-radical distance, r, so that in the secondary radical pair of *Rb. sphaeroides*, where r is of the order of 30 Å, J is sometimes assumed to be zero.

The second spin-spin interaction in a radical pair is the magnetic **dipolar interaction**. This arises from the dipole-dipole coupling between the magnetic moments of the electrons, and is analogous to the classical dipole interaction between a pair of bar magnets. Again, if the radical pairs are tumbling in solution, the dipolar coupling averages to zero, but in the systems considered in this work this interaction is anisotropic with magnitude, D, proportional to r^{-3}. The dipolar coupling is also the origin of the zero field splitting, which removes the degeneracy of the three triplet levels of a radical pair, even in the absence of a magnetic field. The spin Hamiltonian for the dipolar interaction $\hat{\mathrm{H}}_D$ is defined as:

$$\hat{\mathrm{H}}_D = \hat{\boldsymbol{S}} \cdot \boldsymbol{D} \cdot \hat{\boldsymbol{S}}, \tag{1.9}$$

where $\hat{\boldsymbol{S}} = \hat{\boldsymbol{S}}_1 + \hat{\boldsymbol{S}}_2$, and $\boldsymbol{D}$ is the dipolar coupling tensor, a traceless 3 × 3 matrix.

Interactions with other Spins: The Hyperfine Interaction

In direct analogy with the coupling present between two electrons, the hyperfine tensor $\boldsymbol{A}$, describing the interactions between an electron and a magnetic nucleus, has two contributions. The first of these is an isotropic contribution brought about by the Fermi contact interaction between an electron and a nuclear spin [19, 20].

This interaction is non-zero only when the electron has a finite probability of being found at the nucleus, and thus is only present when the spin density has some s-character. The remainder of $\boldsymbol{A}$ is the electron-nuclear counterpart of the dipolar interaction discussed above.

The spin Hamiltonian describing the hyperfine coupling between an electron and a single nucleus can be written:

$$\hat{\mathrm{H}}_{\mathrm{hfc}} = \hat{\boldsymbol{S}} \cdot \boldsymbol{A} \cdot \hat{\boldsymbol{I}}. \tag{1.10}$$

In the above equation, $\hat{\boldsymbol{I}}$ is the total spin angular momentum operator for the nucleus (analogous to $\hat{\boldsymbol{S}}$ for the electron), and $\boldsymbol{A}$ is the full hyperfine tensor. $\hat{\mathrm{H}}_{\mathrm{hfc}}$ is the sum of the isotropic, $\hat{\mathrm{H}}_{\mathrm{i}}$, and anisotropic, $\hat{\mathrm{H}}_{\mathrm{a}}$, contributions:

$$\hat{\mathrm{H}}_{\mathrm{i}} = A\hat{\boldsymbol{S}} \cdot \hat{\boldsymbol{I}} \quad \text{and} \quad \hat{\mathrm{H}}_{\mathrm{a}} = \hat{\boldsymbol{S}} \cdot \boldsymbol{T} \cdot \hat{\boldsymbol{I}}. \tag{1.11}$$

A and $\boldsymbol{T}$ are the isotropic hyperfine coupling constant and hyperfine tensor describing the anisotropic interaction respectively. Since $\boldsymbol{T}$ reflects the dipolar coupling between the spins, and is therefore purely anisotropic, it is always traceless. It is possible to choose a particular axis system (the principal axis system), in which $\boldsymbol{T}$ is also diagonal. However, in an ensemble such as a liquid or a frozen solution, the molecules take many different orientations and $\boldsymbol{T}$ will contain off-diagonal elements. In liquids the situation is of course simplified by the rapid tumbling of the molecules, which causes the dipolar interaction to average to zero. In solids and in frozen solutions, where this is not the case, the system is anisotropic and $\boldsymbol{T}$ is always a tensor.

Fortunately, the hyperfine tensor, $\boldsymbol{A}$, can be simplified by considering the interaction between a magnetic field and the electron spin. In the presence of a strong magnetic field, applied along the z-axis in the laboratory frame, the total spin angular momentum of the electron, $\hat{\boldsymbol{S}}$, will become quantised in this direction. Contributions to $\boldsymbol{A}$, therefore only come from those matrix elements of $\hat{\boldsymbol{S}}$ which are dependent upon $\hat{S}_z$. The spin angular momentum of the nucleus is also quantised. However, since the interactions between the nucleus and the field are 660 times weaker than those between the electron and the field, the influence of the field on $\hat{\boldsymbol{S}}$ is greater than on $\hat{\boldsymbol{I}}$. Therefore, provided the field is not so strong that the total nuclear Zeeman splitting is far greater than the hyperfine interaction, this interaction is still expressed by terms dependent upon $\hat{I}_x$ and $\hat{I}_y$. The simplified hyperfine tensor will thus contain only two parts: the *secular* hyperfine coupling, $\hat{S}_z\hat{I}_z$, and the *pseudo-secular* hyperfine coupling, $\hat{S}_z\hat{I}_x$. The latter should more rigorously also have a contribution from $\hat{S}_z\hat{I}_y$. However the term containing $\hat{I}_y$ can be neglected since it is always possible to rotate the nuclear coordinates in such a way that $\hat{S}_z\hat{I}_y$ vanishes.

The effect of the hyperfine spin Hamiltonian

$$\hat{\mathrm{H}}_{\mathrm{hfc}} = a\hat{S}_z\hat{I}_z + b\hat{S}_z\hat{I}_x \tag{1.12}$$

upon the radical pair is to alter the energy gap between the nuclear spin states, and to cause a degree of mixing of the nuclear sub-levels associated with a particular electronic state, thus allowing nuclear "spin-flips". In the event that b is zero, the hyperfine coupling is purely isotropic. The precise effect of the hyperfine interaction upon the energy levels within the radical pair is discussed in greater detail in Chapter 2.

1.2.4 The Study of Photosynthetic Radical Pairs.

EPR offers some ideal methods for the study of the radical pairs formed in the primary stages of photosynthesis. Indeed, photosynthesis has even been called the "Garden of Eden of the EPR spectroscopist" [26]. Since interest in the photosynthetic reaction centre first arose, EPR techniques have been used together with X-ray crystallography and optical spectroscopy methods to characterise and explore the cofactors within. A number of reviews have been written which describe in detail the research in this area, and the position taken by EPR (see for example [14, 15, 27–30]); the following section gives a few examples.

Prior even to the determination of the structures of the reaction centres of *Rps. viridis* [12] and *Rb. sphaeroides* [11] by X-ray crystallography in the 1980's, EPR methods had made their mark on photosynthesis research, when EPR and electron-nuclear double resonance (ENDOR) studies deduced that the primary donor in bacterial reaction centres is a bacteriochlorophyll dimer [31, 32]. Today, work continues in an attempt to unambiguously determine the structure of PSII in plants, and research is providing a greater understanding of all the processes occuring during the electron transfer chain.

Electron spin echo envelope modulation (ESEEM) is often used alongside ENDOR to explore the interactions between unpaired electrons and neighbouring nuclei, and to determine hyperfine coupling constants (for an example see [33]). ESEEM is also a useful tool for the study of the spin-spin interactions between the unpaired electrons in a radical pair [34–36]. Studies of this nature, as well as experiments involving the selective excitation technique electron-electron double resonance (ELDOR), continuous wave (cw) and Fourier transform (FT) EPR [37, 38] are used to determine the values of the dipolar and exchange coupling constants. Studies which look at the individual radicals created in the electron transfer chain are also performed. ENDOR and the related electron-nuclear-nuclear TRIPLE resonance technique are currently being used to determine the spin-densities on the various cofactors in the RC [39], and since its advent in 1976 [40], high-field (95 GHz and above) EPR has proved extremely useful in determining the anisotropy of the g-tensors of cofactors such as P^+ and Q_A^- [41–43]. In addition, optical spectroscopy has also proved invaluable in studies of the kinetics of charge separation [44] and the nature of temperature-induced changes in reaction centre structures [45–47].

Photosynthetic reaction centres grown as single crystals or made into frozen solutions for the purpose of research by EPR are rarely used in their native states. The presence of the high-spin non-haem iron, Fe^{2+}, causes a large amount of broadening in the EPR spectrum, and is therefore commonly replaced by a diamagnetic Zn^{2+} ion. Problems also occur because of unresolved hyperfine couplings between protons and unpaired electrons, leading to partial or complete deuteration of many samples. Occasionally other isotopic exchanges are made; spin-1/2 ^{15}N for ^{14}N, or ^{13}C for ^{12}C, so that a clearer picture of the effect of the nuclei present can be gained. Models of either a mathematical or a molecular nature are also widely made, to assist in the understanding of the photosynthetic reaction. Mathematical models created for the purpose of analysing and predicting the output of experiments with ESEEM are the subject of this thesis.

1.3 Electron Spin Echo Envelope Modulation

In the context of the study of photosynthetic reaction centres, electron spin echo envelope modulation is one of the most useful techniques available. ESEEM is a type of pulsed EPR experiment yielding spin echoes, which can be used either to study individual radicals, giving information about hyperfine couplings to surrounding magnetic nuclei, or to explore the interactions, *i.e.* the spin-spin couplings, between the two unpaired electrons of a radical pair. ESEEM is frequently used to study the radical pairs formed in the electron transfer chain in the reaction centres of photosynthetic organisms such as *Rb. sphaeroides* and the two plant photosystems. The experiment can give information on, amongst other things, the separation of the radicals [34, 36, 48–52]. A detailed account of the theory used to analyse ESEEM data is given in Chapter 2, and the following section describes the mechanics of the experiment.

1.3.1 Pulsed EPR

In continuous wave (cw) EPR spectroscopy, a large static field $\boldsymbol{B}_0$ is applied to a sample, and transitions between the resulting spin states are excited by incident radiation (usually in the microwave (mw) region of the electromagnetic spectrum). This is also true of nuclear magnetic resonance (NMR), but here, the use of Fourier transform NMR since the 1970's has virtually consigned the cw experiment to history. The stronger interactions, faster relaxation and considerably higher frequencies associated with EPR transitions are principally responsible for the delay in the development of pulsed EPR methods, and it is only in the last 20 years that this field has grown.

The Use of Pulses in EPR

While a cw EPR experiment can only excite transitions at one frequency at a time, a pulse of electromagnetic radiation (emr) contains a range of frequencies and can consequently excite many EPR transitions at once. Indeed, if the EPR spectrum of the sample is sufficiently narrow, *i.e.* the spread of transition frequencies is smaller than the *band-width* of the pulse, then a single mw pulse, placed at the centre of the spectrum, can excite all of the transitions simultaneously. A pulse of length t_p with frequency ω_{mw} can be thought of in the simplest terms as a linearly oscillating magnetic field, with oscillations of amplitude B_1 at frequency ω_{mw}. The full picture however is more complex. The pulse also contains all frequencies in (and just outside of) the range defined by $\omega_{\mathrm{mw}} - 1/t_p \leq \omega_{\mathrm{mw}} + 1/t_p$, with amplitudes dependent upon the distance from ω_{mw}. The band-width of the pulse, *i.e.* the range of frequencies it can excite, is thus inversely proportional to the pulse length, so that a 50 ns pulse has spread of frequencies twice as broad as a 100 ns pulse.

With regard to the ESEEM experiment, this is very important. A short pulse with a broad frequency range, covering the whole of the EPR spectrum, is known as a *hard* pulse, while a longer, narrower pulse is *soft*. When used to study the interactions between the radicals in an RP, ESEEM generally requires non-selective excitation of the EPR spectrum, and hard pulses are used. However, as will be discussed in Chapter 5, it is possible to do ESEEM on radical pairs with selective excitation, so that by applying a soft pulse, only a small number of EPR transitions are excited.

The Effect of a Pulse: The Rotating Frame

The effect of mw pulses upon the magnetisation created by a static field is best understood in terms of the rotating frame. The effect of a strong magnetic field, $\boldsymbol{B}_0$, on a collection of electron spins is to remove the degeneracy of the m_s levels, and to cause the spins to precess about the axis of the field (usually the z-axis) at their Larmor frequencies, $\omega_L = \mu_B g \hbar^{-1} B_0$. ω_L is thus tied to the strength of this magnetic field. EPR experiments are performed at a range of field strengths, and this thesis deals with two: X-band, $B_0 \approx 3400$ G, and W-band, $B_0 \approx 34,000$ G. The precession of spins can be described by the Vector model picture shown in Figure 1.6a. Since both m_s states are occupied, the spins trace out a double cone, each half of which has height 1/2. Prior to the application of mw pulses, no coherence exists between the spins, that is they lie randomly, and therefore evenly distributed about the face of the cone. The Boltzmann distribution ensures that there is an excess of spins in the lowest energy level, which leads to a net magnetisation in the field direction, $\boldsymbol{M}$ (Figure 1.6b).

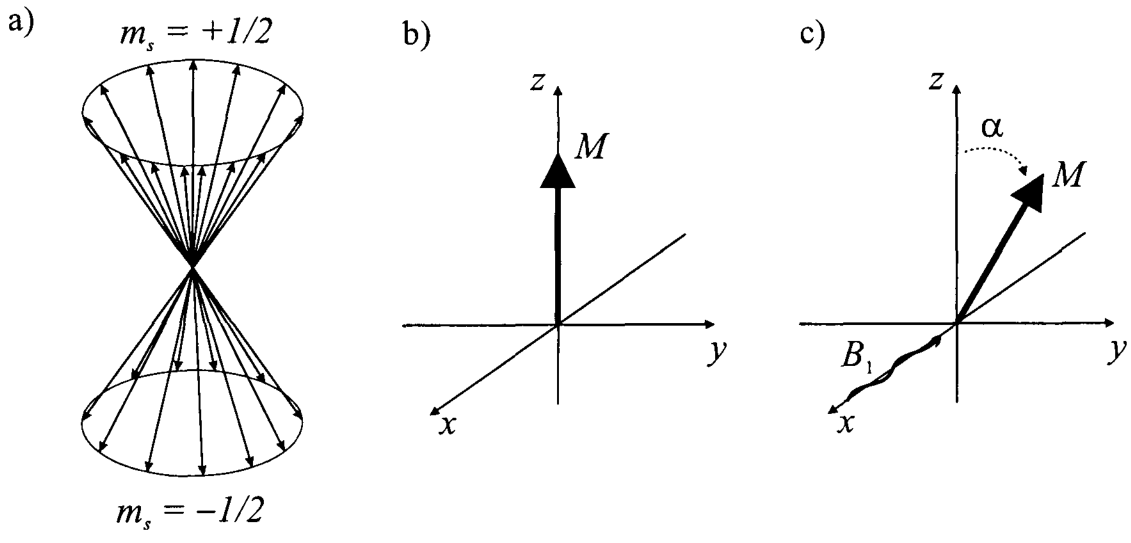

Figure 1.6: a) The Vector model showing electron spins precessing with their Larmor frequencies, ω_L, about the axis of an applied static magnetic field, $\boldsymbol{B}_0$. b) The slight excess of spins in the $m_s = +1/2$ level leads to a net magnetic moment, $\boldsymbol{M}$. c) The effect of an oscillating magnetic field of strength B_1 applied along the x-axis. In the rotating frame $\boldsymbol{M}$ tilts in the yz-plane towards the y-axis.

A mw pulse is now applied along the x-axis. Considering first the case where the pulse is *on resonance*, *i.e.* $\omega_{\mathrm{mw}} = \omega_L$, this pulse is a magnetic field of amplitude B_1 oscillating at ω_L along the x-axis. For convenience, this linearly oscillating field can be viewed as the sum of two counter-rotating components, one of which rotates in the same sense as the spins, with frequency ω_L, and the other in the opposite sense. This latter component does not have a significant effect on the precessing spins, and is neglected. The component rotating with the spins will have the effect of flipping them, and therefore $\boldsymbol{M}$, into the xy-plane. Since both the field and the spins are rotating at the Larmor frequency, this is best viewed in the rotating frame, which itself rotates at this frequency. Hence, in this frame of reference, the movement of $\boldsymbol{M}$ caused by the pulse is a rotation towards the y-axis in the yz-plane, as shown in Figure 1.6c.

For the case of a rectangular pulse exactly on resonance with the Larmor frequency of the spins in the sample, the angle α, through which the net magnetisation $\boldsymbol{M}$ rotates, is determined by the strength of the pulse, B_1, and its duration, t_p, such that:

$$\alpha = \gamma B_1 t_p \tag{1.13}$$

where $\gamma = \mu_B g \hbar$. This means that experiments using weak pulses need longer pulse durations in order to achieve the same flip angle. If the pulse is not exactly on resonance with the spins, then off-resonance effects result. The pulse strength away from the resonance position, B_{eff}, is greater than B_1, and gives rise to a flip-angle $\alpha_{\text{eff}} = \gamma B_{\text{eff}} t_p$. Off-resonance effects are discussed in greater detail in Chapters 3 and 5.

Immediately after the mw pulse is switched off, the system is driven to return to its equilibrium state. This happens by spin-lattice (or longitudinal, T_1) and spin-spin (T_2) relaxation. Spin-lattice relaxation strives to return z-magnetisation to equilibrium. For example, after the application of a $(\pi/2)_x$-pulse, the magnetisation vector, $\boldsymbol{M}$, lies along the y-axis, and no z-magnetisation is present, *i.e.* $M_z = 0$. The return of longitudinal magnetisation due to T_1 is described by the Bloch equation [53],

$$\frac{\mathrm{d}M_z}{\mathrm{d}t} = \frac{M_0 - M_z}{T_1}$$

where M_0 is the z-magnetisation at equilibrium. The second relaxation process, described by T_2, reduces the transverse (measurable x, y) magnetisation by removing coherence between the spins. Again, using the Bloch equations, where $i = x$ or y,

$$\frac{\mathrm{d}M_i}{\mathrm{d}t} = -\frac{M_i}{T_2}.$$

T_2 has the effect of broadening experimental EPR spectra. It can be measured by a simple spin-echo experiment, described in the next section.

1.3.2 The Spin Echo Experiment and ESEEM

The spin-echo experiment by which ESEEM is measured is the EPR analogue of a pulsed NMR experiment devised by Hahn in 1950 [54]. This experiment is described below, and the move to EPR and to ESEEM explained later.

The Hahn Echo in NMR

In a Hahn echo experiment on a system of nuclear spins, two radio frequency (rf) pulses, separated by the time-delay τ, are applied to a sample. The first of these pulses, a $(\pi/2)_x$-pulse, flips the spins into the y-axis. In the rotating frame it is easy to see that if all the spins in the sample are on resonance with the pulse, the decay of transverse magnetisation along the y-axis is purely due to the T_2 relaxation. However, inhomogeneities in the magnetic field, and the different chemical shifts for different spins in the sample, mean that the frequencies at which the spins rotate about the field axis are not identical. Thus the spins "fan out" in the xy-plane resulting in a decay in the magnetisation. If a second pulse[1] is applied at time τ after the first, then an *echo* is observed at time 2τ. Figure 1.7, on the next page, describes the spin-echo experiment on a pair of heteronuclear spins.

The NMR spectrum shown in Figure 1.7a is that of a pair of heteronuclear coupled spins, for example ^{1}H and ^{13}C. The extremely large difference in chemical shifts between the two spins, labelled I and S, means that it is only possible to excite one of them with an rf pulse. The effect of the pulse sequence upon the I spin is depicted in Figure 1.7b. As predicted, the first pulse flips the I-spins onto the y-axis, where the different nuclear Larmor frequencies, due to coupling to the S-spins, cause the I-spins to fan out. Here the I-spin coupled to α_S moves slower than that coupled to β_S. When the second pulse is applied at time τ, it affects only the I-spins as shown, flipping the magnetisation about the x-axis. Now, since the spins are moving back together rather than farther apart, at 2τ the magnetisation is refocussed. The loss of intensity in the magnetisation at the echo is due entirely to T_2 and, by varying the delay period, this experiment can be used to measure this relaxation time (Figure 1.7c).

---

[1] Hahn originally used a second $(\pi/2)_x$-pulse for this purpose. It was pointed out by Carr and Purcell however, that a π_x-pulse is more advantageous [55].

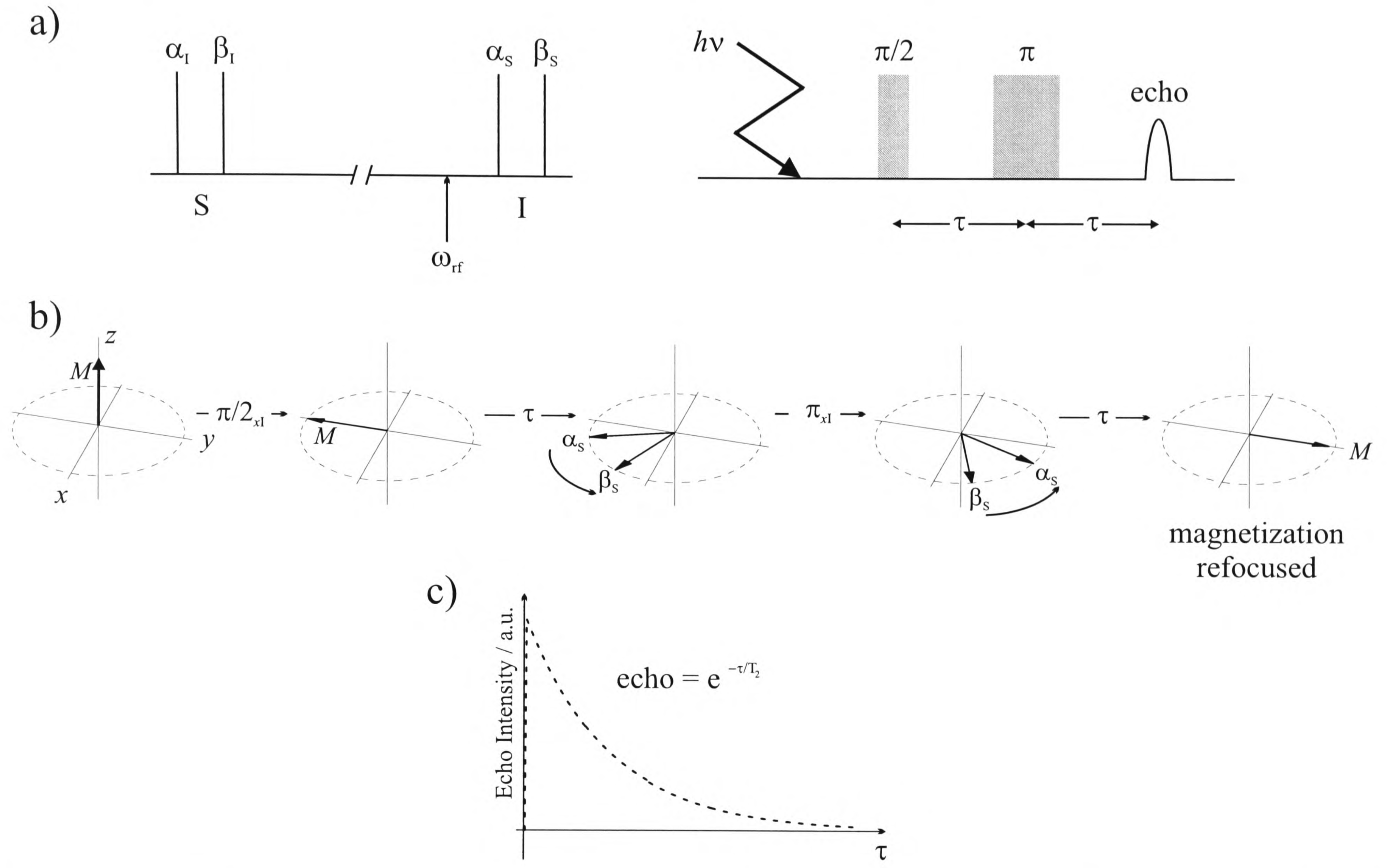

Figure 1.7: The Hahn echo experiment. a) NMR stick spectrum for a heteronuclear system. The two components of the spectrum are of very different chemical shifts such that the rf pulse applied at ω_{rf} can only affect I. The pulse sequence for the experiment is also shown. b) The Vector model representation of the effect of the pulse sequence upon the I-spins. c) Varying the delay time, τ allows a measurement of the transverse relaxation time, T_2 to be made.

Electron Spin Echoes and Echo Modulation

The description of the Hahn echo given above is accurate not only in NMR where heteronuclear spins are considered, but also for some situations in EPR. If an electron is coupled to a nucleus by a purely isotropic hyperfine interaction, similar results are seen. However, electron spin echo experiments on other systems can cause *modulated* signals, from which a wealth of different information may be obtained. For example, an electron-nuclear hyperfine interaction in either a solid or a frozen solution will have an anisotropic contribution. The strength of this coupling can be determined by analysing the modulation of electron spin echoes. Echo modulation also occurs in coupled radical pairs. Here, microwave pulses broad enough to cover the entire EPR spectrum of the pair are used to determine the spin-spin couplings, D and J. The principle difference between the ESEEM arising from an electron-nuclear interaction and an electron-electron interaction, is that in the former case, modulations occur only when there is an anisotropic interaction. This will cause mixing of the nuclear sub-levels, and thus allow otherwise forbidden transitions (*i.e.* nuclear spin-flips) to be excited. Electron-electron modulations can be observed whether the spin-spin coupling is isotropic or anisotropic, and rely only upon allowed transitions. It is the latter case which is described below.

The ESEEM experiment performed on a radical pair is explained using a modification of the Vector model shown in Figure 1.7. Modulation occurs because both spins in the radical pair are affected by the mw pulses. In the absence of anisotropic hyperfine couplings, this is the condition for ESEEM to occur. The stick spectrum shown in Figure 1.8a (next page) represents that of an uncorrelated, coupled radical pair. If hard mw pulses are applied in accordance with the pulse sequence given in Figure 1.7a, with frequency ω_{mw} in the centre of the spectrum, then the behaviour of the spins is shown in Figure 1.8b.

Concentrating once again on the I-spin, the first pulse flips the magnetisation onto the y-axis exactly as before. The spins then fan out at a rate dependent upon the S-spin to which they are coupled; here that coupled to α_{S} is the slower. The difference between this experiment and the Hahn echo arises with the application of the second pulse. In the heteronuclear case, the second pulse (as the first) could only affect the I-spin. In a radical pair however, the pulses affect both I and S, so that not only is the magnetisation due to I flipped about the x-axis, but also that due to S. This has the effect of interchanging the S-spins to which the components of

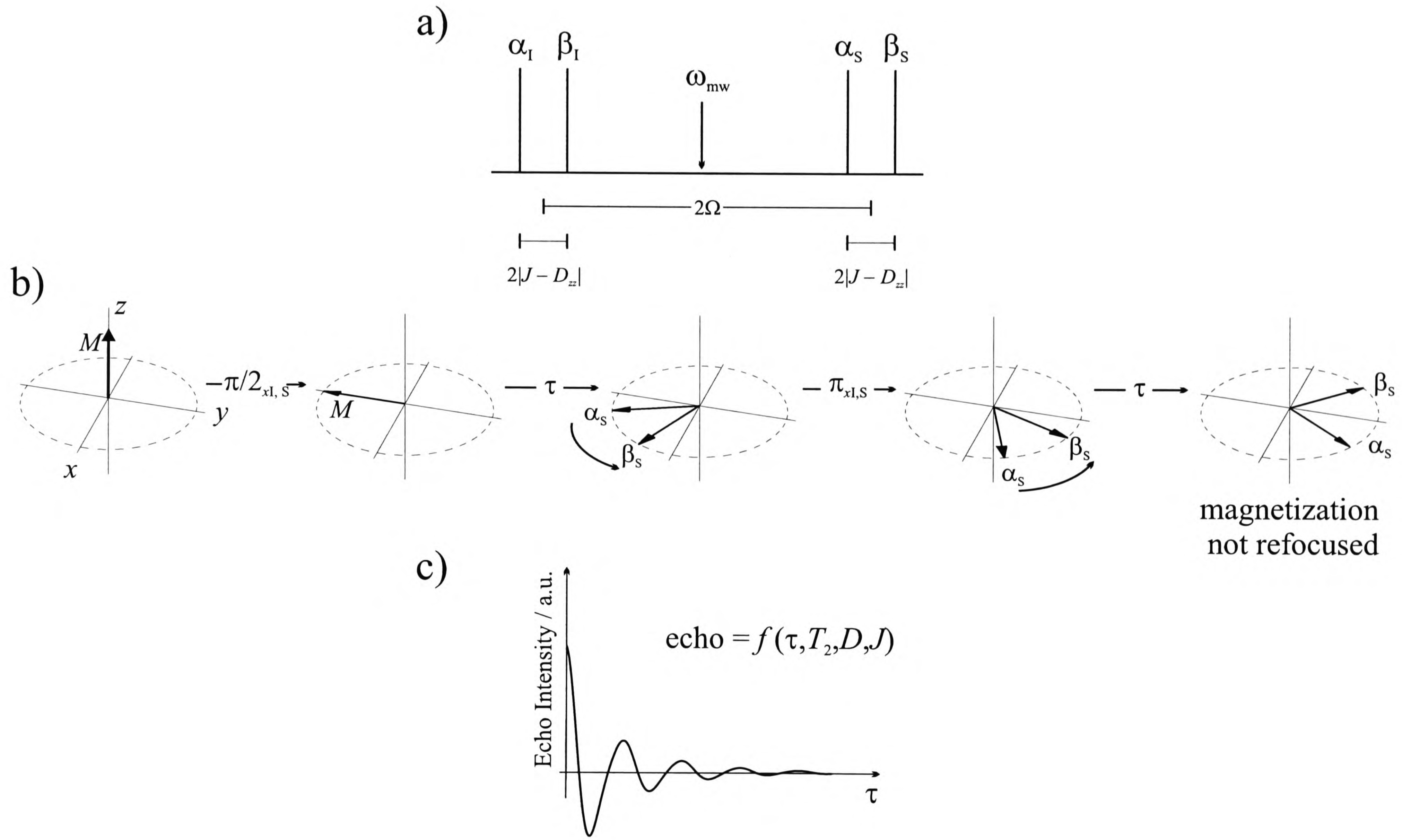

Figure 1.8: The ESEEM experiment for a radical pair. a) The EPR spectrum of two electron spins coupled via an exchange, J, and a dipolar, D, interaction. D_{zz} is the component of the dipolar interaction in the field direction. The two components of the spectrum are spaced by $\Omega = \sqrt{(J + D_{zz}/2)^2 + (\omega_I - \omega_S)^2}$, and each is spilt by the spin-spin coupling. b) The Vector model for this system showing the effect on I of the pulse sequence (shown in Figure 1.7a) with pulses applied in the centre of the EPR spectrum at ω_{mw}. c) The resulting modulated echo depends upon the strength of the spin-spin couplings and the transverse relaxation time, T_2.

I are coupled, as shown. Rather than coming back together at 2τ, the spins actually move further apart, so that at this time they lie either side of the y-axis and the magnetisation is not refocused.

Since it is the strength of the coupling between the electrons (*i.e.* the dipolar and exchange interactions) which determines the relative speeds of the I-spins in the xy-plane, and hence the position of the spins at 2τ, measurement of the strength of the echo with changing delay gives information about these couplings. A simulation of a typical ESEEM spectrum for the radical pair considered is shown in Figure 1.8c. Rather than the smooth exponential decay due solely to T_2, a cosine modulated echo dependent upon τ, T_2, D and J is seen. The precise nature of this echo is explained in Chapter 2, and is explored throughout this thesis.

Chapter 2

ESEEM for the Determination of D and J in $P^+Q_A^-$

Electron spin echo envelope modulation (ESEEM) is widely used in studies of photosynthetic radical pairs for determination of the spin-spin coupling parameters D and J [34–36, 48–52, 56–60]. The secondary radical pair in *Rb. sphaeroides*, $P^+Q_A^-$, is one such species studied by this method. This chapter introduces and investigates the model used to interpret experimental ESEEM data. The effects of including anisotropic hyperfine couplings, which are usually neglected in the model, are also considered.

2.1 Introduction

Previous ESEEM studies on the secondary radical pair of *Rb. sphaeroides* have been performed on both frozen samples of bacterial reaction centres extracted from the organism [34, 49–51, 56, 57], and on single crystals of reaction centres grown in the laboratory [61, 62]. In single crystal studies the sample is placed at an angle to the field and measurements are taken as a function of this angle so that one particular orientation of the radical pair unit cell is considered at a time. These experiments can be used to highlight the anisotropy in the system, which arises from the dipolar and hyperfine interactions and anisotropic g-tensors. Studies on frozen solutions consider all orientations of $P^+Q_A^-$ at once, giving a powder pattern effect which can be used to find the magnitude of the couplings D and J, but which provides no information about the orientation of the radical pair relative to the membrane. In some cases however, studies on frozen solutions can be used to investigate the relative orientations of the two radicals (see Chapter 5). In most EPR experiments Fe^{2+} is replaced by diamagnetic Zn^{2+}. This is done to prevent the the paramagnetic iron atom (which is close to the quinone) broadening the spectrum of $Fe^{2+}Q_A^-$ to the extent that only the P^+ part of the radical pair spectrum is seen. In addition reaction centres are usually grown in fully deuterated form [63] to reduce the broadening caused by unresolved hyperfine couplings to protons.

ESEEM experiments on $P^+Q_A^-$ have hitherto been almost exclusively performed at X-band, i.e, at 9.0 GHz/3,300 G with very short (*e.g.* 10 – 20 ns) pulses. Echo modulations are only observed when both radicals are excited simultaneously. At 9 GHz, the EPR spectrum of $P^+Q_A^-$ has a width of around 20 G. At this frequency a π-pulse of around 20 ns duration has an excitation band width of just under 10 G. Although this pulse is not wide enough to cover the whole spectrum of $P^+Q_A^-$ and be completely non-selective, it can be used to perform the experiment successfully. Figure 2.1 shows that if the pulse is applied at the correct frequency in the centre of the spectrum, both radicals are excited equally and echo modulation will be observed.

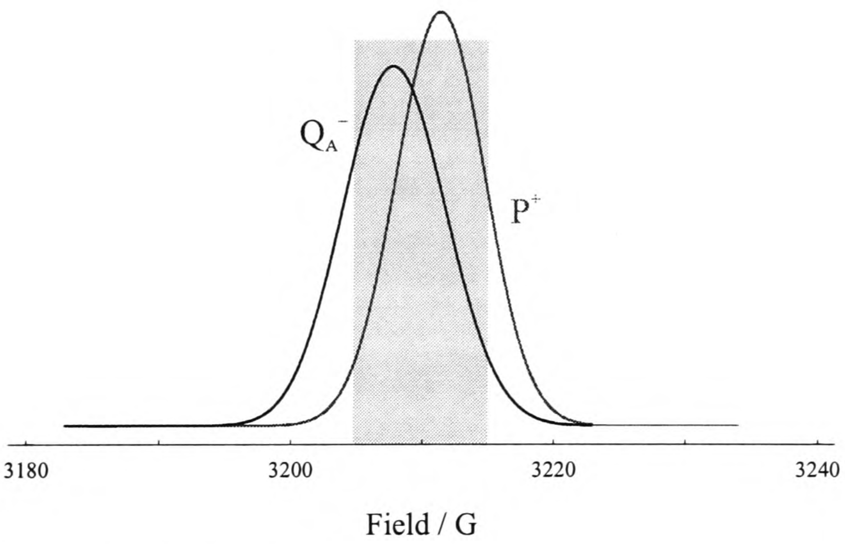

Figure 2.1: X-band EPR spectra of the individual radicals P^+ and Q_A^- in *Rb. sphaeroides.* The shaded area shows the part of the EPR spectrum excited fully by a 10 G microwave pulse applied at 3210 G. Experimentally, pulses are Gaussian rather than square.

The electron transfer chain is initiated by a laser flash which within 500 ps creates first the primary and then the secondary radical pair. The transfer of the electron onto Q_B is blocked at cryogenic temperatures [64], except for native reaction centres frozen under constant illumination [65]. Alternatively the transfer can be prevented either by pre-reduction to Q_B^- or by the removal of this quinone. It is then the secondary radical pair which is subjected to mw pulses of flip angles β and γ along the x-axis (Figure 2.2, overleaf). The ESEEM spectrum is built up by repeated experiments performed at different values of τ.

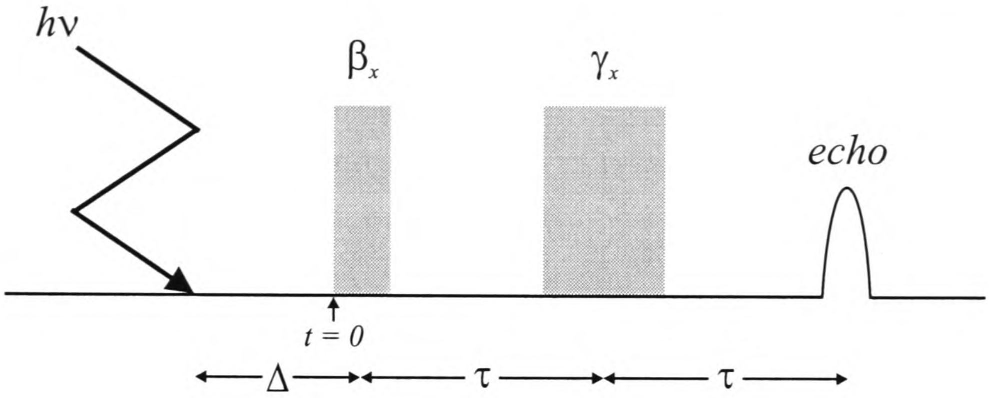

Figure 2.2: The pulse sequence for the ESEEM experiment. Charge separation is created by a laser flash before the two microwave pulses are applied. Usually $\gamma = 2\beta$. The relaxation period, Δ, is kept constant at a value of about 100 ns so that zero quantum coherence relaxes before the β is applied. Echos are recorded in the x- (out-of-phase) or y- (in-phase) channels or both depending upon the nature of the radical pair being studied.

Since $P^+Q_A^-$ is formed from a singlet molecular precursor, it is created in a spin-correlated state[1]. This greatly influences the shape of the ESEEM spectrum, giving it an anti-phase nature. Radical pairs are not always spin-correlated, an example being the pair $Q_A^-Q_B^-$ which is discussed in Chapter 3. $Q_A^-Q_B^-$ is the product of two consecutive reactions and consequently has populations governed by the Boltzmann distribution, which results in a very different spectrum to that seen for $P^+Q_A^-$. In the next section the mathematical model used to interpret spin echo modulation data is considered for the general case (*i.e.* such that it can be applied to either strongly or weakly coupled spin-correlated or uncorrelated radical pairs), and then the specific example of $P^+Q_A^-$ is considered in detail.

2.2 Spin Echo Detection in Radical Pairs

2.2.1 The Liouville-von Neumann Equation

The theory used to calculate the echo modulation function of a radical pair was developed by Mims [66]. This uses the *density-matrix formalism* to calculate the evolution of spins under the influence of a pulse sequence. The formalism states that the density-matrix at a given time, $\hat{\rho}(t)$, describes the populations of the spin states (along the diagonal) and the coherences present in the system (off-diagonal elements) at that time t. For the ESEEM experiment at the X-band frequency with short, hard pulses as described in Section 2.1, the density-matrix at time 2τ is used to calculate the echo modulation. It is assumed that these pulses are hard enough to excite the whole EPR spectrum uniformly. The time-dependence of the

---

[1] Radical pairs created from a triplet precursor have similar characteristics.

density-matrix is governed by the *Liouville-von Neumann* equation (taking $\hbar = 1$)

$$\frac{d\hat{\rho}}{dt} = -i[\hat{\mathrm{H}}, \hat{\rho}] \tag{2.1}$$

where the spin Hamiltonian $\hat{\mathrm{H}}$ describes the magnetic interactions in the radical pair. In ESEEM this will alternately be the Hamiltonian for the pulses, $\hat{\mathrm{H}}_1$, and that which describes the periods of free precession, $\hat{\mathrm{H}}_0$. Both pulses have the same magnetic field strength (B_1), but differ in duration. If the lengths of these two pulses are t_β and t_γ respectively, and if the populations of the states and the coherences present immediately before the β pulse *i.e.* at time $t = 0$, are given by $\hat{\rho}(0)$, then the density-matrix at time 2τ can be calculated using

$$\hat{\rho}(2\tau) = \mathrm{e}^{-i\hat{\mathrm{H}}_0\tau} \cdot \mathrm{e}^{-i\hat{\mathrm{H}}_1 t_\gamma} \cdot \mathrm{e}^{-i\hat{\mathrm{H}}_0\tau} \cdot \mathrm{e}^{-i\hat{\mathrm{H}}_1 t_\beta} \cdot \hat{\rho}(0) \cdot \mathrm{e}^{i\hat{\mathrm{H}}_1 t_\beta} \cdot \mathrm{e}^{i\hat{\mathrm{H}}_0\tau} \cdot \mathrm{e}^{i\hat{\mathrm{H}}_1 t_\gamma} \cdot \mathrm{e}^{i\hat{\mathrm{H}}_0\tau}. \tag{2.2}$$

The function, E_i, giving the echo along each of the axes for transverse (detectable) magnetisation $i = x, y$, can now be obtained from

$$E_i = \mathrm{Tr}[\hat{S}_i \cdot \hat{\rho}(2\tau)] \tag{2.3}$$

where $\hat{S}_i$ is the total electron spin angular momentum operator for the i-axis.

2.2.2 Systems with Isotropic Hyperfine Coupling

It is simple to show that the ESEEM experiment is not sensitive to isotropic hyperfine couplings. In studies on $\mathrm{P^+Q_A^-}$, it is usually assumed that the hyperfine couplings present are purely isotropic, and can therefore be ignored. This assumption is made in the following calculation, where no term relating to the hyperfine coupling is explicitly included in the spin Hamiltonian for the RP. The inclusion of anisotropic hyperfine couplings is reserved for a later section.

Spin Hamiltonian for the Radical Pair

The spin Hamiltonian for a pair of coupled electrons A and B, in the absence of hyperfine couplings to neighbouring nuclei, depends on the Zeeman energy of each electron, and upon the dipolar and exchange couplings between them. This Hamiltonian, $\hat{\mathrm{H}}_0$, can be written

$$\hat{\mathrm{H}}_0 = \omega_\mathrm{A}\hat{S}_{\mathrm{A}z} + \omega_\mathrm{B}\hat{S}_{\mathrm{B}z} - J\left(\frac{1}{2} + 2\hat{\boldsymbol{S}}_\mathrm{A} \cdot \hat{\boldsymbol{S}}_\mathrm{B}\right) + d\left(3\hat{S}_{\mathrm{A}z}\hat{S}_{\mathrm{B}z} - \hat{\boldsymbol{S}}_\mathrm{A} \cdot \hat{\boldsymbol{S}}_\mathrm{B}\right). \tag{2.4}$$

$\omega_i = g_i\mu_\mathrm{B}B_0$ is the Zeeman splitting of electron i, and $d = D_{zz} = D(\cos^2\theta - 1/3)$. D and J are the dipolar and exchange coupling parameters respectively and θ is the angle between the dipolar axis and the field direction. The eigenstates ($|1\rangle \ldots |4\rangle$)

and corresponding eigenvalues ($E_1 \ldots E_4$) of $\hat{\mathrm{H}}_0$ give the four spin states of the radical pair and their energies:

$$\begin{aligned} |1\rangle &= |T_{+1}\rangle & E_1 &= \omega - J + d/2 \\ |2\rangle &= \cos\psi|S\rangle + \sin\psi|T_0\rangle & E_2 &= \Omega - d/2 \\ |3\rangle &= -\sin\psi|S\rangle + \cos\psi|T_0\rangle & E_3 &= -\Omega - d/2 \\ |4\rangle &= |T_{-1}\rangle & E_4 &= -\omega - J + d/2 \end{aligned} \tag{2.5}$$

where

$$\begin{aligned} \omega &= \tfrac{1}{2}(\omega_\mathrm{A} + \omega_\mathrm{B}), \quad & Q &= \tfrac{1}{2}(\omega_\mathrm{A} - \omega_\mathrm{B}) \\ \Omega^2 &= j^2 + Q^2, & \tan 2\psi &= Q/j \end{aligned} \tag{2.6}$$

and j is the strength of the coupling between the two electrons such that

$$j = J + \frac{d}{2}. \tag{2.7}$$

The effect of j is reflected in the coupling angle ψ. For a weakly coupled radical pair, the differences between the resonant frequencies of the electrons is far greater than j ($|Q| \gg |j|$), and $\psi \to \pi/4$. Strongly coupled electrons conversely have $|Q| \ll |j|$ and hence $\psi \to 0$.

In the eigenbasis of $\hat{\mathrm{H}}_0$ the spin Hamiltonian can be written as a diagonal matrix with elements $\langle j|\hat{\mathrm{H}}_0|j\rangle = E_j$. The operator $\mathrm{e}^{i\hat{\mathrm{H}}_0\tau}$ found in equation 2.2 can be therefore written, according to the properties of matrix exponents, as another diagonal matrix, this time with elements $\mathrm{e}^{iE_j\tau}$. 2Ω is the zero quantum frequency, or equivalently the singlet-triplet interconversion frequency. From equations 2.5 it is clear that 2Ω is the energy gap between eigenstates $|2\rangle$ and $|3\rangle$. If these two levels are populated a zero quantum coherence is set up between them which oscillates at the frequency 2Ω. Alternatively this can be viewed as the oscillation between $|S\rangle$ and $|T_0\rangle$ in the coherent superposition of those states making up the eigenstates $|2\rangle$ and $|3\rangle$.

The Pulse Hamiltonian

The Hamiltonian, $\hat{\mathrm{H}}_1$, describing the applied mw pulses reflects the fact that in this analytical approach, both spins are excited equally. If $\hat{S}_{ix}$ is the spin angular momentum operator for the x-component of the spin of electron i, and ω_1 is the strength of the mw pulse, then in the rotating frame

$$\hat{\mathrm{H}}_1 = -\omega_1(\hat{S}_{\mathrm{A}x} + \hat{S}_{\mathrm{B}x}) = -\omega_1\hat{S}_x. \tag{2.8}$$

Before being used in the calculation of $\hat{\rho}(2\tau)$, $\hat{\mathrm{H}}_1$ must be transformed from the product ($|\alpha\alpha\rangle$, $|\alpha\beta\rangle$, $|\beta\alpha\rangle$, $|\beta\beta\rangle$) basis into the eigenbasis of $\hat{\mathrm{H}}_0$. This is done via a transformation matrix U. In the eigenbasis of $\hat{\mathrm{H}}_0$, $\hat{\mathrm{H}}_1$ can now be written:

$$\hat{\mathrm{H}}_1 = -\frac{\omega_1}{\sqrt{2}}\begin{pmatrix} 0 & s & c & 0 \\ s & 0 & 0 & s \\ c & 0 & 0 & c \\ 0 & s & c & 0 \end{pmatrix} \qquad \text{where} \qquad \begin{matrix} s = \sin\psi \\ c = \cos\psi. \end{matrix} \tag{2.9}$$

This spin Hamiltonian has the property

$$\hat{\mathrm{H}}_1^3 = \omega_1^2 \hat{\mathrm{H}}_1;$$

using this relation together with the expansion of a matrix exponential, rotation operators, $\hat{R}^{\pm 1}(\alpha)$, for the pulses can be developed which are used to give the terms $\mathrm{e}^{\pm i \hat{\mathrm{H}}_1 t_\alpha}$:

$$\mathrm{e}^{\pm i \hat{\mathrm{H}}_1 t_\alpha} = \hat{R}^{\pm 1}(\alpha) = \mathbb{1} + \frac{\hat{\mathrm{H}}_1^2}{\omega_1^2}(\cos\alpha - 1) \pm i\frac{\hat{\mathrm{H}}_1}{\omega_1}\sin\alpha \tag{2.10}$$

where $\mathbb{1}$ is the 4 × 4 identity matrix and $\alpha = \omega_1 t_\alpha$.

The Initial Density-Matrix

The density-matrix, $\hat{\rho}(0)$, contains information about the populations (p_i) of, and coherences between, the states $|i\rangle$ after the laser flash and immediately before the first pulse. It is assumed that during the delay Δ immediately after the formation of the radical pairs, any zero-quantum coherences (ZQC) created are relaxed prior to the first pulse [67, 68]. If this is the case then $\hat{\rho}(0)$ is a diagonal matrix with elements p_i representing the populations of the $|i\rangle$ states.

Simplifications

Without making any approximations which may affect the accuracy to which the echo modulation functions are determined, the calculation may be easily simplified to reduce the computation time. Consider the effect of the β pulse. After it is applied, the 4 × 4 density-matrix $\hat{\rho}(\beta) = \mathrm{e}^{-i\hat{\mathrm{H}}_1 t_\beta} \cdot \hat{\rho}(0) \cdot \mathrm{e}^{i\hat{\mathrm{H}}_1 t_\beta}$ has non-zero elements representing the populations of the states and the zero, single and double quantum coherences (ZQC, SQC, DQC) between them. In going on to produce an echo after the remaining τ–γ–τ part of the pulse sequence, only those coherences which are single quantum will result in any contribution. It is therefore feasible to simplify the calculation by removing all terms in $\hat{\rho}(\beta)$ not referring to SQC (*i.e.* equating them to zero).

The calculation may be further simplified by use of the method suggested by Zwanenburg and Hore [69]. Since the only coherences which will contribute to the echo at time 2τ are the single quantum coherences, these coherences are picked out, and their contributions to the echo calculated. All other transitions and coherences are ignored. The echo signal at time 2τ arises from single quantum coherences $|m\rangle \leftrightarrow |n\rangle$ after the τ–γ–τ part of the pulse sequence. These coherences, $\hat{\rho}_{mn}(2\tau)$, are related to the coherences, $\hat{\rho}_{jk}(\beta)$, before the τ–γ–τ sequence by

$$\hat{\rho}_{mn}(2\tau) = \hat{R}^{-1}_{mj}(\gamma)\hat{R}_{kn}(\gamma)\hat{\rho}_{jk}(\beta)\mathrm{e}^{[i(E_n-E_m)\tau - i(E_j-E_k)\tau]}, \tag{2.11}$$

where the ESEEM frequencies

$$(E_n - E_m) - (E_j - E_k) = \begin{cases} \pm 2(J-d) \\ \quad or \\ \pm(2(J-d) \pm 2\Omega) \end{cases}$$

are defined by the energies of the states given in equation 2.5. Hence, at the end of the pulse sequence, the total $\hat{\rho}_{mn}(2\tau)$ for each $|m\rangle \leftrightarrow |n\rangle$ transition is calculated from the sum over all coherences $\hat{\rho}_{jk}(\beta)$.

2.2.3 Echo Modulation Functions for x and y

Using equations 2.2 and 2.3, expressions for E_x and E_y can now be obtained. From the vector diagram showing the path of the spins in ESEEM (Figure 1.8 on page 21) it is clear that a refocussing (γ) pulse of π will lead to the highest echo amplitude. If this angle is chosen, then for an as yet unspecified β pulse and initial density matrix, E_x and E_y become:

$$\begin{aligned} E_x &= P\sin 2\beta\{S_0\sin^2 2\psi + \cos 2\psi[\cos^2\psi S_{-1} - \sin^2\psi S_{+1}]\} \\ &\quad + \sin\beta(p_2 - p_3)\sin^2 2\psi\cos 2\psi[S_0 - \frac{1}{2}S_{+1} - \frac{1}{2}S_{-1}] \qquad (2.12) \\ E_y &= (p_4 - p_1)\sin\beta\{\sin^2 2\psi C_0 + \cos 2\psi[\cos^2\psi C_{-1} - \sin^2\psi C_{+1}]\} \qquad (2.13) \end{aligned}$$

where

$$\begin{aligned} P &= -\tfrac{1}{2}p_1 + p_2\sin^2\psi + p_3\cos^2\psi - \tfrac{1}{2}p_4 \\ S_q &= \sin[2(J - d + q\Omega)\tau] \\ C_q &= \cos[2(J - d + q\Omega)\tau] \end{aligned} \tag{2.14}$$

and the p_i are the populations of the states $|i\rangle$.

2.3 ESEEM of $\mathrm{P^+Q_A^-}$

Having established equations for the in-phase and out-of-phase echoes in the general case of a radical pair with isotropic hyperfine coupling, the particular example of $\mathrm{P^+Q_A^-}$ in *Rb. sphaeroides* can now be considered. Much of the work in this section was done in collaboration with Dr. Christiane Timmel, and is published in *Chemical Physics* [70].

2.3.1 Populations of the Eigenstates Before the β Pulse

The spin-correlated nature of $\mathrm{P^+Q_A^-}$ enforces specific constraints upon the initial populations of the states. In the eigenbasis described in equation 2.5, the only states populated immediately before the β pulse (assuming that any zero quantum coherences de-phase during the time period Δ) are those with singlet character, *i.e.* $|2\rangle$ and $|3\rangle$. The populations of these states are governed by the strength of the coupling between the electrons: $p_2 = \cos^2\psi$ and $p_3 = \sin^2\psi$. Using these populations and equation 2.5, it can be shown that in the case of a strongly coupled radical pair where $\psi = 0$, $|2\rangle = |S\rangle$ is populated leaving $|3\rangle = |T_0\rangle$ empty. When the pair is weakly coupled, $\psi = \pi/4$ giving

$$\begin{aligned} |2\rangle &= \quad \tfrac{1}{\sqrt{2}}|S\rangle + \tfrac{1}{\sqrt{2}}|T_0\rangle, \quad p_2 = \tfrac{1}{2} \\ |3\rangle &= -\tfrac{1}{\sqrt{2}}|S\rangle + \tfrac{1}{\sqrt{2}}|T_0\rangle, \quad p_3 = \tfrac{1}{2}. \end{aligned} \tag{2.15}$$

These populations can be altered by the application of another mw pulse of angle α so that a new pulse sequence, $h\nu$–Δ–α–t, is applied before the β pulse. The α pulse drives some of the population into the triplet states $|1\rangle = |T_{+1}\rangle$ and $|4\rangle = |T_{-1}\rangle$. Radical pairs in triplet states must relax back into singlet states in order to recombine, meaning that in the case of $\mathrm{P^+Q_A^-}$, the α pulse can be used to extend the lifetime of the radical pair.

Using the operator method outlined in Section 2.2 (pg 25), it can be shown that when an α pulse is applied to a sample of singlet-born spin-correlated radical pairs, the populations of the eigenstates are changed from $p_1 = p_4 = 0$, $p_2 = \cos^2\psi$ and $p_3 = \sin^2\psi$ into

$$\begin{aligned} p_1 &= p_4 = \tfrac{1}{4}s^2\sin^2\psi \\ p_2 &= \cos^2\psi(\cos^2\psi + c\sin^2\psi)^2 + (1-c)^2\sin^4\psi\cos^2\psi \\ p_3 &= (1-c)^2\sin^2\psi\cos^4\psi + \sin^2\psi(\sin^2\psi + c\cos^2\psi)^2 \end{aligned} \tag{2.16}$$

where $s = \sin\alpha$ and $c = \cos\alpha$. The populations of $|1\rangle$ and $|4\rangle$ (*i.e.* $|T_{\pm 1}\rangle$) are optimized when $\alpha = \pi/2$. These populations are also governed by the coupling angle,

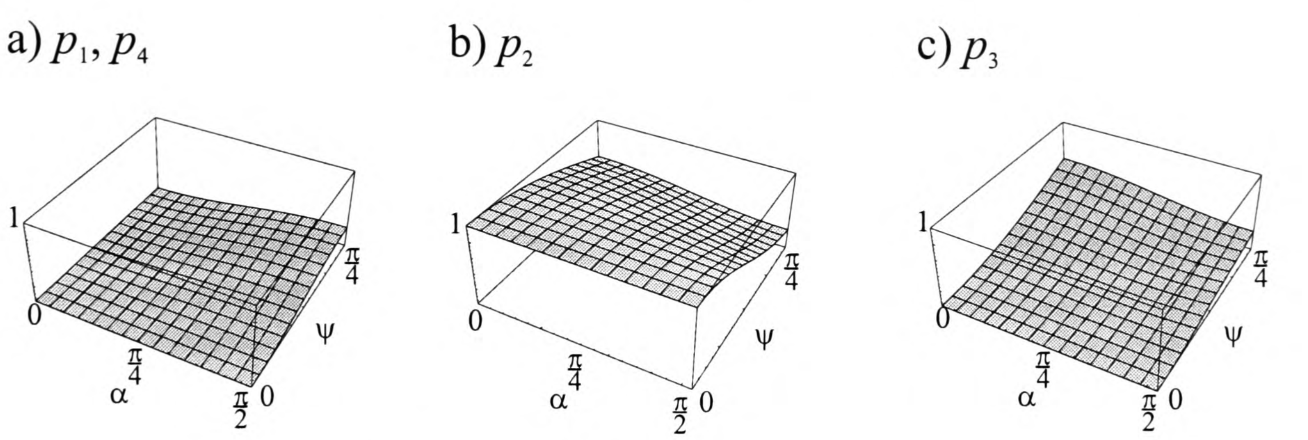

Figure 2.3: Populations of radical pair spin states p_i after an α-pulse, as a function of pulse and coupling angles. Maximum triplet population of $p_1 = p_4 = 1/4$ occurs for $\alpha = \pi/2$ in the weak coupling limit ($\psi = \pi/4$). For strong coupling ($\psi = 0$), $|2\rangle$ becomes entirely singlet and $|3\rangle$ entirely triplet (equation 2.5), in this case, only $|2\rangle$ is populated.

ψ. Figure 2.3 shows the relationships between the populations of the states and the angles α and ψ. For weak coupling, all four states are equally populated with p_1 and p_4 at their maximum population. In the extreme strong coupling case where $\psi = 0$, it is shown that it is not possible for an mw pulse to populate the triplet levels. The expressions given in equation 2.16 can be used to understand experimental observations of microwave pulse effects on $\mathrm{P}^{+}\mathrm{Q}_{\mathrm{A}}^{-}$ lifetimes [71–73].

The ESEEM experiment studied in this chapter utilizes the usual (β, γ) sequence (Figure 2.2), *i.e.* there is no α pulse and $s = 0$, $c = 1$. In this case, the populations once again become $p_1 = p_4 = 0$, $p_2 = \cos^2 \psi$ and $p_3 = \sin^2 \psi$. For $\mathrm{P}^{+}\mathrm{Q}_{\mathrm{A}}^{-}$, X-ray studies have shown the distance between P^{+} and $\mathrm{Q}_{\mathrm{A}}^{-}$ to be of the order of 29 Å. This gives small values of the spin-spin coupling parameters D and J, and together with the incomplete overlap of the individual spectra of P^{+} and $\mathrm{Q}_{\mathrm{A}}^{-}$ means it can be assumed that the weak coupling approximation is appropriate for this radical pair. Hence, ψ is approximately $\pi/4$. Small exchange and dipolar couplings also give rise to a rather narrow EPR spectrum, and hence, an analytical approach in which it is assumed that the mw pulses can cover the entire spectrum is appropriate for this radical pair. Since $\psi \approx \pi/4$, the populations of $|2\rangle$ and $|3\rangle$ are therefore equal at 1/2 and

$$\hat{\rho}(0) = \begin{pmatrix} 0 & 0 & 0 & 0 \\ 0 & \frac{1}{2} & 0 & 0 \\ 0 & 0 & \frac{1}{2} & 0 \\ 0 & 0 & 0 & 0 \end{pmatrix} \tag{2.17}$$

Consideration of equations 2.13 and 2.16 shows that since for a spin correlated radical pair $p_1 = p_4$, the in-phase echo is always zero. This is one of the hallmarks of the behaviour of spin-correlated radical pairs subject to non-selective pulses, and is in direct contrast to that seen in both uncorrelated radical pairs and single radicals.

This strange behaviour was first observed by Thurnauer and Norris in 1980 [74]. They observed a phase shift in the spin echo spectrum of PSI samples which they attributed to spin-spin interactions in the radical pairs. The theory behind the out-of-phase echo behaviour of a spin-correlated radical pair was first investigated by Salikhov *et al.* in 1992 [75], and has been the subject of several other studies since that time [76–79].

2.3.2 E_x and E_y for a Weakly Coupled Radical Pair

The out-of-phase nature of the ESEEM of a weakly coupled spin-correlated radical pair can also be discussed in terms of the *product operator formalism* and the vector model. Here it is compared and contrasted to the analogous model for a radical pair with thermal equilibrium populations.

Taking equations 2.12 and 2.13 and assuming weak coupling (*i.e.* $\psi = \pi/4$) gives the following expressions for E_x and E_y:

$$E_x = P \sin 2\beta S_0 \tag{2.18}$$

$$E_y = (p_4 - p_1) \sin\beta C_0. \tag{2.19}$$

As determined in the previous section, for a spin-correlated radical pair where $(p_1 = p_4)$, no in-phase echo is expected and this leaves a purely out-of-phase signal along the x-axis. When the radical pair is uncorrelated, the quantity P becomes zero, with $p_4 - p_1$ non-zero and positive (see Chapter 3) so that for this radical pair, the echo is in-phase (y) only.

In the limit of weak coupling, the product operators describing the magnetisation in uncorrelated and spin-correlated radical pairs are $I_z + S_z$ and $2I_zS_z$ respectively. The first is the sum of two components, both of which lie along the positive z-axis in the vector model. The latter case also has separate components, one along positive z, the other along the negative axis. This reflects the anti-phase nature of the EPR spectrum of a spin-correlated radical pair (Figure 1.5, page 10). Figure 2.4 (overleaf) shows the effect of the ESEEM pulse sequence on each of these examples beginning immediately after the β pulse. Clearly the anti-phase nature of the magnetisation for the spin-correlated radical pair is the cause of the out-of-phase echo described by equation 2.18.

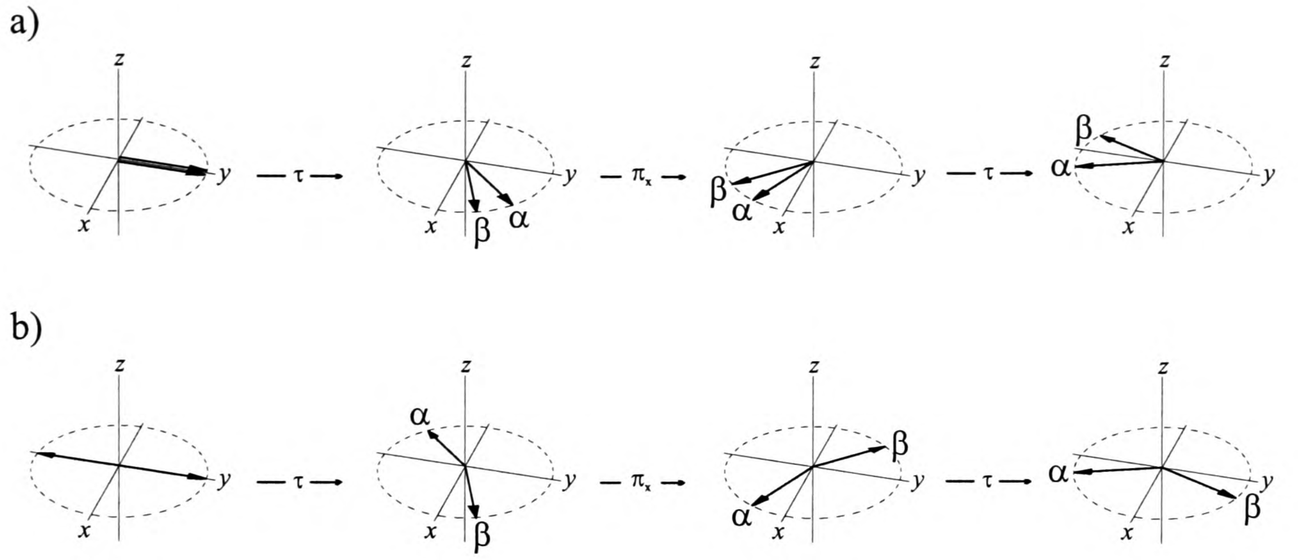

Figure 2.4: Vector model representations of the ESEEM of weakly coupled a) uncorrelated and b) spin-correlated radical pairs. The labels α and β refer to the spin-state of the "other" electron. In all diagrams, α is considered to be the slowest spin. As demonstrated in Chapter 1, the $\pi/2$ pulse not only flips the spins about the x-axis, but also interchanges these labels.

2.3.3 The Dependence of E_x Upon β

Although ZQC are not directly observable in magnetic resonance experiments, they can be converted into transverse magnetisation by mw pulses. However, in $P^+Q_A^-$, contributions to the ESEEM from these coherences (*i.e.* modulations at $S_{\pm1}$ and $C_{\pm1}$) are not observed. Two reasons are apparent for this. First, since $P^+Q_A^-$ is a weakly coupled radical pair, the coupling angle ψ is around $\pi/4$. If this is the case then as equations 2.12 and 2.13 show, the coefficient of $S_{\pm1}$ and $C_{\pm1}$, $\cos 2\psi$, is very close to zero. Secondly, for this radical pair the zero quantum frequency, 2Ω, oscillates a great deal faster than $2(J-d)$ (at around 15 MHz compared to 2 MHz for $2(J-d)$) [70]. This means that echo modulations dependent upon 2Ω have a broad spread of frequencies, de-phase much more rapidly as τ increases and are at a much smaller amplitude than those modulations dependent solely upon D and J. For these reasons it is reasonable to neglect oscillations at 2Ω from now on while considering the secondary radical pair.

If the $S_{\pm1}$ and $C_{\pm1}$ terms in equations 2.12 and 2.13 are equated to zero, then the expressions for E_x and E_y become

$$E_x = S_0 \sin^2 2\psi[P\sin 2\beta + \cos 2\psi(p_2 - p_3)\sin\beta] \tag{2.20}$$

$$E_y = C_0 \sin^2 2\psi(p_4 - p_1)\sin\beta. \tag{2.21}$$

Using equation 2.20 and the populations p_i as given in equation 2.17, the dependence of E_x/S_0 upon ψ and β can be investigated. Figure 2.5 shows the required β pulse angle, β_{opt}, to optimise E_x/S_0 at various coupling angles, and the corresponding

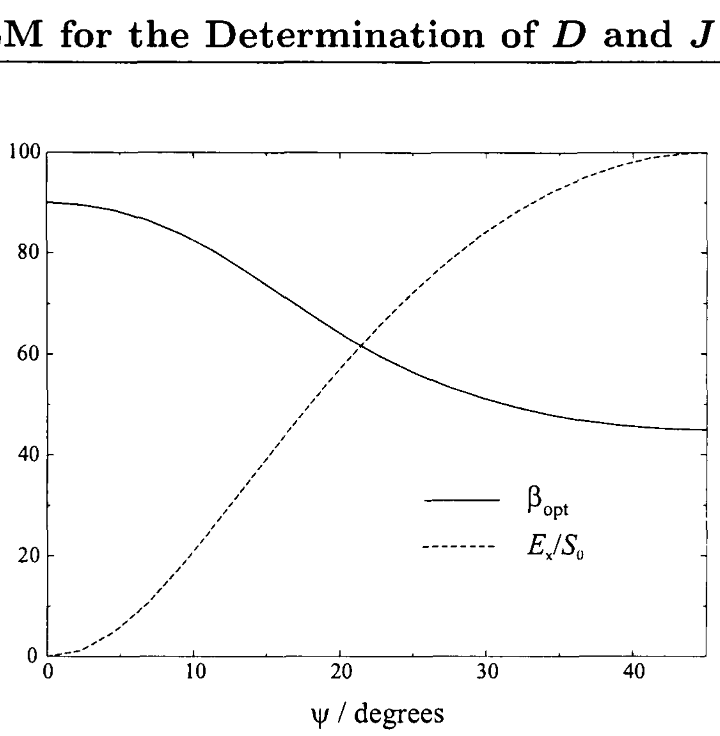

Figure 2.5: The dependence of $\beta_{\rm opt}$ and E_x/S_0 upon the coupling angle. The vertical axis represents both $\beta_{\rm opt}$ in degrees and the value of E_x/S_0 as a percentage of the maximum value occurring when $\psi = \beta = \pi/4$.

amplitudes of E_x/S_0 as a percentage of the maximum. The consequence of the $\sin 2\beta$ dependence of E_x is that where $p_2 = p_3$ (*i.e.* weak coupling), $\beta_{\rm opt}$ is $\pi/4$ rather than $\pi/2$ as may be expected. Clearly, in the case of an SCRP, $\beta = \pi/2$ would give zero amplitude. This $\sin 2\beta$ dependence of the signal intensity has long been known, and manifests itself in chemically induced dynamic nuclear polarisation (CIDNP) as the so called "multiplet effect" [80, 81]. Experiments have shown that changing β does not alter the shape of the ESEEM spectrum, only the amplitude of the echo [49]. The pulse sequence giving maximal echo amplitude for ESEEM studies of spin-correlated radical pairs is therefore $(\beta, \gamma) = (\pi/4, \pi)$ and it is this pulse sequence which is used in all calculations performed for the duration of this thesis, unless otherwise stated.

2.3.4 Echo Modulation in $P^+Q_A^-$

Having determined the ideal pulse sequence and the correct initial density matrix for $P^+Q_A^-$, echo modulation functions can now be determined for this system. Assuming that $P^+Q_A^-$ is a weakly coupled spin-correlated radical pair ($\psi = \pi/4$, populations from equation 2.17), and that the ESEEM pulse sequence is $(\pi/4, \pi)$, then equations 2.12 and 2.13 collapse to give

$$E_x = \frac{S_0}{2} = \frac{\sin 2(J-d)\tau}{2} \qquad (2.22)$$

$$E_y = 0. \qquad (2.23)$$

As expected, only the out-of-phase echo modulated at frequencies corresponding to $2(J-d)$ remains. The dependence of d upon the angle of the dipolar axis, θ, and the unusual initial populations, mean that the ESEEM spectrum of $P^+Q_A^-$ gives rise to a powder pattern in the form of an anti-phase Pake doublet. In principle this means that the values of J and D can be read directly from the frequency domain spectrum. Figure 2.6a shows the powder pattern which builds the ESEEM spectrum. Each orientation of the radical pair gives rise to an anti-phase doublet with a splitting determined by D, J and θ. The Pake pattern is simply a powder average of these anti-phase doublets. When the two Pake spectra are put together as shown, along with the appropriate line broadening, they form the ESEEM spectrum 2.6b. The *canonical frequencies*, $f_\perp$ and $f_\parallel$, seen in Figure 2.6b correspond to the outside edges of the powder patterns. Analysis of equation 2.22 reveals expressions for $f_\parallel$ and $f_\perp$:

$$\begin{array}{rcl} J-d &=& J-D(\cos^2\theta-\frac{1}{3}) \\ \text{at}\quad \theta=0^\circ &\rightarrow& J-\frac{2D}{3} \\ \text{at}\quad \theta=90^\circ &\rightarrow& J+\frac{D}{3} \end{array}$$

and hence

$$f_\parallel=\pm\left(2J-\frac{4}{3}D\right),\qquad f_\perp=\pm\left(2J+\frac{2}{3}D\right). \tag{2.24}$$

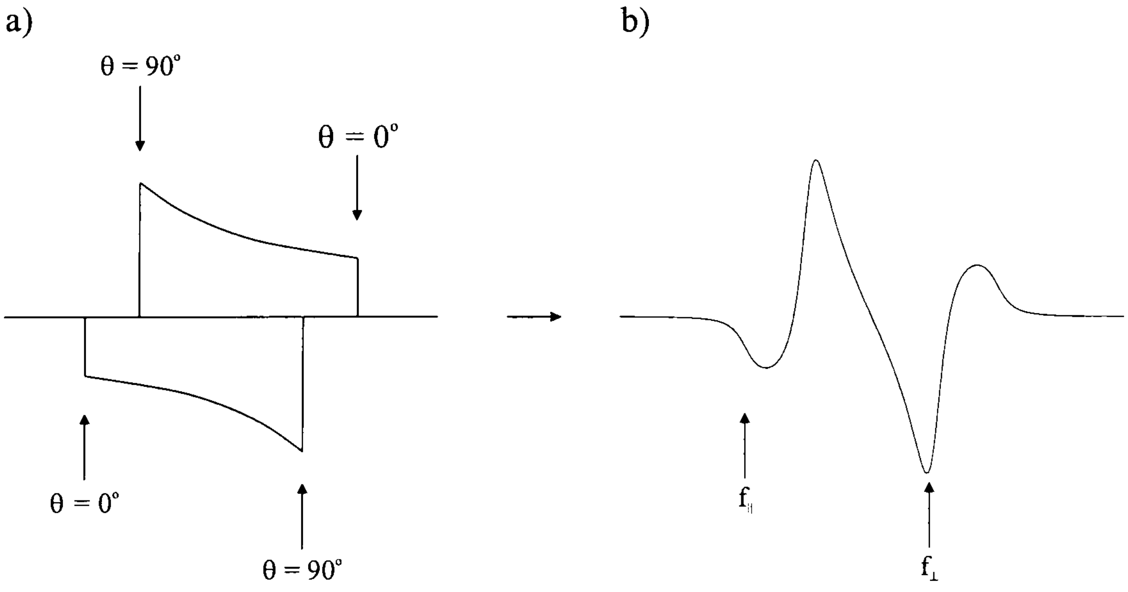

Figure 2.6: a) Anti-phase Pake doublets showing the dependence of frequency upon radical pair orientation. θ is the angle between the magnetic field and the dipolar axis. b) The Pake doublets add to give the ESEEM spectrum from which the canonical frequencies $f_\perp$ and $f_\parallel$ are easily determined. A Lorentzian linebroadening corresponding to the transverse relaxation is added to the spectrum.

As shown in Figure 2.6b, these frequencies lie at the position of the central peak ($f_\perp$) and at the point of inflexion of the outside shoulder of the spectrum ($f_\parallel$). The canonical frequencies are easily measured from the experimental spectrum, and using equations 2.24, D and J may be calculated. This method for the estimation of D and J was developed by Dzuba, Gast and Hoff [34] and has been used in a number of experimental studies done in recent times (for example [49–51, 56]).

Experimentally, the accuracy to which the values of D and J can be determined naturally depends upon the quality of the spectra. Effects such as noise, homogeneous linebroadening and the experimental dead-time will contrive to make the measurement of $f_{\|}$ and $f_{\perp}$ inaccurate. The effects of noise and some contributions to the linebroadening may be reduced by experimental practices such as signal averaging, but the dead-time problem is intrinsic to the ESEEM experiment. The dead-time is the period for which the cavity rings after a pulse, which constrains the delay τ such that it must be longer than the period of ringing to avoid corruption of the echo. For this reason there is always a period at the start of the time-trace for which no data is recorded. Dead-time can cause "sinc-wiggles" in the Fourier transform to the frequency domain: Chapter 4 deals with the particular effects of dead-time, and suggests a possible method for avoiding the problem. Another potential cause of misinterpretation of ESEEM data arises from the assumption that any hyperfine coupling present in $\mathrm{P^+Q_A^-}$ is purely isotropic and consequently that the spectrum of $\mathrm{P^+Q_A^-}$ experiences no effects from anisotropic hyperfine couplings. There is however both experimental [34] and theoretical [66, 82] evidence to suggest that "nuclear ESEEM" effects do occur in the radical pair. The next section is devoted to the calculation of the form of the nuclear ESEEM and to the study of the changes it can make to the interpretation of D and J.

2.4 Nuclear ESEEM

When ESEEM is used to calculate the spin-spin coupling parameters D and J in the secondary radical pair of *Rb. sphaeroides*, it is usually assumed that any effect arising from anisotropic hyperfine couplings is not great enough to alter the spectrum. For this reason, as for the calculation in the last section, anisotropic hyperfine interactions are neglected in the model used to estimate the values of these parameters. Although this assumption gives a reasonable model for the system from which D and J have been estimated, it does not give the whole picture. It has been known since the works of Mims in the late 1960's [66, 82] that anisotropic hyperfine couplings can cause some degree of modulation to a spin echo, by partially allowing otherwise forbidden transitions involving simultaneous electron and nuclear spin flips. Whilst it is expected that these modulations would be of low intensity, it is possible in the case of $\mathrm{P^+Q_A^-}$ that some effect will be observable. Indeed, recent transient EPR experiments on $\mathrm{P^+Q_A^-}$ have shown modulations which are thought to be due to nuclear effects of this type [68].

Spectra recorded by Dzuba *et al.* [34] are pictured in Figure 2.7. The two traces shown were taken from Zn^{2+}-substituted $P^+Q_A^-$ reaction centres at 220K. The solid line shows the spectrum of ^{15}N-enriched centres, the dotted line the native ^{14}N-containing sample. The spectra show additional modulations (marked by arrows) to those usually found for spin-correlated radical pairs or those predicted by the two-electron model. ESEEM experiments performed on P^+ for both ^{15}N-enriched and native reaction centres show strong maxima close to ±2.9 MHz. Since the extra peaks in Figure 2.7 lie approximately ±2.9 MHz either side of the main peaks, Dzuba *et al.* assigned the extra modulations to nuclear ESEEM. This effect was not quantified, *i.e.* the fitting for the determination of D and J did not include any terms to account for a nucleus. With the benefit of hindsight, this may have been a mistake. Surely it is possible that the effect of the nucleus could cause a shift in the positions of $f_\perp$ and $f_\parallel$ leading to errors in the determination of D and J. Furthermore, although the differences between the ^{15}N- and ^{14}N- spectra are small, they do exist. Potentially this could be due to an isotope effect between the different nuclei which may also be an important factor to consider.

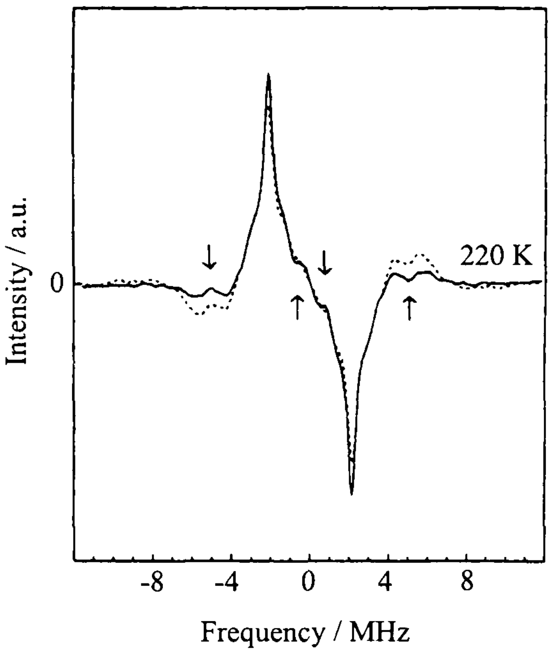

Figure 2.7: Data recorded for $P^+Q_A^-$ in *Rb. sphaeroides* by Dzuba *et al.* [34]. The solid lines show the ESEEM spectra for the ^{15}N- and the dotted lines the ^{14}N-reaction centres, respectively. The arrows mark features which are not expected in an ESEEM spectrum arising solely from electron-electron interactions.

In what follows, the density-matrix formalism was used to calculate the full ESEEM from the weakly coupled, spin-correlated radical pair $P^+Q_A^-$, by using a model containing two electrons, A and B, interacting via spin-spin coupling. In addition, an anisotropic hyperfine coupling was included between electron A and a nearby spin-1/2 nucleus[2], N. Comparison between equation 2.22 and the echo modulation function calculated from this model gave a good indication of the form of the nuclear ESEEM from which the effect upon the determination of D and J from ESEEM spectra could be assessed.

---

[2] This section describes an analytical calculation for a weakly coupled radical pair. Nuclear ESEEM has also been considered for a strongly coupled radical pair, where a numerical calculation is required [83].

2.4.1 The Origin of the Nuclear ESEEM Effect

The calculation of the nuclear ESEEM used the spin Hamiltonian of a weakly coupled radical pair with additional terms to account for the secular and pseudo-secular hyperfine coupling to the nucleus N (as described in Section 1.2.3), and the nuclear Zeeman interaction ω_N. Hence:

$$\begin{aligned}\hat{\mathrm{H}}_0 &= \omega_\mathrm{A}\hat{S}_{\mathrm{A}z} + \omega_\mathrm{B}\hat{S}_{\mathrm{B}z} - J\Big(\frac{1}{2} + 2\hat{S}_{\mathrm{A}z}\hat{S}_{\mathrm{B}z}\Big) + 2D\Big(\cos^2\theta - \frac{1}{3}\Big)\hat{S}_{\mathrm{A}z}\hat{S}_{\mathrm{B}z} \\ &\quad + a\hat{S}_{\mathrm{A}z}\hat{I}_z + b\hat{S}_{\mathrm{A}z}\hat{I}_x - \omega_\mathrm{N}\hat{I}_z. \qquad (2.25)\end{aligned}$$

This three-particle system has $2^3 = 8$ spin states associated with it, the origin of these being best understood by considering the amalgamation of the 4 levels arising from a system of two coupled electrons, and the 4 levels due to the coupling between a single electron and a nucleus. These two energy level diagrams are displayed in Figure 2.8 overleaf, which also shows the allowed and partially allowed EPR transitions in the systems. The diagram shows that the pseudo-secular hyperfine coupling is responsible for the mixing of the nuclear sub-levels. This causes the nuclear ESEEM effect by allowing some degree of simultaneous electron and nuclear spin flip. The eight energy levels in the two-electron, one-nucleus system are therefore those described by Zwanenburg and Hore [69]. Given by the eigenstates of $\hat{\mathrm{H}}_0$ in terms of the product basis and the mixing angles ψ_α and ψ_β where

$$\tan 2\psi_\alpha = \frac{\frac{1}{2}b}{\frac{1}{2}a - \omega_\mathrm{N}} \quad \text{and} \quad \tan 2\psi_\beta = \frac{\frac{1}{2}b}{\frac{1}{2}a + \omega_\mathrm{N}},$$

the eight states are written:

$$\begin{aligned}
|\Psi_{+1}\rangle &= \cos\psi_\alpha|\alpha_\mathrm{A}\alpha_\mathrm{N}\rangle|\alpha_\mathrm{B}\rangle + \sin\psi_\alpha|\alpha_\mathrm{A}\beta_\mathrm{N}\rangle|\alpha_\mathrm{B}\rangle \\
|\Psi_{-1}\rangle &= -\sin\psi_\alpha|\alpha_\mathrm{A}\alpha_\mathrm{N}\rangle|\alpha_\mathrm{B}\rangle + \cos\psi_\alpha|\alpha_\mathrm{A}\beta_\mathrm{N}\rangle|\alpha_\mathrm{B}\rangle \\
|\Psi_{+2}\rangle &= \cos\psi_\alpha|\alpha_\mathrm{A}\alpha_\mathrm{N}\rangle|\beta_\mathrm{B}\rangle + \sin\psi_\alpha|\alpha_\mathrm{A}\beta_\mathrm{N}\rangle|\beta_\mathrm{B}\rangle \\
|\Psi_{-2}\rangle &= -\sin\psi_\alpha|\alpha_\mathrm{A}\alpha_\mathrm{N}\rangle|\beta_\mathrm{B}\rangle + \cos\psi_\alpha|\alpha_\mathrm{A}\beta_\mathrm{N}\rangle|\beta_\mathrm{B}\rangle \\
|\Psi_{+3}\rangle &= \cos\psi_\beta|\beta_\mathrm{A}\alpha_\mathrm{N}\rangle|\alpha_\mathrm{B}\rangle + \sin\psi_\beta|\beta_\mathrm{A}\beta_\mathrm{N}\rangle|\alpha_\mathrm{B}\rangle \\
|\Psi_{-3}\rangle &= -\sin\psi_\beta|\beta_\mathrm{A}\alpha_\mathrm{N}\rangle|\alpha_\mathrm{B}\rangle + \cos\psi_\beta|\beta_\mathrm{A}\beta_\mathrm{N}\rangle|\alpha_\mathrm{B}\rangle \\
|\Psi_{+4}\rangle &= \cos\psi_\beta|\beta_\mathrm{A}\alpha_\mathrm{N}\rangle|\beta_\mathrm{B}\rangle + \sin\psi_\beta|\beta_\mathrm{A}\beta_\mathrm{N}\rangle|\beta_\mathrm{B}\rangle \\
|\Psi_{-4}\rangle &= -\sin\psi_\beta|\beta_\mathrm{A}\alpha_\mathrm{N}\rangle|\beta_\mathrm{B}\rangle + \cos\psi_\beta|\beta_\mathrm{A}\beta_\mathrm{N}\rangle|\beta_\mathrm{B}\rangle
\end{aligned} \qquad (2.26)$$

The relative energies of these states are given by the eigenvalues:

$$\begin{aligned}
\lambda_{\pm1} &= \omega - J + d/2 \pm \omega_\alpha/2 \\
\lambda_{\pm2} &= Q - d/2 \pm \omega_\alpha/2 \\
\lambda_{\pm3} &= -Q - d/2 \mp \omega_\beta/2 \\
\lambda_{\pm4} &= -\omega - J + d/2 \mp \omega_\beta/2
\end{aligned} \qquad (2.27)$$

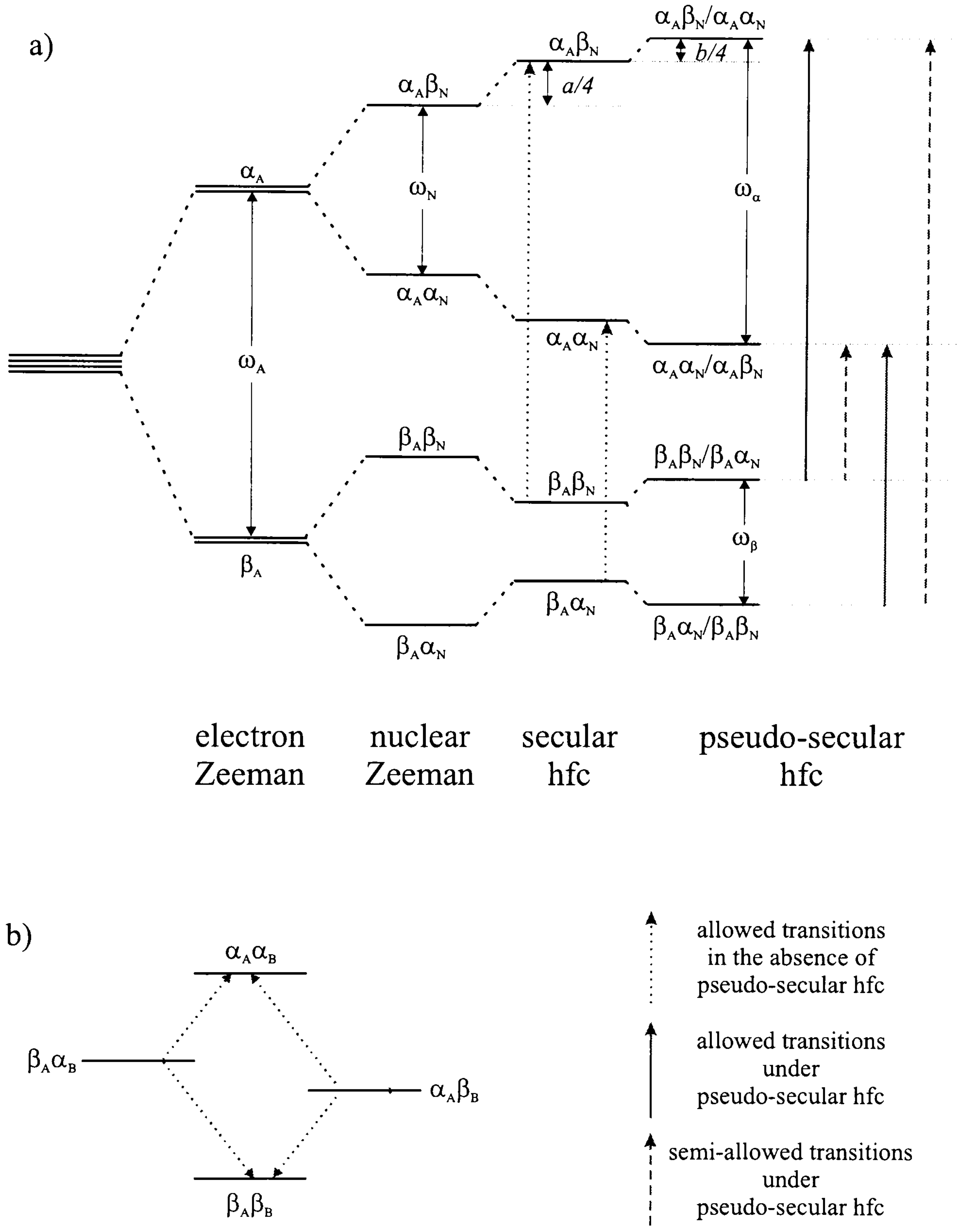

Figure 2.8: Energy level diagrams for the 4 level systems of a) an electron coupling to a spin-1/2 nucleus, and b) two coupled electrons. Diagram a) shows that the four levels arising from the electron and the nucleus are split by the electron and nuclear Zeeman frequencies (ω_A and ω_N), shifted by the secular hyperfine coupling, a, and mixed by the pseudo-secular hyperfine coupling, b. This last interaction partially allows the transitions represented by dashed lines where, within the mixed states, both an electron and a nuclear spin flip occur.

Here ω, Q and d have been defined in the previous calculation. The terms ω_α and ω_β are the NMR frequencies of a nucleus coupled to an $m_s = +1/2$ and $m_s = -1/2$ electron respectively and are given using

$$\begin{aligned} \omega_\alpha &= \sqrt{(\tfrac{a}{2} - \omega_\mathrm{N})^2 + \tfrac{b^2}{4}} \\ \omega_\beta &= \sqrt{(\tfrac{a}{2} + \omega_\mathrm{N})^2 + \tfrac{b^2}{4}} \end{aligned} \tag{2.28}$$

These energy levels are shown schematically in Figure 2.9. Each pair of states $|\Psi_{\pm i}\rangle$ contains two non-identical states which are a mixture of $|\iota_\mathrm{A}\alpha_\mathrm{N}\rangle|\kappa_\mathrm{B}\rangle$ and $|\iota_\mathrm{A}\beta_\mathrm{N}\rangle|\kappa_\mathrm{B}\rangle$ (where ι and κ are the spin states, α or β of the electrons).

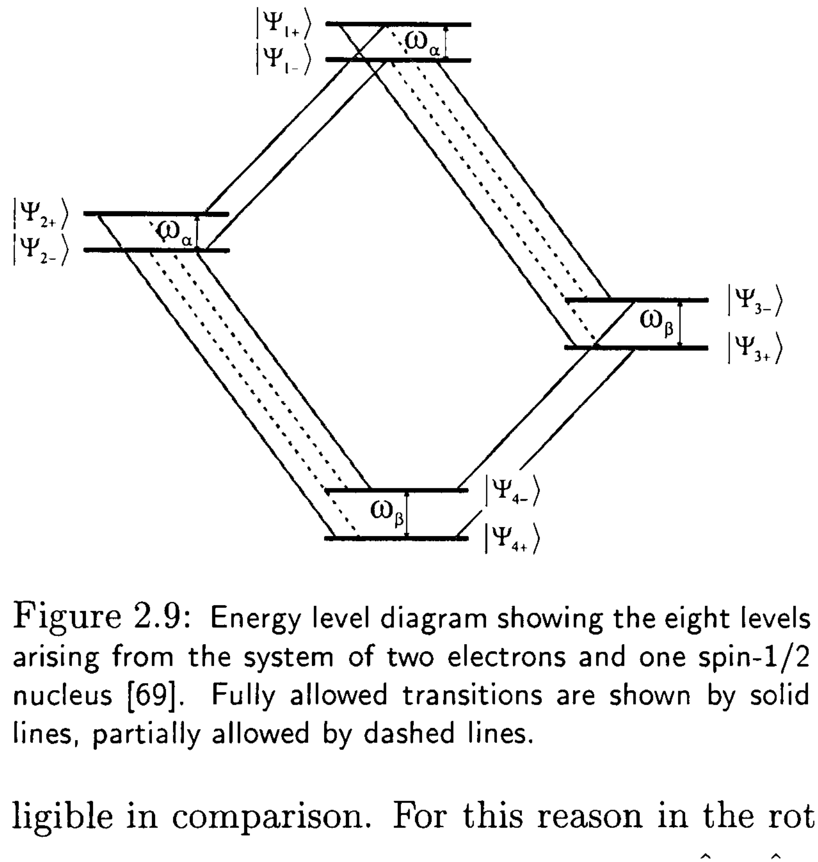

Figure 2.9: Energy level diagram showing the eight levels arising from the system of two electrons and one spin-1/2 nucleus [69]. Fully allowed transitions are shown by solid lines, partially allowed by dashed lines.

The laser flash was once again assumed to populate only those states with singlet character. In the eight level system therefore, the central four states, $|\Psi_{\pm 2}\rangle$ and $|\Psi_{\pm 3}\rangle$, are equally populated ($p_i = 1/4$) and the others empty. The pulse Hamiltonian $\hat{\mathrm{H}}_1$ was developed in a similar manner to that used in Section 2.2.2. The mw pulses affect both electron spins equally, but the magnitude of their effect on the nuclear spin was negligible in comparison. For this reason in the rotating frame $\hat{\mathrm{H}}_1 = -\omega_1 \hat{S}_x$ as before. Once transformed into the eigenbasis of $\hat{\mathrm{H}}_0$, $\hat{S}_x$ could be written

$$\hat{S}_x = \begin{pmatrix} \cdot & \cdot & 1 & 0 & c & s & \cdot & \cdot \\ \cdot & \cdot & 0 & 1 & -s & c & \cdot & \cdot \\ 1 & 0 & \cdot & \cdot & \cdot & \cdot & c & s \\ 0 & 1 & \cdot & \cdot & \cdot & \cdot & -s & c \\ c & -s & \cdot & \cdot & \cdot & \cdot & 1 & 0 \\ s & c & \cdot & \cdot & \cdot & \cdot & 0 & 1 \\ \cdot & \cdot & c & -s & 1 & 0 & \cdot & \cdot \\ \cdot & \cdot & s & c & 0 & 1 & \cdot & \cdot \end{pmatrix} \quad \text{where} \quad \begin{aligned} s &= \sin(\psi_\alpha - \psi_\beta) \\ c &= \cos(\psi_\alpha - \psi_\beta) \end{aligned} \tag{2.29}$$

(the dots represent zeroes, omitted for clarity). $\hat{S}_x$ reflects the coupling within the system. The 2×2 matrices containing s and c indicate the coupling between electron A and the nucleus. The absence of coupling between electron B and the nucleus is indicated by the 2×2 identity matrices. The pulses were applied in the form of rotation operators (equation 2.10) with $\beta = \pi/4$ and $\gamma = \pi$, and the calculation was performed as a straightforward matrix multiplication of equation 2.2 using Mathematica [84].

2.4.2 Echo Modulation in $\mathrm{P}^+\mathrm{Q}_\mathrm{A}^-$ Including the Nuclear ESEEM

Calculations of the echo modulation functions for a pair of weakly coupled electrons, with an anisotropic hyperfine coupling between one of these electrons (A) and a spin-1/2 nucleus (N), gave the following:

$$E_x = \frac{\sin 2(J-d)\tau}{4}[1+f(\tau)] \tag{2.30}$$

$$E_y = 0 \tag{2.31}$$

where $f(\tau)$ in equation 2.30 has the form

$$f(\tau) = 1 - \frac{k}{2}\left[1 - \cos\omega_\alpha\tau - \cos\omega_\beta\tau + \frac{1}{2}\cos(\omega_\alpha - \omega_\beta)\tau + \frac{1}{2}\cos(\omega_\alpha + \omega_\beta)\tau\right] \tag{2.32}$$

with

$$k = \left(\frac{b\omega_\mathrm{N}}{\omega_\alpha\omega_\beta}\right)^2. \tag{2.33}$$

It is encouraging to note that these expressions are consistent with both the echo modulation functions determined for a pair of weakly coupled electrons (equations 2.22 and 2.23), and the echo modulation functions determined by Mims for a single electron coupled to a spin-1/2 nucleus [66]. In the latter case, the *in-phase* echo is given by equation 2.32.

Again, as is expected from a spin-correlated radical pair, the in-phase echo is absent. The out-of-phase echo is strongly influenced by the coupling between the electrons and the nucleus. This echo is modulated at $2(J-d)$ as for a weakly coupled radical pair, but there are extra modulations governed by $[1 + f(\tau)]$. Here $f(\tau)$ gives the modulation caused by the coupling between electron A and the spin-1/2 nucleus, and "1" indicates that there is no coupling between this nucleus and electron B affecting the spectrum.

Looking at equation 2.30 as a whole, it is clear that in addition to the modulations at $2(J-d)$ caused by the spin-spin interactions, the anisotropic hyperfine coupling to A causes modulations at additional frequencies

$$2(J-d) \pm \omega_\alpha$$

$$2(J-d) \pm \omega_\beta$$

$$2(J-d) \pm \omega_\alpha \pm \omega_\beta$$

with amplitudes of $k/2$ or $k/4$. k can be described as the "modulation depth" since its magnitude determines the extent to which E_x deviates from equation 2.22. In the case that $k = 0$, E_x reverts back to the pure electron-electron modulation. This can be achieved if the pseudo-secular hyperfine coupling parameter, b is zero. It is obvious now that it is this anisotropic interaction which causes the modulation at extra frequencies. Moreover, this also proves that at the X-band frequency, where pulses are broad, ESEEM frequencies are not affected in any way by isotropic hyperfine couplings alone.

It is now important to quantify the effect of these extra modulations upon ESEEM spectra by using simulations of experimental data based on these expressions. Simulations demonstrate the extent to which the nuclear modulations alter the pure electron-electron spectrum and can indicate whether these modulations may cause systematic errors in the determination of D and J from experimental spectra of $P^+Q_A^-$.

2.4.3 Simulated ESEEM Spectra for $P^+Q_A^-$

Simulations of ESEEM data were performed using the Fortran 77 program `echo3d2.f` (Appendix A.1.1) by evaluating E_x at each value of τ for which the experiment is recorded. Experimentally τ usually takes values up to around 3 μs with an increment, $\delta\tau$, of between 10 ns and 30 ns. The spectral width (sw) of the recorded frequency domain spectrum is governed by the equation

$$sw = \frac{1}{\delta\tau}. \tag{2.34}$$

For ESEEM spectra recorded from frozen solutions, the shape depends heavily upon the presence of an isotropic distribution of radical pair orientations. It was therefore necessary when simulating such spectra to calculate $E_x(\tau)$ over the whole sphere. Taking the electron-electron axis (dipolar axis, $\boldsymbol{ee}$), to be defined as being along the z-axis, then $\boldsymbol{B}_0$ will take all directions defined by the spherical polar coordinates (θ, ϕ). For simplicity it was then assumed that the electron$_\mathrm{A}$-nuclear axis (the hyperfine axis, $\boldsymbol{en}$) is in the yz-plane and at an angle ξ to the dipolar axis as depicted in Figure 2.10 on the following page. The vectors $\boldsymbol{B}_0$, $\boldsymbol{ee}$ and $\boldsymbol{en}$ were now defined by the following equations:

$$\begin{aligned}
\boldsymbol{B}_0 &= \{\sin\theta\cos\phi, \sin\theta\sin\phi, \cos\theta\} \\
\boldsymbol{ee} &= \{0, 0, 1\} \\
\boldsymbol{en} &= \{0, \sin\xi, \cos\xi\}.
\end{aligned}$$

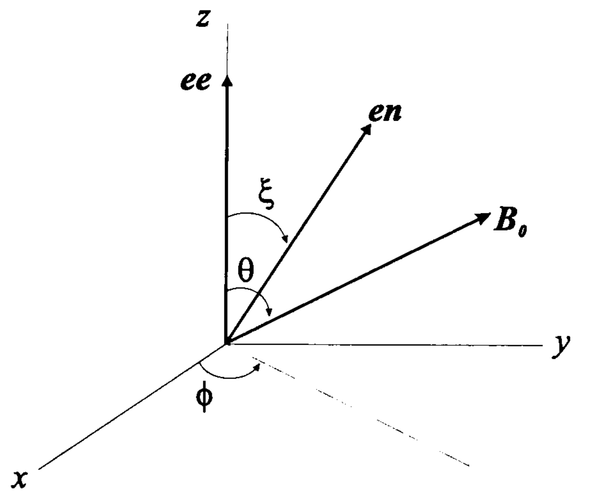

Figure 2.10: The relationship between the electron-electron (*ee*), electron-nuclear (*en*) and magnetic field ($\boldsymbol{B}_0$) vectors in terms of spherical polar coordinates (θ, ϕ) and the angle ξ between the dipolar and hyperfine axes. In the model *ee* is fixed, *en* lies in the yz plane and $\boldsymbol{B}_0$ takes all orientations.

$E_x(\tau)$ (equation 2.30) was the sum of the $E_x(\tau, \theta, \phi)$ terms for each orientation within the hemisphere defined by $\theta : 0 \to \pi/2$, $\phi : 0 \to 2\pi$, *i.e.*

$$E_x(\tau) = \int_0^{\pi/2} \int_0^{2\pi} E_x(\tau, \theta, \phi) \sin\theta d\phi d\theta.$$

Since ω_α, ω_β and k are given by equations 2.28 and 2.33 and $d = D(\cos^2\theta - 1/3)$, the shape of the spectrum depends upon the values of the parameters J, D, a, b and ω_N. An axially symmetric hyperfine coupling was assumed so that parameters a and b were defined by

$$a = A(3\cos^2\varepsilon - 1) \tag{2.35}$$

$$b = 3A\sin\varepsilon\cos\varepsilon. \tag{2.36}$$

So, over an isotropic distribution of angles θ and ϕ, a and b depended only upon A and the angle ε between the magnetic field and the hyperfine axis. Since this angle can be written $\cos\varepsilon = \boldsymbol{B}_0 \cdot \boldsymbol{en} = \sin\theta\sin\phi\sin\xi + \cos\theta\cos\xi$, a and b can be expressed purely in terms of A and ξ. The five parameters which determine the shape of the spectrum were therefore; D, J, A, ω_N and ξ.

For the purpose of the simulations, values of D, J and ω_N were estimated from previous experimental studies. D is thought to be between -1.1 G and -1.4 G [49–51] giving rise to an inter-radical separation (r) of between 27.1 Å and 29.3 Å. At these distances, the exchange interaction, which is largely governed by its inverse proportionality to e^r, can be assumed to be zero. For an example of a spin-1/2 nucleus, ^{15}N may be used. In a 9.4 T NMR field, ^{15}N has an NMR frequency of 40.5 MHz [21]. Moving to the X-band EPR field of 0.33 T, this becomes a frequency of around 1.25 MHz, or $\approx$ 0.5 G. Where the spin-1/2 nucleus is ^{1}H, the nuclear frequency is ten times higher, approximately 5 G. This one-nucleus model is an approximation which can illustrate the type of effects nuclear ESEEM can have in the spectrum of $P^+Q_A^-$. It is therefore not realistic to expect the parameters A and ξ to accurately represent physical quantities, but rather to use them to investigate the extent of the nuclear modulation effect.

Nuclear ESEEM Effect in $P^+Q_A^-$

Simulations performed with $\omega_N = 0.5$ G were used to mimic the possible effect of an ^{15}N nucleus on the ESEEM spectrum. Values of D and J were taken to be -1.4 G and 0.0 G respectively. The transverse (T_2) relaxation was assumed to be exponential, giving rise to a Lorentzian broadening in the frequency domain. The parameter for this broadening was set at 0.05 G. Figure 2.11 on the following page, shows the dependence of the modulation frequencies upon A and ξ. In these simulations τ takes values from zero to 2.8 μs in steps of 45 ns giving a spectral width of about 8 G. In the simulations shown here, the x-axis is converted from frequency to field units, using the conversion 2.8 MHz = 1 G. This is done to allow the values of D and J to be read in Gauss directly from the spectra. The conversion is used in *all* the simulated spectra shown throughout this thesis. Two values of ξ are considered in the figure; zero in a), and 45° in b). It is clear that for values of A such that $0 < A \leq 4$ G, the nucleus has a dramatic effect on the spectra, regardless of the value of ξ. In the spectra shown, as A increases, the intensity at $f_\perp$ begins to decrease and ridges appear between the main peaks at around ± 0.3 G. More importantly with regard to the measurement of D and J, as A moves towards 1 G (at which the maximum effect is observed), changes appear at and just beyond the position of $f_\parallel$. The intensity of these frequencies increase such that it appears that the turning point of this spectral wing has moved to higher frequency. As the value of A becomes larger than about 4 G, the shape of the spectrum returns to a smooth Pake doublet once again.

This behaviour can be explained by consideration of equations 2.33, 2.35 and 2.36 on pages 41 and 43, and Figure 2.8 on page 39. The modulation at extra frequencies when $A < 4$ G arises because of the mixing of the nuclear sub-levels. As can be seen from Figure 2.8, this mixing will only occur when the energy gap between the states $|\beta_A\alpha_N\rangle$ and $|\beta_A\beta_N\rangle$ or between $|\alpha_A\alpha_N\rangle$ and $|\alpha_A\beta_N\rangle$, or both, is approximately the same magnitude as b. This would suggest that the maximum amplitude of the semi-allowed transitions occurs when $\omega_N \approx a \approx b$. Equation 2.33 clearly shows this

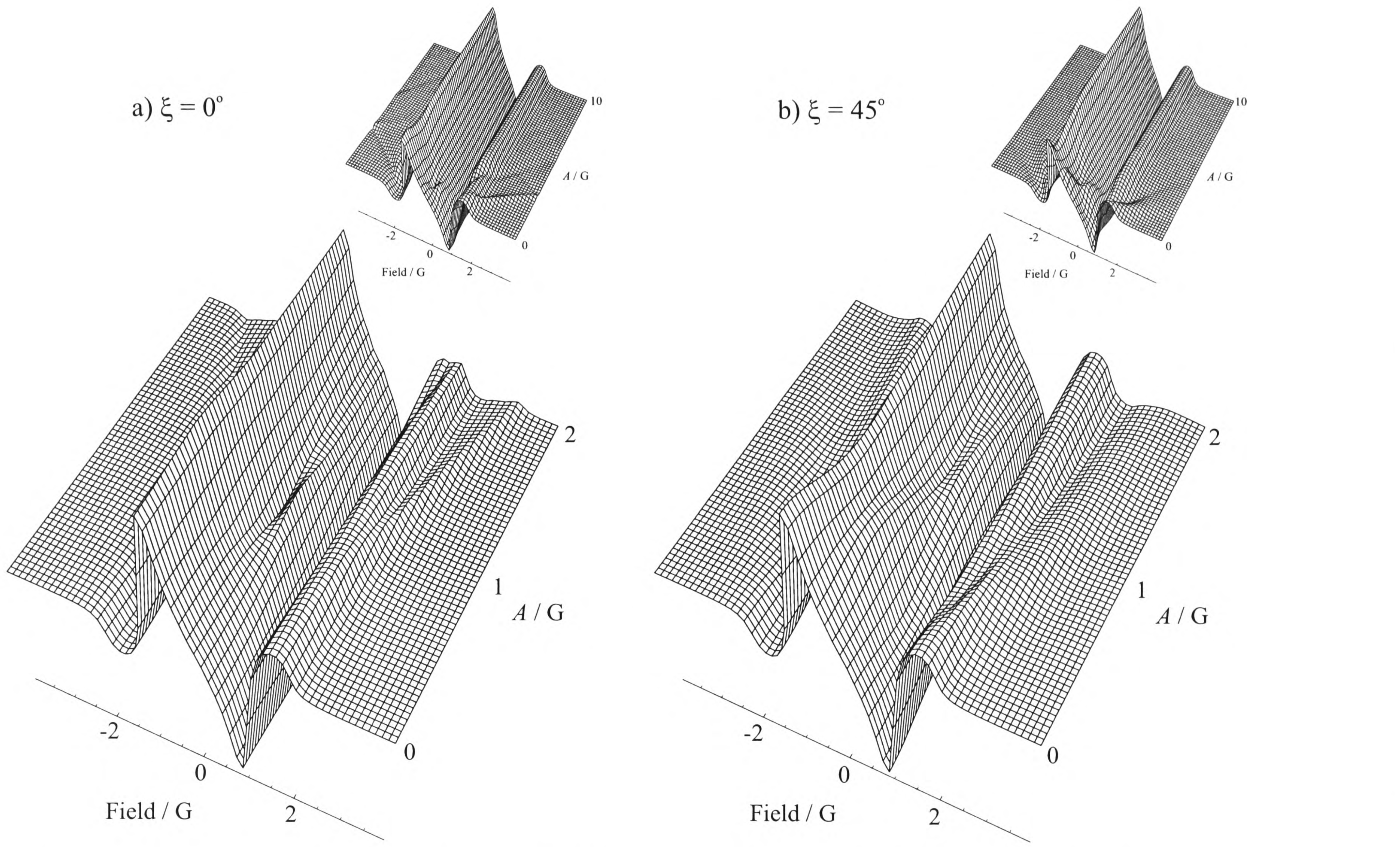

Figure 2.11: The effects of the hyperfine coupling constant, A, upon the ESEEM spectrum. a) $\xi = 0^{\circ}$, b) $\xi = 45^{\circ}$. Main pictures show A from 0 G - 2 G, inset to 10 G. For both values of ξ the effects of the hyperfine coupling are clear; ridges appear at ± 0.3 G and extra features appear beyond the outer shoulder. Insets show that for both values of ξ, the nuclear modulation effects disappear when A becomes larger than 4 G.

to give a large value of k so that deep modulations occur at the frequencies given in equation 2.32. If, on the other hand, A is large ($A > 4$ G) so that for many orientations (θ, ϕ) a and b are greater than ω_N, then the gap between the spin states is no longer a similar size to b, and mixing cannot occur. In this instance, again considering equation 2.33 where a and b are large, k is very small.

Nuclear modulation effects were not observed to any great degree when ω_N was changed to emulate a ^1H hyperfine nucleus ($\omega_N = 5$ G). The reasoning behind this observation is as follows. The above argument for $\omega_N = 0.5$ G suggests then if ω_N is of the order of 5 G, and if a and b are of a similar size ($A \approx 5$ G), modulation should occur since there would be no change in the value of k. However, despite the unchanged modulation depth, these effects were still not seen. This is explained by considering the frequencies at which modulation would occur. Regardless of the constant value of k, the modulation frequencies given by equation 2.32 do alter for increased ω_N, a and b, becoming much faster, thereby having a much larger spread of frequencies and dephasing more quickly than in the case where $\omega_N \approx a \approx b \approx 0.5$ G. These high frequency extra modulations are therefore at low amplitude and are effectively undetectable.

Returning to the situation where $\omega_N = 0.5$ G, the potential effects of nuclear modulations on the determination of D and J in $P^+Q_A^-$ are investigated. Since the positions of the canonical frequencies are usually measured from the positions of the central peak and the turning point of the outer shoulder, the apparent shifting of this turning point has the potential to cause inaccuracies in the measurement of $f_{||}$ and hence D and J. This problem can be more closely studied using a particular example. Figure 2.12a (overleaf) shows the simulated ESEEM spectrum in the case where $D = -1.4$ G, $J = 0$ G and no hyperfine coupling is present ($A = 0$). The positions of $f_\perp$ and $f_{||}$ as calculated from equation 2.24 are shown on the diagram. They lie at 0.93 G and 1.87 G respectively. Figure 2.12b shows the spectrum recorded with the same values of D and J, but with a small hyperfine coupling constant, $A = 0.75$ G with $\xi = 45^\circ$. This spectrum bears a close resemblance to that measured by Dzuba *et al.* shown in Figure 2.7 (page 37). It contains the changes predicted by Figure 2.11; shoulders have appeared at about ±0.3 G, and the intensities of frequencies just beyond $f_{||}$ have increased. It is now not at all obvious where $f_{||}$ lies and as Figure 2.12c shows, the new point of inflexion in 2.12b is misleading. In spectrum 2.12c, D and J have been changed to -1.7 G and 0.01 G respectively. In this example, $f_\perp$ lies at ± 0.93 G and $f_{||}$ at ± 2.47 G. These positions appear to be in exactly the

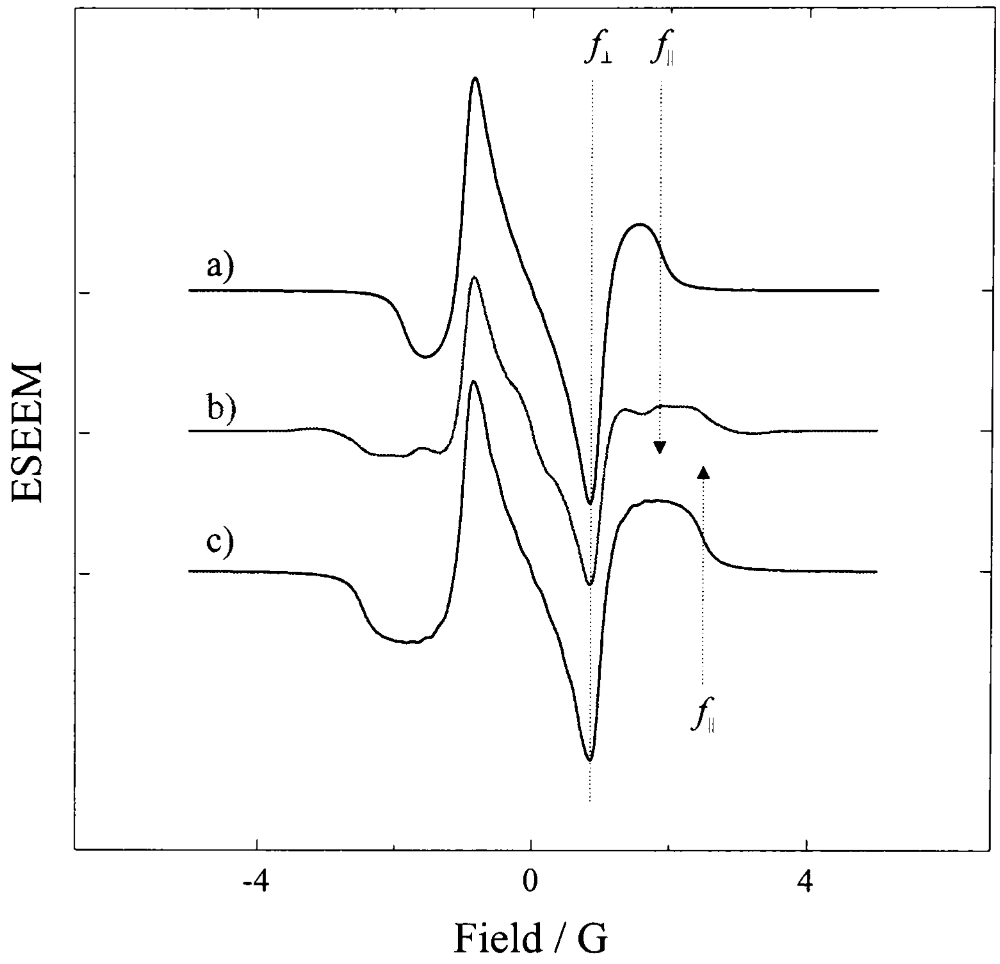

Figure 2.12: Three simulated ESEEM spectra showing the effect of the anisotropic hyperfine coupling as described in the text. a) $D = -1.4$ G, $J = 0$ G and $A = 0$ G. b) $D = -1.4$ G, $J = 0$ G and $A = 0.75$ G with $\xi = 45°$. c) $D = -1.7$ G, $J = 0.01$ G and $A = 0$ G.

same places as those in 2.12b, despite the different values of the spin-spin couplings.

2.4.4 Discussion

The investigations undertaken in this Chapter show that for a weakly coupled radical pair with an anisotropic hyperfine coupling between one electron and a nearby spin-1/2 nucleus, under the correct conditions, nuclear modulations will arise in the ESEEM. These are not only observable [34, 68], but also have the potential to distort the spectrum to the extent that the determination of the spin-spin coupling parameters may be effected.

A further investigation into the effect of nuclear modulations on the ESEEM spectra of $P^+Q_A^-$ is undertaken in Chapter 4, where curve fitting in the time domain is used to determine values for all the parameters in the model.

Chapter 3

ESEEM of a Strongly Coupled Radical Pair: $Q_A^-Q_B^-$

In the previous chapter, the ESEEM of the weakly coupled spin-correlated photosynthetic radical pair $P^+Q_A^-$ was investigated. However, radical pairs formed in photosynthetic reaction centres do not all have the same characteristics as $P^+Q_A^-$. This chapter considers one example of a different type of radical pair, $Q_A^-Q_B^-$. This species turns out to be not only uncorrelated, but also strongly coupled, leading to ESEEM spectra very different to those found for $P^+Q_A^-$.

3.1 Introduction

Recently, EPR spectroscopy of *Rb. sphaeroides* has been used to study the uncorrelated radical pair $Q_A^-Q_B^-$ [85–87]. Curve fitting methods on Q-band (35 GHz) and W-band (95 GHz) EPR spectra have been used to estimate values of the spin-spin coupling parameters, D and J, giving -3.9 G and 5.0 G respectively, with this value of D giving rise to an inter-radical distance, r, of approximately 19.2 Å. X-ray studies [88] have shown however, that the distance is closer to 17 Å, implying a dipolar coupling constant of -5.7 G. Studies using ESEEM experiments have not until now been performed on this RP, and it is possible they could help to determine the true values of D and J. This chapter investigates the viability of using ESEEM at X-band to shed some light on this disputed area.

The Formation of $Q_A^-Q_B^-$

$Q_A^-Q_B^-$ can be formed by one of two different methods. In both cases the radical pair is not generated from a single molecular precursor and consequently contains no spin polarisation. The first method of preparation involves the use of the reducing agent $NaBH_4$ at pH 10.5 to reduce both quinones without altering the oxidation state of the special pair, P [86, 87]. Alternatively, $PQ_A^-Q_B^-$ may by created by two consecutive electron transfer processes. If the transfer of an electron to the second quinone Q_B is not inhibited, then within 100μs of the formation of $P^+Q_A^-$, the electron will move directly to the second quinone, creating $P^+Q_B^-$[16]. If this reaction is performed in the presence of cytochrome c, then P^+ is reduced and the process can be repeated, leading to the creation of $PQ_A^-Q_B^-$ [85].

3.2 ESEEM of a Weakly Coupled Uncorrelated Radical Pair

As a starting point, the ESEEM of a radical pair with thermal equilibrium populations and unspecified $\boldsymbol{g}$-tensors was considered. Here the weak coupling approximation is appropriate, and this example can be used to highlight the differences in the ESEEM of spin-correlated and uncorrelated radical pairs. The calculation used the model developed in Chapter 2, taking the assumption that no anisotropic hyperfine coupling corrupts the pure electron-electron ESEEM.

3.2.1 Theory

An uncorrelated radical pair, AB, will have a very different ESEEM spectrum to that of $P^+Q_A^-$. Since it has been assumed that any hyperfine couplings present in this radical pair are purely isotropic (so that nuclear ESEEM can be ignored), AB has the four eigenstates of a pure electron-electron radical pair given by equation 2.5 in Section 2.2.2, page 26. The initial populations of these levels at thermal equilibrium (the uncorrelated state) are given by the Boltzmann distribution [89]; for a system of two coupled electrons, with spin states $|i\rangle$, the thermal equilibrium populations, p_i, are;

$$p_1 = \tfrac{1}{4}(1 - \tfrac{\hbar\omega}{kT}), \quad p_2 = \tfrac{1}{4}, \quad p_3 = \tfrac{1}{4}, \quad p_4 = \tfrac{1}{4}(1 + \tfrac{\hbar\omega}{kT}).$$

These states, their relative populations, and the allowed EPR transitions between them are pictured in Chapter 1 (Figure 1.5a, page 10). The figure indicates that the Pake doublets forming the ESEEM spectrum are in-phase, unlike those for a spin-correlated radical pair. If weak coupling between the radicals is assumed, then the differences between the ESEEM spectra of AB and $P^+Q_A^-$ are caused by the differences in the initial populations alone. For simplicity $\hbar\omega/kT$ is set to 1, giving initial populations $p_1 = 0$, $p_2 = 1/4$, $p_3 = 1/4$ and $p_4 = 1/2$. Putting these populations and $\psi = \pi/4$ (for weak coupling) into equations 2.12 and 2.13 gives the following echo modulation functions:

$$\begin{aligned} E_x &= 0 && (3.1) \\ E_y &= \frac{1}{2}\sin\beta C_0. && (3.2) \end{aligned}$$

The echo is purely in-phase, which is to be expected from a radical pair with no spin-correlation to cause a phase shift to the x-channel. Clearly the maximum echo occurs when $\beta = \pi/2$, although since $\sin\beta$ merely scales E_y, a pulse of $\pi/4$ still gives an echo signal. With $\beta = \pi/2$, E_y becomes:

$$E_y = \frac{C_0}{2} = \frac{\cos 2(J-d)\tau}{2}, \tag{3.3}$$

where once again, $d = D_{zz} = D(\cos^2\theta - 1/3)$. Comparing this equation with the analogous expression for a spin-correlated radical pair (equation 2.22) it can be seen that the two expressions differ only in that an SCRP gives rise to a sine modulation in the out-of-phase channel, in contrast to the cosine modulated in-phase echo seen here.

Simulations were performed using a modified version of of the Fortran 77 program used in the previous chapter, `echo3d2.f`, setting $A = 0$ to remove modulation due to anisotropic hyperfine interactions (Appendix A.1.1). The program was altered to give a cosine modulation dependent solely upon J and d, and the real part of the Fourier transform was used to create the frequency domain spectrum.

3.2.2 Simulated Spectra

Figure 3.1, on the following page, shows simulated spectra for an uncorrelated radical pair using the weak coupling approximation. Two values of D were used in the simulations; that estimated from W-band EPR of $Q_A^-Q_B^-$ (-3.9 G), and the result from X-ray crystallography studies on the radical (-5.7 G). J was taken from the W-band EPR spectrum and was given the value of 5.0 G. In these simulations, the transverse relaxation time, $T_2 = 0.5$ μs was included in terms of an exponential decay and E_y integrated over all dipolar angles θ, *i.e.*

$$E_y(\tau) = \frac{1}{2}e^{-\frac{\tau}{T_2}} \int_0^{\pi/2} \cos[J - D(\cos^2\theta - 1/3)]\tau \sin\theta d\theta \tag{3.4}$$

The step size, $\delta\tau$, is approximately 9ns, giving a spectral width of around 40 G.

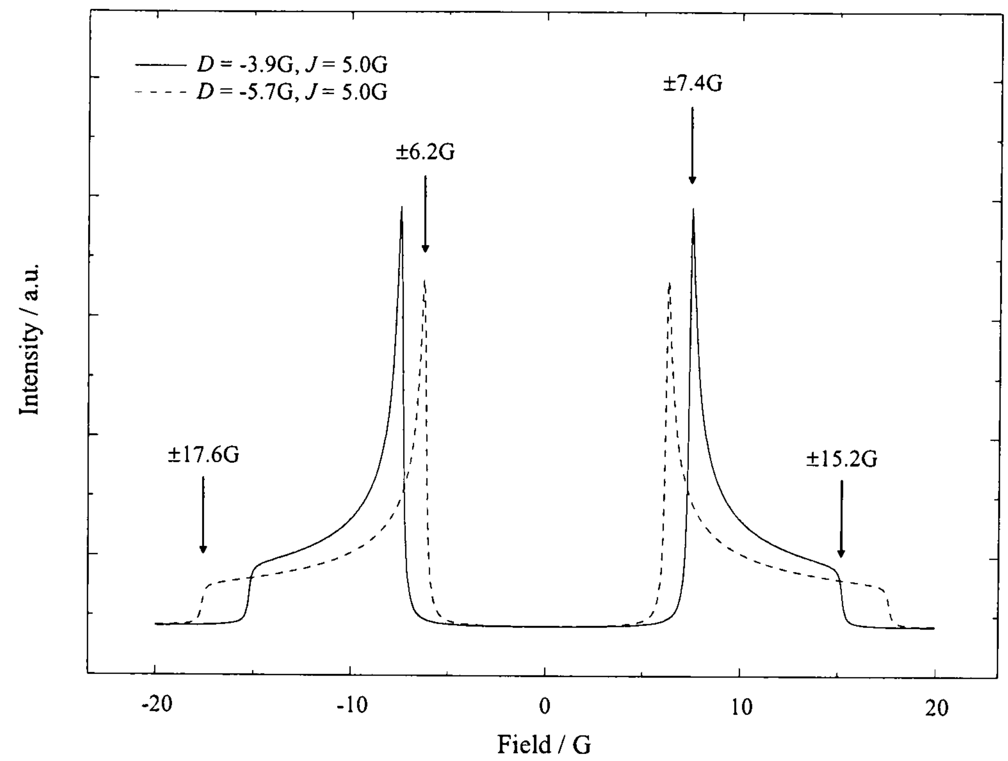

Figure 3.1: ESEEM spectra of a weakly coupled radical pair with thermal equilibrium populations. Spectra are simulated with $J = 5.0$ G and two different values of D: solid lines $D = -3.9$ G, dashed lines $D = -5.7$ G. For each spectrum the positions of $f_\perp$ and $f_\parallel$, as defined in on page 35, are indicated.

The simulated spectra in Figure 3.1 clearly show the Pake doublets created by the powder patterns of D splittings. The large positive exchange coupling, J, gives rise to the large separation between the two components of the spectrum. In each of the spectra in Figure 3.1 the positions of the canonical frequencies are easy to pick out since the two values of D give Pake doublets of different widths. It can therefore be concluded that in the limit of the weak coupling, it should be elementary to use the ESEEM experiment to determine the distance between uncorrelated radicals A and B.

3.2.3 The Radical Pair $Q_A^- Q_B^-$

The weak coupling approximation only applies when $|Q| \gg |j|$. The approach described above can only be used to calculate the ESEEM of the uncorrelated radical pair $Q_A^- Q_B^-$ if the weak coupling approximation is appropriate to this pair. It is certainly valid for $P^+ Q_A^-$ where the distance between the radicals is of the order of 29 Å, and the x, y and z components of the the g-tensors of P^+ and Q_A^- are quite different. Hence there are only very few orientations for which $g_P \approx g_Q$, *i.e.* the radicals are strongly coupled. These orientations make such a small contribution to the ESEEM that they may be neglected. For all other orientations, weak coupling is a good approximation. For $Q_A^- Q_B^-$ however this is not the case. Comparing the two radical pairs, it can be seen that the postulated values of D suggest that the inter-radical distance in $Q_A^- Q_B^-$ is smaller than that of $P^+ Q_A^-$, at approximately 18 Å.

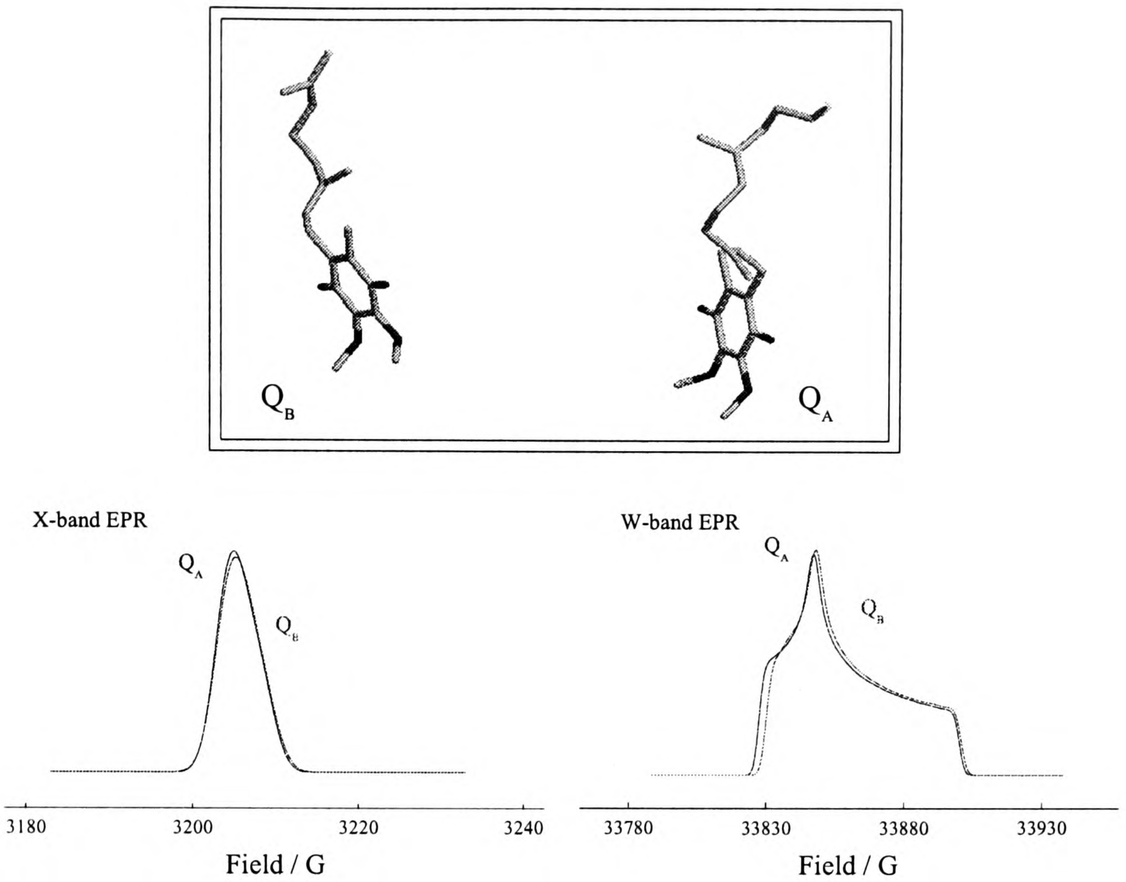

Figure 3.2: Relative orientations of the quinones in $P^+Q_AQ_B^-$, drawn using the X-ray data held in the Brookhaven PDB, entry 1AIG [88]. Also shown are X- and W-band EPR spectra of the quinones indicating the great extent of the similarity between these cofactors.

Moreover, generous estimates give the value of J in $P^+Q_A^-$ to be of the order of +0.01 G [49]. The value of J determined for $Q_A^-Q_B^-$ by cw EPR is around 500 times larger at 5 G [85]. Further evidence comes from consideration of the X- and W-band EPR spectra of the two radicals, and by looking at their relative orientations. X-ray studies of $P^+Q_B^-$ suggest that the two quinone rings are virtually parallel, see Figure 3.2 [88]. The EPR spectra of the radicals at both 9 GHz and 95 GHz overlap almost entirely, and information extracted from the latter experiment indicates that the g-tensors of Q_A^- and Q_B^- are almost identical. This similarity in the both the principal axes and values of the g-tensors of the radicals means that Q will almost always be small, *i.e.* $g_{A_{\text{eff}}} \approx g_{B_{\text{eff}}}$, whatever the field direction, and Q_A^- and Q_B^- are thus strongly coupled.

3.3 ESEEM of a Strongly Coupled Radical Pair

The large values of D and J for the radical pair $Q_A^-Q_B^-$ will lead to a broader spectrum than is seen for $P^+Q_A^-$. It is therefore not realistic to imagine that it could be experimentally possible to produce a pulse hard enough to excite the whole spectrum. The analytical approach outlined in Chapter 2, which relies upon such a hard pulse, cannot be used to calculate the ESEEM of this radical pair. Instead, a numerical calculation must be performed.

3.3.1 Numerical Calculation of the Echo Modulation

Where a hard enough pulse can be produced to validate the analytical approach given in Chapter 2, it is assumed that all the radical pair orientations in the sample are excited equally. A consequence of this is that since all off-resonance effects are refocused, the anisotropy of the $\boldsymbol{g}$-tensors does not affect the ESEEM. However, when using non-uniform excitation, since the modulation due to each radical pair orientation must be considered separately, the $\boldsymbol{g}$-anisotropy of the radicals at particular orientations is vital.

The $\boldsymbol{g}$-tensor of each radical is related to its EPR frequency, ω_A or ω_B, via the *effective* g-value, g_{eff} (assuming $\hbar = 1$):

$$\omega_A = g_{A_{\text{eff}}} \mu_B B_0 \tag{3.5}$$

where

$$g_{A_{\text{eff}}} = \sqrt{\left(g_{Ax}\boldsymbol{n}\cdot\boldsymbol{x}_A\right)^2 + \left(g_{Ay}\boldsymbol{n}\cdot\boldsymbol{y}_A\right)^2 + \left(g_{Az}\boldsymbol{n}\cdot\boldsymbol{z}_A\right)^2}. \tag{3.6}$$

"A" refers to the radical Q_A^-, and similar equations exist for Q_B^-. Here g_{Ai} $(i = x, y, z)$ are the principal components and $\boldsymbol{i}_A$ $(\boldsymbol{i} = \boldsymbol{x}, \boldsymbol{y}, \boldsymbol{z})$ the principal axes of the $\boldsymbol{g}$-tensor of Q_A^-. The x-, y-, and z-axes of the quinone are shown in Figure 3.3. The unit vector $\boldsymbol{n}$, which gives the direction of the magnetic field (B_0) relative to the dipolar axis of the radical pair, is given in polar coordinates such that $\boldsymbol{n} = \boldsymbol{n}(\theta, \phi)$. ω_A is given in angular frequency units, as is the frequency of the static magnetic field, ω (for X-band, $\omega/2\pi = 9$ GHz).

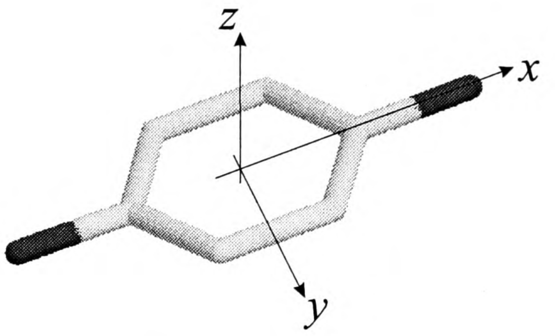

Figure 3.3: Cartesian axes defining the orientation of a quinone. Red areas represent oxygen atoms.

The spin Hamiltonian for this radical pair is that used in Chapter 2:

$$\hat{\mathrm{H}}_0 = \omega_A \hat{S}_{Az} + \omega_B \hat{S}_{Bz} - J\left(\frac{1}{2} + 2\hat{\boldsymbol{S}}_A \cdot \hat{\boldsymbol{S}}_B\right) + D_{zz}\left(3\hat{S}_{Az}\hat{S}_{Bz} - \hat{\boldsymbol{S}}_A \cdot \hat{\boldsymbol{S}}_B\right). \tag{3.7}$$

The calculation uses the density matrix approach outlined in Chapter 2, except that here, the exponential operators are evaluated numerically. It is important to note that the dipolar and exchange terms contain the total spin angular momentum operators of the electrons in this strongly coupled pair, not just the secular parts quantised along the field-axis. In this equation

$$D_{zz} = D\left(\cos^2\theta - \frac{1}{3}\right) \tag{3.8}$$

is the z-component of the total dipolar tensor, $\boldsymbol{D}$, with $\cos^2\theta$ defined by

$$\cos^2\theta = \boldsymbol{n} \cdot \boldsymbol{R}_{\mathrm{AB}} \tag{3.9}$$

and $\boldsymbol{R}_{\mathrm{AB}}$ the unit vector giving the direction of the dipolar axis.

The pulses are defined in terms of a flip-angle, α, and a pulse time, t_p, applied at a given frequency ω_1, such that

$$\alpha = \omega_1 t_p.$$

Once again an integration of the echo modulation function, E_y, is performed over the hemisphere (using Simpson's Rule).

In X-band experiments, the typical π-pulse length is of the order of around 20ns [34, 50, 57]. This corresponds to an mw field (in frequency units) of approximately 25 MHz (width of 9 G). Pulses are applied along the x-axis with detection for the uncorrelated radical pair along the y-axis. These calculations were performed using the Fortran 77 program `spin-echo.f` (Appendix A.1.2).

Data for $Q_A^-Q_B^-$

The calculation of the ESEEM of a strongly coupled RP was performed for the radical pair $Q_A^-Q_B^-$. The principal $\boldsymbol{g}$-tensor components for both Q_A [90] and Q_B [91] have recently been resolved by W-band EPR. Since in *Rb. sphaeroides* both Q_A and Q_B are ubiquinones, the g-value differences between the two stem only from the way in which the radical interacts with the surrounding protein. It is therefore suspected that the $\boldsymbol{g}$-tensors of the two radicals are extremely similar, and indeed the information given in Table 3.1 (overleaf) shows that this is the case [92]. The relative orientations of the radicals are obtained from analysis of the data kept in the Brookhaven Protein Data Base (PDB), entry 1AIG [88]. This data gives the positions of the atomic coordinates of the cofactors in the $P^+Q_AQ_B^-$ state in which the 180° propellor twist and 5 Å shift of Q_B caused by its reduction (as first seen by Stowell *et al.* [88]) are seen.

	Q_A^-	Q_B^-
g_{xx}	2.00647	2.00632
g_{yy}	2.00532	2.00527
g_{zz}	2.00218	2.00213

Table 3.1: Principle g-values used for calculation of the spectra of $Q_A^- Q_B^-$ [92].

If the principal axes of Q_A^- are defined as

$$\begin{aligned} \boldsymbol{x}_\mathrm{A} &= \{1,0,0\} \\ \boldsymbol{y}_\mathrm{A} &= \{0,1,0\} \\ \boldsymbol{z}_\mathrm{A} &= \{0,0,1\} \end{aligned} \tag{3.10}$$

then those of Q_B^- are, by relation

$$\begin{aligned} \boldsymbol{x}_\mathrm{B} &= \{\ 0.684, \quad 0.622, \quad -0.386\} \\ \boldsymbol{y}_\mathrm{B} &= \{\ 0.651, \quad -0.759, \quad -0.062\} \\ \boldsymbol{y}_\mathrm{B} &= \{-0.329, \quad -0.208, \quad -0.924\} \end{aligned} \tag{3.11}$$

and the dipolar vector given by

$$\boldsymbol{R}_\mathrm{AB} = \{-0.352, 0.857, 0.387\}$$

with the distance between Q_A^- and Q_B^- calculated as 17.3 Å.

The g-values given in Table 3.1 and the vectors given in equations 3.10 and 3.11 were used to calculate values of $g_{\mathrm{A_{eff}}}$ and $g_{\mathrm{B_{eff}}}$, and thus to simulate the ESEEM spectrum of $Q_A^- Q_B^-$. It can be noted that the large overlap of the $\boldsymbol{g}$-tensor components, and the near parallel nature of the principal axes of the two radicals, indicate that for all orientations of the RP $g_{\mathrm{A_{eff}}} \approx g_{\mathrm{B_{eff}}}$, so that $Q_A^- Q_B^-$ is indeed a good example of a strongly coupled radical pair.

3.3.2 Simulations of the Spectra of $Q_A^- Q_B^-$: Dependence Upon Off-Resonance Effects and Spin-Spin Coupling

ESEEM spectra for the radical pair $Q_A^- Q_B^-$ were simulated using pulse-angles of $\pi/4$ and π. The pulses were applied at the field position corresponding to the centre of the EPR spectrum of the RP, *i.e.* $g_\mathrm{centre} = 2.0044$. At the X-band frequency of 9 GHz, this corresponds to $B_0 = 3207$ G. The delay time τ took values from 0 to 2.55μs in steps of 10ns and the transverse relaxation time, T_2, which was estimated from

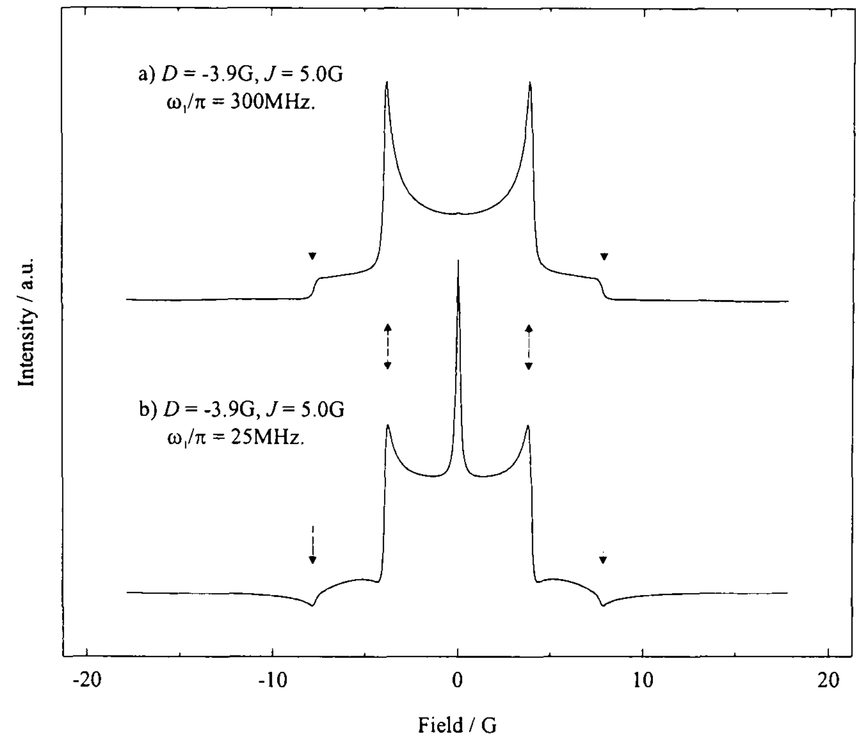

Figure 3.4: Simulated X-band ESEEM spectra of a strongly coupled radical pair, taking $D = -3.9$ G and $J = 5.0$ G. a) $\omega_1/2\pi = 300$ MHz (100 G), b) $\omega_1/2\pi = 25$ MHz (9 G). Both the spectra shown were calculated using the EXORCYCLE pulse sequence, see page 57.

the work of Rohrer *et al.* [93], was 0.5 μs. Figure 3.4 shows the ESEEM spectrum calculated using the values of D and J determined by W-band EPR. Each spectra was simulated using a different pulse strength. It is firstly immediately obvious that these spectra are very different to those obtained for the weakly coupled radical pair. Moreover, it is clear that the strength of the mw pulse has also affected the appearance of the spectrum. Figure 3.4a shows the ESEEM generated by a pulse sequence using a hard pulse of 300 MHz (band-width of 100 G), and 3.4b is that obtained when an experimentally more realistic hard pulse (25 MHz, band-width 9 G) is used. As indicated previously, this corresponds to a π-pulse length of 20ns, the length of the 300 MHz π-pulse being less than 2ns - an impossibly short pulse time, even at X-band. Each of the spectra in Figure 3.4 clearly show a pair of overlapping Pake spectra in which the positions of the canonical frequencies are independent of the pulse strength. However, there are obvious differences in the two spectra; the large spike in the centre of the weaker pulse spectrum, and the slightly inverted nature of the outer shoulders of the powder patterns here. These two features are both caused by off-resonance effects.

Off-Resonance Effects

It was mentioned in Chapter 1 that a sufficiently hard applied mw α-pulse would rotate the magnetisation of every spin by exactly α. This assumption was used in the calculations for Chapter 2 where pulses of infinitely high mw field strength were specified. The numerical calculation used here takes a specific value of ω_1 which in the case of the 25 MHz pulse is not hard enough for the condition to be met.

A hard pulse has $|\gamma B_1| \gg |\Omega_{\rm rot}| = |\omega_L - \omega_{\rm mw}|$ where $\Omega_{\rm rot}$ is the effective precession frequency in the rotating frame, ω_L is the Larmor frequency in the laboratory frame and $\omega_{\rm mw}$ is the frequency of the mw pulse. If however the width of the EPR spectrum of the sample is comparable to the band-width of the pulse, γB_1, then potentially off-resonance effects can appear in the pulsed-EPR spectrum. Figure 3.5 shows the tilted field about which the magnetisation is rotated in this case. A residual effective field $\Delta B_0 = B_0 + \omega_{\rm mw}/\gamma$ results, and it is the resultant field vector ($\boldsymbol{B}_{\rm eff}$) of this field and the $\boldsymbol{B}_1$ field about which the spins are now rotated by an angle $\alpha_{\rm eff} = \gamma B_{\rm eff} t_p$.

These new effective flip angles are different for spins of different Larmor frequencies and will hence create strange effects in the spectrum. Some off-resonance effects may be removed by phase-cycling techniques such as the EXORCYCLE phase cycling procedure [95]. This sequence, which is used here but will be discussed in detail in Chapter 5, removes off-resonance effects caused by imperfections in the mw pulses. However, it is clear from Figure 3.4 that there are off-resonance features in these spectra caused by further effects which are not removed by the EXORCYCLE sequence. It is these off-resonance effects which are discussed in this section.

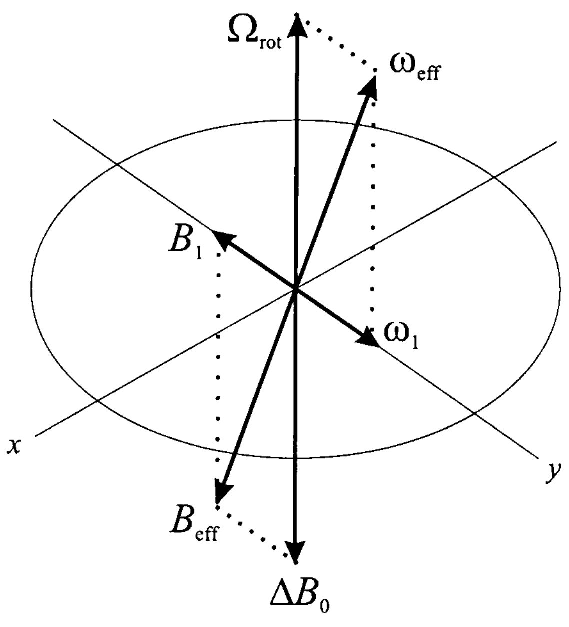

Figure 3.5: The tilted field caused by off-resonance effects in pulsed magnetic resonance experiments. The effective field, $\boldsymbol{B}_{\rm eff}$ is the resultant of the off-set field ($\Delta\boldsymbol{B}_0$) and the field associated with the pulse itself ($\boldsymbol{B}_1$) [94].

The spike in the centre of Figure 3.4b arises from the inability of the 25 MHz pulse to excite the whole spectrum uniformly. For ESEEM to occur, both radicals, A and B, in a radical pair must be simultaneously excited. If more orientations of radical A than radical B are excited by a pulse, then part of the observed echo will come from radical A alone - *i.e.* it is the echo associated with unpaired radical A. The spectrum will in this case show some of the characteristics of single-radical ESEEM. The amalgamation of the unmodulated "single-radical" spectrum, similar to that shown in Figure 1.7 (page 19), and the modulated radical pair spectrum, leads to the spike in the centre of the 25 MHz spectrum of $Q_A^- Q_B^-$. This problem does not arise in the ESEEM of spin-correlated radical pairs where any single-radical contribution would be detected in the in-phase channel, separate from the radical pair ESEEM which is found out-of-phase.

The second off-resonance effect is the slight inversion of the outer shoulders of the Pake spectra in the ESEEM. Since these shoulders correspond to the radical pair orientations with the largest values of $D(\cos^2\theta - 1/3)$, it is unsurprising that they experience the largest off-resonance effect. The inversion is caused by the effective pulse angle flipping the spins into the xy-plane, rather than the y-axis, and causing a degree of dispersion in the resulting signal.

These off-resonance effects were removed under the influence of an extremely hard pulse to give the smooth, clean spectrum shown in Figure 3.4a. The peaks due to the modulations from the spin-spin couplings are the same regardless of the strength of the mw field, and for clarity therefore, the spectra in the rest of this chapter have been calculated using a 300 MHz pulse.

Dependence of the Spectrum of $Q_A^- Q_B^-$ upon D and J

In Figure 3.4a, the features marked by arrows are the edges of the Pake spectra. These arrows correspond to the field positions ±3.9 G and ±7.8 G. In the weak coupling case, features are seen at the positions of the frequencies $f_\perp$ and $f_\parallel$ given by

$$f_\parallel = \pm\left(2J - \frac{4}{3}D\right) \qquad f_\perp = \pm\left(2J + \frac{2}{3}D\right). \tag{3.12}$$

With the values of D and J used to simulate Figure 3.4a, $f_\perp$ and $f_\parallel$ would be seen at ±7.4 G and ±15.2 G respectively. Clearly, there are no features at these field positions in the strong coupling spectrum, and those peaks which do appear lie at field positions corresponding to $\pm D$ and $\pm 2D$.

The simulated spectra shown in Figure 3.4 suggest that if a radical pair is strongly coupled, then the echo modulation arising is independent of the exchange interaction. This hypothesis can be validated by simulation of the spectrum for a variety of values of J while keeping the dipolar coupling the same. Figure 3.6a on the next page, shows the results of such simulations. For two values of D, −3.9 G and −5.7 G, the ESEEM spectra are calculated for J = 3.0 G, 5.0 G and 7.0 G. The spectra are almost identical, indicating that the ESEEM is indeed unaffected by the value of J. It is only when the exchange interaction is so small that the pair is no longer strongly coupled (*i.e.* $J = 0$ in 3.6b) that any change on the spectral shape is seen.

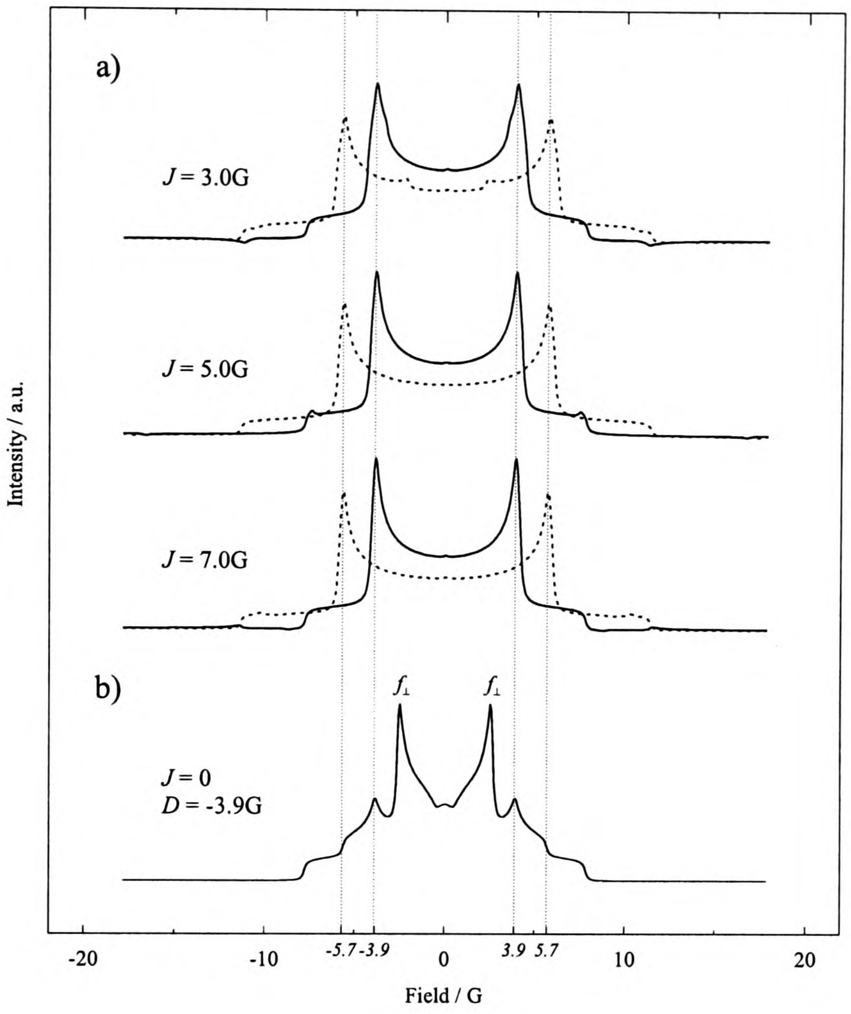

Figure 3.6: a) Simulated ESEEM spectra of a strongly coupled radical pair. Solid lines: $D = -3.9$ G, dotted lines: $D = -5.7$ G, J varying. Each spectrum clearly shows peaks at $\pm D$ and $\pm 2D$. b) ESEEM spectrum for the same pair with $D = -3.9$G and $J = 0.0$ G. Spectra are calculated using the EXORCYCLE pulse sequence.

The Effect of Anisotropic Hyperfine Couplings

Thus far the calculation of the ESEEM of the uncorrelated radical pair $Q_A^-Q_B^-$ has not included the possibility of a contribution from anisotropic hyperfine interactions in the form of nuclear ESEEM. The presence of an effect due to such interactions may alter the shape of the ESEEM spectra, and, as was seen in Chapter 2, reduce the accuracy to which the dipolar coupling can be determined. It is important therefore to be able to predict how great this effect could be.

Nuclear ESEEM can be included in this numerical calculation by the addition of the "nuclear Hamiltonian", $\hat{H}_N$, to that given in equation 3.7. If a spin-1/2 nucleus with an axial hyperfine coupling identical to that used in the previous chapter is included, then $\hat{H}_N$ contains terms for the secular, a, and pseudo-secular, b, hyperfine interactions, and the nuclear Zeeman interaction, ω_N. These terms, give

$$\hat{H}_N = a\hat{S}_{Az}\hat{I}_z + b\hat{S}_{Az}\hat{I}_x - \omega_N\hat{I}_z. \tag{3.13}$$

As before, a and b are defined by the hyperfine coupling constant, A, and the angle between the dipolar and hyperfine axes, ξ (equations 2.35 and 2.36 on page 43).

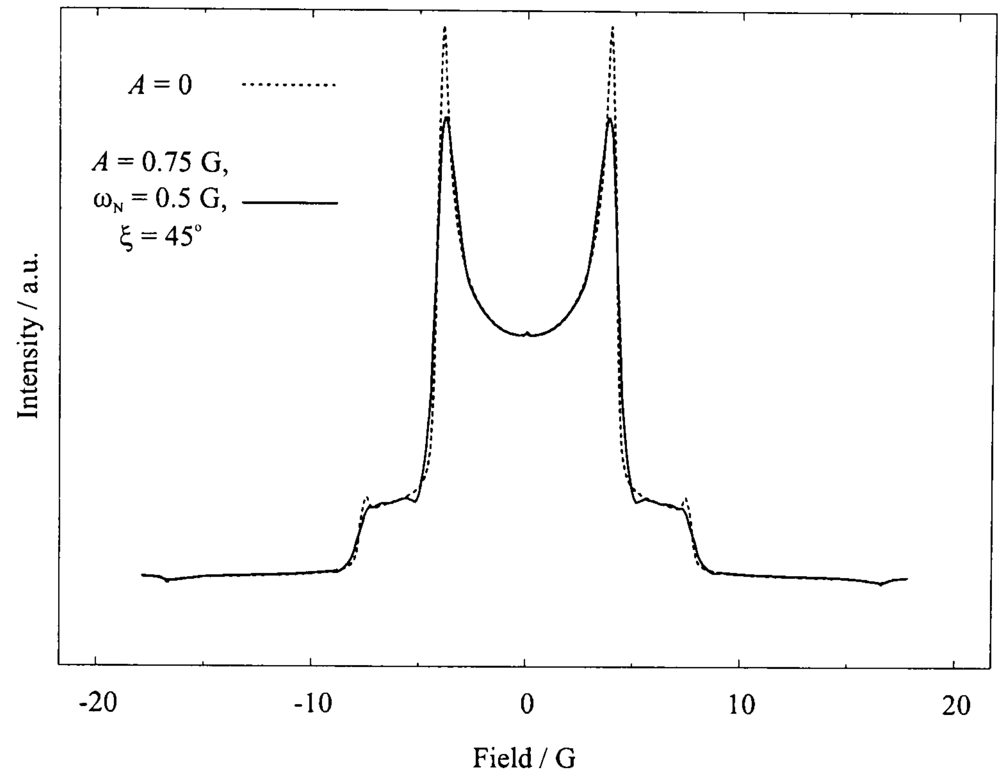

Figure 3.7: Simulated ESEEM spectra for a strongly coupled radical pair, with (solid line) and without (dashed line) the inclusion of a single spin-1/2 nucleus on one radical. Parameters for the nucleus (defined in Chapter 2) are $A = 0.75$ G, $\omega_N = 0.5$ G and $\xi = 45°$. In both, $D = -3.9$ G and $J = 5.0$ G. Spectra were calculated using the EXORCYCLE pulse sequence.

In Chapter 2, the values of the parameters A and ξ were chosen in an ad-hoc fashion. Those values used for the simulations in Figures 2.11 and 2.12 gave the spectra most closely resembling the experimental data [34]. Since, as yet, there is no experimental data for the ESEEM of $Q_A^-Q_B^-$, this method can not be employed here, and it is difficult to say which values A, ω_N and ξ should take. However, it is thought that the coupling from nitrogen nuclei on the special pair, rather than any nuclei on the quinone radical, is the principle cause of the ESEEM of $P^+Q_A^-$ [68]. It is therefore reasonable to assume that the nuclear ESEEM seen in $Q_A^-Q_B^-$ will not be greater than that produced using the parameter values used in Chapter 2. Hence, in the following simulation, the parameters for the spin-1/2 nucleus in $Q_A^-Q_B^-$ were taken to be

$$A = 0.75 \text{ G}, \ \omega_N = 0.5 \text{ G and } \xi = 45^o.$$

The resulting spectrum, with $D = -3.9$ G and $J = 5.0$ G, is shown in Figure 3.7. As seen in the spectra in Chapter 2, nuclear modulations have had the effect of slightly reducing the intensity of the signal. There is, however, no change in the positions of the peaks which still lie at $\pm D$ and $\pm 2D$. It is unlikely therefore that the presence of anisotropic hyperfine couplings will affect the accuracy to which this method may be used to experimentally determine the inter-radical distance in $Q_A^-Q_B^-$.

3.4 Discussion and Consideration of $I^-Q_A^-$

3.4.1 Interpretation of the Strong Coupling Spectra

The echo modulation functions calculated in Chapter 2 (equations 2.12 and 2.13, page 29) give a complete picture of the ESEEM of any radical pair regardless of the strength of the coupling between the electrons or the initial starting populations. They can therefore be used to explain the appearance of the simulated spectra for $Q_A^-Q_B^-$.

The in-phase echo for the general radical pair, equation 2.13, gives:

$$E_y = (p_4 - p_1)\sin\beta\{\sin^2 2\psi C_0 + \cos 2\psi[\cos^2\psi C_{-1} - \sin^2\psi C_{+1}]\}.$$

Where there is strong coupling, so that $\psi \to 0$, this becomes

$$E_y = (p_4 - p_1)\sin\beta C_{-1} \tag{3.14}$$

$$\text{with} \quad C_{-1} = \cos[2(J - d - \Omega)\tau]. \tag{3.15}$$

Since for strong coupling $Q \ll j$ then $\Omega^2 = j^2 + Q^2 \approx j^2$ leaving $\Omega \approx j = J + d/2$. Now,

$$\begin{aligned} C_{-1} &= \cos[2(J - d - J - d/2)\tau] \\ &= \cos[(-3d)\tau] \end{aligned}$$

so that for the canonical orientations $\theta = 0^\circ$ and $\theta = 90^\circ$

$$\begin{aligned} -3d \quad &= \quad -3D(\cos^2\theta - \tfrac{1}{3}) \\ \text{at} \quad \theta = 0^\circ \quad &\to \quad -2D \\ \text{at} \quad \theta = 90^\circ \quad &\to \quad D \end{aligned}$$

which will result in spectra with features at $\pm D$ and $\pm 2D$ like those shown in Figure 3.6. These calculations show that the spectra are indeed independent of J. This relationship can also be explained by considering the parts of the Hamiltonian (equation 3.7) governing the spin-spin coupling, *i.e.*

$$\hat{\text{H}}_J = -J\left(\frac{1}{2} + \hat{\boldsymbol{S}}_\text{A} \cdot \hat{\boldsymbol{S}}_\text{B}\right), \qquad \hat{\text{H}}_D = D_{zz}\left(3\hat{S}_{\text{A}z}\hat{S}_{\text{B}z} - \hat{\boldsymbol{S}}_\text{A} \cdot \hat{\boldsymbol{S}}_\text{B}\right).$$

Equation 2.3 in Chapter 2 defined the echo modulation function for the i-echo as

$$E_i = \text{Tr}[\hat{S}_i \cdot \hat{\rho}(2\tau)] \tag{3.16}$$

where $\hat{S}_i = \hat{S}_{Ai} + \hat{S}_{Bi}$ is the total spin angular momentum operator in the i-direction. For a spin-correlated radical pair this is the transverse magnetisation along the x-axis, and for an uncorrelated radical pair, that along the y-axis. $\hat{\rho}(2\tau)$ is the density matrix at time 2τ. The Liouville-von Neumann equation

$$\frac{d\hat{\rho}}{dt} = -i[\hat{\mathrm{H}}, \hat{\rho}]$$

describes the evolution of $\hat{\rho}(t)$ with time under the influence of the Hamiltonian, $\hat{\mathrm{H}}$. If this Hamiltonian is the sum of two components so that $\hat{\mathrm{H}} = \hat{\mathrm{H}}_1 + \hat{\mathrm{H}}_2$ and $\hat{\mathrm{H}}_2$ commutes both with $\hat{\mathrm{H}}_1$ and with $\hat{S}_y$, the following simplification occurs. Since $[\hat{\mathrm{H}}_1, \hat{\mathrm{H}}_2] = 0$, $\hat{\rho}$ evolves under $\hat{\mathrm{H}}$ to give

$$\hat{\rho}(t) = \mathrm{e}^{-i\hat{\mathrm{H}}_2 t} \cdot \mathrm{e}^{-i\hat{\mathrm{H}}_1 t} \cdot \hat{\rho}(0) \cdot \mathrm{e}^{i\hat{\mathrm{H}}_1 t} \cdot \mathrm{e}^{i\hat{\mathrm{H}}_2 t}.$$

E_y then becomes

$$\begin{aligned} E_y &= \mathrm{Tr}[\mathrm{e}^{-i\hat{\mathrm{H}}_2 t} \cdot \mathrm{e}^{-i\hat{\mathrm{H}}_1 t} \cdot \hat{\rho}(0) \cdot \mathrm{e}^{i\hat{\mathrm{H}}_1 t} \cdot \mathrm{e}^{i\hat{\mathrm{H}}_2 t} \cdot \hat{S}_y] \\ &= \mathrm{Tr}[\mathrm{e}^{-i\hat{\mathrm{H}}_2 t} \cdot \mathrm{e}^{-i\hat{\mathrm{H}}_1 t} \cdot \hat{\rho}(0) \cdot \mathrm{e}^{i\hat{\mathrm{H}}_1 t} \cdot \hat{S}_y \cdot \mathrm{e}^{i\hat{\mathrm{H}}_2 t}] \\ &= \mathrm{Tr}[\mathrm{e}^{-i\hat{\mathrm{H}}_1 t} \cdot \hat{\rho}(0) \cdot \mathrm{e}^{i\hat{\mathrm{H}}_1 t} \cdot \hat{S}_y] \end{aligned}$$

i.e. since $\hat{\mathrm{H}}_2$ commutes both $\hat{\mathrm{H}}_1$ and with $\hat{S}_y$, it has no effect upon the echo modulation. An analogous result is obtained if the magnetisation along the x-axis is considered, where $\hat{\mathrm{H}}_2$ commutes with $\hat{S}_x$.

Attention now returns to the strongly coupled radical pair. For such a pair where $\omega_A = \omega_B = \omega_{AB}$, the Hamiltonian (in the absence of anisotropic hyperfine coupling) is given by

$$\hat{\mathrm{H}} = \omega_{AB}(\hat{S}_{Az} + \hat{S}_{Bz}) + \hat{\mathrm{H}}_J + \hat{\mathrm{H}}_D,$$

so that $\hat{\mathrm{H}}_1 = \omega_{AB}(\hat{S}_{Az} + \hat{S}_{Bz})$ and $\hat{\mathrm{H}}_2 = \hat{\mathrm{H}}_J$ or $\hat{\mathrm{H}}_D$. Hence, when $\hat{\mathrm{H}}_2 = \hat{\mathrm{H}}_J$, it commutes with both $\hat{\mathrm{H}}_1$ and $\hat{S}_y$, and J will have no effect upon the echo modulation. This is not the case when $\hat{\mathrm{H}}_2 = \hat{\mathrm{H}}_D$ due to the $\hat{S}_{Az}\hat{S}_{Bz}$ term. $\hat{\mathrm{H}}_D$ can therefore split the spectrum, whereas $\hat{\mathrm{H}}_J$ cannot.

When the coupling between the electrons in the model for $Q_A^-Q_B^-$ is reduced *i.e.* by setting $J = 0$ (Figure 3.6b), this condition is relaxed and weak features can be seen at the positions of $f_\perp$ and $f_\parallel$: the spectrum looks like a sum of those above and that shown in Figure 3.1.

3.4.2 The Radical Pair $I^- Q_A^-$

By way of testing the hypothesis formed above, it is sensible to consider the results of the same simulations performed for the radical pair $I^- Q_A^-$. This pair, like $Q_A^- Q_B^-$, is in an uncorrelated state. However, the very different nature of the porphyrin ring and the quinone imply that regardless of the relative orientation of the two cofactors, the coupling between them is likely to be weaker than that in $Q_A^- Q_B^-$. The relative orientations of the radicals were computed using data taken from the Brookhaven PDB database, entry 4RCR [11], and gave vectors along the principal axis:

$$\begin{aligned} \boldsymbol{x}_I &= \{\ 0.847, \quad 0.179, \ -0.500\} & \boldsymbol{x}_Q &= \{1,0,0\} \\ \boldsymbol{y}_I &= \{0.0748, \quad 0.891, \quad 0.448\} \quad \text{and} & \boldsymbol{y}_Q &= \{0,1,0\} \\ \boldsymbol{z}_I &= \{0.5261, \ -0.417, \quad 0.741\} & \boldsymbol{z}_Q &= \{0,0,1\}. \end{aligned}$$

where the x and y axes of the porphyrin were those joining opposite nitrogen atoms in the ring. These gave

$$\boldsymbol{R}_{IQ} = \{0.215, -0.701, 0.680\} \text{ with } r = 13.5\,\text{Å}.$$

Principal g-values were taken from the work of Polenova and McDermott [96]. Their study used a model of a bacterial reaction centre with the g-values of I as follows:

$$g_{xx} = 2.0038, \quad g_{yy} = 2.0038, \quad g_{zz} = 2.0029.$$

The dipolar coupling constant was estimated using the value of r determined from the X-ray structure, so that $D = -11.4$ G. The exchange interaction between I^- and the ubiquinone Q_A^- in *Rb. sphaeroides* is known to be somewhere between 1 G and 5 G [97–99].

Figure 3.8 on the next page, shows a) simulated X- and W-band powder EPR spectra of each radical and b) the results of simulations of the ESEEM with various values of J. It is immediately obvious that the EPR spectra of the two radicals overlap very little compared to those of Q_A^- and Q_B^-. This would suggest that despite the larger value of D and the comparable values of J, the coupling between I^- and Q_A^- is far weaker than between the two quinone radicals. This idea is re-enforced by the spectral simulations. In each case, although the principal feature is the peak at $\pm D$, the peaks at $f_\perp$ and $f_\parallel$ are more prominent than in the simulations of $Q_A^- Q_B^-$.

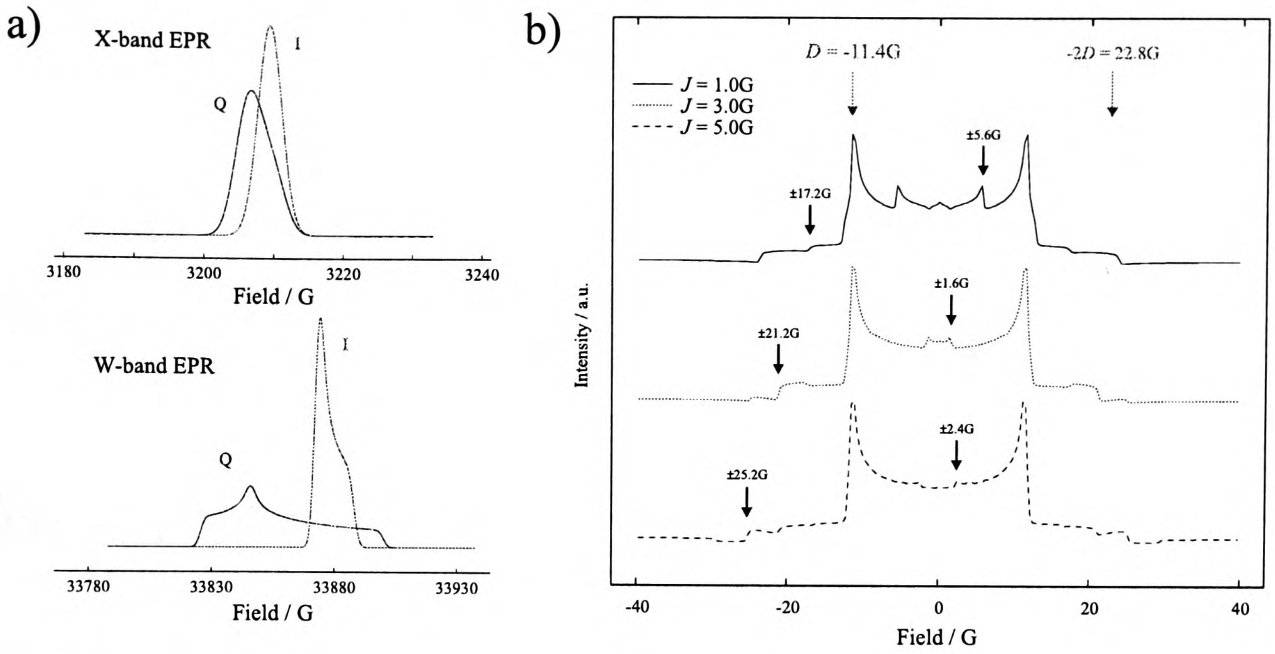

Figure 3.8: a) Simulated X- and W-band EPR spectra for the radicals in $I^-Q_A^-$. b) Simulated ESEEM spectra for this radical pair with $D = -11.4$G, J varying. Spectra are calculated using the EXORCYCLE pulse sequence.

3.4.3 Conclusion

To conclude that $Q_A^-Q_B^-$ will produce ESEEM spectra as expected for a strongly coupled radical pair, *i.e.* with peaks positioned at $\pm D$ and $\pm 2D$, requires evidence that despite fairly small dipolar and exchange couplings, the two electrons are indeed strongly coupled. This evidence has been found by considering both the X-ray data which indicated that the reduced quinones are near parallel, and the W-band EPR spectra revealing very similar $\boldsymbol{g}$-tensors for Q_A and Q_B. This means that for all radical pair orientations, the EPR frequencies of the two radicals are almost the same, making them near equivalent, *i.e.* very strongly coupled. The spectra simulated for $Q_A^-Q_B^-$ clearly show the features at $\pm D$ and $\pm 2D$ expected for a strongly coupled radical pair, and it is hoped that these results will be confirmed experimentally at the Technische Universität, Berlin in the group of Prof. W. Lubitz.

In contrast to the results obtained for $Q_A^-Q_B^-$, spectra simulated for a radical pair with slightly weaker coupling, $I^-Q_A^-$, showed similarities both to the ESEEM of a strongly coupled and to a weakly coupled uncorrelated radical pair. This may suggest that to some degree the extent of the coupling could be ascertained from an ESEEM spectrum. However, within the bounds of the effects of homogeneous line-broadening and noise, this is by no means certain to be the case. These spectra can more probably be used (depending on the quality and the effect of dead-time) to accurately determine the size of D. From this point, the exchange interaction can be determined using a one-dimensional curve fit to the EPR spectrum.

Chapter 4

Distance Determination in Spin-Correlated Radical Pairs

Recently, experiments have been performed to determine whether the primary acceptor in the reaction centre of *Rb. sphaeroides* changes its orientation or position upon oxidation to Q_A^- [38, 56, 57]. The results of these experiments have brought into question the accuracy to which the spin-spin coupling parameters, D and J, may be determined by ESEEM. In this chapter, experimental ESEEM data for $P^+Q_A^-$ in *Rb. sphaeroides* are analysed using a curve fitting procedure in the time domain, and the precision to which D and J can be measured is explored using the method of Cramér-Rao lower bounds [100–103]. These lower bounds are also used to determine an optimal sampling strategy for the experiment. The work contained in this chapter is published in *Chemical Physics Letters* [104].

4.1 The Question of Experimental Accuracy

In Chapter 2 the ESEEM of a weakly coupled radical pair, such as $P^+Q_A^-$, was shown to be sensitive to the sizes of the spin-spin coupling parameters D and J. It was also noted that data recorded from an ESEEM experiment which are transformed into the frequency domain, are at the mercy of the effects of noise, inhomogeneous line-broadening, nuclear ESEEM and the "sinc-wiggles" which result from an imperfect extrapolation of the experimental dead-time. In an experiment where ESEEM is used to detect a very small change in the inter-radical distance, r, such as that anticipated for Q_A as it is reduced in the electron transfer process of photosynthesis, it cannot be considered unlikely that these factors may either conceal or augment any apparent difference in the spectrum.

The question then arises: how best to interpret ESEEM data so that they can be used, as is theoretically possible, to detect very small changes in the sizes of D and J accurately? The answer lies in fitting the experimental data to a curve in the time domain, having made no prior assumption about the values of D, J or the relaxation time T_2. As will be seen, this method avoids the problem of experimental dead-time, and can determine the coupling constants with considerably greater accuracy than is usual in a frequency domain analysis.

Background: Light and Dark Structural Changes

The phenomenon of light induced structural changes in the reaction centres of photosynthetic bacteria was first noted by McElroy *et al.* in 1974 [105]. Using optical methods and studies of the recombination kinetics, they discovered that in *Rb. sphaeroides* the oxidised primary donor P^+ is trapped when the RCs are frozen under constant illumination. The first evidence of a functional change in these reaction centres upon freezing in the light was obtained by Kleinfeld *et al.* ten years later [65]. They considered light- and dark-frozen Q_B depleted reaction centres. The first sample is frozen in the dark in the native, uncharged state, PQ_A. A second sample is frozen under constant illumination, and is consequently in the charge separated state $P^+Q_A^-$, with any structural changes frozen in. Once the light source is removed, $P^+Q_A^-$ reverts to PQ_A, but the structural changes remain. Using optical spectroscopy methods, the lifetimes of the $P^+Q_A^-$ radical pairs produced by a laser flash were measured. Kleinfeld *et al.* observed that the lifetime of the light-frozen radical pair was five times longer than that for the sample frozen in the dark. They explained this anomaly in terms of a shift of the quinone Q_A, of 1 Å on reduction, the extra distance between the radicals being responsible for the increased lifetime. Serious EPR-based investigations with regard to a possible movement of Q_A^-, began at around the same time as X-ray studies performed by Stowell *et al.* [88] on light- and dark-frozen samples of *Rb. sphaeroides* showed unambiguously that the secondary quinone (Q_B) moves a distance of approximately 5 Å *and* undergoes a propellor twist of 180° upon reduction to Q_B^-. A similar twist by Q_A had previously been ruled out by transient EPR studies at X-band [38]. Transient EPR is extremely sensitive to changes in the g-anisotropy of a radical, and would therefore clearly show spectral differences if a reorientation of Q_A had occured. No such change was seen for *Rb. sphaeroides*, and it was concluded that a twist in the primary quinone does not occur.

However, if the distance between the two radicals in a radical pair is greater than 20 Å, then transient EPR is unable to detect small changes in this distance. In $P^+Q_A^-$

r is approximately 29 Å, so an EPR study performed to prove that Q_A does not twist cannot be used to determine whether or not it shifts by the 1 Å predicted by Kleinfeld. ESEEM however, with its strong dependence upon the dipolar coupling between P^+ and Q_A^-, is sensitive enough to detect a difference in r of this size, and has thus been used in two independent studies for the purpose of determining whether or not the primary quinone in *Rb. sphaeroides* does indeed move on reduction [56, 57].

ESEEM studies on light- and dark-frozen samples of $P^+Q_A^-$ in *Rb. sphaeroides* were performed independently by Borovykh *et al.* [56] and Zech *et al.* [57]. In the former study two different types of sample were used: fresh (stored under liquid nitrogen for no more than one week) and aged (stored for a period of more than three months). Using a parabolic extrapolation of the dead-time period, they presented their results in the frequency domain. For aged samples they saw no dependence upon the manner of freezing of the positions of $f_\perp$ and $f_\parallel$. They did however see a small shift in the positions of the canonical frequencies when comparing the spectra taken from light- and dark-frozen fresh samples. If it is assumed that J remains the same for the two different cases, then this difference corresponds to a change in r of 0.4 ± 0.2Å. It was also suggested that this change is not observed for the aged samples because of a larger distribution of inter-radical distances, which leads to a broadening of the spectrum and hence camouflages any small change in D. The second study performed by Zech *et al.* [57] studied only aged samples and compared ESEEM data for light- and dark-frozen centres in the time-domain. The two recorded spectra were virtually identical and showed no evidence of a shift in the position of Q_A nor a greater distribution of inter-radical distances in either case.

On studying the spectra presented in these papers it is immediately obvious that the frequency domain spectra recorded by Borovykh *et al.* [56] (shown in Figure 4.1 on page 69) suffer greatly from the imperfect nature of the dead-time extrapolation. In each of the four spectra sinc-wiggles are very pronounced, but in two cases they are much more obvious than in the others. The possibility should not be ruled out that these features may distort the data to the extent that very small differences could be misinterpreted. In contrast, data left in the time domain, although not able to give such an attractive method for the determination of D and J, does not develop this problem, and could possibly be used to determine more accurately whether a small spectral change has taken place.

The next section describes the fitting of ESEEM data to various model functions in the time domain to determine the values of D and J. The accuracy to which these fits allow the parameters to be estimated was then calculated using the method of Cramér-Rao lower bounds.

4.2 Cramér-Rao Lower Bounds and Curve Fitting in the Time Domain

Although ESEEM data is usually analysed in the frequency domain, curve fitting the data in the time domain is also an attractive proposition. By performing the Fourier transform to allow the frequencies present to be simply and attractively displayed, the positions of the canonical frequencies can be easily measured, leading in turn to the easy extraction of the values if D and J. However, experimental data recorded in the time domain and *not* Fourier transformed are impervious to the effects of the experimental dead-time, which can corrupt the Fourier transform spectrum and lead to misinterpretation of the data therein.

The method of Cramér-Rao lower bounds can be used to show that if the correct model is used to perform a curve fit in the time domain, the values of the experimental parameters can be determined to a very high degree of precision.

4.2.1 Time Domain vs. Frequency Domain Curve Fitting

The accuracy to which a parameter can be determined from experimental data naturally depends on the quality of the fit of the data to a model function. It is important therefore, when analysing experimental results, that the theory behind the model function accurately describes the physical situation. An incorrect model function can lead, as was shown in Chapter 2, to a misinterpretation of the data. The quality of a model fit also depends upon external influences. Experimental noise is one such influence as, in the case of ESEEM fitted to a model in the frequency domain, is the experimental dead-time. The nature of the corruption that this phenomenon can cause is investigated in the next section.

Experimental Dead-Time

The ESEEM data presented by Borovykh *et al.* [56], which is also pictured in Figure 4.1a on the next page, clearly shows the sinc-wiggles associated with an imperfect extrapolation of the dead-time period. Experimentally these problems arise because

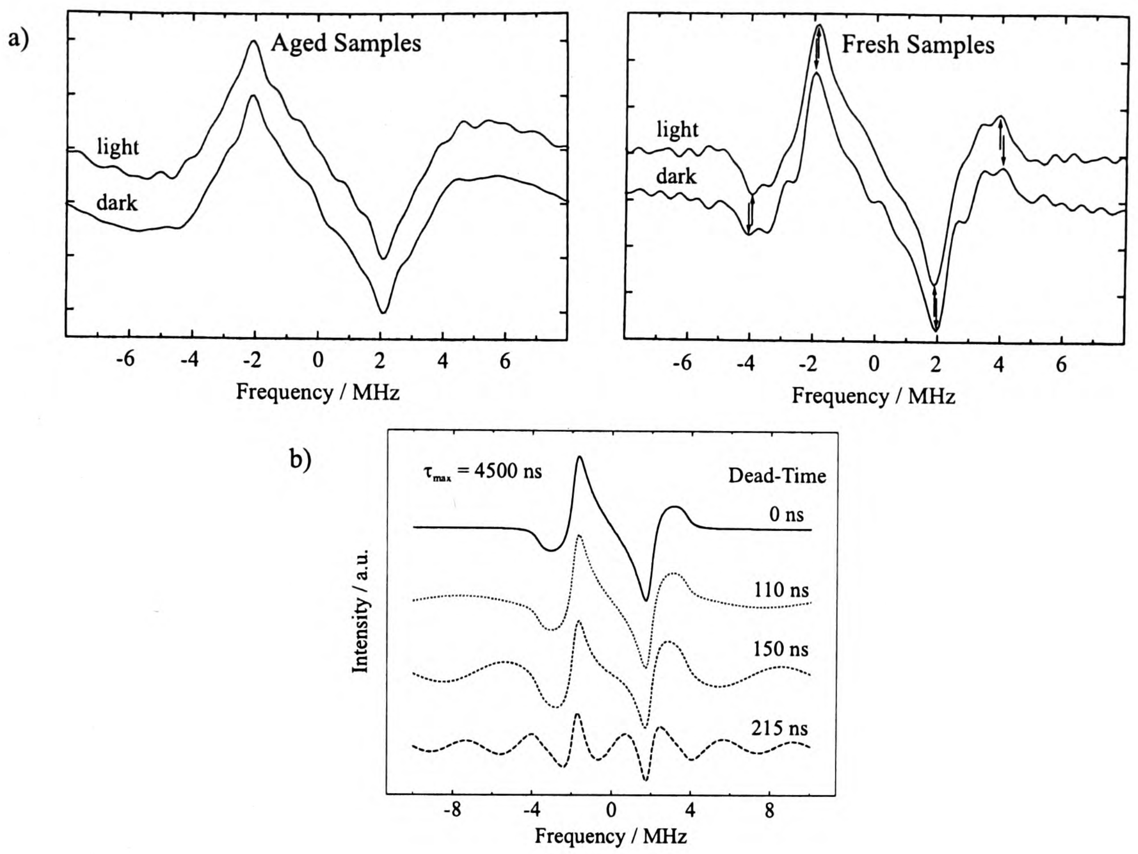

Figure 4.1: a) ESEEM data recorded for light- and dark-frozen aged and fresh samples of $P^+Q_A^-$ in *Rb. sphaeroides* (Borovykh et. [56]). All four spectra are affected by sinc-wiggles brought about by the dead-time extrapolation. The fresh samples show a slight change in the positions of the canonical frequencies. b) Simulated ESEEM spectra showing the effect of dead-time "sinc-wiggles". In each case $\tau_{\mathrm{max}} = 4500$ ns. In the top trace the spectrum is complete, in those below, the length of the dead-time period is indicated. All echo amplitudes during the dead-time are set to zero. A large amount of corruption can occur even if the dead-time is less than 5% of the total signal (bottom).

after the application of an mw pulse, the EPR cavity "rings" in such a way that it is not possible for an accurate measurement of an echo signal to be taken. Hence, in order for the data collected in an ESEEM experiment to give a faithful picture of the echo signal present for a time delay τ, the period between the second pulse and the echo (and between the first and second pulses) must be greater than the length of time for which the cavity rings. Cavity ringing and hence dead-time typically lasts for between 80 ns and 160 ns. The time domain data recorded by an ESEEM experiment will therefore always have a region at the start of the trace during which is impossible to accurately record the echo, and the shape of the signal is unknown. Unfortunately, the sine Fourier transform (FT) into the frequency domain requires that all the points in the time domain are known, implying that some method of extrapolation of the data back to the origin is needed. This extrapolation is done in a variety of ways, either by use of the Maximum Entropy Method [106], or by filling in the missing data by hand. Examples of the latter are equating all missing echo signals to zero, a linear extrapolation between the origin and the first recorded point τ_1, and joining the first two recorded points, τ_1 and τ_2 to the origin with a parabolic curve (Dzuba *et al.* [50]).

Despite these various methods of extrapolation, it seems unlikely that such simple techniques could be used to accurately piece together the information in the first part of the trace. Indeed, it was shown in Chapter 2 that even in the absence of hyperfine couplings to nearby nuclei, the echo modulation function is a complicated expression which is governed by a sine modulation dependent upon an isotropic distribution of radical orientations. This coupled with the fact that even the first few *recorded* points may be slightly corrupted by the cavity ringing suggest that a perfect extrapolation of the dead-time is extremely unlikely to be achieved.

It is also important to consider that the earlier a data point appears in a time trace, the more information it will contain with regard to the Fourier transform. This suggests that small errors in the extrapolation of the dead-time period will lead to much larger problems in the frequency domain. Figure 4.1b shows the effect upon the frequency domain spectrum of different lengths of dead-time in the time domain. In all cases the dead-time points have had their amplitudes set to zero. The ESEEM spectra were simulated with the program `echo3d2.f` (Appendix A.1.1) with $D = -1.4$ G, $J = 0$. No nuclei were included, so the hyperfine coupling constant A (defined in Chapter 2), was set to zero. $\delta\tau = 36$ ns was used, with the final value of τ being $\tau_{\mathrm{max}} = 4.5$ μs. The spectra shown all have a different number of dead-time points and the figure clearly shows how increasing dead-time can cause undesirable sinc-wiggles in the spectrum. The position of the strongest feature $f_{\perp}$ never alters, but this is not so for $f_{\parallel}$. This has consequences for the fitting of the spectrum to obtain the values of D and J. Since the values of these parameters are obtained by simultaneously solving equations for $f_{\perp}$ and $f_{\parallel}$, a change in one of these frequencies can lead to an incorrect estimation of D and J.

It is entirely sensible therefore to find an alternative method with which to fit a model to the data. The obvious choice for this is a least squares curve fit in the time domain where, since no Fourier transform is needed, the missing points at the start of the trace can simply be ignored. The precision to which the fit can be used to determine the sizes of D and J still depends upon it being an accurate representation of the physical situation but, since errors will not be introduced in the dead-time period, this and the experimental noise will be the only factors which affect the accuracy of the fit.

4.2.2 The Theory of Cramér-Rao Lower Bounds: The Determination of Experimental Accuracy

When the value of an experimental parameter is determined by a least squares fit to a model function, the accuracy to which the value is obtained can be assessed by considering the standard deviation of the parameter. This reveals information about the effect of experimental noise on the model fitting. The standard deviation of a parameter can be calculated by repeated curve fittings to "experimental data" with different sets of random noise. This "Monte Carlo" method, although reliable, is extremely time consuming if enough fittings are performed to allow a reasonable estimation of the standard deviation to be made. For this reason, the alternative and quicker method of Cramér-Rao lower bounds can be used instead [100–103].

The Cramér-Rao lower bound (CRLB) of a parameter, $s(\theta_k)$, puts a fundamental limit on the accuracy to which the parameter (θ_k) can be determined by experiment. The standard deviation of the parameter, as determined by a Monte Carlo approach, will not be smaller than the CRLB, and when a least squares fit to a model function is used, the CRLB will often equal the standard deviation. The CRLB of the parameter θ_k is calculated using

$$s(\theta_k) = \sqrt{(\boldsymbol{F}^{-1})_{kk}} \tag{4.1}$$

where $\boldsymbol{F}$ is the Fisher information matrix. Hence the lower bound is equal to the square root of the k^{th} diagonal element of the inverse of $\boldsymbol{F}$. If the experimental noise is Gaussian with standard deviation σ, and only one acquisition is taken at each point, n, *i.e.* no signal averaging, then the elements of $\boldsymbol{F}$ are given by

$$F_{jk} = \frac{1}{\sigma^2}\sum_n \Re\left(\frac{\partial y_n^*}{\partial \theta_j}\frac{\partial y_n}{\partial \theta_k}\right). \tag{4.2}$$

where θ_j and θ_k are the parameters of the model, and $\Re$ denotes the real part. F_{jk} is then the sum of the derivatives calculated for each data point *i.e.* y_n is the value of the model function at the n^{th} data point where $n = 1, 2, \ldots, N$.

Cramér-Rao Lower Bounds and the Model for ESEEM

An investigation into the use of Cramér-Rao lower bounds was undertaken by considering the simple model function for the ESEEM; that of a pair of coupled electrons as discussed in Chapter 2. Using equation 2.22 (pg 34) and taking an isotropic distribution of orientations over the sphere, the ESEEM at $\tau = \tau_n$ will be given by:

$$y_n = h\mathrm{e}^{-\tau_n/T_2} \int_0^{2\pi}\int_0^{\pi} \sin[2\{J - D(\cos^2\theta - 1/3)\}\tau_n] \sin\theta d\theta d\phi. \tag{4.3}$$

Here the value of y_n for a given τ_n is dependent upon the dipolar coupling, D, the exchange interaction, J, the relaxation time, T_2 and an amplitude parameter, h. The method of Cramér-Rao lower bounds was used to calculate the precision to which these parameters may be determined by a χ^2 least squares fit to an experimental data set. For the function given in equation 4.3, the partial derivatives of y_n with respect to each of the four parameters in the curve fit are:

$$\begin{aligned}
\frac{\partial y_n}{\partial D} &= 2h\tau_n \mathrm{e}^{-\tau_n/T_2} \int_0^{2\pi}\int_0^{\pi} \cos[2(J - d)\tau_n](\cos^2\theta - 1/3)\sin\theta d\theta d\phi \\
\frac{\partial y_n}{\partial J} &= 2h\tau_n \mathrm{e}^{-\tau_n/T_2} \int_0^{2\pi}\int_0^{\pi} \cos[2(J - d)\tau_n]\sin\theta d\theta d\phi \\
\frac{\partial y_n}{\partial T_2} &= h\frac{\tau_n}{(T_2)^2} \mathrm{e}^{-\tau_n/T_2} \int_0^{2\pi}\int_0^{\pi} \sin[2(J - d)\tau_n]\sin\theta d\theta d\phi \\
\frac{\partial y_n}{\partial h} &= \mathrm{e}^{-\tau_n/T_2} \int_0^{2\pi}\int_0^{\pi} \sin[2(J - d)\tau_n]\sin\theta d\theta d\phi
\end{aligned}$$

where $d = D(\cos^2\theta - 1/3)$. For the purposes of this example typical values of the four parameters were chosen:

$$D = -1.4 \text{ G}, \;\; J = 0.0 \text{ G}, \;\; T_2 = 0.37\ \mu\text{s and } h = 1,$$

and the value of σ/h as estimated from an experimental spectrum [57] was 0.01. The lower bounds were then easy to calculate. First the derivatives of y_n with respect to D, J, T_2 and h were determined and the Fisher information matrix calculated for each value of τ_n. With $\tau_1 = 0$, $\tau_N = 3.75$ μs and $\delta\tau = 10$ ns, the following Cramér-Rao lower bounds are given:

$$\begin{aligned}
s(D) &= 0.0100 \text{ G}, & s(J) &= 0.00328 \text{ G} \\
s(T_2) &= 0.0163\ \mu\text{s}, & s(h)/\sigma &= 2.61.
\end{aligned}$$

The calculation was performed using Mathematica with the program `crlb.m` (Appendix A.2). These values indicate that with this model and this value of σ, the standard deviation of each parameter is small, and that the parameters can therefore be determined very accurately from a least squares fit.

Cramér-Rao lower bounds can also be used to calculate the effect of missing data (*e.g.* dead-time) upon experimental accuracy. The calculation performed above assumed that every value of τ_n has a measured experimental value associated with it. In ESEEM of course this is not the case, and how greatly the missing data will affect the accuracy of a time domain fit can be determined. If the value of y_n in equation 4.3 is only calculated for those τ_n where a data point could be taken, then the F_{jk} and consequently the CRLBs change. The relationship between the number of points missing in the dead-time and $s(D)$ is shown in Figure 4.2a where $N = 375$. Also shown in Figure 4.2b is the relationship between the total number of points and $s(D)$.

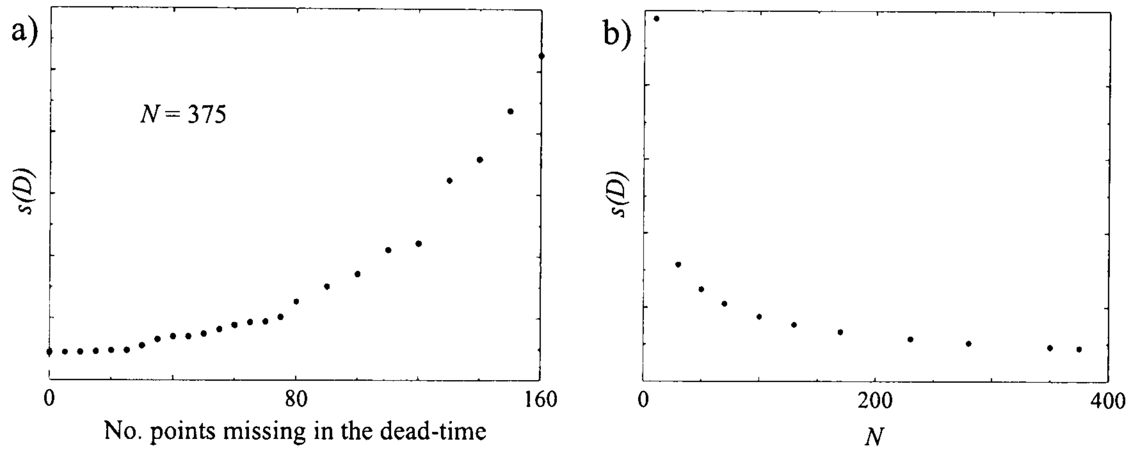

Figure 4.2: a) The effect of the dead-time on the Cramér-Rao lower bound of D. In the absence of dead-time, $N = 375$ corresponding to $\tau_{\max} = 3.75$ μs. b) The relationship between the total number of points N and the lower bound in the absence of dead-time. Here $\delta\tau$ is fixed at 10 ns.

The values of the lower bounds calculated using the above method are very much smaller than those generally estimated in ESEEM experiments on $P^+Q_A^-$. A Monte Carlo approach can be used to verify that the values given are in fact appropriate. The standard deviations of the four parameters can be found if for many different sets of random Gaussian noise, σ_n, the function

$$\chi^2 = \sum_n \left(y_n^{exp} - y_n^{calc} \right)^2 \tag{4.4}$$

is minimized. In the above equation y_n^{exp} is the echo amplitude at time point τ_n in the experimental data and y_n^{calc} is the same amplitude in the model function for a given set of parameter values. For each set of noise (*i.e.* each experiment), values of D^{exp}, J^{exp}, T_2^{exp} and h^{exp} were determined where the θ_k^{exp} are close to those used to calculate y_n^{calc} with deviation caused by the noise. The spread of the values of θ_k^{exp} gives the standard deviation of the parameter. When this calculation was performed by the Mathematica program `monte.m` (Appendix A.2), it took about 10^4 times longer than the calculation of the Cramér-Rao lower bounds but returned almost exactly the same results for the $s(\theta_k)$. Cramér-Rao lower bounds are therefore suitable for calculating the error in a parameter. Thus the $s(\theta_k)$ are small, because this method assumes that in the absence of experimental noise, the model is a perfect fit to the recorded data. In other words, CRLBs calculate only the effect of the experimental noise on a spectrum, and indeed, CRLBs are proportional to the percentage of noise present in the spectrum. This method is only useful therefore if the model gives a reasonable picture of the physical situation.

4.2.3 Fitting the Two Electron Model in the Time Domain

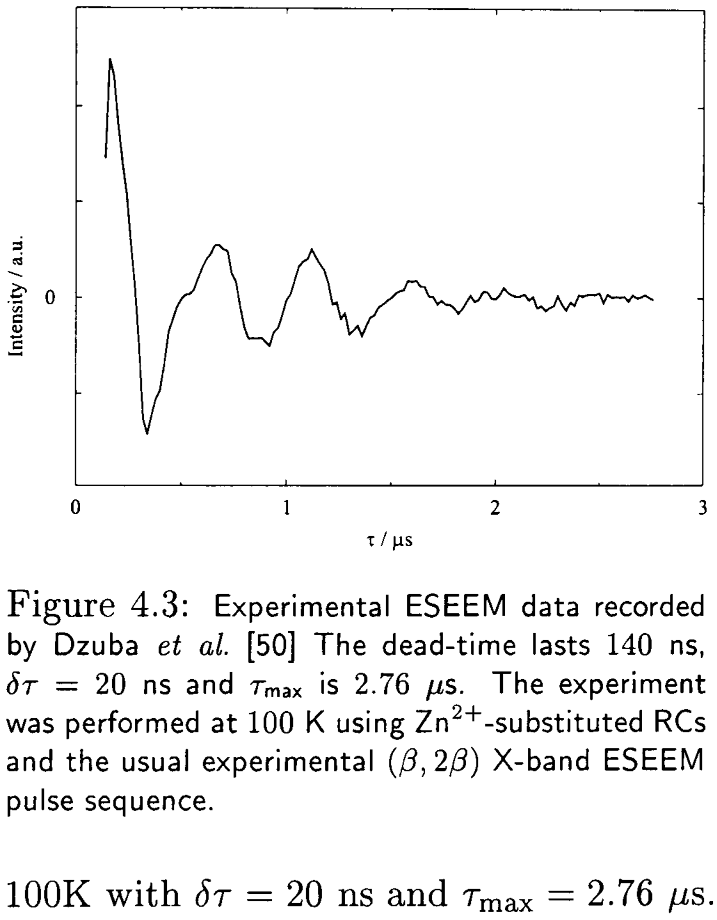

Figure 4.3: Experimental ESEEM data recorded by Dzuba *et al.* [50] The dead-time lasts 140 ns, $\delta\tau$ = 20 ns and $\tau_{\max}$ is 2.76 μs. The experiment was performed at 100 K using Zn^{2+}-substituted RCs and the usual experimental $(\beta, 2\beta)$ X-band ESEEM pulse sequence.

A time domain least squares fit was used to determine values of D and J in $P^+Q_A^-$ by using real experimental data. The accuracy to which these parameters are determined is assessed by CRLBs. The data set chosen was that recorded by Dzuba *et al.* and published in *Chemical Physics Letters* [50]. The time trace shown in Figure 4.3 is typical of those obtained for the ESEEM of $P^+Q_A^-$ in Zn^{2+}-substituted reaction centres, and indeed similar spectra have been taken on other occasions by other authors [34, 49, 51, 57]. Here ESEEM is recorded at 100K with $\delta\tau = 20$ ns and $\tau_{\max} = 2.76$ μs. Dzuba *et al.* used two different extrapolations to recover the signal during the 140 ns dead-time period; a linear "fit" from the origin to the first recorded point, and a parabolic fit using the first two recorded points and the origin. The data was recorded using the same $h\nu$-Δ-β-τ-γ-τ-echo sequence at X-band as discussed in Chapter 2. If it is initially assumed that there is no nuclear ESEEM effect from neighbouring nuclei, then the experimental trace can be approximated by the echo modulation function given in equation 2.22 (page 34) and fitted using the model in equation 4.3.

The curve fit was performed using data points between $\tau_1 = 200$ ns and $\tau_{\max} = 2760$ ns. The first few recorded points were neglected since it is possible that they may also have been slightly corrupted by the cavity ringing. The four-parameter least squares fit was performed using a search along the line of steepest descent in χ^2

so that values of D, J, T_2 and h are found to minimize equation 4.4 (`curve.m` in Appendix A.2). Using this approach, the following values of D, J, T_2 and h were obtained:

$$\begin{array}{ll} D = -1.166 \text{ G}, & J = +0.0051 \text{ G} \\ T_2 = 1.15 \ \mu\text{s}, & h/\sigma = 134 \end{array} \quad \text{with } \chi^2 = 0.356. \qquad (4.5)$$

The value of σ was estimated by comparison of the last 1 μs of the experimental results with the simulated trace. A value of $\sigma = 0.02$ was used. The parameters listed in equation 4.5 were used to plot the ideal fit. The simulation and the experimental data are shown in Figure 4.4a. The values of the parameters given in equation 4.5

	D / G	s(D) / G	J / G	s(J) / G	χ^2	r / Å
a) Electron Only	-1.166	0.0055	+0.0051	0.0019	0.3650	28.78±0.05
b) One Nucleus	-1.166	-	+0.0051	-	0.2100	≈28.78
c) Two Nuclei	-1.166	0.0082	+0.0090	0.0030	0.0885	28.78±0.07

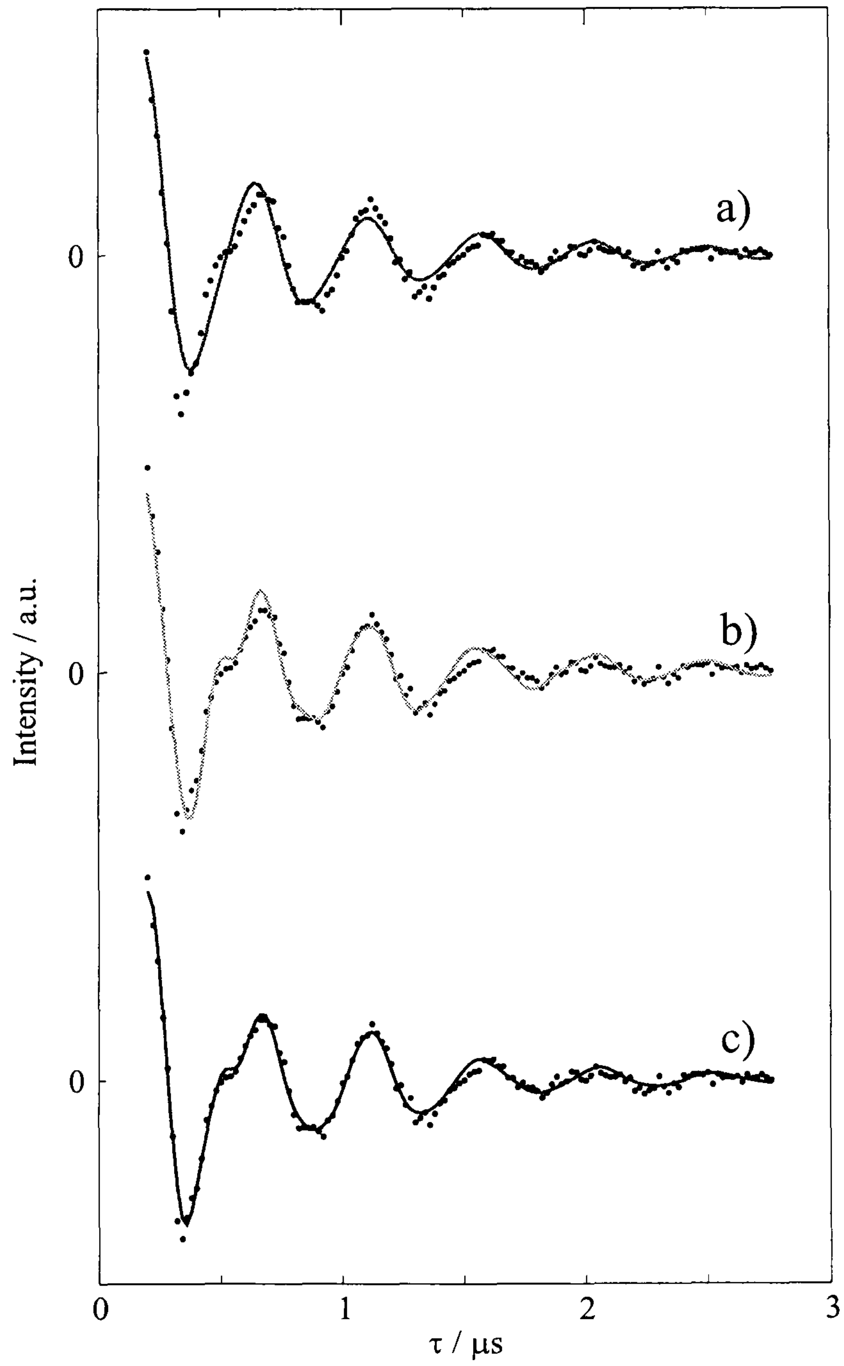

Figure 4.4: Time domain least squares best fits as determined by three different models. a) the best fit determined from the two-electron model. b) best fit using a model with two electrons and a single spin-1/2 nucleus. c) the best fit determined from the two-electron, two-nucleus model. The latter shows the optimum fitting that was achieved.

can be compared to those determined by the frequency domain fitting performed by Dzuba *et al.* where the spin-spin coupling parameters were assigned the values:

$$D = -1.15 \text{ G}, \qquad J = +0.007 \text{ G}.$$

The Cramér-Rao lower bounds for the time domain fitting were calculated as shown above. For the values of D, J, T_2 and h given they are:

$$\begin{aligned} s(D) &= 0.0055 \text{ G}, \quad s(J) = 0.0019 \text{ G} \\ s(T_2) &= 0.043\ \mu\text{s}, \quad s(h)/\sigma = 2.52. \end{aligned} \tag{4.6}$$

Dzuba *et al.* gave much larger estimates of the experimental errors based upon the quality of their fit: ±0.05 G for D and ±0.015 G for J. These estimates appear to have been made "by eye", or some similar method rather than a calculation based upon several sets of independent data. Taking D from equation 4.5 the distance between P^+ and Q_A^- was calculated using

$$D/\text{G} = -\frac{2.78 \times 10^4}{(r/\text{Å})^3}. \tag{4.7}$$

This gives $r = 28.78 \pm 0.05$ Å. The value calculated by Dzuba *et al.* from the same data with a slightly different value of D was a little larger, at 28.9 Å ± 0.4 Å.

Value of and Error in D

The value of $s(D)$ calculated by Cramér-Rao lower bounds and therefore the accuracy to which r may be determined depends upon both the value of σ/h and T_2. $s(D)$ is directly proportional to σ/h and inversely proportional to T_2: as the relaxation time increases, $s(D)$ becomes smaller because the slower the signal disappears into the experimental noise, the more accurately the parameters can be determined. It is useful to use the relation between $s(D)$ and σ/h to determine the signal to noise ratio required for a particular precision in r. If for example $s(r) = 0.1$ Å were required, (*i.e.* one quarter of that estimated in [50]), then it turns out that $h/\sigma \approx 65$, which corresponds to a noise level just over twice as high as that actually seen in the data (Figure 4.3).

The Value of J

The value of J determined by the curve fit is very small in comparison to D, and compares well with that obtained from previous ESEEM studies [34, 49, 51, 57] and from spin-polarised EPR spectra [38]. However, an inter-radical distance of nearly 30 Å may in fact mean that J is negligible. If this curve fitting calculation is repeated with J fixed at zero, then the following values of the remaining parameters are obtained:

$$D = -1.153 \text{ G}, \quad T_2 = 1.14 \ \mu\text{s}, \quad h/\sigma = 133 \tag{4.8}$$

with $\chi^2 = 0.361$, and Cramér-Rao lower bounds:

$$s(D) = 0.0017 \text{ G}, \quad s(T_2) = 0.045 \ \mu\text{s}, \quad s(h)/\sigma = 2.50. \tag{4.9}$$

The largest change between the value of the parameters seen here in equation 4.8 and in equation 4.5 is that of the value of D. This change can be explained by considering how D and J relate to $f_\perp$. The values of the spin-spin coupling parameters extracted from the data are principally controlled by the strong modulation at this frequency so that if D_0 is the value of D obtained from the fitting when it is assumed that $J = 0$, then $f_\perp = 2J + 2D/3 \approx 2D_0/3$. If D and J are taken from equation 4.5, this gives a value of $D_0 = -1.15$ G, in agreement with the value found by the 3 parameter curve fit, equation 4.8.

Validity of the Two-Electron Model

Quite clearly curve fitting experimental data to a mathematical model can only give accurate values of the physical parameters governing the experimental result if the model is a good fit to the data. Moreover, Cramér-Rao lower bounds can only give accurate information if this is the case. Although the model used for the fitting in Figure 4.4a broadly fits the data, it is far from perfect: there are features in the experimental spectrum, such as the shoulder occurring at around $\tau = 0.5$ μs, which are not, and cannot be fitted using the two-electron model for ESEEM. Hence, to precisely determine the values of D and J using a least squares fit, a slightly different model must be used.

Chapter 2 introduced the concept of nuclear ESEEM and gave examples of the type of effects that this can have on the spectrum of a weakly coupled radical pair such as $P^+Q_A^-$. It is possible that these extra modulations could be the cause of some of the features which prevent the two-electron model providing a perfect fit to the experimental data. In the next section, the nuclear ESEEM is added to the two-electron model, bringing about a considerably better fit than has previously been seen. The fit is so close to the experimental data that it is realistic to use CRLBs to determine the accuracy to which the values of D, J and T_2 are measured from the spectrum.

4.2.4 Extending the Model: The Addition of Nuclear Modulation

The inclusion of a nucleus into the mathematical model complicates the least squares fit considerably. With four parameters, a minimisation based upon a path of steepest descent was a straightforward operation, which was completed in several minutes. However, as was highlighted when the two-electron, one-nucleus model was introduced, the relationship between the hyperfine axis and the orientation of the static field plays an important role in the evolution of the spins and therefore the form of the ESEEM, and the surface upon which a global minimum must be found becomes too textured for this simple fitting procedure to cope with on a reasonable time-scale. Therefore, when considering both the electron-electron and the nuclear ESEEM, a different approach, using the so-called "spiral" algorithm was used.

The Spiral Algorithm for a Least-Squares Fit

Most least squares fitting computations use one of two methods. The first, a search along the line of steepest descent as used in the four parameter curve fit in the previous section, will *always* find at least a local minimum, but by the nature of the algorithm many iterations may need to be performed in order to achieve this. If the initial parameter set is a vector, $\boldsymbol{p_m}$, and the parameter set after one iteration is $\boldsymbol{p_{m+1}}$, then for steepest descent,

$$\boldsymbol{p_{m+1}} = \boldsymbol{p_m} + \alpha_m \boldsymbol{\delta d}$$

where if *npar* is the number of parameters on the curve fit, $\boldsymbol{\delta d}$ is a vector of length *npar* giving the direction of the path of steepest descent and α_m is the step size. $\boldsymbol{\delta d}$ is dependent upon the Jacobian matrix, $\boldsymbol{J}$, and the experimental and simulated data. If $\boldsymbol{s}$ is the vector containing the experimental data, *i.e.* for ESEEM, the echo amplitudes of each value of τ_n, and $\boldsymbol{\sigma}(\boldsymbol{p_m})$ the data simulated from the parameter set $\boldsymbol{p_m}$ also written as a vector, then the elements of $\boldsymbol{J}$ are $J_{ij} = \partial\sigma_i / \partial p_{m_j}$ and

$$\boldsymbol{\delta d} = \boldsymbol{J}^T \cdot (\boldsymbol{s} - \boldsymbol{\sigma}(\boldsymbol{p_m})).$$

The second fitting procedure uses the direction vector $\boldsymbol{\delta t}$ determined from the first order terms of a Taylor series expansion about $\boldsymbol{p_m}$. This vector is governed by the Hessian matrix, $\boldsymbol{H} = \boldsymbol{J}^T \cdot \boldsymbol{J}$ so that

$$\boldsymbol{\delta t} = \boldsymbol{H}^{-1} \cdot \boldsymbol{\delta d}.$$

Using this method a local minimum is not always reached, but in the event that one is found, it is found quickly and efficiently.

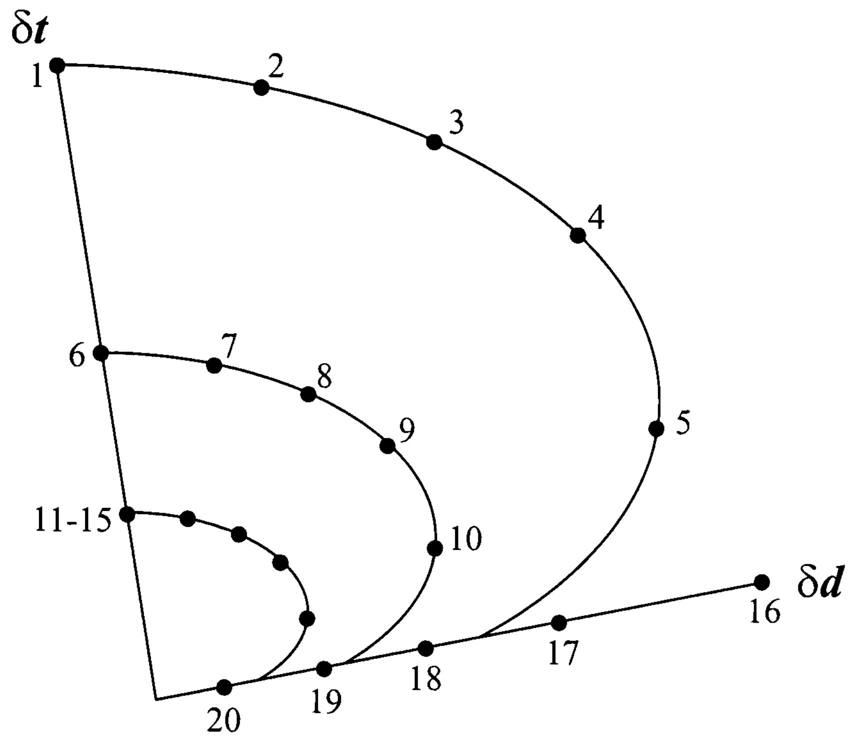

Figure 4.5: Schematic diagram describing the path of the spiral algorithm. The vector in the direction determined by the first order Taylor series and that for the path of steepest descent are $\boldsymbol{\delta t}$ and $\boldsymbol{\delta d}$ respectively.

The spiral algorithm [107] uses both of these methods so that a minimum is always found in the most efficient manner. Figure 4.5 shows the path of the algorithm. The vectors $\boldsymbol{\delta t}$ and $\boldsymbol{\delta d}$ are both scaled to the length of the maximum step size, and as shown, the algorithm searches first as far along $\boldsymbol{\delta t}$ as possible. If this leads to an increase in χ^2, then the algorithm moves to point 2 on the spiral path between $\boldsymbol{\delta t}$ and $\boldsymbol{\delta d}$ and so on as shown in the figure until finally $\boldsymbol{\delta d}$ is searched. The global minimum is located using an extensive search requiring many different sets of starting parameters.

The Addition of a Single Nucleus

For the model of the two-electron, one spin-1/2 nucleus system, the program `spiral.f` (Appendix A.1.3) was constructed to calculate the functions derived in Section 2.4, *i.e.*

$$y_n = he^{-\tau_n/T_2} \int_0^{2\pi}\int_0^{\pi} \sin[2\{J - D(\cos^2\theta - 1/3)\}\tau_n]\frac{1}{2}[1 + f(\tau)] \sin\theta d\theta d\phi. \qquad (4.10)$$

where the nuclear modulation function $f(\tau)$ is once again:

$$f(\tau) = 1 - \frac{k}{2}\left[1 - \cos\omega_\alpha\tau - \cos\omega_\beta\tau + \frac{1}{2}\cos(\omega_\alpha - \omega_\beta)\tau + \frac{1}{2}\cos(\omega_\alpha + \omega_\beta)\tau\right]. \quad (4.11)$$

D, J and T_2 were held at the values given in equation 4.5, and this algorithm was used to quickly check that the new model was likely to lead to an improvement in the fit. Hence, a four parameter fit was once again performed where the optimum values of the hyperfine coupling, A, the resonance frequency of the nucleus, ω_{N}, the electron-nuclear angle, ξ and h were found. This fitting, a simulation of which is shown in Figure 4.4b (page 75), greatly improves the fit to the data: the shoulder at 0.5 μs is clearly seen, and χ^2 has dropped by a third to $\chi^2 = 0.21$. The values of A, ω_{N} and ξ turn out to be

$$A = 1.17 \text{ G} \quad \omega_{\mathrm{N}} = 0.45 \text{ G} \quad \psi = 2.29^{\circ}. \tag{4.12}$$

To find the model function which gave the deepest global minimum, and thus the best fit to the data, several different approaches and models were used. These included the following:

- repeating the fit with the single nucleus, allowing the values of the parameters D, J and T_2 to be free variables. The fit improved only slightly with this modification.
- approximation of $f(\tau)$ (equation 4.11) to a sum of cosine modulations *i.e.* $f(\tau)^{approx} = [c_1 + c_2 \cos\omega_2 + ...]$. This retained the form of $f(\tau)$ but simplified the function slightly and reduced the number of parameters used, leading to a faster search.
- increasing the speed of the fitting program by reducing the number of orientations (θ, ϕ) that the magnetic field can take. This gave a starting point which when used in the full fitting quickly reached a deep minimum.
- changing the form of the relaxation from mono-exponential (*i.e.* $h\mathrm{e}^{-\tau/T_2}$) to bi-exponential ($h_a\mathrm{e}^{-\tau/T_a} + h_b\mathrm{e}^{-\tau/T_b}$). A good fit to the model enabled the 0.14 μs to 0.2 μs region of the experimental data to be used. However, this model turned out have an unrealistic extrapolation back to $\tau = 0$.

The model which gave the best fit was found after an extensive search. For the model used the two-electron model in equation 4.3 is further modified by the inclusion of another nucleus, giving an excellent fit to the data.

4.2.5 The Two-Nucleus Model: Deconvolution of the Nuclear and Electron ESEEM Spectra

The nuclear ESEEM of the radical pair $\mathrm{P^+Q_A^-}$ is in reality a complicated function with contributions from the many different nuclei associated with each radical. The one-nucleus model used in Chapter 2 gave a reasonable indication of the types of effects that the nuclear ESEEM can have. A curve fitting using the same model with the addition of a second spin-1/2 nucleus, this time with a coupling to the other electron, although itself not necessarily physically realistic, was shown to have a plausible effect on the ESEEM. The echo modulation function for the two-electron, two-nucleus model is an extension of equation 4.10 and is given by:

$$y_n = h\mathrm{e}^{-\tau_n/T_2} \int_0^{2\pi} \int_0^{\pi} \sin[2\{J - D(\cos^2\theta - 1/3)\}\tau_n]\frac{1}{2}[f_{\mathrm{A}}(\tau) + f_{\mathrm{B}}(\tau)] \sin\theta d\theta d\phi. \quad (4.13)$$

For each nucleus, A and B, $f_i(\tau)$ has the form of equation 4.11 with parameters A_i, $\omega_{i\mathrm{N}}$ and ξ_i. If either A_{A} or A_{B} are zero, the function reverts back to that given by equation 4.10, and, in the limit that both are zero, the two-electron model returns.

A global minimum for this 10 dimensional surface was located by an extensive search, the best fit curve is shown in Figure 4.4c (page 75). The model gave a significantly improved fit to the data, coinciding almost perfectly with a large part of the curve; χ^2 is 5 times lower than for the two-electron fit, at $\chi^2 = 0.0885$. When σ was estimated from the last 1 μs of the fit, and had the value 0.019, the best fit parameters for the model were:

$$\begin{aligned} D &= -1.166 \text{ G} \quad & J &= +0.009 \text{ G} \\ T_2 &= 0.93\ \mu\text{s} \quad & h/\sigma &= 247.2 \end{aligned} \quad (4.14)$$

$$\begin{aligned} A_{\mathrm{A}} &= 1.19 \text{ G} \quad & \omega_{\mathrm{AN}} &= 0.432 \text{ G} \quad & \xi_{\mathrm{A}} &= 2.30^{\circ} \\ A_{\mathrm{B}} &= 1.56 \text{ G} \quad & \omega_{\mathrm{BN}} &= 0.610 \text{ G} \quad & \xi_{\mathrm{B}} &= 39.2^{\circ} \end{aligned} \quad (4.15)$$

These values can be compared with those determined by the two-electron model (equation 4.5). D has not changed and J has roughly doubled, but is still very small, and T_2 is slightly reduced. These results indicate that although it is clear that the anisotropic hyperfine interactions change the form of the ESEEM, they do not seem to significantly alter the position of the dominating canonical frequency, $f_{\perp}$. This is in agreement with the result from Chapter 2. There, in Figure 2.12 (page 47), it was shown that $f_{\parallel}$ can be shifted considerably by the anisotropic hyperfine interaction, but that the position of $f_{\perp}$ remains essentially constant. If both this result from Chapter 2, and the unchanged value of D in the two models used here, are considered, this suggests that the time domain curve fitting, rather than a frequency domain fit, is the superior method of determining D and J since the effect of the nuclear ESEEM does not lead to a misinterpretation of the data.

Having achieved an excellent fit to the experimental data using the two-electron, two-nucleus model, in order to have confidence that the fit is true, the validity of the model was tested.

The Validity of the Two-Nucleus Model

Although the two "nuclei" in the two-electron, two-nucleus model do not actually represent physical nuclei in the radical pair, it can be shown that this model does give a physically meaningful approximation of the ESEEM of $P^+Q_A^-$. The values of the hyperfine parameters of the nuclei were used to simulate the ESEEM that would arise solely from the interaction in the absence of the dominating spin-spin interactions. This was achieved by "de-convolving" the electron-electron interaction from the model, *i.e.* evaluating

$$e^{-\tau/T_2} \int_0^{2\pi} \int_0^{\pi} \frac{1}{2}[g_A(\tau) + g_B(\tau)] \sin\theta d\theta d\phi. \tag{4.16}$$

Here, $g_i(\tau)$ is the time dependent part of the function $f_i(\tau)$ (equation 4.11), *i.e.* that part involving only the nuclear terms defined by:

$$\begin{aligned} g_i(\tau) &= f_i(\tau) + \frac{k_i}{2} - 1 \\ &= \frac{k_i}{2}\left[\cos\omega_{i\alpha}\tau + \cos\omega_{i\beta}\tau - \frac{\cos(\omega_{i\alpha}+\omega_{i\beta})\tau}{2} - \frac{\cos(\omega_{i\alpha}-\omega_{i\beta})\tau}{2}\right] \end{aligned} \tag{4.17}$$

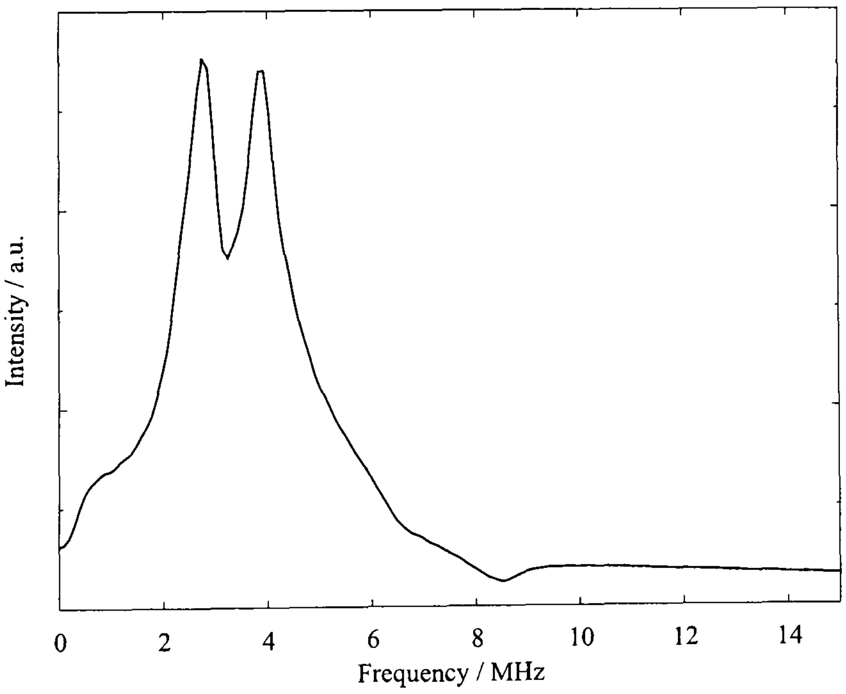

Figure 4.6: Simulated frequency domain spectrum of the nuclear ESEEM (equation 4.16) derived from the de-convolution of the dominant electron-electron interaction. The spectrum shows similarities to those obtained from single radical studies of the individual radicals.

Using the values of the hyperfine parameters given in equation 4.15, the function in equation 4.16 was evaluated for all values of τ and transformed into the frequency domain. The result is shown in Figure 4.6. The spectrum shows principal peaks at 2.8 MHz and 3.9 MHz, with a smaller, broader feature at just below 1 MHz. The information shown compares very favourably with that obtained from two pulse X-band ESEEM studies of the individual radicals. A study of P^+ in *Rhodospirillum rubrum* shows ESEEM spectra for the radical with a strong peak at 2.64 MHz and a weaker feature at 0.9 MHz [108]. Q_A^- in *Rb. sphaeroides* is found to have a prominent peak at around 4.1 MHz [109]. These results give confidence that this model is valid for this radical pair. Two "effective spin-1/2" nuclei were used to represent the overall effect of all the hyperfine couplings on the two radicals, and Figure 4.6 is consistent with independent data for P^+ and Q_A^-, even though the values of A_i and $\omega_{i\mathrm{N}}$ determined by the curve fit do not represent real nuclei. Within the context of this model they therefore give a reasonable approximation of the *effect* of the magnetic nuclei which are present.

Having concluded that the fit was excellent, and the model sound, the precision to which D and J had been determined was calculated. The two-electron, two-nucleus model gave Cramér-Rao lower bounds for D, J, T_2 and h as follows:

$$\begin{array}{ll} s(D) = 0.0047\ \mathrm{G} & s(J) = 0.0017\ \mathrm{G} \\ s(T_2) = 0.029\ \mu\mathrm{s} & s(h)/\sigma = 5.18. \end{array} \tag{4.18}$$

The greater number of parameters used in this fit as compared to the two-electron model, would suggest that the accuracy to which each can be determined by the model fitting should be reduced. This is not what these results show. This discrepancy is caused by the larger value of h/σ needed for the 10 parameter fit. The increase in fitting amplitude comes from the nuclear ESEEM reducing the amplitude of the spectrum (see Chapter 2). Since the CRLBs are inversely proportional to h/σ, if this is scaled from 247.2 (as for the 10-parameter fit) down to 134 (for the 4-parameter fit) and the other CRLBs scaled accordingly, they become

$$s(D) = 0.0082\ \mathrm{G}, \quad s(J) = 0.0030\ \mathrm{G}, \quad s(T_2) = 0.051\ \mu\mathrm{s}. \tag{4.19}$$

These values are still very small, indeed $s(D)$ is less than 1% of D, but with a correct model fitting, and a good signal to noise ratio as seen in this data, the parameters can truly be determined to great accuracy.

The best fit simulations for the two-electron and the two-electron, two-nucleus models were next transformed into the frequency domain and compared with the experimental data. The dead-time problem was handled by setting y_n to zero for $\tau < 0.2$ μs for which data are not recorded, in *all* traces. The sinc-wiggles were then the same for each spectrum and the differences between the data sets could be considered without concern for this effect. The data are plotted in Figure 4.7.

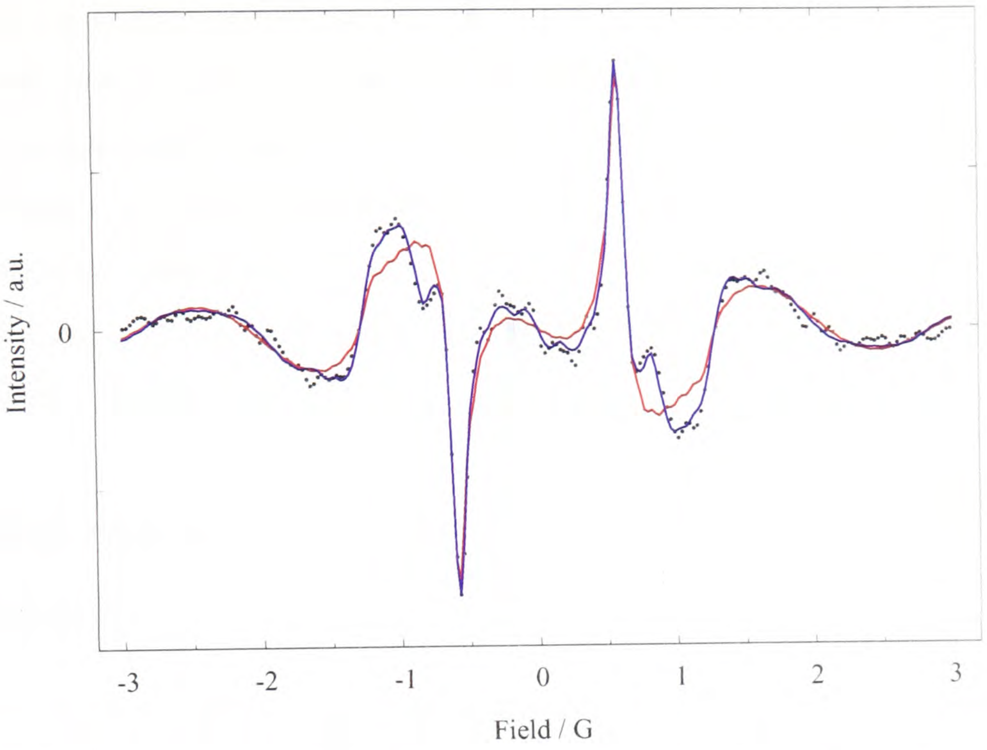

Figure 4.7: Sine Fourier transforms of the time traces shown in Figure 4.4a and c. In each case all ESEEM is set to zero for $\tau < 0.2$ μs so that the sinc-wiggles are the same for all spectra. The dotted trace is that for the experimental data taken by Dzuba *et al.* [50], the red trace is the 4 parameter fit for the two-electron model (a), and the blue, the result of adding two nuclei to the model (c).

The two-electron, two-nucleus model gave a far more faithful fit to the experimental data than the pure electron model. This is unsurprising considering the quality of this fit in the time domain. What is interesting however is the large difference in the appearance of the shoulders at $f_{||}$ between the two model fitting plots. Despite the identical values of D and the minute values of J used in each model, these shoulders are very different in the two cases and it can not be ruled out that this could lead to different determinations of D in each case. This re-iterates the point made in Chapter 2, that the effect of the nuclear ESEEM on the higher frequency signals is such that it can cause a problem in the determination of D and J in the frequency domain. What has come to light here, is that this is not a problem for time domain analysis.

4.2.6 Conclusion

Although the fitting of experimental ESEEM data to a model function in the time domain does not offer such an attractive or quick method of determining D and J as is found by measuring the positions of $f_{\perp}$ and $f_{||}$ in the frequency domain, the advantages of this method are clear.

First, any uncertainty in the values of the parameters caused by the extrapolation of the dead-time is removed, since the entire dead-time period is ignored. Secondly, that certainly in the case if $P^+Q_A^-$, the two-electron, two-nucleus model gives a valid and excellent fit to the experimental data with realistic values of all the parameters, combined with extremely high precision. Finally, the use of an accurate model fit in the time domain does both of the above *and* by determining the values of D and J directly rather than via the positions of the canonical frequencies, any shifts in these frequencies caused by nuclear modulations are accounted for by the model. This means that a misinterpretation of the data giving incorrect values of D and J is considerably less likely.

4.3 Optimisation of Experiments by Cramér-Rao Lower Bounds

Cramér-Rao lower bounds were used earlier in this chapter to calculate the precision to which a parameter may be determined from a set of experimental data. In this section, the relationship between the number of data points taken and the value of the lower bound was exploited for the purpose of determining the sampling pattern which gives the smallest lower bounds and hence the greatest accuracy in the parameters determined by a curve fit.

4.3.1 Theory

To perform some experiments, a particular procedure is repeated several times in order that a set of experimental results may be obtained. In the ESEEM experiment, this procedure is the pulse sequence $h\nu$–Δ–β–τ–γ–τ–echo, where the data set is built up by varying the value of the delay time, τ. Before data can be recorded, the experimentalist must answer several questions relating to the experiment, namely: how many data points will be taken? what should the distance ($\delta\tau$) between them be? to what extent should signal averaging be performed? The answers to these questions are of course related to the nature of the experiment itself, but it would be useful to know which pattern of data points would best serve to give precise information. This "optimum sampling strategy" can be determined using the method of Cramér-Rao lower bounds.

Consider an experiment in which the number of times the experimental procedure can be repeated is constrained, perhaps by time or by a limited supply of sample, or in the case of ESEEM, if the sample can only be subjected to a certain number of laser flashes before it begins to degrade. Let the number of points at which data is to be recorded be N. The value of M gives the extent of the signal averaging, so that the total number of times data is recorded is $N \times M$, and the total length of the experiment, τ_{max}, is proportional to this. In the case that the experiment is constrained so that the maximum possible number of times data can be recorded is N_{max}, then if $N = N_{\text{max}}$ values of τ are considered, $M = 1$. However, if improved signal averaging is required, then the sampling must change so that $N < N_{\text{max}}$ allows $M > 1$. There will therefore be a trade-off between N and M: is it better to have as many points as possible or to have fewer points with a greater precision in each?

Let $s_M(\theta_k)$ be the Cramér-Rao lower bound of the parameter θ_k with M measurements taken per value of τ. Hence, $s_1(\theta_k)$ is the lower bound when the experiment is performed without signal averaging. The relationship between the lower bound and the number of measurements taken at each point is

$$s_M(\theta_k) = \frac{1}{\sqrt{M}} s_1(\theta_k),$$

and, since $N \times M$ is fixed, this also means that

$$s_M(\theta_k) \propto \sqrt{N} s_1(\theta_k).$$

So, rather than optimising the experiment by changing both M and N to minimise $s_M(\theta_k)$, one can calculate $s_1(\theta_k)$ for various N and use these values to minimise $\sqrt{N} s_1(\theta_k)$ with respect to N. This gives the best compromise between signal-averaging and number of data points for the experiment.

4.3.2 Optimal Sampling Strategy for the ESEEM of $\text{P}^+\text{Q}_\text{A}^-$

An optimum sampling strategy for the ESEEM of the weakly coupled radical pair $\text{P}^+\text{Q}_\text{A}^-$ was found by considering the value of τ_{max} required to give the lowest values of $s(D)\sqrt{N}$ and $s(J)\sqrt{N}$, where N was the number of points between τ_1 and τ_{max} for which the ESEEM is measured. For ease of calculation, the model used was that given by equation 4.3 which describes the two-electron system. Values of the spin-spin couplings and T_2 were taken from equation 4.5, and h/σ is set to 1. $s(D)\sqrt{N}$ and $s(J)\sqrt{N}$ were then calculated for different values of N from 10 to 129, with $\delta\tau = 20$ ns. The first point taken was $\tau_1 = 0.2$ μs, so that τ_{max} (in μs) was related to N by

$$\tau_{\text{max}} = N\delta\tau + 0.18.$$

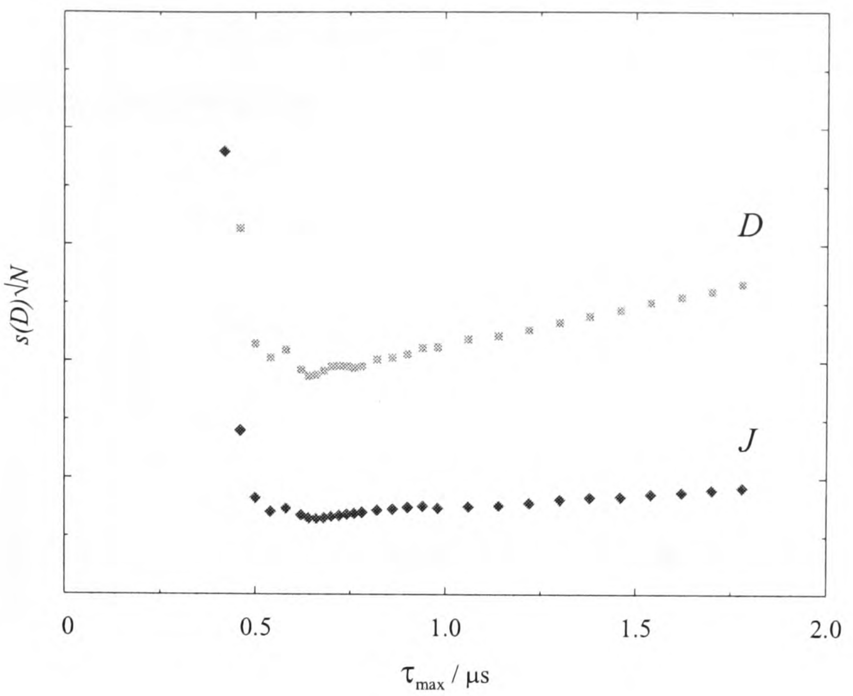

Figure 4.8: The relationship between the scaled Cramér-Rao lower bounds for D and J as determined by the model fit in equation 4.3. For both $s(D)\sqrt{N}$ and $s(J)\sqrt{N}$, a minimum is found for $\tau_{\mathrm{max}} = \tau_{\mathrm{max:opt}} = 0.66$ μs.

Figure 4.8 shows the relationships between $s(D)\sqrt{N}$ and $s(J)\sqrt{N}$ and τ_{max}. For both D and J, very small N means that the CRLBs are high, indicating that not enough information can be gathered with so few points. A minimum occurs for both D and J at $\tau_{\mathrm{max}} = 0.66$ μs ($N = 24$), after which as N increases further, the loss of extra signal averaging causes the lower bounds to increase. If $N = 129$ so that $\tau_{\mathrm{max}} = 2.76$ μs, as was used by Dzuba *et al.* [50], with $h/\sigma = 1$, then $s(D)\sqrt{N}$ was almost twice that given when $N = 24$ and $\tau_{\mathrm{max}} = 0.66$ μs. Similar results were seen for J. These results mean that the precision with which these two parameters could be determined could be doubled by cutting the acquisition time by three-quarters (*e.g.* 0.66 μs instead of 2.76 μs) and by having four times as much signal averaging.

The number of points that must be taken between $\tau_1 = 0.2$ μs and $\tau_{\mathrm{max}} = 0.66$ μs was also assessed. Was there any benefit in altering $\delta\tau$ from 20 ns? This was investigated by using the lower bounds and by considering the Sampling Theorem [110]. This theorem states that to unambiguously define the frequencies within a signal, there must be at least two samples taken per cycle of the highest frequency. This is called the *Nyquist Condition.* For the example considered here where $\tau_{\mathrm{max:opt}} = 0.66$ μs, it turned out that so long as N was greater than or equal to 5, *i.e.* $\delta\tau \leq 115$ ns, then $s(D)$ and $s(J)$ were essentially independent of N. This is unsurprising when considering the spectral width associated with $\delta\tau = 115$ ns. The relationship between the spectral width (sw) and the increment in τ is $sw = (\delta\tau)^{-1}$. If $\delta\tau = 115$ ns, this leads to a spectral width of ≈ 9 MHz ≈ 3.5 G. For $D \approx 1.17$ G and $J \approx 0$ G as determined by the curve fit, the spectrum lies between $-f_{||}$ and $+f_{||}$, *i.e.* has a width of $2|2J - \frac{4}{3}D| = 3.12$ G. Any value of N giving $\delta\tau \leq 115$ ns is therefore suitable for sampling the spectrum.

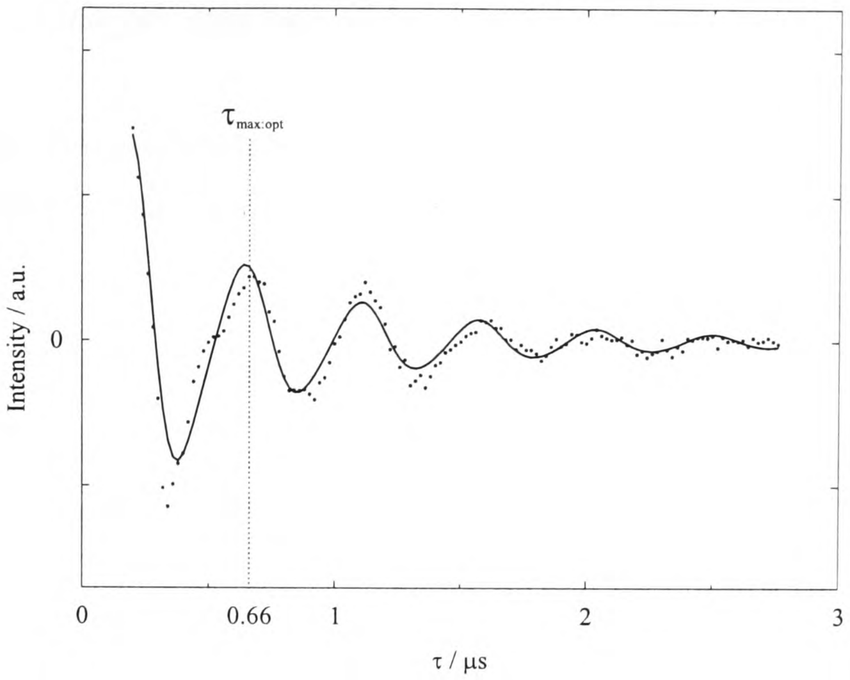

Figure 4.9: Experimental trace taken by Dzuba *et al.* [50] and the simulation determined by the 4 parameter fit, indicating the amount of the spectrum to be sampled if the precision in D and J is to be optimised.

Figure 4.4a (see page 75) was re-plotted to show how much of the time domain spectrum, has to be sampled for the precision of D and J to be optimised. Figure 4.9 shows that $\tau_{\mathrm{max:opt}}$ lies near the second maximum of the experimental data, long before the signal disappears into the noise. It is clear that this signal truncation is useless if the data is to be Fourier transformed into the frequency domain, since the extent of corruption arising from the partial curve would be enormous. This theory does suggest however, that if the signal averaging is increased by the amount calculated, and that if the data is fitted to a model in the time domain, then even though only a small part of the signal is detected, it is the most important part, and provided that the number of points taken is high enough, all the information needed to accurately determine D and J will be present within about one complete cycle of the simulated signal.

4.3.3 Conclusion

The time domain curve fitting method suggested earlier in this chapter may be refined by use of an optimal sampling strategy. Provided an accurate and valid model can be found to describe the experimental data, the sampling strategy, determined using Cramér-Rao lower bounds, allows experimental parameters to be determined from a time domain curve fit with the greatest possible precision. In the example given, the time domain curve was truncated. Rather than reduce the information available from the recorded trace, the accuracy to which D and J were determined was increased since it is the first full cycle of the ESEEM which contains the greatest share of the information. The points in this region were then measured to a high precision, using increased signal averaging.

This Cramér-Rao lower bounds method of determining an optimum sampling strategy may be applied to any experiment where the data can be analysed in their raw form.

Chapter 5

ESEEM of $P^+Q_A^-$: Simulations at W-Band

Hitherto this thesis has been concerned with the electron spin echo envelope modulation spectroscopy experiment, performed on photosynthetic radical pairs, at the X-band frequency of 9 GHz. The attention is now turned to the possibility of performing similar experiments at a higher frequency band, namely the W-band frequency of 95 GHz. ESEEM experiments on the secondary radical pair of *Rb. sphaeroides* at W-band have the potential to make a direct correlation between the relative orientations of the radicals P^+ and Q_A^- and the axis of the dipolar coupling between them [111].

5.1 Background

Although the X-band ESEEM experiment is useful in determining the magnitude of the dipolar and exchange coupling constants, it does have its limitations. The nature of the X-band ESEEM experiment is to excite every radical pair in a sample of reaction centres uniformly, using a sequence of non-selective pulses. The spectrum resulting from Fourier transformation of the time trace turns out to be a powder average of anti-phase doublets with splitting $2D(\cos^2\theta - 1/3)$, where θ is the angle between the dipolar axis, and the direction of the magnetic field, $\boldsymbol{B}_0$ [76].

If an experiment is performed at the X-band frequency of 9 GHz (B_0 = 0.33 T) on a frozen solution of reaction centres, *i.e.* the type of experiment so far considered in this thesis, the magnitudes of the spin-spin coupling parameters may be determined to high precision, but no orientational information is given at all. Information about the orientation of the dipolar axis with respect to the membrane axes can be obtained from X-band ESEEM studies on single crystals. This experiment has been performed for PSI crystals by Bittl *et al.*, who determined an angle of 27±5° between the crystallographic *c*- and dipolar axes [112]. However, at X-band even this experiment can only give information about the relationship between the dipolar vector and the laboratory coordinate system, and can shed no more light upon the relative orientations of the two radicals in the RP than the experiment using a frozen solution.

Information about the relative orientations of the radicals P^+ and Q_A^- in *Rb. sphaeroides* can be obtained from EPR experiments performed at high-field. At 95 GHz, where the g-tensors are well resolved, spectral position can be better assigned to orientations of the radicals with respect to the magnetic field. In this way the principal values of the g-tensors of these radicals have been determined by both cw EPR [41] and time-resolved EPR (TREPR) [90] studies. This information is not available from X-band spectra where the g-tensors are not resolved, and spectral simulations cannot unambiguously reveal the relative orientations of P^+ and Q_A^- and the dipolar axis.

With the g-tensors of the radicals fully resolved, the advantages of both the X-band ESEEM and the W-band TREPR experiments may be exploited. In an ESEEM experiment at W-band, using selective excitation, the modulation in the out-of-phase echo, measured at one specific field position within the TREPR spectrum, could theoretically be used to give information about the relationship between the relative orientations of the two radicals and the spin-spin coupling between them.

5.2 Theory

For ESEEM at X-band, two criteria apply which are not fulfilled in experiments at higher fields. First, it can be assumed that the EPR spectra of the individual radicals overlap sufficiently that for all orientations of $P^+Q_A^-$ the radicals will interact through the exchange and dipolar couplings. Secondly, it is assumed that the mw pulses applied during the experiment are sufficiently broad-band to excite all of these radical pairs uniformly. At W-band however, the spectral positions of the P^+ and Q_A^- radicals overlap only in a small region of the EPR spectrum. In addition, it is not experimentally possible to create broad-band excitation at 95 GHz, and the pulses are very selective. Since ESEEM requires that both spins are excited equally by the mw pulses, these two factors conspire to make the ESEEM experiment at

W-band very different from, and far more difficult to perform, than its lower field counterpart.

5.2.1 EPR of $P^+Q_A^-$

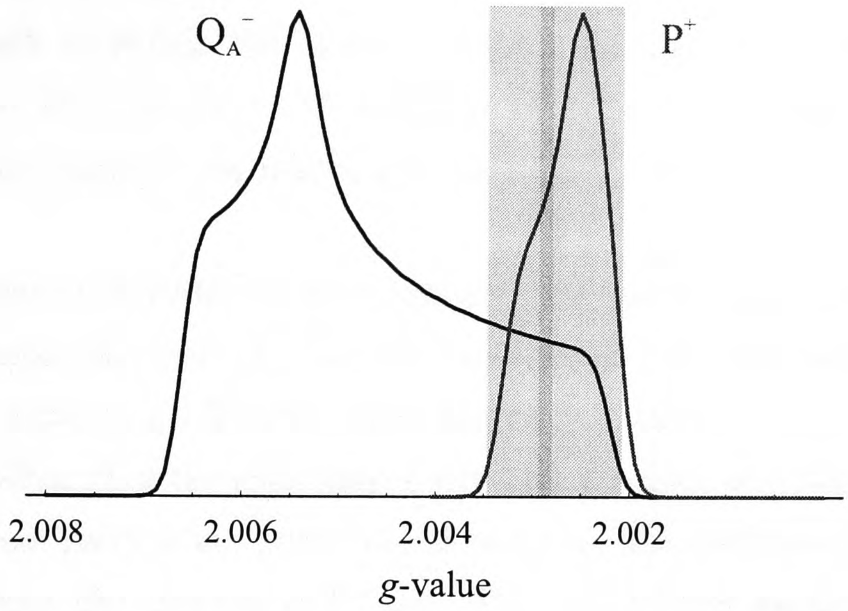

Figure 5.1: W-band EPR spectra of the two radicals P^+ and Q_A^- simulated using the principal g-values determined by cw EPR [41]. The lightly shaded area shows the region of overlap between the spectra where ESEEM can be observed. The dark shading shows the maximum bandwidth of an mw pulse applied at this field. The two spectra have been scaled to the same height.

Figure 5.1 shows W-band EPR spectra of P^+ and Q_A^-, simulated using the principal values of the $\boldsymbol{g}$-tensors determined by cw EPR [41], given in Table 5.1. The figure shows that at 95 GHz, these spectra are well resolved, and that there is only a small g-value range in which the two overlap. Using the conversion from g-value to field position, B_{res}:

$$B_{\text{res}}(g) = \frac{95 \times 10^9 2\pi}{8.7965 \times 10^6 g},$$

this means that the EPR spectra of P^+ and Q_A^- overlap in the 20 G region between $B_{\text{res}} = 33,870$ G and $B_{\text{res}} = 33,890$ G.

	P^+	Q_A^-
g_{xx}	2.0033	2.0066
g_{yy}	2.0025	2.0054
g_{zz}	2.0021	2.0022

Table 5.1: Principal g-values of P^+ and Q_A^- determined by cw EPR [41], used in the calculations in this chapter.

If it were possible to apply a pulse at W-band that was hard enough to cover the entire W-band EPR spectrum of width almost 100 G, then the narrowness of the overlap region between the spectra of P^+ and Q_A^- would not matter, and the spectrum obtained from an ESEEM spectrum at this frequency would look similar to that obtained at X-band. However, a pulse of this width would need to have $\omega_1/2\pi \approx 250$ MHz, which is impossible to achieve at 95 GHz. The exact nature of the pulses which can be created at this field strength are discussed in the next section, and at this point it is enough to reveal that it is unrealistic to hope to be able to generate a pulse wider than 10 G ($\omega_1/2\pi = 25$ MHz) at W-band in the best case [113], and 2 G (5 MHz) under realistic conditions for this experiment.

In the simulations described in this chapter, the narrowness of the pulses used strongly influenced the spectra that were calculated for high-field ESEEM experiments. If the condition for ESEEM is to be met, *i.e.* that both spins are excited by the pulses, it is clear that the experiment will only produce out-of-phase echo modulation from radical pairs when pulses are applied at field positions within the region of overlap between the spectra of P^+ and Q_A^-. To a good approximation in fact, with a pulse of only 2 G band-width, it is reasonable to assume that the resonant frequencies of the two electrons must be identical. In other words, a requirement for ESEEM of radical pairs at high field (taking $\hbar = 1$) is that

$$\omega_P = g_P \mu_B B_0 = g_Q \mu_B B_0 = \omega_Q, \tag{5.1}$$

i.e. that

$$g_P = g_Q. \tag{5.2}$$

In the above equations g_P and g_Q are the *effective* g-values of the radicals in a particular field direction, $\boldsymbol{n}(\theta, \phi)$. Thus, using selective pulses at W-band, one can measure the dipolar coupling between radical pairs at a particular orientation with respect to the magnetic field, thereby getting from one experiment information which has previously required both X-band ESEEM and W-band EPR results.

The effective g-values, which were defined in Chapter 3, depend upon the field direction as well as the principal axes and g-values of the radical. Hence, for P^+,

$$g_P = \sqrt{\left(g_{Px}\boldsymbol{n}\cdot\boldsymbol{x}_P\right)^2 + \left(g_{Py}\boldsymbol{n}\cdot\boldsymbol{y}_P\right)^2 + \left(g_{Pz}\boldsymbol{n}\cdot\boldsymbol{z}_P\right)^2}. \tag{5.3}$$

A similar expression can be given for Q_A. In the above expression the $\boldsymbol{i}_P$ are the vectors defining the principal Cartesian axes of P^+ with respect to the axes of Q_A^-. In the calculations which follow, these axes were calculated from the X-ray data stored in the Brookhaven Protein Data Base, entry 4RCR [11]. The axes of the quinone were defined as described in Chapter 3, and the x and y axes of P^+ set in the plane defined by the two vectors joining opposite nitrogens in the porphyrin ring. When the $\boldsymbol{i}_Q$ vectors define the Cartesian axes of the system,

$$\begin{array}{lcl} \boldsymbol{x}_Q = \{1,0,0\} & & \boldsymbol{x}_P = \{-0.550, \; -0.230, \; 0.803\} \\ \boldsymbol{y}_Q = \{0,1,0\} & \text{and} & \boldsymbol{y}_P = \{\;0.107, \; 0.934, \; 0.341\} \\ \boldsymbol{z}_Q = \{0,0,1\} & & \boldsymbol{z}_P = \{-0.828, \; 0.274, \; -0.489\} \end{array} \tag{5.4}$$

From the same data set, the dipolar vector between the two radicals was given as

$$\boldsymbol{R}_{PQ} = \{0.348, 0.883, 0.316\}.$$

Figure 5.2 shows the relative orientations of these radicals in *Rb. sphaeroides*, and the dipolar vector between them.

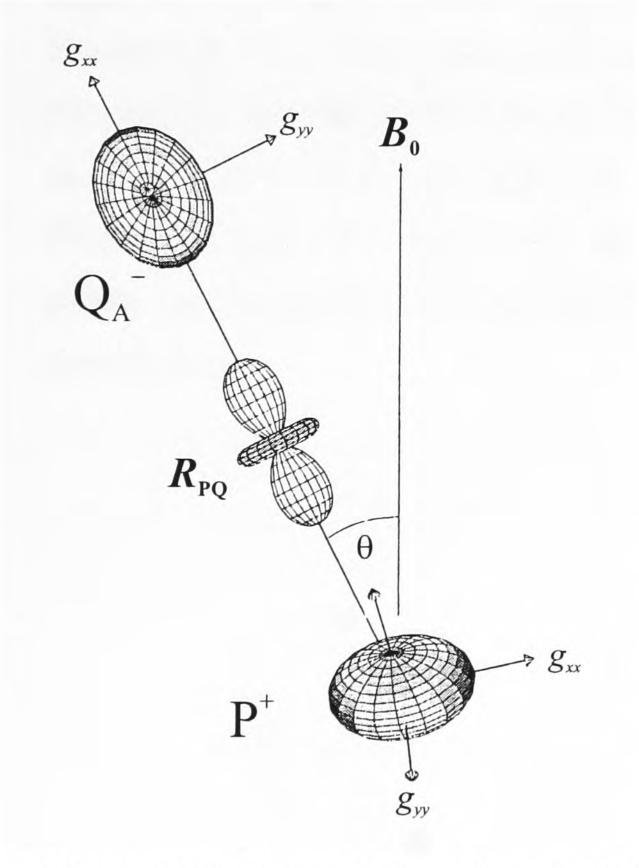

Figure 5.2: The relative orientations of the radicals P^+ and Q_A^- in *Rb. sphaeroides*, and the dipolar vector between them.

To enable the prediction of ESEEM spectra arising from the echo modulation in $P^+Q_A^-$ at 95 GHz, all those radical pair orientations for which $g_P = g_Q$ were determined. This was achieved by finding all those field directions, $\boldsymbol{n}(\theta, \phi)$, for which

$$g_d = g_P - g_Q = 0. \tag{5.5}$$

The calculation was performed by the Mathematica program `g-equal.m` (Appendix A.2). The tips of these vectors, $\boldsymbol{n}$, were plotted on the hemisphere defined by the axes of Q_A^-. They form the loop shown in Figure 5.3 on the next page. At the orientations shown in the figure, the spin echo signal from the radical pair is modulated. Initially, the hyperfine interactions between the electrons and nearby nuclei were neglected, and this led to modulations occurring at frequencies corresponding to $2|J - D_{zz}|$, where

$$D_{zz} = D(\cos^2\theta - 1/3), \qquad \text{with} \qquad \cos\theta = \boldsymbol{n} \cdot \boldsymbol{R}_{PQ}. \tag{5.6}$$

It was previously suggested in this thesis that for the radical pair $P^+Q_A^-$, which has an inter-radical distance of almost 29 Å, it can be assumed that $J = 0$ G. If this

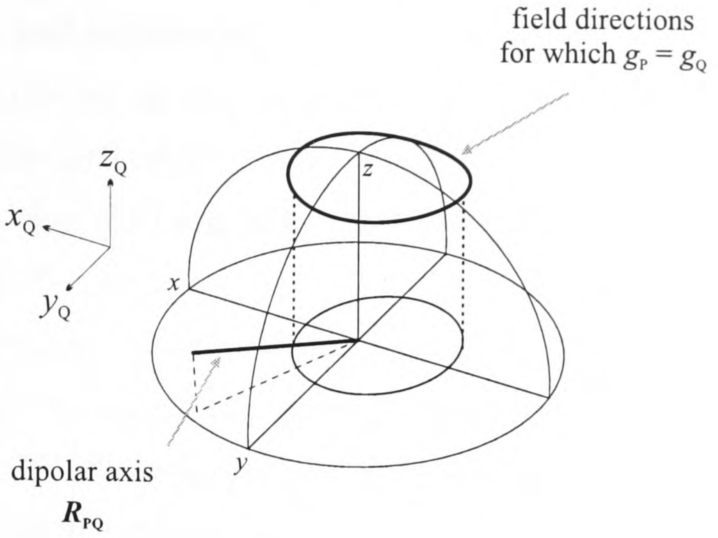

Figure 5.3: The orientations $\boldsymbol{B}_0$ with respect to the axes of g_Q for which $g_P = g_Q$, plotted on the sphere defined by the Cartesian axes of Q_A^-. The direction of the dipolar axis is also shown.

is the case, then the modulation of the spin echo is dependent solely upon $2|D_{zz}|$. Equations 5.3 and 5.6 were used to calculate the effective g-values, $g_{\text{eff}} = g_{\text{Peff}} = g_{\text{Qeff}}$, and the dipolar couplings, D_{zz}, corresponding to the field directions shown in Figure 5.3. The relationship between g_{eff} and D_{zz} for these field vectors is shown in Figure 5.4. The field directions for which $g_d = 0$ correspond to $2.0026 \leq g_{\text{eff}} \leq 2.0033$ and to dipolar coupling angles $48^{\circ} \leq \theta \leq 103^{\circ}$, giving $-0.14 \text{ G} \leq D_{zz} \leq +0.41 \text{ G}$. Figures 5.3 and 5.4 show that each field position ($\equiv g_{\text{eff}}$) excited by the selective pulses corresponded to **two** radical pair orientations, each of which gave rise to a distinct D_{zz}.

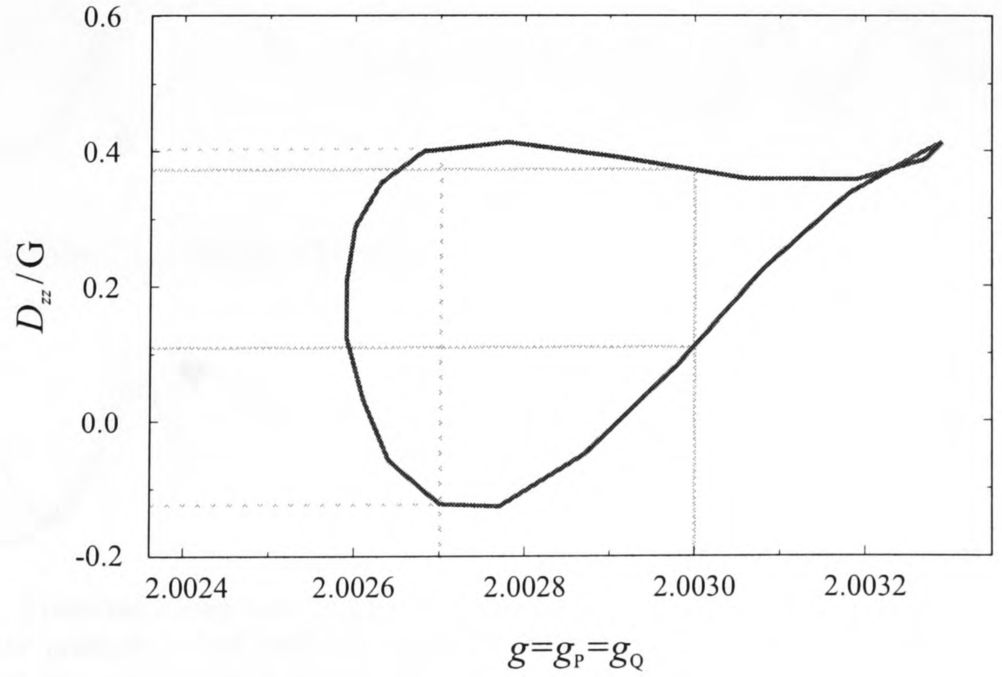

Figure 5.4: The value of D_{zz} is calculated for those field directions where $g_P = g_Q$. Each of these field directions corresponds to two different radical pair orientations and hence two different dipolar couplings. The values of D_{zz} associated with $g = 2.0027$ and $g = 2.0030$ are highlighted.

It should be expected that the shape of the ESEEM spectra obtained at W-band will be very different from those measured for a frozen solution at X-band. In the absence of exchange and anisotropic hyperfine couplings, every excited radical pair orientation will give rise to an anti-phase doublet with splitting $2|D_{zz}|$. At X-band this gives the familiar anti-phase Pake doublet. At W-band however, the theory given above suggests that for each field position at which the mw pulses are applied, the radical pair must be close to one of two particular orientations if there is to be appreciable excitation. For each field position used therefore, the resulting ESEEM spectrum will simply be a sum of the **two** anti-phase doublets arising from these orientations. Of course, the splitting and phase of these doublets are determined by the value of D_{zz}, and it is therefore this parameter which determines the shape of the ESEEM spectrum and can be measured from it. For example, Figure 5.4 shows that $g_{\text{eff}} = 2.0027$ clearly leads to one positive and one negative value of D_{zz}, whereas when $g_{\text{eff}} = 2.0030$, both are positive. The resulting ESEEM spectra for these field positions will therefore be very different, as shown schematically in Figure 5.5. When both values of D_{zz} are positive, the ESEEM will have an EEAA pattern, quite different from the EAEA pattern arising when the values are of opposite polarity. In this way an ESEEM experiment performed at W-band will be used to study directly the relationship between the dipolar coupling and the relative orientation of the radical pair.

$D_{zz(1)}$ positive and $D_{zz(2)}$ negative

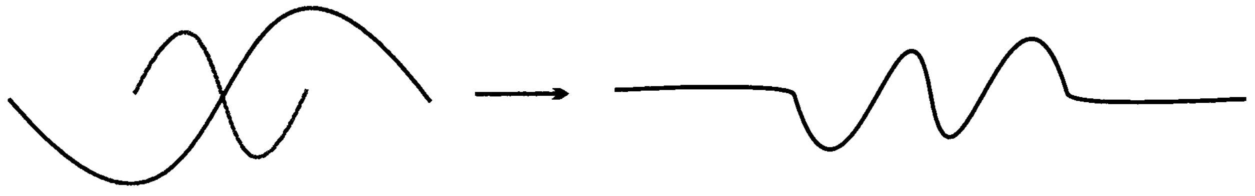

$D_{zz(1)}$ and $D_{zz(2)}$ both positive

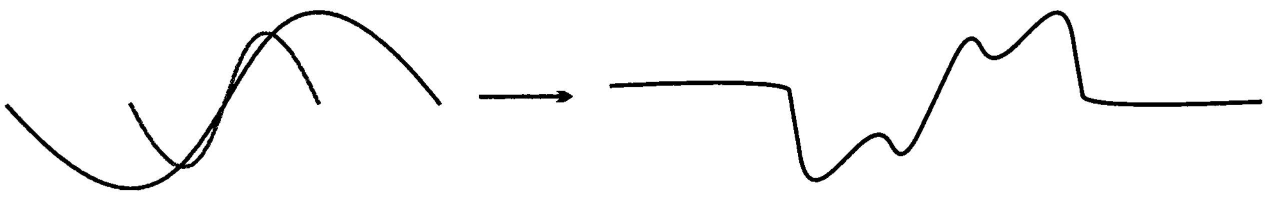

Figure 5.5: Predicted schematic ESEEM spectra determined by the phase and magnitude of D_{zz} for a given field position. Two different types of pattern; EEAA (*e.g.* $g = 2.0030$) and EAEA (*e.g.* $g = 2.0027$) will be seen. In the diagrams, the x-axis is frequency, and the y-axes ESEEM intensity.

Before embarking upon the calculation of W-band ESEEM spectra, the nature of the pulses applied at this field strength are studied in more detail.

5.2.2 ESEEM Using Selective Pulses

In addition to changing the nature of the echo modulation which is created in an ESEEM experiment at high field, the selective pulses used at 95 GHz alter the manner in which the experiment is performed. These changes arise as a result of the longer duration of the selective pulses, and from the increased importance of the off-resonance effects caused by narrow-band pulses exciting many radicals in the sample only partially.

Length of Selective Pulses

For a rectangular pulse, the relationship between pulse angle, α, and pulse duration, t_p, is

$$\alpha = \gamma B_1 t_\alpha = \omega_1 t_\alpha. \tag{5.7}$$

Hence at W-band, where B_1 is approximately five times lower than at X-band, pulses must be five times longer. When the pulse duration is short, *i.e.* 5 ns and 20 ns for a $\pi/4$ and a π pulse respectively, it is reasonable to assume that the pulses are short enough, compared to the values of τ for which information is recorded, that the evolution of spins during the pulse need not be included in the calculation of the ESEEM. The time domain spectrum is therefore calculated by assuming that equal delay times τ are measured from the centres of infinitesimally short pulses (Figure 2.2, page 25). At W-band, the potential evolution frequencies will be ten times larger and the pulse durations five times longer ($t_{\pi/4}$ = 25 ns and t_π = 100 ns). In this case the evolution becomes important and the pulse lengths must be taken into account in the calculation of the ESEEM.

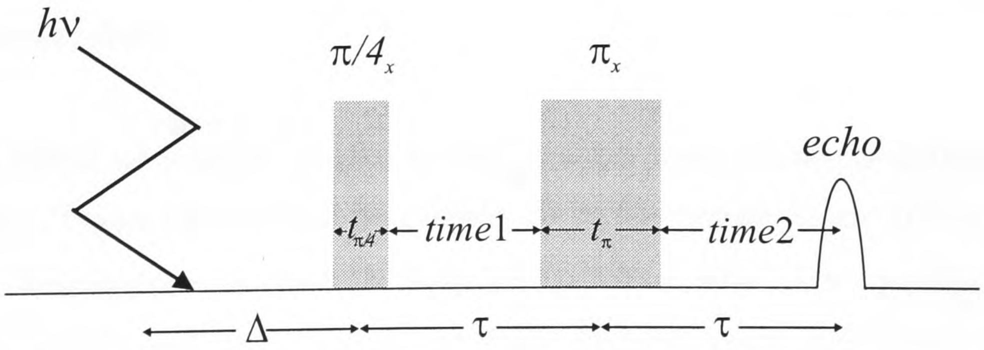

Figure 5.6: The ESEEM pulse sequence for the experiment at W-band. The long pulse durations are now significant and must now be considered. The experimental results are still however given as a function of τ.

The pulse sequence used to calculate the echo in the simulations in this chapter was

$$h\nu\text{-}\Delta\text{-}t_{\pi/4}\text{-}time1\text{-}t_\pi\text{-}time2\text{-}\text{echo}$$

where the spaces between the pulses, *time*1 and *time*2, were defined by

$$time1 = \tau - \frac{t_{\pi/4}}{2} - \frac{t_\pi}{2}, \quad \text{and} \quad time2 = \tau - \frac{t_\pi}{2}.$$

The W-band pulse sequence used in these calculations is shown in Figure 5.6 on the previous page. The calculation was performed using these new pulse lengths, but the echo output was, as usual, given as a function of τ.

Off-Resonance Effects: Use of the EXORCYCLE

The soft pulses used at W-band have two other effects upon the experimental procedure of the ESEEM. Firstly, and advantageously, at 95 GHz the ESEEM experiment will have a considerably lower dead-time period than its X-band counterpart. This is because at W-band, for a cavity with a specified Q-factor, the resonator ringing time is ten times shorter than at X-band. Additionally, the lower power of the mw pulses means that saturation of the detector does not occur [114].

The W-band ESEEM experiment described here does have a kind of "dead-time" however. This is caused by the long pulse durations. Looking back to Figure 5.6, it is obvious that τ cannot be so short as to make the period between the two pulses negative. For example, in the figure shown, $\tau = 0$ would give a corrupted data point. In practice this will lead to a short period at the start of the spectrum in which the echo cannot be detected, and the trace would need to be extrapolated in some way (as is often done for X-band experiments). In the simulations which follow, however, there is no problem associated with negative values of *time*1 or *time*2. Indeed, by allowing the pulses to overlap in this way one can still calculate the complete echo modulation and avoid the need to extrapolate back to $\tau = 0$ as would be required for experimental data.

The second effect of narrow pulses is the introduction of off-resonance effects into the spectrum. These effects will be caused by other orientations of the radical pair, whose EPR frequencies lie just outside of the area where the pulses are applied, being only partially excited. These partially flipped spins will cause off-resonance effects in the spectrum. Off-resonance effects, similar to those described in Chapter 3, will always occur in pulsed EPR experiments, unless a hard enough pulse can be applied to fully excite the entire spectrum. The effects even occur in the X-band spectrum of the weakly coupled radical pair $P^+Q_A^-$, since the applied pulses, although hard enough to allow ESEEM to take place, do not actually affect every spin in the sample equally. However, in the X-band experiment, the majority of spins are fully excited, and the off-resonance effect becomes negligible in comparison to the true ESEEM. Unfortunately, in the simulated W-band experiment, the off-resonance effect will be large in comparison to the desired signal, and to prevent corruption of the spectrum, it will have to be removed using phase cycling techniques.

45°	180°	Detection
+*x*	+*x*	+*x*
+*x*	-*y*	-*x*
+*x*	-*x*	+*x*
+*x*	+*y*	-*x*

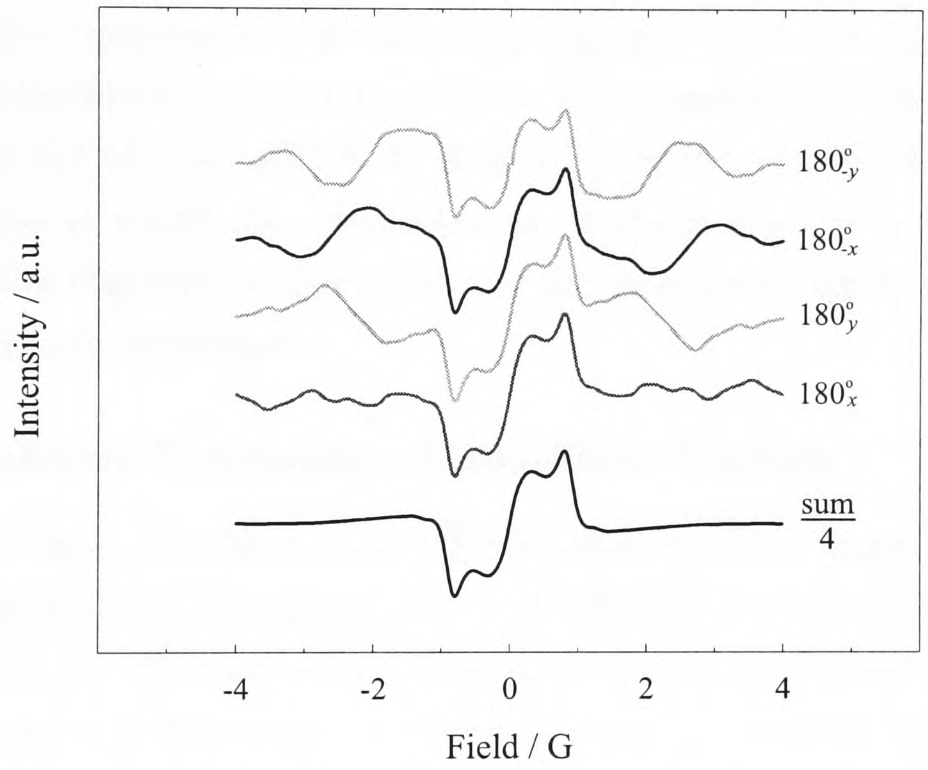

Figure 5.7: Use of the EXORCYCLE phase cycling procedure. The table indicates the four pulse sequences used; the first pulse is 45° (or 90°), the second 180°. The spectra show the ESEEM data recorded from each, and the scaled sum of all four. This phase cycling procedure is used in the simulation of all the spectra in this chapter.

The particular phase cycling sequence used in the following calculations is EXORCYCLE. Developed by Bodenhausen, Freeman and Turner in 1977 [95] to remove "ghost" and "phantom" artifacts in two-dimensional NMR spectra, the EXORCYCLE procedure is ideal for eliminating the off-resonance effects in W-band ESEEM spectra. The procedure, which is shown in Figure 5.7, works using *difference spectroscopy*. A ghost signal will appear in a magnetic resonance spectrum if the refocusing (180°) pulse does not fully excite the spectrum and some transverse magnetisation escapes the effect of this pulse. Since this magnetisation is not affected by a 180°_{+x} pulse, it will be equally unaffected by a refocusing pulse phase-shifted from $+x$ by 90° (or indeed 45°). This pulse inverts the sense of the desired echo so that it is detected along $-x$ rather than $+x$. The sum of these two signals will therefore be the desired echo at twice the amplitude, with the ghost signal removed. Phantom signals arise when there are imperfections of a similar nature in both the β and γ pulses. Both signals are removed by the phase cycling procedure illustrated in Figure 5.7, which shows that the sum of the four spectra gives a clean spectrum. This phase cycling procedure is used in all the spectra simulated in this chapter.

5.3 Simulated Out-of-Phase ESEEM Spectra of $P^+Q_A^-$

Out-of-phase ESEEM spectra were simulated using an adaptation of the numerical calculation program used in Chapter 3, `spin-echo.f` (Appendix A.1.2). Initially, any hyperfine couplings in the system were ignored. The spin Hamiltonian for the system was therefore that given in equation 3.7 on page 53. The program was altered to allow the out-of-phase echo to be detected from this spin-correlated radical pair, and the field at which the calculations are performed set to 3.4 T. The spectral simulations in this chapter give an idea of the information which could be obtained from this type of experiment.

5.3.1 Spectral Dependence Upon Field Position

Simulations were performed using the two-pulse sequence given in Figure 5.6, so that an mw pulse of strength $\omega_1/2\pi = 5$ MHz ($B_1 = 1.8$ G) had $t_{\pi/4} = 25$ ns and $t_\pi = 100$ ns. The pulses were applied at various field positions lying between $g = g_P = g_Q = 2.0024$ ($B_{\text{res}} = 33,888$ G), and $g = 2.0035$ ($B_{\text{res}} = 33,869$ G). The dipolar, D, and exchange, J, coupling parameters were set at -1.24 G and 0 G respectively, and the relaxation time (estimated from the results of Rohrer *et al.* [93]) was $T_2 = 0.5$ μs. Data were calculated for fifty values of τ with $\delta\tau = 50$ ns, so that $\tau_{\text{max}} = 2.45$ μs.

The theory presented earlier predicted that spectra should be modulated at frequencies given by

$$D_{zz} = D[(\boldsymbol{n} \cdot \boldsymbol{R}_{\text{PQ}})^2 - 1/3]$$

with full excitation occurring for the two orientations given in Figure 5.4 for each field position. Hence the spectra resulting from such a set of simulations should display the information given in Figure 5.4, *i.e.* should show a correlation between field position and D_{zz}. Figure 5.8 (overleaf) indicates that this was exactly the case. Two predicted spectral shapes (Figure 5.5) are very much in evidence. The spectrum for $g = 2.0027$ clearly shows the EAEA line-shape in contrast to the EEAA shape

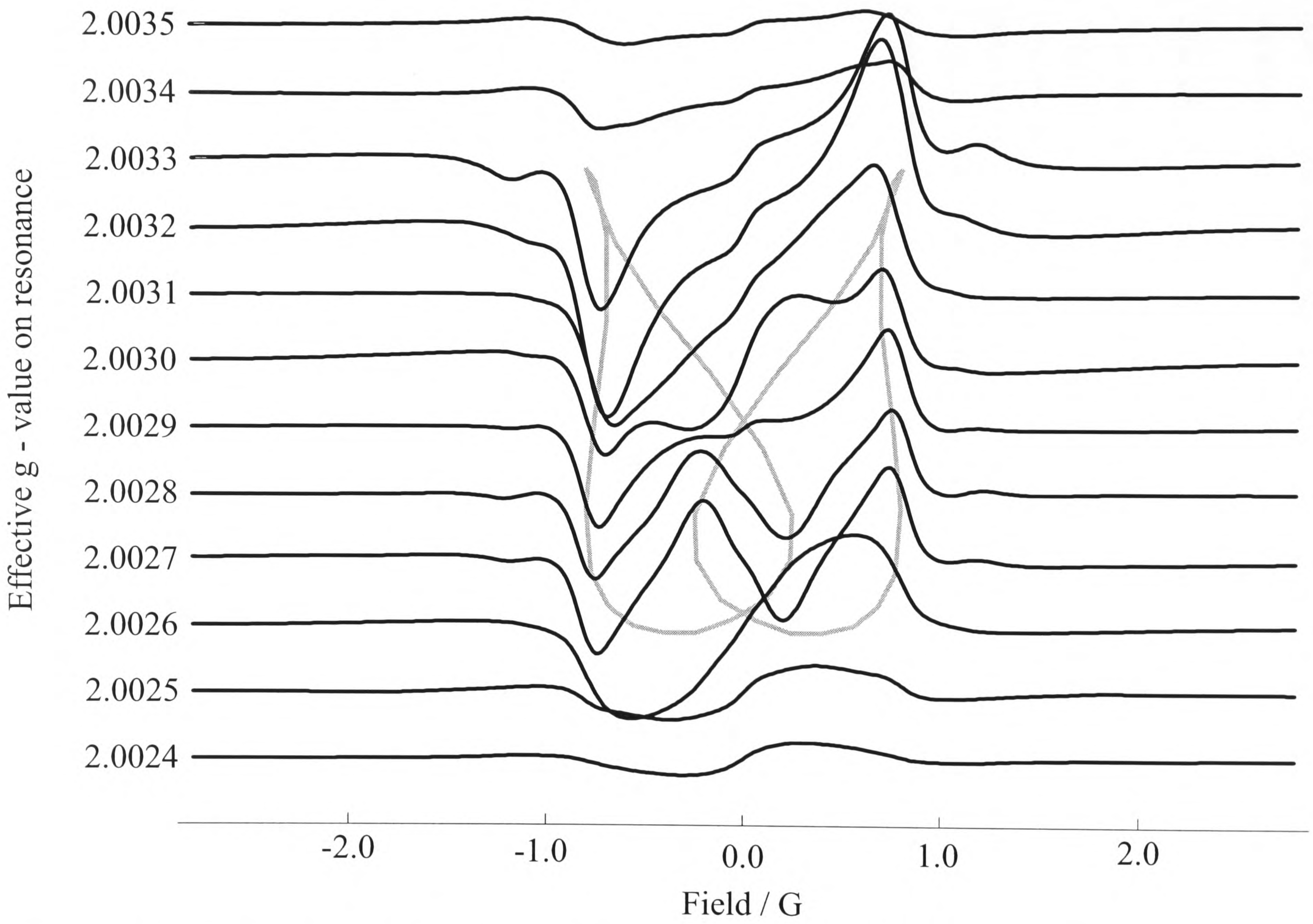

Figure 5.8: Simulated ESEEM spectra with $\omega_1/2\pi = 5$ MHz for g-values in the overlap region of P^+ and Q_A^-. The two predicted spectral shapes are seen. Overlaid is the loop taken from Figure 5.4. For each peak in any spectrum, the baseline of the spectrum and a perpendicular from the peak cross in the place where the loop lies. Here D_{zz} has been multiplied by 2 so that the loop accurately predicts the positions of the spectral peaks. Includes EXORCYCLE.

of the $g = 2.0030$ spectrum. The "loop" calculated to show the correlation between g and D_{zz} (Figure 5.4) has been overlaid on the spectra. It lies so that for all values of g, the baseline of the relevant spectrum and the perpendicular from a peak in the spectrum cross at the loop, showing that the spectra truly reveal the D_{zz} splittings as predicted.

Use of a More Selective Pulse

The spectra given in Figure 5.8 give confidence that this experiment can be used to correlate the relative orientation of the radicals and the dipolar axis. However, the question should be asked: if the mw pulse has a B_1 lower than 2 G, how much will this alter the spectra? Will the same information still be obtained? With the equipment available, this could indeed be a serious concern. The spectra were therefore re-calculated using pulses with a lower B_1-field, *i.e.* $B_1 = 0.9$ G, $\omega_1/2\pi = 2.5$ MHz.

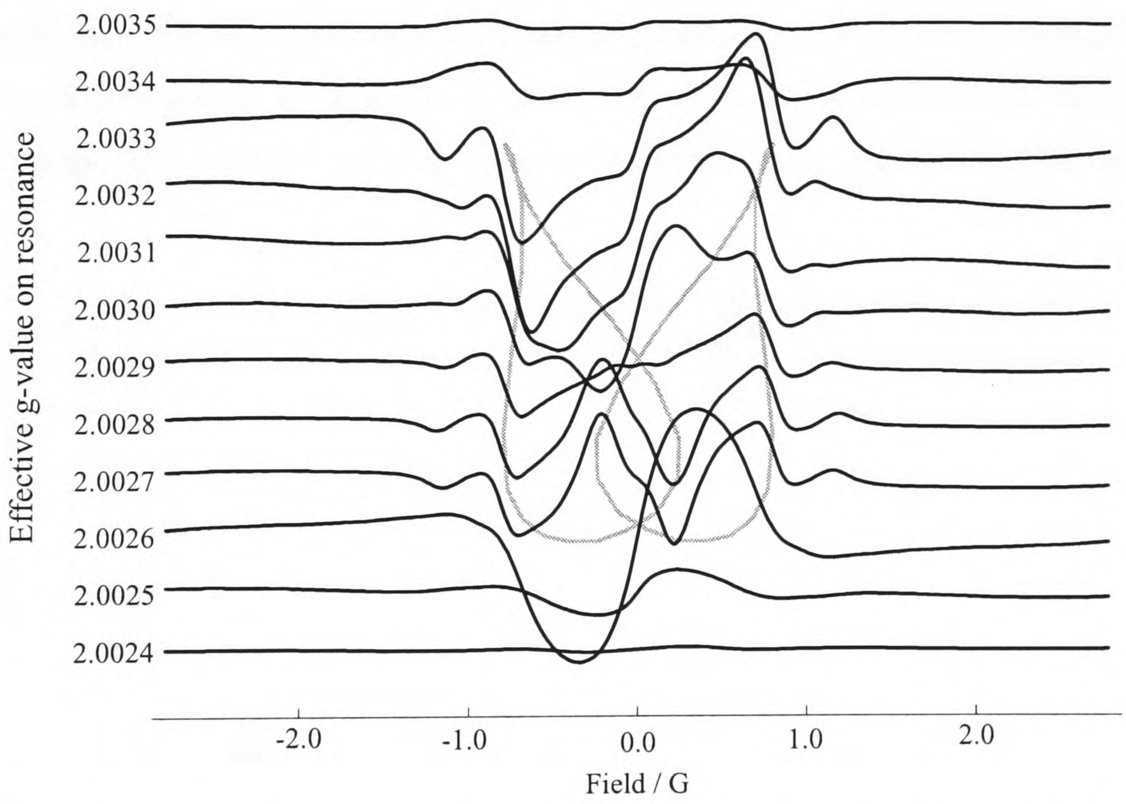

Figure 5.9: Simulated ESEEM spectra with $\omega_1/2\pi = 2.5$ MHz for the same g-values used in Figure 5.8. The weaker pulses cause greater off-resonance effects, some of which are not cancelled by EXORCYCLE phase cycling.

These pulses were twice as long as those used previously, so that $t_{\pi/4} = 50$ ns and $t_\pi = 200$ ns, and twice as selective. They therefore gave rise to proportionately larger off-resonance effects, many of which were removed by the phase cycling process. The spectra, shown in Figure 5.9, are less smooth than those produced from the harder pulse. Despite this they do, to a good approximation, still give the information required from the experiment. Clearly the use of a stronger pulse is preferable, but the simulations in Figure 5.9 show that even with an extremely selective pulse, the experiment can give useful results.

The Effect of the Exchange Interaction

Hitherto in this chapter, simulations have been performed in the absence of an exchange interaction. This assumption is not unrealistic with such a large separation between the radicals (29 Å). However, various fittings to frequency domain data [34, 49, 51, 57], and the time domain curve fit performed in Chapter 4, have suggested that J may be small and positive. If this is the case, then the following questions can be asked: what sort of effect will a small positive exchange interaction have upon the spectra shown in Figure 5.8? Could this experiment be used to determine the value of J for a given sample? These questions were answered by including an exchange interaction, $J = +0.01$ G (the value determined by Bittl *et al.* [49] and the upper limit in the time domain curve fit in Chapter 4), to the spectra created with the 5 MHz pulse. The new spectra are shown in Figure 5.10. Compared to those shown in Figure 5.8 they are only very slightly different. If this experiment were to be used to determine J, an extremely good signal-to-noise ratio would be required, and it is likely that the X-band experiment would be more useful for this purpose.

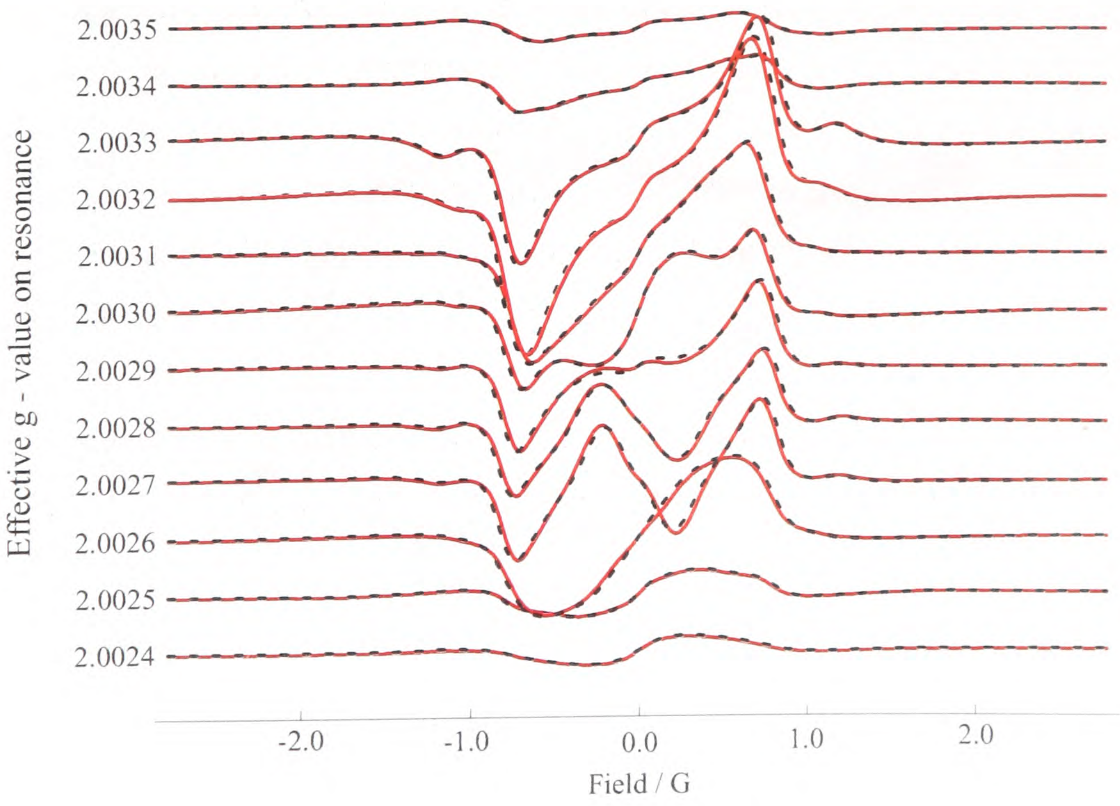

Figure 5.10: Dotted lines: the simulated ESEEM spectra shown in Figure 5.8. Red lines: the same spectra with an exchange interaction of $J = +0.01$ G included.

The Effect of Rotating the Special Pair

EPR studies are occasionally performed in which it is useful to remove one of the cofactors from the reaction centre and replace it with another, similar species. Particular examples of studies of this type have involved the removal of the primary acceptor. In plant photosystem PSI, the acceptor A_1 has been replaced by Vitamin K, duroquinone or naphthquinone, and the effect on the electron transfer chain studied [115, 116]. It is of interest in these substitutions to determine whether the replacement quinone takes the same orientation as the native acceptor. W-band ESEEM, with its sensitivity to the relative orientation of the cofactors, could be used to observe any changes arising during substitution.

The information contained in an W-band ESEEM experiment is essentially held in the plot of $g = g_P = g_Q$ vs. D_{zz}, demonstrated by Figure 5.4. Figure 5.8 shows that the loop predicts the positions of the splittings seen in the W-band ESEEM spectra. Thus it follows that a change in the loop linking g and D_{zz} implies a difference in the values of D_{zz} for which splittings are seen, and consequently a change in the ESEEM spectra. The effect upon the ESEEM spectra of a small rotation of one of the cofactors can therefore be determined by calculating the relevant loops.

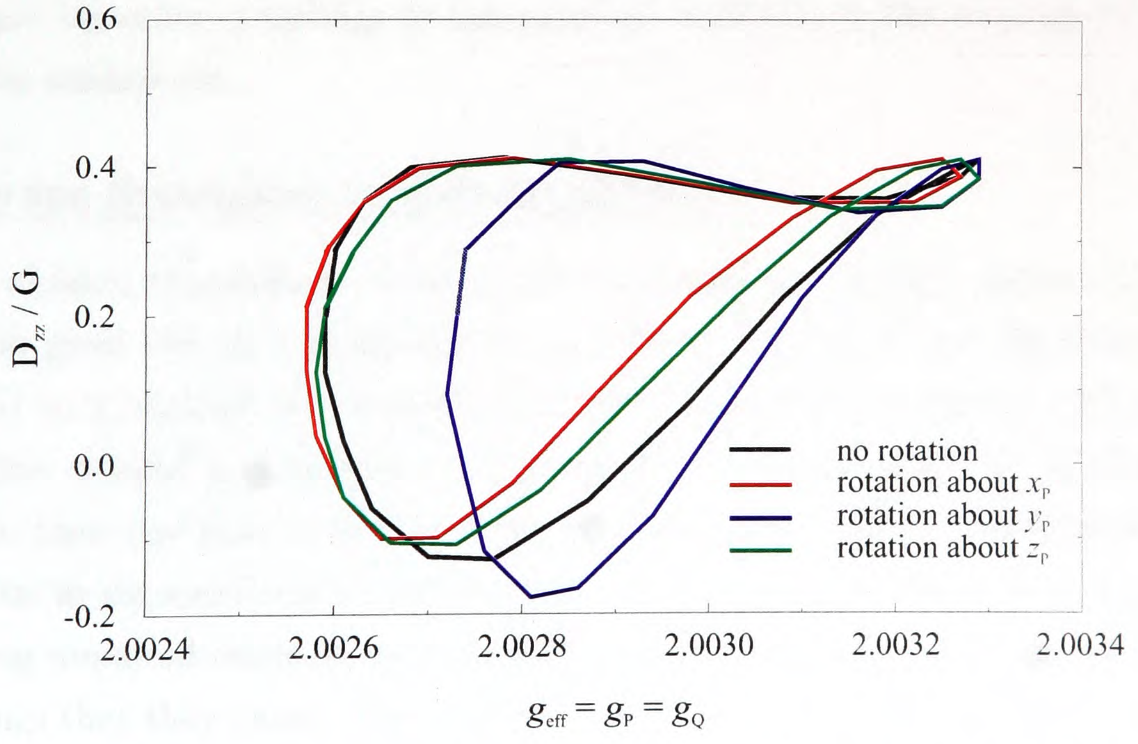

Figure 5.11: The calculation leading to Figure 5.4 is repeated for the cases of a 10° rotation about the three principal axes of P^+. Relatively little change is seen unless the rotation is about y_P (blue).

Although a reaction centre preparation in which the special pair has rotated is unlikely, it is the *relative* orientation of the radicals with respect to each other and the dipolar axis that may affect the ESEEM. For the purposes of the following calculation it was not important which of the radicals was rotated, and P^+ was chosen for convenience. The axes of the special pair, P^+, given by equation 5.4, were rotated by 10° in each of the x, y, z directions in turn, thus altering the relative orientation of P^+ and Q_A^-. The relationship between the z-component of the dipolar interaction (D_{zz}) and the g-value, g, for which $g_P = g_Q$ was then explored by the method used in Section 5.2.1, *i.e.* plots were made of g vs. D_{zz}. These loops are shown for each of the three rotation directions, in Figure 5.11 (previous page). The diagram indicates that a rotation about either the principal x or z axis of P^+ will only slightly affect the W-band ESEEM spectra, but that a much larger change will be seen if a rotation around y_P is performed. This should lead to considerably different W-band ESEEM spectra, including a dramatic loss of intensity in the spectra for $g = 2.0026$ and $g = 2.0027$.

5.3.2 Consideration of the Hyperfine Interaction

In the W-band ESEEM simulations performed so far, hyperfine interactions have been omitted for reasons of convenience. However, it would be foolish to overlook the effects that the presence of nearby nuclei can have upon the ESEEM. The subject of anisotropic hyperfine couplings has already been considered for ESEEM at X-band, and it will shortly be discussed for W-band. First however, the effects of unresolved isotropic hyperfine couplings to the unpaired electrons in the radicals P^+ and Q_A^- must be considered.

Hyperfine Broadening in W-Band ESEEM

In the absence of couplings either to other electrons or to nearby nuclei, an unpaired electron gives rise to a single line in an EPR spectrum. If this electron becomes coupled to a nucleus, the isotropic part of the hyperfine interaction will cause the EPR line to split in accordance with the strength of the coupling, A, and if there is more than one nucleus affecting the electron in this way, an additional splitting will arise in the spectrum for each nucleus. In reality there will be very many nuclei affecting unpaired electrons in this manner, and it is impossible to resolve all of the splittings that they cause. The overall effect therefore of the many isotropic hyperfine couplings to an electron, is the broadening of the EPR line, giving it a Gaussian line-shape with a width reflecting the spread of the couplings.

It has already been shown that with the extremely selective pulses available for W-band ESEEM, the condition for echo modulation to occur is $g_P \approx g_Q$. It is now time to consider the effect of the hyperfine broadening on the ESEEM spectra simulated so far. This broadening will have the effect of shifting the resonance position of a radical away from where it is expected on the basis of the g-value and B_0 alone. This will mean that instead of approximately equal g-values for P^+ and Q_A^-, echo modulation could occur when

$$g_P \approx g_Q \pm \Delta g, \tag{5.8}$$

where Δg is determined by the hyperfine interactions. The inhomogeneous broadenings due to unresolved hyperfine couplings for deuterated P^+ and Q_A^- used in these calculations were taken from Prisner *et al.* [90]: 3.3 G and 3.0 G for P^+ and Q_A^- respectively. A line broadening of 3.3 G for P^+ will mean that instead of a sharp peak at field position B_P, the EPR spectrum of P^+ for a given orientation of the radical is a Gaussian, centred at B_P with a width a little over 3 G. The same is true for Q_A^- where the curve is centred at B_Q. Thus the condition for ESEEM (*i.e.* $B_P \approx B_Q$) is relaxed and there is a high probability of echo modulation occurring everywhere in the region governed by $|B_P - B_Q| \leq 3$ G. This field shift can be translated into a shift in effective g-value using the relation

$$\frac{\Delta g}{g} = \frac{\Delta B}{B}$$

where $g \approx 2$ and $B \approx 34,000$ G so that $\Delta g = 2 \times 10^{-4}$, *i.e.* for each of the two radicals this corresponds to an effective g-value shift of ± 0.0001. Unresolved hyperfine couplings from native reaction centres (*i.e.* ^{1}H-containing) are much greater, for example 10 G for P^+ and 7 G for Q_A^- [90]. The effect that the hyperfine broadening has on W-band ESEEM spectra was studied by considering the plots of D_{zz} vs. g_{eff} and the simulated spectra.

The program `g-equal.m` (Appendix A.2) was used once again, this time to find values of $\boldsymbol{n}$, g and D_{zz} which gave $g_P - g_Q = \pm 0.0002$. Since the hyperfine broadenings for P^+ and Q_A^- are small, these new field direction vectors lie close to those already shown in Figure 5.3, so that the condition for modulation is relaxed, and ESEEM is seen principally from orientations for which $|g_P - g_Q| \leq 0.0002$.

Calculations of these field directions and the associated D_{zz} and g-values produced the plots given in Figure 5.12a on page 107. Here the plots corresponding to $g_P - g_Q = 0, +0.0002$ and -0.0002 are labelled g_0, g_+ and g_- respectively. Rather than sharp peaks at those D_{zz} values indicated by g_0, the ESEEM spectra now show signals broadened in the range indicated by g_+ and g_-. For example, consider the case where $g_P = 2.0030$. It was previously assumed that for echo modulation to occur

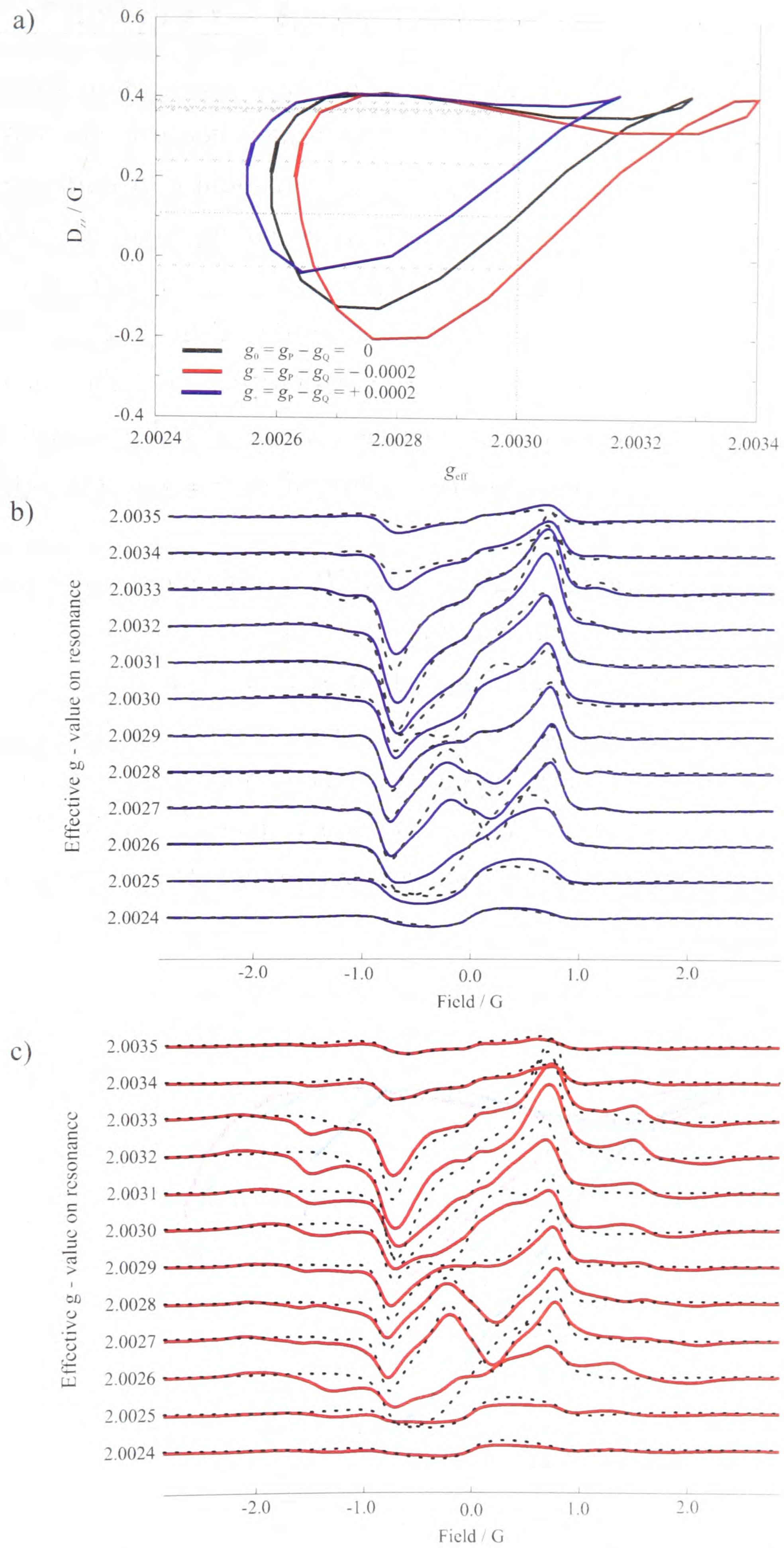

Figure 5.12: a) Plots of $g_{\text{eff}} = (g_P + g_Q)/2$ vs. D_{zz} for the upper and lower limits of the broadening caused by unresolved hyperfine couplings. b) and c) Dotted lines: the simulated ESEEM spectra shown in Figure 5.8. Blue lines: the same spectra with the inhomogeneous broadening associated with the hyperfine coupling taken from Prisner *et al.* [90] included. Red lines: the simulations repeated after the inclusion of a spin-1/2 nucleus. For these simulations, $A = 0.75$ G, $\omega_N = 0.5$ G and $\xi = 45^\circ$.

$g_Q = 2.0030$ was also required, giving resonances corresponding to $D_{zz} = 0.11$ G and 0.37 G. However, although these values give the positions of the maximum intensity ESEEM signal, the hyperfine broadening means that echo modulation can also occur for $-0.02 \text{ G} \leq D_{zz} \leq 0.24$ G and $0.36 \text{ G} \leq D_{zz} \leq 0.39$ G. This gives the broadened spectrum seen in Figure 5.12b (page 107). The hyperfine broadened ESEEM spectra for all the g-values studied are shown in this figure. The line-broadenings reduce the orientational selectivity of the experiment, and may influence the quality of the information available.

Despite the effect seen in Figure 5.12b for W-band, this hyperfine line-broadening does not affect ESEEM spectra recorded at X-band in any way. Since in the latter case hard pulses are used, $g_P = g_Q$ is not a condition for echo modulation, and small changes in the effective g-values caused by the line-broadening are simply refocused by the π-pulse. This is in contrast to the effect of hyperfine broadening in a cw EPR spectrum. Here, due to the increased effect of g-anisotropy at higher field and the field-independence of the hyperfine coupling, a greater field strength reduces the importance of the isotropic hyperfine broadening.

Having considered the effect of the isotropic hyperfine coupling upon the ESEEM spectra of $P^+Q_A^-$ at W-band, it is now important to study the potential effects of anisotropic hyperfine couplings in the form of the nuclear ESEEM.

Nuclear ESEEM at 95 GHz

The ESEEM of $P^+Q_A^-$ at X-band has already been considered in Chapters 2 and 4 of this thesis. The results of simulations have shown that the nuclear ESEEM arising from anisotropic hyperfine couplings is likely to be small, but will have a distinct effect upon spectra. It is possible therefore that the ESEEM of this radical pair at W-band will also be affected in a similar manner.

Simulations of the ESEEM of $P^+Q_A^-$ at W-band with an anisotropic hyperfine interaction included were performed by altering the Hamiltonian used in the numerical calculation in the same manner as for the calculations in Chapter 3. The resulting Hamiltonian has additional terms for the secular and pseudo-secular hyperfine couplings, and the nuclear Zeeman interaction (equation 3.13, page 59) associated with an axially symmetric hyperfine interaction. Once again the variables for the nuclear ESEEM are those used for $P^+Q_A^-$ in Chapter 2:

- the hyperfine coupling constant, $A = 0.75$ G,
- the nuclear Zeeman interaction, $\omega_N = 0.5$ G,
- the angle between the electron-electron and electron-nuclear vectors, $\xi = 45^o$.

The variables above gave a reasonable picture of the type of effect anisotropic hyperfine couplings could have upon the ESEEM of $P^+Q_A^-$ at X-band. The purpose of the following calculation was to give an idea of the nature and size of the effect upon W-band spectra.

Figure 5.12c on page 107 shows W-band ESEEM spectra calculated with nuclear ESEEM included. The same values of g_{eff} were considered. Each spectrum has lost intensity, in much the same way as was seen in the simulations of X-band spectra in previous chapters. The spectra are broadened slightly, but the positions of the peaks due to the dipolar coupling have not changed in any of the spectra shown. This is also a result reminiscent of those in Chapter 2: at X-band the position of $f_\perp$ is unaffected by the inclusion of the nuclear ESEEM. However, X-band ESEEM spectra did show a change in the modulations around $f_{||}$. A similar effect is seen in Figure 5.12c, where for many of the g-values considered, an additional modulation arises at around 4 MHz.

It can be concluded that although anisotropic hyperfine interactions may affect the W-band ESEEM spectra of $P^+Q_A^-$, they are unlikely to shift the positions of the peaks corresponding to values of $2D_{zz}$, and the interpretation of the spectra will not be altered.

5.4 Experimental Considerations for ESEEM at W-Band

Whilst pulsed EPR experiments at X-band are common-place and straightforward to perform, the same experiments at W-band are, with today's equipment, still rare. The difficulties associated with selective pulses were discussed earlier, and in this section another experimental problem, which arises from the short wavelength of the microwave pulses required is considered. A pulse applied to a sample at $B_0 = 34,000$ G must have a frequency of around 95 GHz. Use of the simple relation between the frequency and wavelength of an electromagnetic wave leads to $\lambda_{mw} \approx 3$ mm. To get resonance the resonator must therefore be ≈ 3 mm, meaning that the sample tube into which the frozen reaction centres are placed is very small. This has the advantage that the experiment can be performed even when only a very small quantity of sample is available. However, in practice it can be quite difficult to prepare such a tiny sample for an experiment, and the signals from the ESEEM are consequently rather weak [117].

5.4.1 Comparison of the In-Phase and Out-of-Phase Echoes

In an X-band experiment, where all the radical pairs in a sample of bacterial reaction centres are excited uniformly, all the ESEEM signal recorded by the spectrometer is due to *radical pairs*, and will be out-of-phase. When the experiment is repeated at W-band this may not necessarily be the case.

The narrow mw pulses used for W-band ESEEM mean that when a pulse is applied at a particular field position, for certain radical pairs the out-of-phase condition, $g_\mathrm{P} \approx g_\mathrm{Q}$, is met, while for others it is not, and only one radical is excited. Hence, both in-phase and out-of-phase signals occur and obscure each other. If this is the case then accurate phase adjustment in this experiment is vital if information is to be obtained from the out-of-phase echo. With the X-band ESEEM experiment phase adjustment is relatively simple since only one signal is present, and this can be interpreted immediately as the out-of-phase signal. Since the W-band experiment has both an in-phase and an out-of-phase signal, both of which are weak as a consequence of the low mw power available, the assignment of the axes is much harder. In fact, to define the axes x and y requires knowledge of the shape of the in-phase signal and its magnitude in comparison to that seen out-of-phase. If the in-phase signal is much larger than the out-of-phase, then it is possible that this desired signal will be hidden and the experiment cannot be performed.

Simulations of In-Phase ESEEM at 95 GHz

Simulations of the in-phase ESEEM were performed using the `spin-echo` program. The phase of the detection was shifted by $\pi/2$ in order to observe the predicted un-modulated signal. The value of $\omega_1/2\pi$ was 2.5 MHz, so that $t_{\pi/4} = 50$ ns and $t_\pi = 200$ ns. D and J remained at -1.24 G and 0 G respectively, with $T_2 = 500$ ns as before, and 50 values of τ were used with $\delta\tau = 50$ ns. The signal was calculated in the same g-value range as the out-of-phase echo data, and was highly dependent upon the field position of the pulses. The calculated in- (dotted lines) and out-of-phase (solid lines) time domain traces are shown in Figure 5.13 (next page), where the in-phase traces are shown at one third of their actual amplitude. Each trace is the sum of the four EXORCYCLE components. The figure suggests with some

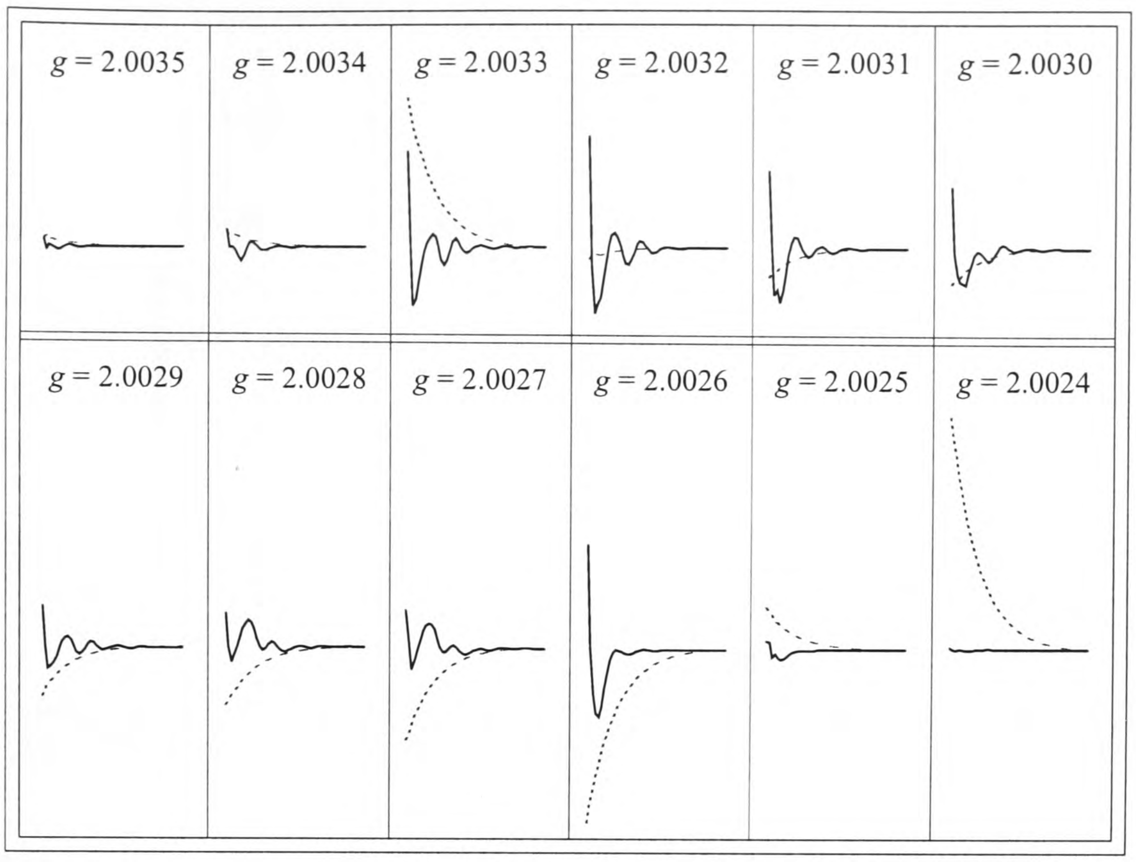

Figure 5.13: Comparison of the in- (dotted) and out-of-phase (solid) time domain echo signals for the g-values considered in this chapter. In-phase signals are shown at *one-third* of their actual intensity. The x-axis in each block is the delay time, τ. All spectra have been subjected to EXORCYCLE phase cycling.

confidence that for the majority of g-values studied, despite the in-phase signal being in general of greater amplitude than that out-of-phase, it is unlikely to be large enough to totally obscure the desired signal from this experiment. The out-of-phase signals corresponding to the values of g_{eff} in the centre of the overlap region are easily the most intense, and for the most part this is where the lowest intensity in-phase echoes are seen.

It is also of use to look at the individual components of the EXORCYCLE spectra at a particular g-value, as these are the signals which will be observed on the oscilloscope during the experiment. These signals could be calculated for any of the g-values used, and in Figure 5.14 (on the following page) they are shown for $g_{\text{eff}} = 2.0028$. With the exception of the very large peaks at the start of each spectrum, it seems unlikely that the difference in the in- and out-of-phase signals will be of a nature which could imply that the out-of-phase ESEEM data cannot be recorded, and that it should be possible to correctly set the phase of the detector so that the out-of-phase signal can be accurately measured.

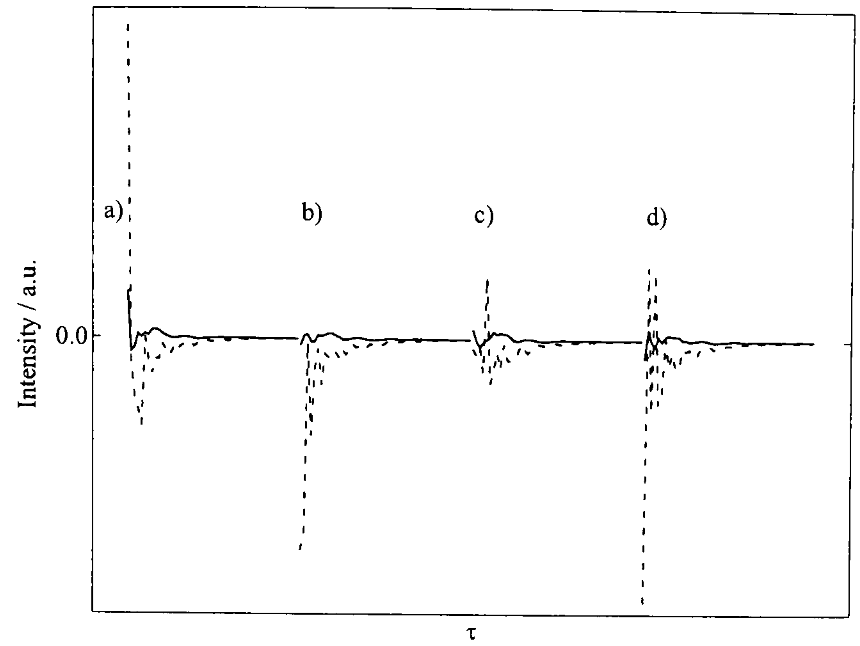

Figure 5.14: g_{eff} = 2.0028. Plots a) – d) show the four components of the ESEEM in the EXORCYCLE. The dotted lines give the in-phase and the solid lines the out-of-phase time domain spectra.

Field Swept Echoes at W-band

If the phase of the W-band spectrometer is correctly chosen, then since selective excitation is used, it should be possible to record an in-phase field swept echo which is a reasonable approximation to the TREPR spectrum obtained at this frequency. Such a TREPR spectrum has previously been recorded for $P^+Q_A^-$ in deuterated Zn^{2+}-substituted *Rb. sphaeroides* [90, 118]. In a pulsed EPR experiment, the field swept echo is recorded by keeping the value of τ in the ESEEM pulse sequence constant, and stepping the B_0 field strength. The program used to calculate W-band ESEEM spectra was also able to simulate the field swept echoes. Since the in-phase echo after the EXORCYCLE phase cycling is unmodulated (Figure 5.13), apart from at the very start of the trace, the value of τ chosen does not affect the form of the field swept echo, only its overall amplitude, and in the simulation performed, $\tau = 500$ ns. The phase cycled in-phase field swept echo is shown in Figure 5.15 (overleaf). It was calculated in the absence of hyperfine line-broadening, and gave the sharp signal seen. This does have the same shape as recorded TREPR signals. If this field swept trace could be reproduced experimentally, it could be used to check that the spectrometer phase is correct, so that the ESEEM experiment can proceed.

The out-of-phase field swept echo can also be calculated or measured. This trace is less useful, since the out-of-phase echo is modulated and the shape of the field swept echo is subsequently highly dependent upon the value of τ chosen. However, the trace can be used to show how much weaker the out-of-phase signal is likely to be than the in-phase echo. The out-of-phase field swept echo calculated with $\tau = 500$

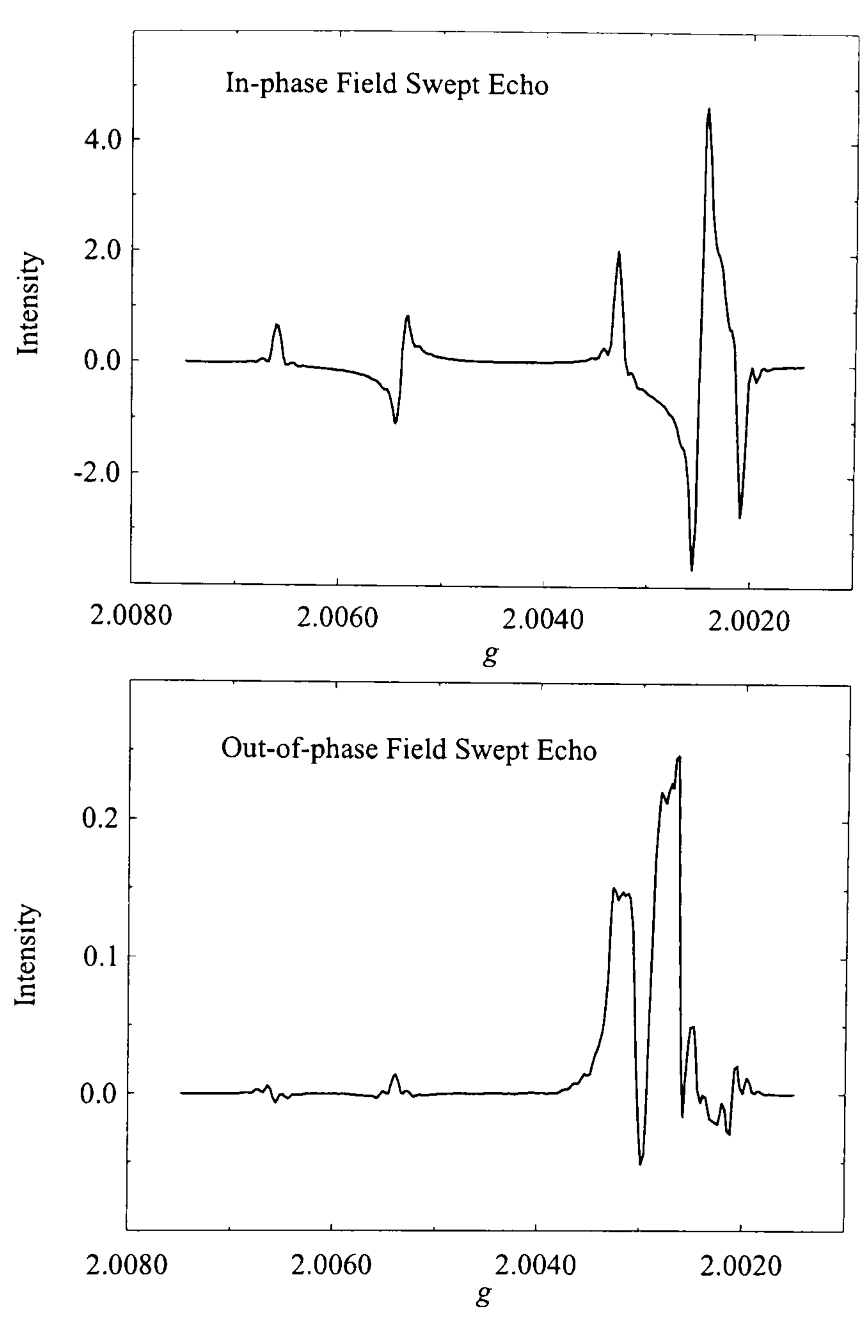

Figure 5.15: In- and out-of-phase field swept echoes for $P^+Q_A^-$. The value of τ used is 500 ns and the spectra have been calculated for field positions corresponding to $g = 2.0015$ – $g = 2.0075$. The top spectrum resembles the TREPR spectrum taken for this radical pair at 95 GHz [90, 118].

ns is shown in Figure 5.15. As would be expected, it shows regions of maximum intensity for g between 2.0024 and 2.0035, and is approximately twenty times less intense than the in-phase spectrum.

5.4.2 Future Echo Modulation Experiments at W-band

The simulations of modulated echoes at W-band for $P^+Q_A^-$ in *Rb. sphaeroides* performed in this chapter have used a standard ESEEM pulse sequence and have required the orientations of the radicals to be such that the resonant frequencies of P^+ and Q_A^- are very similar. However, if it were technically possible for selective mw pulses to be applied sequentially at different frequencies, then echo modulation would be observable from radical pair orientations where the effective g-values of the two radicals are rather different.

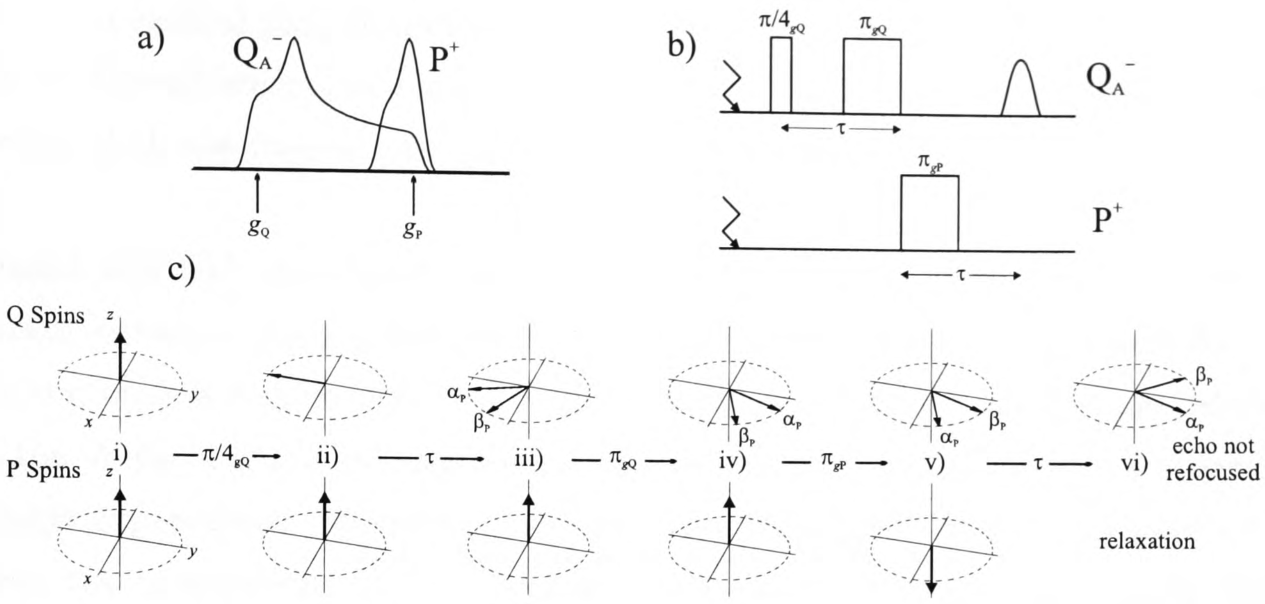

Figure 5.16: Details of a selective ESEEM experiment to study the echo modulation in Q_A^- due to spin-spin coupling to P^+. a) the field positions at which the pulses in the sequence shown in b) are applied. The first and second pulses effects only the Q-spins with the correct g-value. The third pulse will swap the P-spins to which these may be coupled, hence as shown in c) the echo at time 2τ is not refocused.

Consider the radical pair $P^+Q_A^-$, oriented such that the resonant frequencies of the two radicals lie in the positions shown in the EPR spectrum in Figure 5.16a. This particular radical pair orientation would not give rise to any significant echo modulation in the W-band experiment discussed earlier. However, under the pulse sequence also given in this figure, modulation could be observed. In this experiment the three pulses shown in Figure 5.16b are applied. The first is a $\pi/4$-pulse applied to Q_A^-, and, after a delay of τ, a π-pulse is applied at the same frequency. Immediately after this, the P^+ spins are flipped by a frequency-shifted π-pulse. Since P^+ and Q_A^- are coupled via D and J, the Q-spins are not refocused and echo modulation is observed. In principle, different areas of the spectrum could be investigated if either the frequency of the microwaves, or the B_0 field were shifted.

If the rapid change of microwave frequency required for this pulse sequence can be achieved experimentally, then this type of experiment could be used to detect echo modulation from particular radical pair orientations wherever the EPR frequencies of the individual radicals lie, thereby extending the W-band ESEEM experiment with selective pulses discussed in this chapter.

5.5 Conclusion

This chapter has concentrated upon the ESEEM of radical pairs obtained from an experiment performed at high-field. The increased resolution of the g-tensors at 95 GHz, and the narrow band-width of the applied microwave pulses, mean that the number of radical pair orientations for which echo modulation can occur is far less than at X-band where, to a good approximation, the ESEEM spectrum is a powder average of all the radical pair orientations in the sample.

W-band ESEEM can therefore be used, as demonstrated, to show a direct correlation between the dipolar interaction and the $\boldsymbol{g}$-tensors of the radicals. This information is available if both X-band ESEEM and TREPR spectra are recorded, but the W-band ESEEM experiment can correlate the information they give within a single experiment. Moreover, calculation of the "loop" diagrams ($D(g)$), which reflect the orientations of the radicals and the respective strength of the dipolar coupling, can be used to predict the positions of the resonances expected in this experiment.

The experiments described in this chapter have been attempted by Drs. Stephan Zech and Robert Bittl in the group of Prof. W. Lubitz at the Technische Universität, Berlin. Although at this stage only those experiments giving information for radical pair orientations in which the resonance positions of P^+ and Q_A^- are equal are possible, in the future, as the technology and the theory advance, it may be possible to use ESEEM at W-band for a range of applications.

Appendix A

Listings

A.1 Fortran 77 Programs

A.1.1 echo3d2.f

```
c...................................................................

c       program echo3d2.f

c       C.E. Fursman, November 1996

c       adapted from echo1.f (PJH)

c       Calculates the ESEEM spectrum of a spin-correlated radical pair
c       and its Fourier transform. The simulation includes a single
c       spin-1/2 nucleus on one of the radicals. Valid only when
c       infinitely hard pulses are assumed. Theory given in Chapter 2.

        program echo3d2

        implicit double precision (a-h,o-z)
        double precision echo(4096), time(4096)
        double complex y(4096)
        double precision j,j_gauss
        double precision k
        character*32 fn

c       Constants

        pi = 3.1415926535d0
        half_pi = 0.5d0*pi
        gauss_to_hertz = 2.0d0*pi*2.8d6
        one_third = 1.0d0/3.0d0

c       Default values

        j_gauss = 0.0d0
        dipolar_gauss = -1.4d0
        mtime = 10
        ntheta = 50
        sp_width_gauss = 10.0d0
        width_gauss = 0.05
        psi = 0.0d0
        nphi = 100

c       Get parameters

        call gdd('Hyperfine coupling constant (Gauss) ?',aconst_gauss)
        call gdd('Nuclear Zeeman interaction ?',wnuc_gauss)
        call gdd('Angle xi (Degrees) ?',psi)
        call gdd('Exchange interaction (Gauss)          ?',j_gauss)
        call gdd('Dipolar  interaction (Gauss)          ?',dipolar_gauss)
        call gid('Number of times = 2**n.  n =          ?',mtime)
        call gid('Number of theta points                ?',ntheta)
        call gdd('Linebroadening (Gauss)                ?',width_gauss)
        call gdd('Spectral width (Gauss)                ?',sp_width_gauss)

c Get file names

        call gs('File for eseem                         ?',fn)
        open(3,file=fn)
        call gs('File for  FT spectrum                  ?',fn)
        open(2,file=fn)

c       Conversions, etc.
```

```
      aconst=aconst_gauss*gauss_to_hertz
      wnuc=wnuc_gauss*gauss_to_hertz
      j = j_gauss*gauss_to_hertz
      dipolar = dipolar_gauss*gauss_to_hertz
      width = width_gauss*gauss_to_hertz
      ntime = 2**mtime
      sp_width = sp_width_gauss*2.8d6
      delta_t = 1.0d0/sp_width
      time_max = delta_t*(ntime-1.0d0)
      psi = psi*3.1415926535d0/180.0d0

c     Calculate ESEEM spectrum from the given parameters. Uses an
c     intergration over the whole sphere.

      spsi = dsin(psi)
      cpsi = dcos(psi)

      do 2 itime=1,ntime
      echo(itime) = 0.0d0
      time(itime) = (itime-1.d0)*delta_t

      do 1 itheta=1,ntheta
      theta = (itheta-1.d0)*pi/(ntheta-1.d0)
      stheta = dsin(theta)
      ctheta = dcos(theta)

      do 11 iphi=1,nphi
      phi = (iphi-1.d0)*2*pi/(nphi-1.d0)
      stheta = dsin(theta)
      ctheta = dcos(theta)
      sphi = dsin(phi)
      cphi = dcos(phi)

      cen = (stheta*sphi*spsi + ctheta*cpsi)
      sen = dsqrt(1.0d0 - cen*cen)
      a=(3.0d0*cen*cen - 1)*aconst
      b=3.0d0*cen*sen*aconst
      d = dipolar*(ctheta*ctheta - one_third)
      walpha=sqrt((0.5d0*a - wnuc)*(0.5d0*a - wnuc) + (0.5d0*b)*(0.5d0*b))
      wbeta=sqrt((0.5d0*a + wnuc)*(0.5d0*a + wnuc) + (0.5d0*b)*(0.5d0*b))
      k=0.5d0*(b*wnuc/(walpha*wbeta))*(b*wnuc/(walpha*wbeta))
      f = 2.0d0*(j-d)
      freq_mod = f
      freq_mod1= f + walpha
      freq_mod2= f - walpha
      freq_mod3= f + wbeta
      freq_mod4= f - wbeta
      freq_mod5= f + (walpha + wbeta)
      freq_mod6= f - (walpha + wbeta)
      freq_mod7= f + (walpha - wbeta)
      freq_mod8= f - (walpha - wbeta)
      echo(itime) = echo(itime) +
     & ((1.0d0/32.0d0)*(16.0d0 - 8.0d0*k)*dsin(freq_mod*time(itime))
     & + (k/8.0d0)*dsin(freq_mod1*time(itime))
     & + (k/8.0d0)*dsin(freq_mod2*time(itime))
     & + (k/8.0d0)*dsin(freq_mod3*time(itime))
     & + (k/8.0d0)*dsin(freq_mod4*time(itime))
     & - (k/16.0d0)*dsin(freq_mod5*time(itime))
     & - (k/16.0d0)*dsin(freq_mod6*time(itime))
     & - (k/16.0d0)*dsin(freq_mod7*time(itime))
     & - (k/16.0d0)*dsin(freq_mod8*time(itime)))*stheta
 11   continue

 1    continue

 2    continue

c     Fourier transform

      do 5 itime = 2, ntime, 2
      echo(itime) = -echo(itime)
 5    continue

      do 3 itime = 1, ntime
      echo(itime) = echo(itime)*dexp(-time(itime)*pi*width)
      write(3,*)real(time(itime)),real(echo(itime))
      y(itime) = dcmplx(echo(itime),0.0d0)
 3    continue

      call fft(mtime,y,1.d0)

c     Output
      m = ntime/2+1
      do 4 itime=2,ntime
      freq = (itime - m)/time_max
      write(2,*)real(freq/2.8d6),real(dimag(y(itime)))
 4    continue

      stop
      end
```

```
c..................................................................

c      Fourier transform

       subroutine fft(kk,a,sn)
       implicit double precision (a-h,o-z)
       double complex a(8192), b, eq, el, en
       integer inu(14)
       data inu/1,2,4,8,16,32,64,128,256,512,1024,2048,4096,8192/
       n = 2**kk
       n2 = n/2
       e = sn*3.1415926536d0
       j = 1 + n2
       do 1 i=2,n
       k = kk - 1
       m = n2
       if(i-j) 2, 4, 4
2      b = a(j)
       a(j) = a(i)
       a(i) = b
4      l = j-m
       if(l) 5, 5, 3
3      j=l
       m = inu(k)
       k = k-1
       if(k)5, 5, 4
5      j = j + m
1      continue
       k = 1
6      if(k-n) 9,8,8
9      l = k + k
       c2 = dcos(e)
       eq =dcmplx(c2,dsin(e))
       el = dcmplx(1.d0, 0.d0)
       c2 = c2+c2
       do 10 m=1,k
       do 7 i=m,n,l
       j = i + k
       b = el*a(j)
       a(j) = a(i) - b
       a(i) = a(i) + b
7      continue
       en = eq*c2 - el
       x = dble(en)
       y = dimag(en)
       en = en*0.5d0*(3.d0- x*x - y*y)
       el = eq
       eq = en
10     continue
       k = l
       e = 0.5d0*e
       go to 6
8      continue
       return
       end

c..................................................................
```

A.1.2 spin-echo.f

```
c..................................................................

c      program spin-echo.f

c      C.E. Fursman, February 1999

c      adapted from spin-echo.f (PJH)

c      Calculates the ESEEM spectrum from a radical pair, and its Fourier
c      transform. Pulses of any length and any angle can be used. The
c      program for evolution of the spins during long pulses. In Chapter
c      3 this program is used to calculate the ESEEM of a strongly
c      coupled radical pair with thernal equilibrium populations, at
c      X-band (program shown).

c      In Chapter 5 it is adapted to simulate spectra from a SCRP at
c      95 GHz.

c      Program includes the EXORCYCLE phase cycling procedure, and the
c      effect of unresolved isotropic hyperfine couplings.


       program spin_echo

       implicit double precision (a-h,o-z)

       common / one / dipolar, exchange
       common / comran / icr, jcr
```

```
        common / constants / pi
        common / bits / czero, eye
        common / times / t45, t90, t180
        common / ops /  e0(4), v0(4,4), v0_transpose(4,4),
     &         pulse45_0(4,4), pulse45_0_inverse(4,4),
     &         pulse45_2(4,4), pulse45_2_inverse(4,4),
     &         pulse45_1(4,4), pulse45_1_inverse(4,4),
     &         pulse45_3(4,4), pulse45_3_inverse(4,4),
     &         pulse90(4,4), pulse90_inverse(4,4),
     &         pulse180(4,4), pulse180_inverse(4,4),
     &         sabxe(4,4), sabye(4,4), sabze(4,4),
     & saz(4,4), sbz(4,4), sasb(4,4), sazsbz(4,4),
     & sabx(4,4),  saby(4,4),  sabz(4,4)

        double precision signal_0(512), signal_1(512), signal_2(512),
     &  signal_3(512)
        double precision spec_0(1024), spec_1(1024), spec_2(1024),
     &  spec_3(1024)
        double precision tau(512)
        double precision time1(512), time2(512)
        double precision theta(513), phi(513), wth(513), wph(513)
        double precision sth(513), cth(513), sph(513), cph(513)
        double precision m_0(3), m_1(3), m_2(3), m_3(3), nb(3)
        double precision new_delay

        double complex rho_0(4,4), rho_1(4,4), rho_2(4,4), rho_3(4,4)
        double complex rho_0i(4,4), rho_1i(4,4), rho_2i(4,4), rho_3i(4,4)
        double complex rho_i(4,4)
        double complex czero, eye
        double complex pulse45_0, pulse45_0_inverse
        double complex pulse45_2, pulse45_2_inverse
        double complex pulse45_1, pulse45_1_inverse
        double complex pulse45_3, pulse45_3_inverse
        double complex pulse90, pulse90_inverse
        double complex pulse180, pulse180_inverse

        real smax, rspec(1024)

        integer*4 icr, jcr

        character*32 fn
        character*1 plot, hfc, cycle

c-------------------------------------------------

        icr = 5763476
        jcr =-3274654

c-------------------------------------------------

 1000   format(1x, 4e12.5)

        call gs(' Output file for echo modulation    ?',fn)
        open(2,file=fn)

        call gs(' Output file for echo spectrum      ?',fn)
        open(3,file=fn)

c       call gs('Output file for negative taus      ?',fn)
c       open(4,file=fn)

        write(6,*)

c-------------------------------------------------

        off_res_cutoff = 100.0d0
        call gdd(' Multiple of w1 beyond which off-res effects are ignored  ?',
     & off_res_cutoff)
        write(6,*)

c-------------------------------------------------

        width_P = 3.30d0
        width_Q = 3.00d0
        call gs(' Include hyperfine couplings (y/n)  ?', hfc)
        if(hfc.eq.'y')then
           write(6,*)
           call gdd('  Linewidth for P (Gauss)            ?',width_P)
           call gdd('  Linewidth for Q (Gauss)            ?',width_Q)
        end if
        write(6,*)

c-------------------------------------------------

        call gs(' Exorcycle (y/n)  ?', cycle)
        write(6,*)

c-------------------------------------------------

        call two_spin
        call get_parameters(w, field, w1, dtau, t2, ntau, nspec, nth,
nph, plot)
```

```
        write(6,1001)t45*1.0d9, t180*1.0d9
 1001   format(//,1x,   ' flip1 degree pulse = ', 1pe12.4, ' ns', /,
     &  1x,           ' flip2 degree pulse = ',    e12.4, ' ns', /)

        write(6,1002)field
 1002 format(1x,   ' field  =  ',1pe12.6, /)

c------------------------------------------------
c       integration over the half sphere.

        theta_step = 0.5*pi/(nth-1.0)
        phi_step   = 2.0*pi/(nph-1.0)

        do ith=2,nth-1,2
        wth(ith) = 4.0
        end do
        do ith=3,nth-2,2
        wth(ith) = 2.0
        end do
        wth(1) = 1.0
        wth(nth) = 1.0
        do ith=1,nth
        theta(ith) = (ith-1.0)*theta_step
        sth(ith) = dsin(theta(ith))
        cth(ith) = dcos(theta(ith))
        wth(ith) = wth(ith)*theta_step*sth(ith)/3.0
        end do

        do iph=2,nph-1,2
        wph(iph) = 4.0
        end do
        do iph=3,nph-2,2
        wph(iph) = 2.0
        end do
        wph(1) = 1.0
        wph(nph) = 1.0
        do iph=1,nph
        phi(iph) = (iph-1.0)*phi_step
        sph(iph) = dsin(phi(iph))
        cph(iph) = dcos(phi(iph))
        wph(iph) = wph(iph)*phi_step/3.0
        end do

c------------------------------------------------
c       calculation of the delays between long pulses.

        do 4 itau = 1,ntau
        signal_0(itau) = 0.0
        signal_1(itau) = 0.0
        signal_2(itau) = 0.0
        signal_3(itau) = 0.0
        tau(itau) = (itau-1.0)*dtau
        time1(itau) = tau(itau) - 0.5*t45 - 0.5*t180
        time2(itau) = tau(itau) - 0.5*t180
 4      continue

        new_delay = 132.0d-9 - 0.5*t180

c------------------------------------------------
c       Calculation of echo without EXORCYCLE

        if(cycle.eq.'n')then

        do 15 ith = 1,nth

        do 15 iph = 1,nph

           weight = wth(ith)*wph(iph)

           nb(1) = sth(ith)*cph(iph)
           nb(2) = sth(ith)*sph(iph)
           nb(3) = cth(ith)

           call calc_parameters(field, nb, wP, wQ, dzz, aj, hfc, width_P, width_Q)

           wP_off = dabs(w-wP)/w1
           wQ_off = dabs(w-wQ)/w1
           if(wP_off.gt.off_res_cutoff .or. wQ_off.gt.off_res_cutoff) go to 15

           call operators(w, wP, wQ, aj, dzz, w1)

           call singlet_state(rho_i,v0, v0_transpose)

           call pulse(rho_i, rho_0i, pulse45_0, pulse45_0_inverse)

           do 11 itau=1,ntau

              do i=1,4
              do j=1,4
              rho_0(i,j)=rho_0i(i,j)
              end do
```

```
              end do
c             call echo(rho_0, e0, tau(itau), tau(itau), pulse180)
              call echo(rho_0, e0, time1(itau), time2(itau), pulse180)


              call detection(rho_0, sabxe, sabye, sabze, m_0)

              signal_0(itau) = signal_0(itau) + m_0(1)*weight

 11    continue

 15      continue

      end if

c-----------------------------------------------------

c       Calculation of echo with EXORCYCLE

      if(cycle.eq.'y')then

        do 25 ith = 1,nth

        do 25 iph = 1,nph

           weight = wth(ith)*wph(iph)

           nb(1) = sth(ith)*cph(iph)
           nb(2) = sth(ith)*sph(iph)
           nb(3) = cth(ith)

           call calc_parameters(field, nb, wP, wQ, dzz, aj, hfc, width_P,
width_Q)

           wP_off = dabs(w-wP)/w1
           wQ_off = dabs(w-wQ)/w1
           if(wP_off.gt.off_res_cutoff .or. wQ_off.gt.off_res_cutoff) go to 25

           call operators(w, wP, wQ, aj, dzz, w1)

           call singlet_state(rho_i,v0, v0_transpose)

           call pulse(rho_i, rho_0i, pulse45_0, pulse45_0_inverse)
           call pulse(rho_i, rho_2i, pulse45_2, pulse45_2_inverse)
           call pulse(rho_i, rho_1i, pulse45_1, pulse45_1_inverse)
           call pulse(rho_i, rho_3i, pulse45_3, pulse45_3_inverse)

           do 21 itau=1,ntau

              do i=1,4
              do j=1,4
              rho_0(i,j)=rho_0i(i,j)
              rho_1(i,j)=rho_1i(i,j)
              rho_2(i,j)=rho_2i(i,j)
              rho_3(i,j)=rho_3i(i,j)
              end do
      end do

c             call echo(rho_0, e0, tau(itau), tau(itau), pulse180)
c             call echo(rho_1, e0, tau(itau), tau(itau), pulse180)
c             call echo(rho_2, e0, tau(itau), tau(itau), pulse180)
c             call echo(rho_3, e0, tau(itau), tau(itau), pulse180)

              call echo(rho_0, e0, time1(itau), time2(itau), pulse180)
              call echo(rho_1, e0, time1(itau), time2(itau), pulse180)
              call echo(rho_2, e0, time1(itau), time2(itau), pulse180)
              call echo(rho_3, e0, time1(itau), time2(itau), pulse180)


              call detection(rho_0, sabxe, sabye, sabze, m_0)
              call detection(rho_1, sabxe, sabye, sabze, m_1)
              call detection(rho_2, sabxe, sabye, sabze, m_2)
              call detection(rho_3, sabxe, sabye, sabze, m_3)

              signal_0(itau) = signal_0(itau) - m_0(2)*weight
              signal_1(itau) = signal_1(itau) - m_1(1)*weight
              signal_2(itau) = signal_2(itau) + m_2(2)*weight
              signal_3(itau) = signal_3(itau) + m_3(1)*weight

 21    continue

 25     continue

      end if

c-----------------------------------------------------
c       Write ESEEM to file

        write(6,1004)
 1004   format(//)
```

```
1003   format(1x,i3,1pe12.4,2e12.4)

       do itau=1,ntau
       if(time1(itau).lt.0.0d0 .or. time2(itau).lt.0.0d0)
     &      write(6,1003)itau, tau(itau), time1(itau), time2(itau)
       end do

       if(cycle.eq.'y')then

          do itau=1,ntau
          rspec(itau) = 0.25*sngl(signal_0(itau) + signal_1(itau)
     &              + signal_2(itau) + signal_3(itau))
        end do

          do itau=1,ntau
          write(2,1005)sngl(tau(itau)), rspec(itau),
     &       sngl(signal_0(itau)), sngl(signal_1(itau)),
     &      sngl(signal_2(itau)), sngl(signal_3(itau))
          end do

       else

          do itau=1,ntau
          write(2,1005)sngl(tau(itau)), sngl(signal_0(itau))
          end do

       end if

1005   format(1x, 6e14.5)

       write(6,1004)
       close (2)

c--------------------------------------------------
c      Plot ESEEM on screen

       if(plot.eq.'y')then
       smax = 0.0
       do itau=1,ntau
       if(abs(rspec(itau)).gt.smax)smax=abs(rspec(itau))
       end do
       call xgraph(rspec, smax, ntau, 'ESEEM')
       end if

c--------------------------------------------------
c      Fourier transform ESEEM, write to file &
c      plot on screen

       if(cycle.eq.'y')then

          call spectrum(signal_0, spec_0, ntau, nspec, dtau, t2)
          call spectrum(signal_1, spec_1, ntau, nspec, dtau, t2)
          call spectrum(signal_2, spec_2, ntau, nspec, dtau, t2)
          call spectrum(signal_3, spec_3, ntau, nspec, dtau, t2)

       else

          call spectrum(signal_0, spec_0, ntau, nspec, dtau, t2)

       end if

       if(cycle.eq.'y')then

          do k=1,nspec
          rspec(k) = 0.25*sngl(spec_0(k) + spec_1(k) + spec_2(k) + spec_3(k))
          end do

          do k=1,nspec
          freq = (k-nspec*0.5-1.0)/(nspec*dtau)
          write(3,1005) sngl(freq/2.8e6), rspec(k),
     &       sngl(spec_0(k)), sngl(spec_1(k)),
     &       sngl(spec_2(k)), sngl(spec_3(k))
          end do

       else

          do k=1,nspec
          freq = (k-nspec*0.5-1.0)/(nspec*dtau)
          write(3,1005) sngl(freq/2.8e6), sngl(spec_0(k))
          end do

       end if

       close (3)

c--------------------------------------------------

       if(plot.eq.'y')then
       smax = 0.0
       do k=1,nspec
       if(abs(rspec(k)).gt.smax)smax=abs(rspec(k))
       end do
```

```
        call xgraph(rspec, smax, nspec, 'ESEEM spectrum')
        end if

        end
c.....................................................................

        subroutine get_parameters(w, field, w1, dtau, t2, ntau, nspec, nth,
nph, plot)

c       Values of parameters are input from screen

        implicit double precision (a-h,o-z)

        common / one / dipolar, exchange
        common / constants / pi
        common / times / t45, t90, t180


        character*1 plot

c       flip1 = angle of first x-pulse (Degrees)
c       flip2 = angle of second x-pulse (Degrees)
c       w     =  transmitter frequency (Hz)
c       field =  field at centre of sectrum (G)
c       w1    =  microwave field strength (Hz)
c       dtau  = interval between tau values (ns)
c       t2    =  echo damping time (ns)
c       ntau  =  number of tau values <=512
c       nth   =  number of theta values <=513
c       nph   =  number of phi values <=513

        dipolar = -3.9d0
        exchange = 5.0d0

        g_centre = 2.0044
        pi = 3.1415926535
        two_pi = pi+pi

        flip1= 45
        flip2= 180
        w    = 9.0d9
        w1   = 300.0d6
        dtau = 10.0d0
        t2   = 500.0d0
        ntau = 256
        nspec= 512
        nth  = 513
        nph  = 513


        call gdd('  D (Gauss) ',dipolar)
        call gdd('  J (Gauss) ',exchange)
        call gdd('  flip1  (Degrees)            ',flip1)
        call gdd('  flip2  (Degrees)    ',flip2)
        call gdd('  w     (Hz)          ',w)
        call gdd('  g_centre           ',g_centre)

        field = 2.0*pi*w/(8.7965d6*g_centre)

        call gdd('  w1    (Hz)          ',w1)
        call gdd('  dtau  (ns)          ',dtau)
        call gid('  ntau  (<=512)       ',ntau)

        write(6,1000)(ntau-1.0)*dtau
 1000   format(/,2x,'max time = ',1pe12.4,' ns',/)

        call gdd('  t2    (ns)          ',t2)
        call gid('  nspec (<=1024, >=2*ntau) ',nspec)
        call gid('  nth   (<=513)       ',nth)
        call gid('  nph   (<=513)       ',nph)

c       call gs ('  Plot on screen (y/n)  ?      ',plot)
        plot = 'n'

        w  = w*two_pi
        w1 = w1*two_pi
        dtau = dtau*1.0d-9
        t2 = t2*1.0d-9

        t45  = flip1*pi/(180.0d0*w1)
        t180 = flip2*pi/(180.0d0*w1)

c       write(6,*) dipolar, exchange

        return
        end
c.....................................................................

        subroutine calc_parameters(field, nb, omegaP, omegaQ, dzz, aj,
     &         hfc, width_P, width_Q)
```

```
      implicit double precision (a-h,o-z)

      common / one / dipolar, exchange
      common /comran/ icr, jcr

      integer*4 icr, jcr

      double precision dirgPx(3), dirgPy(3), dirgPz(3), dirPQ(3), nb(3)

      character*1 hfc

c     data for the principle axes of the cofactors in question

      data dirgPx/  0.684045, 0.622189, -0.385722  /
      data dirgPy/  0.650863, -0.759349, -0.062335    /
      data dirgPz/  -0.329318, -0.208412, -0.924388    /
      data dirPQ/  -0.35199, 0.857429, 0.383676   /
      data gQx,gQy,gQz /  2.00647, 2.00532, 2.00218  /
      data gPx,gPy,gPz /  2.00632, 2.00527, 2.00213  /

      one_third = 1.0/3.0
c     z = (Bohr magneton)*2*pi/(Planck's constant*10^4)
      z = 8.7965d6
      conv = z*field

c     calculation of the effective g-values and EPR frequencies

      call orthog(dirgPx,dirgPy,dirgPz)
      call cosine(nb,dirPQ,cosPQ)

      call cosine(nb,dirgPx,ax)
      call cosine(nb,dirgPy,ay)
      call cosine(nb,dirgPz,az)

      gP = dsqrt((gPx*ax)**2 + (gPy*ay)**2 + (gPz*az)**2)
      gQ = dsqrt((gQx*nb(1))**2 + (gQy*nb(2))**2 + (gQz*nb(3))**2)

      omegaP = gP*conv
      omegaQ = gQ*conv

c     standard deviation of HFC equals half width of gaussian distribution
      hfc_P = width_P*z
      hfc_Q = width_Q*z

      if(hfc.eq.'y')then
         omegaP = omegaP + rnm(0.0d0, hfc_P)
         omegaQ = omegaQ + rnm(0.0d0, hfc_Q)
      end if
c     write(6,*) dipolar, exchange

c     write(9,*)omegaP,omegaQ

      dzz = dipolar*(2.0*z)*(cosPQ**2 - one_third)
      aj  = exchange*(2.0*z)

      return
      end

c.................................................................

      subroutine operators(w, wa, wb, aj, dzz, w1)

c     Calculates operators etc.

      implicit double precision (a-h,o-z)

      common / constants / pi
      common / bits / czero, eye
      common / times / t45, t90, t180
      common / ops /  e0(4), v0(4,4), v0_transpose(4,4),
     &                pulse45_0(4,4), pulse45_0_inverse(4,4),
     &                pulse45_2(4,4), pulse45_2_inverse(4,4),
     &                pulse45_1(4,4), pulse45_1_inverse(4,4),
     &                pulse45_3(4,4), pulse45_3_inverse(4,4),
     &                pulse90(4,4), pulse90_inverse(4,4),
     &                pulse180(4,4), pulse180_inverse(4,4),
     &                sabxe(4,4), sabye(4,4), sabze(4,4),
     &          saz(4,4), sbz(4,4), sasb(4,4), sazsbz(4,4),
     &          sabx(4,4),  saby(4,4),  sabz(4,4)

      double precision h0(4,4), h1x(4,4), h1y(4,4)
      double precision e01_0(4), e01_2(4), e01_1(4), e01_3(4)

      double complex pulse45_0, pulse45_0_inverse
      double complex pulse45_2, pulse45_2_inverse
      double complex pulse45_1, pulse45_1_inverse
      double complex pulse45_3, pulse45_3_inverse
      double complex pulse90, pulse90_inverse
      double complex pulse180, pulse180_inverse
      double complex v01_0(4,4), v01_2(4,4), v01_1(4,4), v01_3(4,4)
      double complex h01_0(4,4), h01_2(4,4), h01_1(4,4), h01_3(4,4)
```

```
      double complex dummy(4,4)
      double complex czero, eye

c     h0 Hamiltonian without microwave field
c     h1 Microwave Hamiltonian
c     h01 Hamiltonian with microwave field

      do i=1,4
         do j=1,4
            h0(i,j) = wa*saz(i,j) + wb*sbz(i,j) - 2.0*aj*sasb(i,j) - w*sabz(i,j)
     &       + dzz*(3.0*sazsbz(i,j) - sasb(i,j))
             h1x(i,j) = w1*sabx(i,j)
             h1y(i,j) = w1*saby(i,j)
         end do
      end do

      call eigensystem_R(h0,e0,v0)

      do i=1,4
      do j=1,4
      v0_transpose(i,j) = v0(j,i)
      end do
      end do

      do i=1,4
      do j=1,4
      h0(i,j) = 0.0
      end do
      h0(i,i) = e0(i)
      end do

c     Transform h1 to eigenbasis of h0

      call matrix_multiply_RRR(v0_transpose, h1x, v0, h1x)
      call matrix_multiply_RRR(v0_transpose, h1y, v0, h1y)

      do i=1,4
         do j=1,4
            h01_0(i,j) = h0(i,j) + h1x(i,j)
            h01_2(i,j) = h0(i,j) - h1x(i,j)
            h01_1(i,j) = h0(i,j) + h1y(i,j)*eye
            h01_3(i,j) = h0(i,j) - h1y(i,j)*eye
         end do
      end do

      call eigensystem_C(h01_0,e01_0,v01_0)
      call eigensystem_C(h01_2,e01_2,v01_2)
      call eigensystem_C(h01_1,e01_1,v01_1)
      call eigensystem_C(h01_3,e01_3,v01_3)

c     Propagators for 45, 90 and 180 degree pulses

      call propagator(e01_0, v01_0, pulse45_0,  pulse45_0_inverse,  t45)
      call propagator(e01_2, v01_2, pulse45_2,  pulse45_2_inverse,  t45)
      call propagator(e01_1, v01_1, pulse45_1,  pulse45_1_inverse,  t45)
      call propagator(e01_3, v01_3, pulse45_3,  pulse45_3_inverse,  t45)
      call propagator(e01_0, v01_0, pulse180, dummy, t180)


c     Transform operators into eigenbasis of h0

      call matrix_multiply_RRR(v0_transpose, sabx, v0, sabxe)
      call matrix_multiply_RRR(v0_transpose, saby, v0, sabye)
      call matrix_multiply_RRR(v0_transpose, sabz, v0, sabze)

 1000 format(1x,8e12.5)

      return
      end

c.........................................................................

      subroutine two_spin

c     Set up spin operators

      implicit double precision (a-h,o-z)

      common / constants / pi
      common / bits / czero, eye
      common / ops /  e0(4), v0(4,4), v0_transpose(4,4),
     &               pulse45_0(4,4), pulse45_0_inverse(4,4),
     &               pulse45_2(4,4), pulse45_2_inverse(4,4),
     &               pulse45_1(4,4), pulse45_1_inverse(4,4),
     &                pulse45_3(4,4), pulse45_3_inverse(4,4),
     &               pulse90(4,4), pulse90_inverse(4,4),
     &                pulse180(4,4), pulse180_inverse(4,4),
     &                sabxe(4,4), sabye(4,4), sabze(4,4),
     &        saz(4,4), sbz(4,4), sasb(4,4), sazsbz(4,4),
     &        sabx(4,4),  saby(4,4),  sabz(4,4)

      double complex czero, eye
```

```
      double complex pulse45_0, pulse45_0_inverse
      double complex pulse45_2, pulse45_2_inverse
      double complex pulse45_1, pulse45_1_inverse
      double complex pulse45_3, pulse45_3_inverse
      double complex pulse90, pulse90_inverse
      double complex pulse180, pulse180_inverse

      eye  = dcmplx(0.0, 1.0)
      czero = dcmplx(0.0, 0.0)

      do 1 i=1,4
      do 1 j=1,4
      saz(i,j) =  0.0
      sbz(i,j) =  0.0
      sasb(i,j) =  0.0
      sazsbz(i,j) =  0.0
      sabx(i,j) =  0.0
      saby(i,j) =  0.0
      sabz(i,j) =  0.0
1     continue

      saz(1,1) = +0.5
      saz(2,2) = +0.5
      saz(3,3) = -0.5
      saz(4,4) = -0.5

      sbz(1,1) = +0.5
      sbz(2,2) = -0.5
      sbz(3,3) = +0.5
      sbz(4,4) = -0.5

      sasb(1,1) = +0.25
      sasb(2,2) = -0.25
      sasb(3,3) = -0.25
      sasb(4,4) = +0.25
      sasb(2,3) = +0.5
      sasb(3,2) = +0.5

      sazsbz(1,1) = +0.25
      sazsbz(2,2) = -0.25
      sazsbz(3,3) = -0.25
      sazsbz(4,4) = +0.25

      sabx(1,2) = +0.5
      sabx(1,3) = +0.5
      sabx(2,4) = +0.5
      sabx(3,4) = +0.5
      sabx(2,1) = +0.5
      sabx(3,1) = +0.5
      sabx(4,2) = +0.5
      sabx(4,3) = +0.5

c     Imaginary part of saby

      saby(1,2) = -0.5
      saby(1,3) = -0.5
      saby(2,4) = -0.5
      saby(3,4) = -0.5
      saby(2,1) = +0.5
      saby(3,1) = +0.5
      saby(4,2) = +0.5
      saby(4,3) = +0.5

      sabz(1,1) = +1.0
      sabz(4,4) = -1.0

      return
      end

c.....................................................................

      subroutine pulse(rho1, rho2, prop, prop_inverse)

c      Effect of a pulse on a density matrix

c     prop = pulse propagator
c     prop_inverse = inverse of prop
c     rho1  = input  density matrix
c     rho2  = output density matrix

      implicit double precision (a-h,o-z)

      common / bits / czero, eye
      common / ops /  e0(4), v0(4,4), v0_transpose(4,4),
     &               pulse45_0(4,4), pulse45_0_inverse(4,4),
     &               pulse45_2(4,4), pulse45_2_inverse(4,4),
     &               pulse45_1(4,4), pulse45_1_inverse(4,4),
     &               pulse45_3(4,4), pulse45_3_inverse(4,4),
     &               pulse90(4,4), pulse90_inverse(4,4),
     &               pulse180(4,4), pulse180_inverse(4,4),
     &               sabxe(4,4), sabye(4,4), sabze(4,4),
     &          saz(4,4), sbz(4,4), sasb(4,4), sazsbz(4,4),
```

```
     &          sabx(4,4),  saby(4,4),  sabz(4,4)

      double complex rho1(4,4), rho2(4,4), prop(4,4), prop_inverse(4,4)
      double complex czero, eye
      double complex pulse45_0, pulse45_0_inverse
      double complex pulse45_2, pulse45_2_inverse
      double complex pulse45_1, pulse45_1_inverse
      double complex pulse45_3, pulse45_3_inverse
      double complex pulse90, pulse90_inverse
      double complex pulse180, pulse180_inverse

      call matrix_multiply_CCC(prop_inverse, rho1, prop, rho2)

      return
      end

c.................................................................

      subroutine propagator(e, v, prop, prop_inverse, time)

c     Calculates a pulse propagator

c     e     =  eigenvalues of hamiltonian, h0+h1
c     v     =  eigenvectors of hamiltonian, h0+h1
c     time  =  pulse duration
c     prop  =  propagator
c     prop_inverse  =  inverse of prop

      implicit double precision (a-h,o-z)

      common / bits / czero, eye

      double precision e(4)
c     double complex work(4,4)
      double complex v(4,4), v_dagger(4,4)
      double complex prop(4,4), prop_inverse(4,4), b(4,4)
      double complex czero, eye

      do 1 i=1,4
      do 4 j=1,4
      b(i,j) = czero
 4    continue
      b(i,i) = cdexp(eye*e(i)*time)
 1    continue

 1000 format(1x, 8e12.4)

c     write(6,*)'v in propagator'
c     write(6,1000)((v(i,j),i=1,4),j=1,4)

      do 2 i=1,4
      do 2 j=1,4
      v_dagger(i,j) = dconjg(v(j,i))
 2    continue

c     write(6,*)'v.v_dagger'
c     call matrix_multiply_CC(v, v_dagger, work)
c     write(6,1000)((work(i,j),i=1,4),j=1,4)

      call matrix_multiply_CCC(v, b, v_dagger, prop)

      do 3 i=1,4
      do 3 j=1,4
 3    prop_inverse(i,j) = dconjg(prop(j,i))

c     write(6,*)'prop.prop_inverse'
c     call matrix_multiply_CC(prop, prop_inverse, work)
c     write(6,1000)((work(i,j),i=1,4),j=1,4)

      return
      end


c.................................................................

      subroutine singlet_state(rho, v, v_transpose)

c     Initial density matrix for the RP

c     rho     =  singlet density matrix
c     v       =  eigenvectors of hamiltonian h0

      implicit double precision (a-h,o-z)

      common / bits / czero, eye

      double precision v(4,4), v_transpose(4,4)
      double complex czero, eye
      double complex rho(4,4)

      do 1 i=1,4
      do 1 j=1,4
```

```
      rho(i,j) =  czero
 1    continue

      rho(2,2) = dcmplx(0.25,0.0)
      rho(3,3) = dcmplx(0.25,0.0)
      rho(4,4) = dcmplx(0.50,0.0)

      call matrix_multiply_RCR(v_transpose, rho, v, rho)

      return
      end

c.....................................................................

      subroutine echo(rho, e, time1, time2, pulse180)

c     Effect of a refocussing sequence on a density operator
c     time1 - 180 - time2

c     pulse180 =  180 degree pulse propagator
c     rho      =  initial density matrix
c     rho1     =  final density matrix
c     e  =  eigenvalues of hamiltonian h0

      implicit double precision (a-h,o-z)

      common / bits / czero, eye

      double precision e(4)

      double complex czero, eye
      double complex rho(4,4), pulse180(4,4), u(4,4), uinv(4,4)
      double complex delay1(4,4), delay2(4,4)

      do 4 i=1,4
      do 4 j=1,4
      delay1(i,j) = czero
 4    delay2(i,j) = czero

      do 1 k=1,4
      delay1(k,k) = cdexp(eye*e(k)*time1)
      delay2(k,k) = cdexp(eye*e(k)*time2)
 1    continue

      call matrix_multiply_CCC(delay1, pulse180, delay2, u)

      do 3 i=1,4
      do 3 j=1,4
 3    uinv(i,j) = dconjg(u(j,i))

      call matrix_multiply_CCC(uinv, rho, u, rho)

      return
      end


c.....................................................................

      subroutine detection(rho, sabxe, sabye, sabze, m)

c     Calculates observable magnetizations

c     rho     =  density operator
c     sabxe   =  x-component of magnetization
c     sabye   =  y-component of magnetization
c     sabze   =  z-component of magnetization

      implicit double precision (a-h,o-z)

      common / bits / czero, eye

      double precision sabxe(4,4), sabye(4,4), sabze(4,4)
      double precision m(3)
      double complex rho(4,4)
      double complex czero, eye

      do 1 i=1,3
      m(i) = 0.0
 1    continue

      do 2 j=1,4
      do 2 k=1,4
      m(1) = m(1) + rho(j,k)*sabxe(k,j)
      m(2) = m(2) + rho(j,k)*sabye(k,j)*eye
      m(3) = m(3) + rho(j,k)*sabze(k,j)
 2    continue

      return
      end

c.....................................................................
```

```
      subroutine fft(kk,a,sn)

c     Fourier transform

      implicit double precision (a-h,o-z)

      double complex a(1024), b, eq, el, en
      integer inu(14)
      data inu/1,2,4,8,16,32,64,128,256,512,1024,2048,4096,8192/

      n = 2**kk
      n2 = n/2
      e = sn*3.1415926536
      j = 1 + n2
      do 1 i=2,n
      k = kk - 1
      m = n2
      if(i-j) 2, 4, 4
    2 b = a(j)
      a(j) = a(i)
      a(i) = b
    4 l = j-m
      if(l) 5, 5, 3
    3 j=l
      m = inu(k)
      k = k-1
      if(k)5, 5, 4
    5 j = j + m
    1 continue
      k = 1
    6 if(k-n) 9,8,8
    9 l = k + k
      c2 = dcos(e)
      eq =dcmplx(c2,dsin(e))
      el = dcmplx(1.0, 0.0)
      c2 = c2+c2
      do 10 m=1,k
      do 7 i=m,n,l
      j = i + k
      b = el*a(j)
      a(j) = a(i) - b
      a(i) = a(i) + b
    7 continue
      en = eq*c2 - el
      x = dble(en)
      y = dimag(en)
      en = en*0.5*(3.0- x*x - y*y)
      el = eq
      eq = en
   10 continue
      k = l
      e = 0.5*e
      go to 6
    8 continue
      return
      end


c.......................................................................

       subroutine spectrum(s, spec, ntau, nspec, dtau, t2)

c      Calculates spectrum from echo modulation

       implicit double precision (a-h,o-z)

       double precision s(512), spec(1024)
       double complex y(1024), czero

c      s =  echo modulation
c      ntau =  number of tau values
c      nspec =  number of points in spectrum
c      dtau =  tau increment
c      t2 =  echo damping time
c      y =  complex spectrum
c      spec =  real spectrum

       czero = dcmplx(0.0, 0.0)

       do 1 i=1,ntau
       tau = (i-1.0)*dtau
       y(i) = dcmplx(s(i)*exp(-tau/t2), 0.)
1      continue

       do 2 i=2,ntau,2
2      y(i) = -y(i)

       do 3 i=ntau+1, nspec
3      y(i) = czero

       kk=nint(log(real(nspec))/log(2.0))
       call fft(kk, y, -1.d0)
```

```
      do 4 i = 1, nspec
      spec(i) = dreal(y(i))
 4    continue

      return
      end

c.......................................................................

      subroutine eigensystem_R(h, e, v)

c     Eigenvalues & eigenvectors of a real symmetric matrix

      implicit double precision (a-h,o-z)

      double precision h(4,4), e(4), v(4,4)
      double precision dh(4,4), work(4)

      ifail = 0
      n = 4

      do 1 i=1,4
      do 1 j=1,4
      dh(i,j) = h(i,j)
 1    continue

      call f02abf(dh, n, n, e, v, n, work, ifail)

      return
      end

c.......................................................................

      subroutine eigensystem_C(h, e, v)

c     Eigenvalues & eigenvectors of a complex Hermitian matrix

      implicit double precision (a-h,o-z)

      double complex h(4,4), v(4,4)
c     double complex v_dagger(4,4), work(4,4)
      double precision hr(4,4), hi(4,4), e(4)
      double precision vr(4,4), vi(4,4), wk1(4), wk2(4), wk3(4)

      ifail = 0
      n = 4

      do i=1,4
      do j=1,4
      hr(i,j) = dreal(h(i,j))
      hi(i,j) = dimag(h(i,j))
      end do
      end do

      call f02axf(hr, n, hi, n, n, e, vr, n, vi, n, wk1, wk2, wk3, ifail)

      do i=1,4
      do j=1,4
      v(i,j) = dcmplx(vr(i,j), vi(i,j))
      end do
      end do

c     write(6,*)'v in eigensystem_C'
c     write(6,1000)((v(i,j),i=1,4),j=1,4)

c     do i=1,4
c     do j=1,4
c     v_dagger(i,j) = dconjg(v(j,i))
c     end do
c     end do

c     call matrix_multiply_CC(v, v_dagger, work)
c     write(6,*)'v.v_dagger'
c     write(6,1000)((work(i,j),i=1,4),j=1,4)
 1000 format(1x, 8e12.5)

      return
      end

c.......................................................................

c     subroutine eigensystem(h, evals, evecs)

c     Eigenvalues & eigenvectors of a real symmetric matrix

c     implicit double precision (a-h,o-z)

c     double precision h(4,4), evals(4), evecs(4,4)
c     double precision work(4)

c     ifail = 0
```

```
c       n = 4

c       do 1 i=1,4
c       do 1 j=1,4
c       evecs(i,j) = h(i,j)
c 1     continue

c       n = 4
c       np = 4

c       call tred2(evecs, n, np, evals, work)
c       call tqli(evals, work, n, np, evecs)

c       return
c       end

c.......................................................................

      subroutine tred2(a,n,np,d,e)
      implicit double precision (a-h,o-z)
      double precision  a(np,np),d(np),e(np)
      if(n.gt.1)then
        do 18 i=n,2,-1
          l=i-1
          h=0.
          scale=0.
          if(l.gt.1)then
            do 11 k=1,l
              scale=scale+dabs(a(i,k))
11          continue
            if(scale.eq.0.)then
              e(i)=a(i,l)
            else
              do 12 k=1,l
                a(i,k)=a(i,k)/scale
                h=h+a(i,k)**2
12            continue
              f=a(i,l)
              g=-sign(dsqrt(h),f)
              e(i)=scale*g
              h=h-f*g
              a(i,l)=f-g
              f=0.
              do 15 j=1,l
                a(j,i)=a(i,j)/h
                g=0.
                do 13 k=1,j
                  g=g+a(j,k)*a(i,k)
13              continue
                if(l.gt.j)then
                  do 14 k=j+1,l
                    g=g+a(k,j)*a(i,k)
14                continue
                endif
                e(j)=g/h
                f=f+e(j)*a(i,j)
15            continue
              hh=f/(h+h)
              do 17 j=1,l
                f=a(i,j)
                g=e(j)-hh*f
                e(j)=g
                do 16 k=1,j
                  a(j,k)=a(j,k)-f*e(k)-g*a(i,k)
16              continue
17            continue
            endif
          else
            e(i)=a(i,l)
          endif
          d(i)=h
18      continue
      endif
      d(1)=0.
      e(1)=0.
      do 23 i=1,n
        l=i-1
        if(d(i).ne.0.)then
          do 21 j=1,l
            g=0.
            do 19 k=1,l
              g=g+a(i,k)*a(k,j)
19          continue
            do 20 k=1,l
              a(k,j)=a(k,j)-g*a(k,i)
20          continue
21        continue
        endif
        d(i)=a(i,i)
        a(i,i)=1.
        if(l.ge.1)then
          do 22 j=1,l
```

```
            a(i,j)=0.
            a(j,i)=0.
22        continue
        endif
23    continue
      return
      end

c......................................................................

      subroutine tqli(d,e,n,np,z)
      implicit double precision (a-h,o-z)
      double precision d(np),e(np),z(np,np)
      if (n.gt.1) then
        do 11 i=2,n
          e(i-1)=e(i)
11      continue
        e(n)=0.
        do 15 l=1,n
          iter=0
1         do 12 m=l,n-1
            dd=dabs(d(m))+dabs(d(m+1))
            if (dabs(e(m))+dd.eq.dd) go to 2
12        continue
          m=n
2         if(m.ne.l)then
            if(iter.eq.30)pause 'too many iterations'
            iter=iter+1
            g=(d(l+1)-d(l))/(2.*e(l))
            r=dsqrt(g**2+1.)
            g=d(m)-d(l)+e(l)/(g+sign(r,g))
            s=1.
            c=1.
            p=0.
            do 14 i=m-1,l,-1
              f=s*e(i)
              b=c*e(i)
              if(dabs(f).ge.dabs(g))then
                c=g/f
                r=dsqrt(c**2+1.)
                e(i+1)=f*r
                s=1./r
                c=c*s
              else
                s=f/g
                r=dsqrt(s**2+1.)
                e(i+1)=g*r
                c=1./r
                s=s*c
              endif
              g=d(i+1)-p
              r=(d(i)-g)*s+2.*c*b
              p=s*r
              d(i+1)=g+p
              g=c*r-b
              do 13 k=1,n
                f=z(k,i+1)
                z(k,i+1)=s*z(k,i)+c*f
                z(k,i)=c*z(k,i)-s*f
13            continue
14          continue
            d(l)=d(l)-p
            e(l)=g
            e(m)=0.
            go to 1
          endif
15      continue
      endif
      return
      end

c......................................................................

      subroutine matrix_multiply_CC(a, b, c)

c     Multiply two double complex matrices:  a.b = c

      implicit double precision (a-h,o-z)

      common / bits / czero, eye

      double complex a(4,4), b(4,4), c(4,4), d(4,4)
      double complex czero, eye

      do 1 i=1,4
      do 1 j=1,4
      d(i,j) = czero
      do 1 k=1,4
      d(i,j) = d(i,j) + a(i,k)*b(k,j)
 1    continue

      do 2 i=1,4
```

```
      do 2 j=1,4
      c(i,j) = d(i,j)
 2    continue

      return
      end
c.................................................................

      subroutine matrix_multiply_RC(a, b, c)

c     Multiply a real matrix by a double complex matrix:  a.b = c

      implicit double precision (a-h,o-z)

      common / bits / czero, eye

      double complex b(4,4), c(4,4), d(4,4)
      double precision a(4,4)
      double complex czero, eye

      do 1 i=1,4
      do 1 j=1,4
      d(i,j) = czero
      do 1 k=1,4
      d(i,j) = d(i,j) + a(i,k)*b(k,j)
 1    continue

      do 2 i=1,4
      do 2 j=1,4
      c(i,j) = d(i,j)
 2    continue

      return
      end
c.................................................................

      subroutine matrix_multiply_CR(a, b, c)

c      Multiply a double complex matrix by a real matrix:  a.b = c

      implicit double precision (a-h,o-z)

      common / bits / czero, eye

      double complex a(4,4), c(4,4), d(4,4)
      double precision b(4,4)
      double complex czero, eye

      do 1 i=1,4
      do 1 j=1,4
      d(i,j) = czero
      do 1 k=1,4
      d(i,j) = d(i,j) + a(i,k)*b(k,j)
 1    continue

      do 2 i=1,4
      do 2 j=1,4
      c(i,j) = d(i,j)
 2    continue

      return
      end
c.................................................................

      subroutine matrix_multiply_RR(a, b, c)

c     Multiply two real matrices:  a.b = c

      implicit double precision (a-h,o-z)

      common / bits / czero, eye

      double precision a(4,4), b(4,4), c(4,4), d(4,4)
      double complex czero, eye

      do 1 i=1,4
      do 1 j=1,4
      d(i,j) = 0.0
      do 1 k=1,4
      d(i,j) = d(i,j) + a(i,k)*b(k,j)
 1    continue

      do 2 i=1,4
      do 2 j=1,4
      c(i,j) = d(i,j)
 2    continue

      return
      end
```

```
c......................................................................

      subroutine matrix_multiply_CCC(a, b, c, d)

c     Multiply three double complex matrices:  a.b.c = d

      implicit double precision (a-h,o-z)

      common / bits / czero, eye

      double complex a(4,4), b(4,4), c(4,4), d(4,4), e(4,4)
      double complex czero, eye

      call matrix_multiply_CC(a, b, e)
      call matrix_multiply_CC(e, c, d)

      return
      end

c......................................................................

      subroutine matrix_multiply_RCR(a, b, c, d)

c     Multiply a real by a double complex by a real matrix:  a.b.c = d

      implicit double precision (a-h,o-z)

      common / bits / czero, eye

      double complex b(4,4), d(4,4), e(4,4)
      double precision a(4,4), c(4,4)
      double complex czero, eye

      call matrix_multiply_RC(a, b, e)
      call matrix_multiply_CR(e, c, d)

      return
      end

c......................................................................

      subroutine matrix_multiply_RRR(a, b, c, d)

c     Multiply three real matrices:  a.b.c = d

      implicit double precision (a-h,o-z)

      common / bits / czero, eye

      double precision a(4,4), b(4,4), c(4,4), d(4,4), e(4,4)
      double complex czero, eye

      call matrix_multiply_RR(a, b, e)
      call matrix_multiply_RR(e, c, d)

      return
      end

c......................................................................

c     Calculate cosine of angle between two vectors

      subroutine cosine(a,b,cos_angle)

      implicit double precision (a-h,o-z)
      double precision a(3), b(3)

      ab = a(1)*b(1) + a(2)*b(2) + a(3)*b(3)
      aa = a(1)*a(1) + a(2)*a(2) + a(3)*a(3)
      bb = b(1)*b(1) + b(2)*b(2) + b(3)*b(3)

      cos_angle = ab/dsqrt(aa*bb)

      return
      end

c.................................................................

c     Ensure that g-tensor axes are exactly orthogonal

      subroutine orthog(x,y,z)

      implicit double precision (a-h,o-z)
      double precision x(3), y(3), z(3)

      z(1) = x(2)*y(3) - x(3)*y(2)
      z(2) = x(3)*y(1) - x(1)*y(3)
      z(3) = x(1)*y(2) - x(2)*y(1)

      y(1) = z(2)*x(3) - z(3)*x(2)
      y(2) = z(3)*x(1) - z(1)*x(3)
```

```
      y(3) = z(1)*x(2) - z(2)*x(1)

      xmag = dsqrt(x(1)*x(1) + x(2)*x(2) + x(3)*x(3))
      ymag = dsqrt(y(1)*y(1) + y(2)*y(2) + y(3)*y(3))
      zmag = dsqrt(z(1)*z(1) + z(2)*z(2) + z(3)*z(3))

      do 1 i=1,3
      x(i) = x(i)/xmag
      y(i) = y(i)/ymag
      z(i) = z(i)/zmag
1     continue

      return
      end

c.............................................................

      double precision function ran(dummy)

      implicit double precision (a-h, o-z)
      integer*4 dummy, i, j

      common /comran/ i,j

      i = i + ishft(i,2) + ishft(i,3) + ishft(i,6) + ishft(i,7)
     +      + ishft(i,8) + ishft(i,10) + ishft(i,11) + ishft(i,16)

      j = j + ishft(j,-15)
      j = j + ishft(j,17)

      ran = abs(real(ieor(i,j)) / 2.147484E9)

      return
      end

c.............................................................

      double precision function rnm(rmean,sd)

      implicit double precision (a-h, o-z)
      integer*4 icr, jcr, dum

      common /comran/ icr, jcr

      external ran

    1 u = ran(dum)
c     print*,u,icr,jcr
      if (u.eq.0.d0) goto 1
      s = 1.d0
      if (u.gt.0.5) then
         u = 1.d0 - u
         s = -1.d0
      end if

      t = sqrt(-2*log(u))
      c0 = 2.515517
      c1 = 0.802853
      c2 = 0.010328
      d1 = 1.432788
      d2 = 0.189269
      d3 = 0.001308
      t2 = t*t
      t3 = t*t2
      x = s*(t-(c0+c1*t+c2*t2) / (1.d0+d1*t+d2*t2+d3*t3))

      rnm = rmean + x*sd

      return
      end

c.............................................................
```

A.1.3 spiral.f

```
c.............................................................
c.............................................................

c       program spiral.f

c       C.E. Fursman, September 1998

c       adapted from spiral1.f (PJH)

c       To find a local minimum in any function with any number of
c       variables using the method described in Chapter 4. Here the
c       model is that used in the program echo3d2.f which calculates
c       the ESEEM of a radical pair with one anisotropic hyperfine
```

```
c     coupling to a spin-1/2 nucleus.
c     The spiral program is used to a fit of up to 10 variables


      PROGRAM spiral


      double precision x(138),y(138)

      parameter(maxpar=10,maxpts=138)

      common / one /  x(maxpts),y(maxpts)
      common / two / STEP(maxpar), lambda, check
      common / three / nits
      common / four / b0step(maxpar)
      character*10 ex

      DIMENSION b0(maxpar),x(maxpts),y(maxpts)

      REAL lambda
      LOGICAL check


c     Number of parameters

      npar=10

c     getting 'data'

      ex = 'data'
      npt = 129

      open(1,file = ex)
      do 17 i=1, npt
      read (1,*) x(i),y(i)
 17   continue


c     Get guesses of parameter values
      b0(1)=1.14460
      b0(2)=1.0
      b0(3)=0.462524
      b0(4)=0.5
      b0(5)=0.242267
      b0(6)=90
      b0(7)=4.0
      b0(8)=1.0d-6
      b0(9)=-1.2
      b0(10)=0.0

      CALL GRD('GUESS A (hfi coupling)    ?', b0(1))
      CALL GRD('GUESS A2 (hfi coupling)    ?', b0(2))
      CALL GRD('GUESS wn (nuclear larmour)    ?', b0(3))
      CALL GRD('GUESS wn2 (nuclear larmour)    ?', b0(4))
      CALL GRD('GUESS psi (e-e to e-n angle)    ?', b0(5))
      CALL GRD('GUESS psi2 (e-e to e-n angle)   ?', b0(6))
      call grd('Guess amp ?',b0(7))
      call grd('Guess t2 (secs) ?',b0(8))
      call grd('Guess D (Gauss) ?',b0(9))
      call grd('Guess J (Gauss) ?',b0(10))


c     Get maximum step sizes for each parameter
      step(1)=0.1
      step(2)=0.1
      step(3)=0.1
      step(4)=0.1
      step(5)=10
      step(6)=10
      step(7)=0.1
      step(8)=0.1d-6
      step(9)=0.1
      step(10)=0.1
      CALL GRD('MAx STEP IN A   ?', STEP(1))
      CALL GRD('MAx STEP IN A2   ?', STEP(2))
      CALL GRD('MAx STEP IN wn    ?', STEP(3))
      CALL GRD('MAx STEP IN wn2    ?', STEP(4))
      CALL GRD('MAx STEP IN psi    ?', STEP(5))
      CALL GRD('MAx STEP IN psi2    ?', STEP(6))
      CALL GRD('MAx STEP IN amp    ?', STEP(7))
      CALL GRD('MAx STEP IN t2    ?', STEP(8))
      CALL GRD('MAx STEP IN D    ?', STEP(9))
      CALL GRD('MAx STEP IN J    ?', STEP(10))

c     Get step sizes in each parameter for calculation of gradients

      b0step(1)=0.001
      b0step(2)=0.001
      b0step(3)=0.001
      b0step(4)=0.001
      b0step(5)=0.1
```

```
      b0step(6)=0.1
      b0step(7)=0.001
      b0step(8)=0.001d-6
      b0step(9)=0.001
      b0step(10)=0.001
      call grd('Integration step for A   ?', b0step(1))
      call grd('Integration step for A2   ?', b0step(2))
      call grd('Integration step for wn   ?', b0step(3))
      call grd('Integration step for wn2   ?', b0step(4))
      call grd('Integration step for psi    ?', b0step(5))
      call grd('Integration step for psi2    ?', b0step(6))
      call grd('Integration step for amp   ?', b0step(7))
      call grd('Integration step for t2    ?', b0step(8))
      call grd('Integration step for D    ?', b0step(9))
      call grd('Integration step for J    ?', b0step(10))

      NSPIRAL = 3
      NPOINTS = 5

c     Tolerances
      epsilon =1.0e-5
      epsilon2=1.0e-5
      lambda  =1.0e-5
      CALL GRD('EPSILON  ?',EPSILON)
      CALL GRD('EPSILON2 ?',EPSILON2)
      CALL GRD('lambda   ?',lambda)
c     CALL GI('check INVERSION OF HESSIAN  ?', 0, 1, I)
      i = 0
      check = (I.EQ.1)

      WRITE(6,*)

      CALL SPIRAL(b0, NPAR, NPT, NSPIRAL, NPOINTS, EPSILON,
     &     EPSILON2)

      WRITE(6,*)
      WRITE(6,*)(b0(I),I=1,10)
      WRITE(6,*)
      WRITE(6,*) ' nits = ', nits
      WRITE(6,*)

      STOP
      END

C.................................................................


      SUBROUTINE FUNCT(F, b, NPAR, NPT)

c
c     Calculates model function points at search position b
c


      implicit double precision (a,c,d,e,g,h,o-z)
      double precision echo(138), time(138), g(138), g2(138)
      double precision wth(257), wph(65)
      double precision j,j_gauss
      double precision k, k2

      parameter(maxpar=10,maxpts=138)
      DIMENSION b(maxpar), F(maxpts)
      common / one /  x(maxpts),y(maxpts)
      common / three / nits

      nits = nits + 1

      aconst_gauss = b(1)
      aconst_gauss2 = b(2)
      wnuc_gauss = b(3)
      wnuc_gauss2 = b(4)
      psinuc = b(5)
      psinuc2 = b(6)
      amp = b(7)
      t2 = b(8)
      dipolar_gauss = b(9)
      j_gauss = b(10)

c- - - - - - - - - - - - - - - - - - - - - - - - - - - - - - - - - - - - -

c     program work (eseem)

c     Constants

      pi = 3.1415926535d0
      half_pi = 0.5d0*pi
      gauss_to_hertz = 2.0d0*pi*2.8d6
      one_third = 1.0d0/3.0d0

c     Default values
```

```
c        t2 = 0.925d-6
c        dipolar_gauss = -1.155d0
c        j_gauss = 4.83d-3


c        t2 = 0.000001143d0
c        dipolar_gauss = -1.153d0
c        j_gauss = 0.0d0
         ntheta = 257
         nphi = 65
         time_max = 0.00000276d0

c        Conversions, etc.

         aconst=aconst_gauss*gauss_to_hertz
         aconst2=aconst_gauss2*gauss_to_hertz
         wnuc=wnuc_gauss*gauss_to_hertz
         wnuc2=wnuc_gauss2*gauss_to_hertz
         psi = psinuc*3.1415926535d0/180.0d0
         psi2 = psinuc2*3.1415926535d0/180.0d0
         dipolar = dipolar_gauss*gauss_to_hertz
         j = j_gauss*gauss_to_hertz
         delta_t = 0.00000002d0

c        Calculate ESEEM

         spsi = dsin(psi)
         cpsi = dcos(psi)
         spsi2 = dsin(psi2)
         cpsi2 = dcos(psi2)
         theta_step=0.5*pi/(ntheta-1.0d0)
         phi_step=2.0d0*pi/(nphi-1.0d0)

         do 12 i=1,138
         echo(i) = 0.0d0
12       time(i) = i*delta_t

         wth(1)=1.0d0
         wth(itheta)=1.0d0
         do 50 itheta=2,ntheta-1,2
50       wth(itheta)=4.0d0
         do 51 itheta=3,ntheta-2,2
51       wth(itheta)=2.0d0

         wph(1)=1.0d0
         wph(iphi)=1.0d0
         do 52 iphi=2,nphi-1,2
52       wph(iphi)=4.0d0
         do 53 iphi=3,nphi-2,2
53       wph(iphi)=2.0d0


         do 14 itheta=1,ntheta
         theta = (itheta-1.d0)*theta_step
         stheta = dsin(theta)
         ctheta = dcos(theta)
         d = dipolar*(ctheta*ctheta - one_third)

         do 13 iphi=1,nphi
         ph = (iphi-1.d0)*phi_step
         sphi = dsin(ph)
         cphi = dcos(ph)
         cen = (stheta*sphi*spsi + ctheta*cpsi)
         sen = dsqrt(1.0d0 - cen*cen)
         cen2 = (stheta*sphi*spsi2 + ctheta*cpsi2)
         sen2 = dsqrt(1.0d0 - cen2*cen2)

         ah = (3.0d0*cen*cen - 1)*aconst
         ch = 3.0d0*cen*sen*aconst
         ah2 = (3.0d0*cen2*cen2 - 1)*aconst2
         ch2 = 3.0d0*cen2*sen2*aconst2

         xp = 0.5d0*ah + wnuc
         xm = 0.5d0*ah - wnuc
         xb = 0.25d0*ch*ch
         xp2 = 0.5d0*ah2 + wnuc2
         xm2 = 0.5d0*ah2 - wnuc2
         xb2 = 0.25d0*ch2*ch2

         walpha = sqrt(xm*xm + xb)
         wbeta  = sqrt(xp*xp + xb)
         xx = ch*wnuc/(walpha*wbeta)
         k = xx*xx

         walpha2 = sqrt(xm2*xm2 + xb2)
         wbeta2  = sqrt(xp2*xp2 + xb2)
         xx2= ch2*wnuc2/(walpha2*wbeta2)
         k2 = xx2*xx2


         do 15 i=1,138
```

```
      wat = walpha*time(i)
      wbt = wbeta*time(i)
      wat2 = walpha2*time(i)
      wbt2 = wbeta2*time(i)

      g(i) = 1.0d0 - dcos(wat) - dcos(wbt) +
     &        0.5d0*(dcos(wat+wbt)+dcos(wat-wbt))
      g(i) = 1.0d0 - 0.5d0*k*g(i)
      g2(i) = 1.0d0 - dcos(wat2) - dcos(wbt2) +
     &                0.5d0*(dcos(wat2+wbt2)+dcos(wat2-wbt2))
      g2(i) = 1.0d0 - 0.5d0*k2*g2(i)

      tjdt=2.0d0*(j-d)*time(i)

      echo(i) = echo(i) + dsin(tjdt)*(g2(i)+g(i))*stheta
     &         *wth(itheta)*wph(iphi)

 15   continue
 13   continue
 14   continue

      scale = pi/(36.0d0*(ntheta-1.0d0)*(nphi-1.0d0))

      do 16 i = 1, 138
      echo(i) = amp*scale*echo(i)*dexp(-time(i)/t2)
 16   continue

      do 8 i=1, 129
      f(i)=-echo(i+9)
 8    continue

      RETURN
      END
c- - - - - - - - - - - - - - - - - - - - - - - - - - - - - - - - - - - -

c.....................................................................

      subroutine jacobian(jt, b, npar, npt)

c
c     Calculates transpose of Jacobian matrix
c     jt(i,j) = df(j)/db(i)
c     i = 1,2,...npar
c     j = 1,2,...npt
c
       double precision x(138),y(138)


      parameter(maxpar=10,maxpts=138)
      dimension b(maxpar)
      dimension b0(maxpar),f0(maxpts),f1(maxpts)
      real jt(maxpar, maxpts)
      common / one / x(maxpts), y(maxpts)
      common / four / b0step(maxpar)

      do 1 i=1,npar
 1    b0(i)=b(i)

      call funct(f0,b0,npar,npt)
      do 3 i=1,npar
      b0(i)=b0(i)+b0step(i)
      call funct(f1,b0,npar,npt)
      do 2 j=1,npt
 2    jt(i,j)=(f1(j)-f0(j))/b0step(i)
      b0(i)=b0(i)-b0step(i)
 3    continue

      return
      end
c.....................................................................

      subroutine spiral(b0, npar, npt, nspiral, npoints, epsilon,
     &    epsilon2)

      double precision x(138),y(138)


      parameter(maxpar=10,maxpts=138)
      dimension b(maxpar),b0(maxpar),s(maxpar),d(maxpar),
     &          t(maxpar), f(maxpts)
      real jt(maxpar,maxpts), mu

      common / one /  x(maxpts),y(maxpts)

      tau =  0.001


      phi0 = phi(b0, npar, npt)
```

```
  500   continue
        write(6,*)(b0(i),i=1,npar), phi0

        call jacobian(jt, b0, npar, npt)
        call funct(f, b0, npar, npt)

c       calculate direction of steepest descent <d>

        do 10 i=1,npar
        d(i) = 0.
        do 20 j=1,npt
        d(i) = d(i) + jt(i,j)*(y(j) - f(j))
   20   continue
   10   continue

c       calculate taylor series direction <t>

        call taylor(jt, d, t, npar, npt)

c       scale <d> to same length as <t> - r0

        r0 = 0.
        a0 = 0.
        do 11 i1=1,npar
        r0 = r0 + t(i1)*t(i1)
        a = a + d(i1)*d(i1)
   11   continue
        r0 = sqrt(r0)
        a = r0/(sqrt(a))
        cosgamma = 0.
        do 21 i1=1,npar
        d(i1) = d(i1)*a
        cosgamma = cosgamma + t(i1)*d(i1)
   21   continue

c       calculate angle between <d> and <t> - gamma

        cosgamma = cosgamma/(r0*r0)
        gamma = acos(cosgamma)
        singamma = sin(gamma)
        beta = gamma*0.5

        do 600 ns = 1,nspiral

c       test for taylor series convergence

        amax = 0.
        do 100 i=1,npar
        a = abs(t(i)/(b0(i) - tau))
        if(a .gt. amax) amax = a
  100   continue
        if(a.le.epsilon) then
        write(6,1000)
 1000   format(/,'  taylor series convergence')
        go to 5000
        end if

c       search along <t>

        do 30 i1=1,npar
        b(i1) = b0(i1) + t(i1)
   30   continue
        a = phi(b, npar, npt)
        if(a.le.phi0) then
        phi0 = a
        do 31 i1=1,npar
        b0(i1) = b(i1)
   31   continue
c       write(6,1003) ns, 1
        go to 500
        end if

c       search along spirals  <s>

        mu = 0.05
        do 400 np=2,npoints
        mu = (mu+mu)/(1.+mu)
        a = mu*singamma / (1. + mu*(cosgamma - 1.) )
        theta = atan(a)
        xi = r0 * mu * singamma / sin(theta)
        a = 1. / tan(beta)
        r = 1. - theta*a - (1. - gamma*a)*(theta*theta)/(gamma*gamma)
        r = r * r0
        do 40 i1=1,npar
        s(i1) = d(i1)
        s(i1) = t(i1)*(1.-mu) + s(i1)*mu
        s(i1) = s(i1)*r/xi
        b(i1) = b0(i1) + s(i1)
   40   continue
        a = phi(b, npar, npt)
        if(a.le.phi0) then
```

```
      phi0 = a
      do 41 i1=1,npar
      b0(i1) = b(i1)
   41 continue
c     write(6,1003) ns, np
      go to 500
      end if

  400 continue

      a = 1./3.
      do 50 i1=1,npar
      t(i1) = a*t(i1)
      d(i1) = a*d(i1)
   50 continue

  600 continue

c     search along direction of steepest descent

      a = 0.
      a1 = 0.
      do 60 i1=1,npar
      a = a + s(i1)*s(i1)
      a1 = a1 + d(i1)*d(i1)
   60 continue
      a = sqrt(a/a1)
      do 70 i1=1,npar
      d(i1) = d(i1)*a
   70 continue

      ng = 1
  700 continue
      do 80 i1=1,npar
      d(i1) = d(i1)*0.5
      b(i1) = b0(i1) + d(i1)
   80 continue
      a = phi(b, npar, npt)
      if(a.le.phi0) then
      phi0 = a
      do 81 i1=1,npar
      b0(i1) = b(i1)
   81 continue
  240 continue
c     write(6,1004) ng
      go to 500
      end if

c     test for gradient convergence

      a = 0.
      do 90 i1=1,npar
      a = a + d(i1)*d(i1)
   90 continue
      a = sqrt(a)
      if(a.lt.epsilon2) then
      write(6,1001)
 1001 format(/, '  gradient convergence')
      go to 5000
      end if
      ng = ng + 1
      go to 700

 5000 continue

 1003 format(2x, ' ns = ', i4, '  np = ', i4)
 1004 format(2x, ' ng = ', i4)
      return
      end

c.................................................................

      function phi(b, npar, npt)

c
c     calculates sum of squared residuals at search position b
c
      double precision x(138),y(138)

      parameter (maxpar=10,maxpts=138)
      dimension b(maxpar), f(maxpts)
      common / one /  x(maxpts),y(maxpts)


      call funct(f, b, npar, npt)

      phi = 0.
      do 10 i=1,npt
      a = f(i) - y(i)
      phi = phi + a*a
   10 continue
```

```
      return
      end

c.................................................................

      subroutine taylor(jt, d, t, npar, npt)
c
c     calculates <t> the taylor series vector
c     hessian = jt*j
c     <t> = hessian inverse *
c     <d> = gradient vector
c

      parameter(maxpar=10,maxpts=138)
      real jt(maxpar,maxpts), lambda
      double precision dh(maxpar+1,maxpar+1)
      dimension h(maxpar,maxpar),t(maxpar),d(maxpar),scale(maxpar)
      common / two / step(maxpar), lambda, check
      logical check

      do 10 i=1,npar
      do 20 j=1,npar
      h(i,j) = 0.
      do 30 k=1,npt
      h(i,j) = h(i,j) + jt(i,k)*jt(j,k)
   30 continue
   20 continue
   10 continue

c     scaling

      do 40 i=1,npar
      scale(i) = 1./sqrt(h(i,i))
      d(i) = d(i)*scale(i)
      do 50 j=1,i
      h(j,i) = h(j,i)*scale(i)*scale(j)
      h(i,j) = h(j,i)
   50 continue
   40 continue

      do 60 i=1,npar
      h(i,i) = h(i,i) + lambda
   60 continue

c     invert hessian

      do 25 i=1,npar
      do 26 j=1,npar
      dh(j,i) = dble(h(j,i))
   26 continue
   25 continue

      ifail = 0
      call f01adf(npar, dh, maxpar+1, ifail)

      do 27 i=1,npar
      do 28 j=1,i
      h(i,j) = sngl(dh(i+1,j))
      h(j,i) = h(i,j)
   28 continue
   27 continue

      if(check) then
      do 200 i=1,npar
      do 210 j=1,npar
      c = 0.
      do 220 k=1,npar
      if(i.le.k) then
      hik = sngl(dh(i,k))
      else
      hik = sngl(dh(k,i))
      end if
      c = c + hik * h(k,j)
  220 continue
      write(6,*)i,j,c
  210 continue
  200 continue
      end if

      amax = 0.
      do 70 i=1,npar
      t(i) = 0.
      do 80 j=1,npar
      t(i) = t(i) + h(i,j)*d(j)
   80 continue
      t(i) = t(i)*scale(i)
      a = abs(t(i)/step(i))
      if(a.gt.amax) amax = a
```

```
 70   continue

      if(amax.gt.1.) then
      do 110 i=1,npar
      t(i) = t(i)/amax
110   continue
      end if

      return
      end

c..............................................................
```

A.2 Mathematica Programs

A.2.1 Mathematica Library

```
NormaliseVector[v_]:= v/Sqrt[v.v];

(* Normalise a vector *)


Orthonormalise[{vx_,vy_,vz_}]:=(
             a=Cross[vx,vy];
             b=Cross[a,vx];
             {NormaliseVector[vx],NormaliseVector[b],
             NormaliseVector[a]}      );

(* Ensure 3 vectors are orthonormal *)


NormaliseRows[m_]:= Map[NormaliseVector,m];

(* Normalise the rows of a square matrix *)


OrthoNormQ[m_]:= Simplify[m.Transpose[m]]
             ===IdentityMatrix[Length[m]];

(* Tests whether a square matrix has orthonormal rows *)


MTrace[m_] :=
     Together[Sum[m[[j,j]],{j,1,Length[m]}]];

(* Trace of a square matrix *)


SimpTerms[f_]:=Sum[Simplify[f[[i]]],{i,1,Length[f]}];

(* Simplify an expression term-by-term. *)


Com[a_,b_]:=Together[a.b-b.a];

(* Commutator of two matrices *)


ComQ[a_,b_]:=Com[a,b]===ZeroMatrix[Length[a]];

(* Tests whether two matrices commute *)


IP[A_, B_] :=
     Flatten[Map[Flatten,Map[Transpose,
     Outer[Times, A, B],{1}],{2}],1]

IP[a_,b_,c_] :=IP[IP[a,b],c];
IP[a_,b_,c_,d_] :=IP[IP[a,b,c],d];
IP[a_,b_,c_,d_,e_] :=IP[IP[a,b,c,d],e];
IP[a_,b_,c_,d_,e_,f_] :=IP[IP[a,b,c,d,e],f];

(* Direct products *)
```

A.2.2 Program Listings

crlb.m

```
(*------------------------crlb.m------------------------*)
(* CEF April 1998                                       *)
```

```
(* This program is used to calculate the Cramer-Rao lower    *)
(* bounds of the curve fit using the two-electron model      *)
(* given particular values of the fit parameters and an      *)
(* estimate of the noise (sigma).                            *)


lookupS=<<lookS;
lookupC=<<lookC;

(* lookup tables: the model function is an intergral which  *)
(* can be solved in terms of Fresnel equations. The lookup  *)
(* tables are a library of the values of these functions    *)
(* (lookupS for sine, lookupC for cosine) for a given value *)
(* of the associated variable x1                            *)


AFS[z_]:=(
        x1=Floor[z*1000];
        y1=lookupS[[x1]];
        y2=lookupS[[x1+1]];
        y1 + (y2-y1)(z*1000 - x1) );

AFC[z_]:=(
        x1=Floor[z*1000];
        y1=lookupC[[x1]];
        y2=lookupC[[x1+1]];
        y1 + (y2-y1)(z*1000 - x1) );


c=1.76*10^7;
e=10^-6;

(* input parameters                                          *)

a=1.0; t2=0.37; d=-1.4; j=0;
dt=0.01; npt=375; sig=0.01;


(* calculation of the model function in terms of the Fresnel*)
(* equations AFC and AFS, as given above.                    *)



ESE[t_,a_,t2_,d_,j_]:=(
        x=N[2.*Sqrt[-d*c*t/Pi]];
        y=N[2.*c*(d/3. + j)*t];
        N[-a*Exp[-t/(t2*e)]*(Cos[y]AFS[x] + Sin[y]AFC[x])/x]
        );

(* derivatives with repect to each variable                  *)

yA[t_]:=        ESE[t,a,t2,d,j]/a;
yD[t_]:=        (ESE[t,a,t2,d+10^-5,j]-ESE[t,a,t2,d,j])/10^-5;
yJ[t_]:=        (ESE[t,a,t2,d,j+10^-5]-ESE[t,a,t2,d,j])/10^-5;
yT[t_]:=        ESE[t,a,t2,d,j]*t/(t2*t2*e);


(* formation of the Ficher information matrix                *)


g=Table[0.,{npt},{4},{4}];

Do[ t=i*dt*e + (0.2 - dt)*e;
        ya=yA[t];  yd=yD[t];  yj=yJ[t];  yt=yT[t];
        g[[i]]={{ya^2,ya*yd,ya*yj,ya*yt},
                {ya*yd,yd^2,yd*yj,yd*yt},
                {ya*yj,yd*yj,yj^2,yj*yt},
                {yt*ya,yt*yd,yt*yj,yt^2}},
                        {i,1,npt}];

f=Table[0.,{4},{4}];
Do[f=f+g[[i]],{i,1,npt}];  f=f/sig^2;

(* calculation and output of the lower bounds                *)

finv=Inverse[f];
crlbA=Sqrt[finv[[1,1]]];
crlbD=Sqrt[finv[[2,2]]];
crlbJ=Sqrt[finv[[3,3]]];
crlbT=Sqrt[finv[[4,4]]];

z={crlbA,crlbT,crlbD,crlbJ}


(*----------------------------------------------------------*)
```

monte.m

```
(*-----------------------monte.m-------------------------*)
(* CEF April 1998                                       *)

(* calculates the standard deviation in the 4 parameters of *)
(* the model fitting by repeatedly using a chi-squared fit  *)
(* and different sets of random noise to find a best fit to *)
(* 'experimental' data.                                 *)

(* model calculated using lookup tables and Fresnel     *)
(* as crlb.m                                            *)


lookupS=<<lookS;
lookupC=<<lookC;

<<Statistics'ContinuousDistributions'

(* opening output stream for the values of each parameter   *)

nloop=500;
testA001 = testT001 = testD001 = testJ001 = Table[0,{nloop}];

(* calculation is repeated 500 times to allow an accurate   *)
(* estimation of the standard deviation of each parameter   *)
(* to be used.                                              *)

Loop[]:=(

a=1.0;  t2=0.37;  d=-1.4;  j=0.0;  sigma=0.001;
tmax=3.0;  npt=375;  dt=tmax/npt;

c=1.76*10^7;  e=10^-6;

AFS[z_]:=(
        x1=Floor[z*1000];
        y1=lookupS[[x1]];
        y2=lookupS[[x1+1]];
        y1 + (y2-y1)(z*1000 - x1) );

AFC[z_]:=(
        x1=Floor[z*1000];
        y1=lookupC[[x1]];
        y2=lookupC[[x1+1]];
        y1 + (y2-y1)(z*1000 - x1) );

Experiment[t_]:=(
        x=N[2.*Sqrt[-d*c*t/Pi]];
        y=N[2.*c*(d/3. + j)*t];
        N[-a*Exp[-t/(t2*e)]*(Cos[y]AFS[x] + Sin[y]AFC[x])/x]
                + Random[NormalDistribution[0,1]]*sigma
        );

Calculated[t_,atr_,t2tr_,dtr_,jtr_]:=(
        x=N[2.*Sqrt[-dtr*c*t/Pi]];
        y=N[2.*c*(dtr/3. + jtr)*t];
        N[-atr*Exp[-t/(t2tr*e)]*(Cos[y]AFS[x]
        + Sin[y]AFC[x])/x]
        );

Expt = Table[Experiment[i*dt*e], {i,1,npt}];


(* compare experimental and calculated data             *)

Chisq[atr_,t2tr_,dtr_,jtr_]:=
        N[Sum[(Expt[[i]]- Calculated[N[i*dt*e],
        atr,t2tr,dtr,jtr])^2,{i,1,npt}]];


FM = FindMinimum[Chisq[atr,t2tr,dtr,jtr],
{atr, { 0.995*a,  1.005*a}},
{t2tr,{ 0.995*t2, 1.005*t2}},
{dtr, { 0.995*d,  1.005*d}},
{jtr, {-0.001,    0.001}}
];

(* output trial values to file ready for calculation of SD *)

testA001[[k]]=atr /.FM[[2,1]];
testT001[[k]]=t2tr/.FM[[2,2]];
testD001[[k]]=dtr /.FM[[2,3]];
testJ001[[k]]=jtr /.FM[[2,4]];


)


Do[Loop[],{k,1,nloop}]
```

```
(*---------------------------------------------------------*)
```

curve.m

```
(*-------------------------curve.m-------------------------*)
(* CEF April 1998                                          *)

(* calculates the values of D, J, t2 and a giving the      *)
(* best fit of the two-electron model to experimental      *)
(* data                                                    *)

(* model calculated using lookup tables and Fresnel        *)
(* as crlb.m                                               *)

lookupS=<<lookS;
lookupC=<<lookC;

Expt=<<dzuba;

(* initial starting values                                 *)

a=1.0;  t2=0.37;  d=-1.4;  j=0.0;
tmax=2.76;  npt=138;  dt=tmax/npt;

c=1.76*10^7;  e=10^-6;

AFS[z_]:=(
        x1=Floor[z*1000];
        y1=lookupS[[x1]];
        y2=lookupS[[x1+1]];
        y1 + (y2-y1)(z*1000 - x1) );

AFC[z_]:=(
        x1=Floor[z*1000];
        y1=lookupC[[x1]];
        y2=lookupC[[x1+1]];
        y1 + (y2-y1)(z*1000 - x1) );


Calculated[t_,atr_,t2tr_,dtr_,jtr_]:=(
        x=N[2.*Sqrt[-dtr*c*t/Pi]];
        y=N[2.*c*(dtr/3. + jtr)*t];
        N[-atr*Exp[-t/(t2tr*e)]*(Cos[y]AFS[x]
        + Sin[y]AFC[x])/x]
        );

(* a chi-squared fit is used. Mathematica uses a path of    *)
(* steepest descent to find a minimum on the 4-dimensional  *)
(* surface                                                  *)

Chisq[atr_,t2tr_,dtr_,jtr_]:=N[Sum[(Expt[[i]]-
Calculated[N[i*dt*e],atr,t2tr,dtr,jtr])^2,{i,10,npt}]];


FM = FindMinimum[Chisq[atr,t2tr,dtr,jtr],{atr,{0.95*a,1.05*a}},
                {t2tr,{0.95*t2,1.05*t2}},{dtr,{0.95*d,1.05*d}},
                {jtr,{-0.01,0.01}}];


(*---------------------------------------------------------*)
```

g-equal.m

```
(*-----------------------g-equal.m-------------------------*)
(* CEF January 1999                                        *)

(* find the orientations of the P+Q- radical pair for which *)
(* the g-tensors have the same value.                      *)

<<library;

(* principle axes of the two radicals these have been      *)
(* Orthonormalised                                         *)

xp={-0.550383, -0.229523, 0.802744}; xq={1, 0, 0};
yp={0.107485, 0.933991, 0.340745}; yq={0, 1, 0};
zp={-0.827965, 0.273823, -0.489382}; zq={0, 0, 1};

(* principle values of the g-tensors when the field is     *)
(* along the x,y,z axes                                    *)
```

```
gpx=2.0033;                    gqx=2.0066;
gpy=2.0025;                    gqy=2.0054;
gpz=2.0021;                    gqz=2.0022;

(* creating unit vector normal to the field, these vectors  *)
(* will be unit by definition                               *)

n[th_,ph_]:={Sin[th] Cos[ph], Sin[th] Sin[ph], Cos[th]};

(* calculating the g-tensors                                *)

gpsq[th_,ph_]:=((gpx n[th,ph].xp) (gpx n[th,ph].xp)
              + (gpy n[th,ph].yp) (gpy n[th,ph].yp)
              + (gpz n[th,ph].zp) (gpz n[th,ph].zp));

gp[th_,ph_]:=Sqrt[gpsq[th,ph]];

gqsq[th_,ph_]:=((gqx n[th,ph].xq) (gqx n[th,ph].xq)
              + (gqy n[th,ph].yq) (gqy n[th,ph].yq)
              + (gqz n[th,ph].zq) (gqz n[th,ph].zq));

gq[th_,ph_]:=Sqrt[gqsq[th,ph]];


(* calculating the difference                               *)

g[th_,ph_]:=gp[th,ph] - gq[th,ph];


(* plotting the surface                                     *)

surf=Plot3D[g[th,ph],{th,0,Pi/2},{ph,0,2 Pi}]

cont=ContourPlot[g[th,ph],{th,0,Pi/2},{ph,0,2 Pi},
        Contours ->{0}]


(*----------------------------------------------------------*)
```

Bibliography

[1] J. W. Schopf. *Sci. Am.*, **239** (1978) 85.

[2] M. K. Campbell. *Biochemistry.* Saunders College Publishing, Second Ed., 1995.

[3] J. Deisenhofer, H. Michel and R. Huber. *TIBS*, **10** (1985) 243.

[4] G. McDermott, S. M. Prince, A. A. Freer, A. M. Hawthornthwaite-Lawless, M. Z. Papiz, R. J. Cogdell and N. W. Isaacs. *Nature*, **374** (1995) 517.

[5] S. M. Prince, M. Z. Papiz, A. A. Freer, G. McDermott, A. M. Hawthornthwaite-Lawless, R. J. Cogdell and N. W. Isaacs. *J. Mol. Biol.*, **268** (1997) 412.

[6] M. Z. Papiz, S. M. Prince, A. M. Hawthornthwaite-Lawless, G. McDermott, A. A. Freer, N. W. Isaacs and R. J. Cogdell. *TIPS*, **1** (1996) 198.

[7] V. Sundstroem and T. Pullerits. *J. Phys. Chem.*, **103** (1999) 2327.

[8] A. M. Hawthornthwaite and R. J. Cogdell in *The Chlorophylls.* CRC Boca Raton, H. Scheer (ed.), 1993.

[9] D. W. Reed and R. K. Clayton. *Biophys. Res. Commun.*, **30** (1968) 471.

[10] R. Emerson and W. Arnold. *J. Gen. Physiol.*, **16** (1932) 191.

[11] J. P. Allen, G. Feher, T. O. Yeates, H. Komiya and D. C. Rees. *Proc. Natl. Acad. Sci. USA*, **84** (1987) 5730.

[12] J. Deisenhofer, O. Epp, K. Miki, R. Huber and H. Michel. *J. Mol. Biol.*, **180** (1984) 385.

[13] C. H. Chang, J. Tiede, J. Norris and M. Schiffer. *Biochemistry*, **30** (1986) 5352.

[14] K. Möbius. *Specialist Periodical Report: ESR*, **14** (1995) 203.

[15] D. Stehlik and K. Möbius. *Ann. Rev. Phys. Chem.*, **48** (1997) 745.

[16] G. Feher, J. P. Allen, M. Y. Okamura and D. C. Rees. *Nature*, **339** (1989) 111.

[17] W. Gerlach and O. Stern. *Z. Phys.*, **8** (1921) 110.

[18] G. E. Uhlenbeck and S. Goudsmit. *Die Naturwissenschaften*, **13** (1925) 953.

[19] P. W. Atkins. *Molecular Quantum Mechanics.* OUP, Second Ed., 1983.

[20] P. W. Atkins. *Quanta: A Handbook of Concepts.* OUP, Second Ed., 1991.

[21] P. J. Hore. *Nuclear Magnetic Resonance.* Oxford Science Publications, 1995.

[22] B. Brocklehurst and K. A. McLauchlan. *Int. J. Radiat. Biol.*, **69** (1996) 3.

[23] K. M. Salikov, Yu. N. Molin, R. Z. Sagdeev and A. L. Buchachenko. *Spin Polarization and Magnetic Effects in Radical Reactions.* Elsevier, Yu. N. Molin (ed.), 1984.

[24] J. A. Weil, J. R. Bolton and J. E. Wertz. *Electron Paramagnetic Resonance: Elementary Theory and Practical Applications.* John Wiley and Sons, Inc., 1994.

[25] N. M. Atherton. *Principles of Electron Spin Resonance.* Ellis Horwood PTR Prentice Hall, 1993.

[26] A. J. Hoff in *Photosynthesis.* Elsevier, J. Amesz (ed.), 1987.

[27] A. J. Hoff in *The Photosynthetic Bacteria II.* Academic Press, J. Deisenhofer and J. R. Norris (eds.), 1992.

[28] A. J. Hoff. *Quart. Rev. Biophys.*, **14** (1981) 4.

[29] A. J. Hoff. *Quart. Rev. Biophys.*, **17** (1984) 2.

[30] A. Angerhofer and R. Bittl. *Photochemistry and Photobiology*, **63** (1996) 11.

[31] J. R. Norris, R. A. Uphaus, H. L. Crespi and J. J. Katz. *Proc. Natl. Acad. Sci.*, **68** (1971) 625.

[32] G. Feher and M. Y. Okamura in *The Photosynthetic Bacteria.* Plenum Press, R. K. Clayton and W. R. Sistrom (eds.), 1978.

[33] I. H. Davies, P. Heathcote, D. J. Maclachlan and M. C. W. Evans. *Biochem. Biophys. Acta*, **1143** (1993) 183.

[34] S. A. Dzuba, P. Gast and A. J. Hoff. *Chem. Phys. Lett.*, **236** (1995) 595.

[35] P. Moenne-Loccoz, P. Heathcote, D. J. Maclachlan, M. C. Berry, I. H. Davis and M. C. W. Evans. *Biochemistry*, **33** (1994) 10037.

[36] S. G. Zech, J. Kurreck, H.-J. Eckert, G. Renger, W. Lubitz and R. Bittl. *FEBS Lett.*, **414** (1997) 454.

[37] A. J. Hoff. *Quart. Rev. Biophys.*, **14** (1981) 599.

[38] J. S. van den Brink, R. J. Hulsebosch, P. Gast, P. J. Hore and A. J. Hoff. *Biochemistry*, **33** (1994) 13668.

[39] W. Lubitz, M. Plato and K. Möbius in *The Chlorophylls.* CRC Boca Raton, H. Scheer (ed.), 1993.

[40] O. Ya. Grinberg, A. A. Dubinskii, V. F. Shuvalov, L. G. Oranskil, V. I. Kurochkin and Ya. S. Lebedev. *Dokl. Phys. Chem.*, **230** (1976) 523.

[41] O. Burghaus, M. Plato, M. Rohrer, K. Möbius, F. MacMillan and W. Lubitz. *J. Phys. Chem.*, **97** (1993) 7639.

[42] R. A. Issacson, F. Lendzian, E. C. Abresch, W. Lubitz and G. Feher. *Biophys. J.*, **69** (1995) 311.

[43] R. Klette, J. T. Törring, M. Plato, B. Bönigk and W. Lubitz. *J. Phys. Chem.*, **97** (1993) 2015.

[44] C. Kirmaier and D. Holten. *Photosynth. Res.*, **13** (1987) 225.

[45] A. J. Hoff, E. L. Lous, K. W. Moehl and A. J. Dijkman. *Chem. Phys. Lett.*, **114** (1985) 39.

[46] E. L. Lous and A. J. Hoff. *Photosynth. Res.*, **9** (1986) 89.

[47] E. L. Lous and A. J. Hoff in *The Photosynthetic Bacterial Reaction Centre - Structure and Dynamics.* Plenum Press, J. Breton and A. Vermeglio (eds.), 1989.

[48] A. J. Hoff, P. Gast, S. A. Dzuba, C. R. Timmel, C. E. Fursman and P. J. Hore. *Spectrochimica Acta A*, **54** (1990) 2283.

[49] R. Bittl and S. G. Zech. *J. Phys. Chem. B*, **101** (1997) 1429.

[50] S. A. Dzuba, P. Gast and A. J. Hoff. *Chem. Phys. Lett.*, **268** (1997) 273.

[51] S. G. Zech, W. Lubitz and R. Bittl. *Ber. Bunsenges. Phys. Chem.*, **100** (1996) 2041.

[52] H. Hara, S. A. Dzuba, A. Kawamori, A. Akabori, T. Tomo, K. Satoh, M. Iwaki and S. Itoh. *Biochem. Biophys. Acta*, **1322** (1997) 77.

[53] F. Bloch. *Phys. Rev.*, **70** (1946) 460.

[54] E. L. Hahn. *Phys. Rev.*, **80** (1950) 580.

[55] H. Y. Carr and E. M. Purcell. *Phys. Rev.*, **94** (1954) 630.

[56] I. V. Borovykh, S. A. Dzuba, I. I. Proskuyrakov, P. Gast and A. J. Hoff. *Biochem. Biophys. Acta*, **1363** (1998) 182.

[57] S. G. Zech, R. Bittl, A. T. Gardiner and W. Lubitz. *Appl. Magn. Reson.*, **13** (1997) 517.

[58] S. A. Dzuba, A. Kawamori, M. Iwaki, S. Itoh and Yu. D. Tsvetkov. *Chem. Phys. Lett.*, **264** (1997) 238.

[59] M. Iwaki and S. Itoh. *J. Chem. Phys. B*, **102** (1998) 10440.

[60] S. G. Zech, A. J. van der Est and R. Bittl. *Biochemistry*, **36** (1997) 9774.

[61] J. P. Allen and G. Feher. *Proc. Natl. Acad. Sci.*, **81** (1984) 4795.

[62] J. P. Allen, R. A. Isaacson, A. McPherson and G. Feher. *Biophys. J.*, **45** (1984) A256.

[63] A. van der Est, R. Bittl, W. Lubitz and D. Stehlik. *Chem. Phys. Lett.*, **212** (1993) 561.

[64] W.W. Parson in *The Photosynthetic Bacteria.* Plenum Press, New York, R. K. Clayton and W. R. Sistrom (eds.), 1978.

[65] D. Kleinfeld, M. Y. Okamura and G. Feher. *Biochemistry*, **23** (1984) 5780.

[66] W. B. Mims. *Phys. Rev. B*, **5** (1972) 2409.

[67] S. A. Dzuba, M. Bosch and A. J. Hoff. *Chem. Phys. Lett.*, **248** (1996) 427.

[68] R. Bittl, A. van der Est, A. Kamlowski, W. Lubitz and D. Stehlik. *Chem. Phys. Lett.*, **226** (1994) 349.

[69] G. Zwanenburg and P. J. Hore. *J. Magn. Reson. A*, **114** (1995) 139.

[70] C. R. Timmel, C. E. Fursman, A. J. Hoff and P. J. Hore. *Chem. Phys.*, **226** (1998) 271.

[71] S. A. Dzuba, I. I. Proskuryakov, R. J. Hulsebosch, M. K. Bosch, P. Gast and A. J. Hoff. *Chem. Phys. Lett.*, **253** (1996) 361.

[72] B. van Dijk, P. Gast and A. J. Hoff. *Phys. Rev. Lett.*, **77** (1996) 4478.

[73] B. van Dijk, P. Gast and A. J. Hoff. *J. Phys. Chem. A*, **101** (1997) 719.

[74] M. C. Thurnauer and J. R. Norris. *Chem. Phys. Lett.*, **76** (1980) 557.

[75] K. M. Salikhov, Yu. E. Kandrashkin and A. K. Salikhov. *Appl. Magn. Reson.*, **3** (1992) 199.

[76] J. Tang, M. C. Thurnauer and J. R. Norris. *Chem. Phys. Lett.*, **219** (1994) 283.

[77] J. Tang, M. C. Thurnauer and J. R. Norris. *Appl. Magn. Reson.*, **9** (1995) 23.

[78] J. Tang and J. R. Norris. *Chem. Phys. Lett.*, **233** (1995) 192.

[79] J. Tang, M. C. Thurnauer, A. Kubo, H. Hara and A. Kawamori. *J. Phys. Chem.*, **106** (1997) 7471.

[80] S. Schäublin, A. Hoehener and R. R. Ernst. *J. Magn. Reson.*, **13** (1974) 196.

[81] S. Schäublin, W. Wokaun and R. R. Ernst. *Chem. Phys.*, **14** (1976) 285.

[82] L. G. Rowan, E. L. Hahn and W. B. Mims. *Phys. Rev. A*, **137** (1965) 61.

[83] S. A. Dzuba. *Chem. Phys. Lett.*, **278** (1997) 333.

[84] S. Wolfram. *Mathematica. A System for doing Mathematics by Computer.* Addison Wesley, Redwood City, CA, 1991.

[85] W. Lubitz. Personal Communication.

[86] R. Calvo, W. Hofbauer, F. Lendzian, W. Lubitz, M. L. Paddock, E. C. Abresch, R. A. Isaacson, M. Y. Okamura and G. Feher. *Biophys. J.*, **76** (1999) A392.

[87] R. Calvo, M. L. Paddock, E. C. Abresch, R. A. Isaacson, M. Y. Okamura and G. Feher. *Biophys. J.*, **74** (1998) A135.

[88] M. H. Stowell, T. M. McPhillips, S. M. Soltis, D. C. Rees, E. Abresch and G. Feher. *Science*, **276** (1997) 812.

[89] P. J. Hore in *Advanced EPR.* Elsevier Science Publishers B.V., A. J. Hoff (ed.), 1989.

[90] T. F. Prisner, A. van der Est, W. Lubitz, D. Stehlik and K. Möbius. *Chem. Phys.*, **194** (1995) 361.

[91] R. A. Isaacson, F. Lendzian, E. C. Abresch, W. Lubitz and G. Feher. *Biophys. J.*, **69** (1995) 311.

[92] R. Bittl. Personal Communication.

[93] M. Rohrer, P. Gast, K. Möbius and T. F. Prisner. *Chem. Phys. Lett.*, **259** (1996) 523.

[94] R. R. Ernst, G. Bodenhausen and A. Wokaun. *Principles of Nuclear Magnetic Resonance in One and Two Dimensions.* Clarendon Press, Oxford, 1987.

[95] G. Bodenhausen, R. Freeman and D. L. Turner. *J. Magn. Reson.*, **27** (1977) 511.

[96] T. Polenova and A. E. McDermott. *J. Phys. Chem. B*, **103** (1999) 535.

[97] P. Gast and A. J. Hoff. *Biochem. Biophys. Acta*, **546** (1979) 520.

[98] A. J. Hoff and P. Gast. *J. Phys. Chem.*, **108** (1984) 104.

[99] M. Y. Okamura, R. A. Isaacson and G. Feher. *Biochem. Biophys. Acta*, **546** (1979) 394.

[100] J. P. Norton. *An Introduction to Identification.* Academic Press, San Diego, CA, 1986.

[101] A. van den Bos in *Handbook of Measurement Science.* Wiley, New York, P. H. Sydenham (ed.), 1982.

[102] P. Hodgkinson and P. J. Hore. *Adv. Magn. Opt. Reson.*, **20** (1997) 187.

[103] P. Hodgkinson, K. J. Holmes and P. J. Hore. *J. Magn. Reson. A*, **120** (1996) 18.

[104] C. E. Fursman and P. J. Hore. *Chem. Phys. Lett.*, **303** (1999) 593.

[105] J. D. McElroy, D. C. Mauzerall and G. Feher. *Biochem. Biophys. Acta*, **333** (1974) 261.

[106] W. H. Press, S. A. Teukolsky, W. T. Vetterling and B. P. Flannery. *Numerical Recipes in C: The Art of Scientific Computing.* Cambridge University Press, Second Ed., 1992.

[107] A. Jones. *Comput. J.*, **13** (1970) 301.

[108] A. De Groot, A. J. Hoff, R. de Beer and H. Scheer. *Chem. Phys. Lett.*, **113** (1985) 286.

[109] M. K. Bosch, P. Gast, A. J. Hoff, A. P. Spoyalov and Yu. D. Tsvetkov. *Chem. Phys. Lett.*, **239** (1995) 306.

[110] R. Freeman. *A Handbook of Nuclear Magnetic Resonance.* Addison Wesley Longman Limited, Second Ed., 1997.

[111] C. R. Timmel, S. G. Zech and P. J. Hore. Personal Communication.

[112] R. Bittl, S. G. Zech, P. Fromme, H. T. Witt and W. Lubitz. *Biochemistry*, **36** (1997) 12001.

[113] T. F. Prisner. *Adv. Magn. Opt. Reson.*, **20** (1997) 245.

[114] T. F. Prisner, M. Rohrer and K. Möbius. *Appl. Magn. Reson.*, **7** (1994) 167.

[115] I. Sieckman, A. van der Est, H. Bottin, P. Setif and D. Stehlik. *FEBS Lett.*, **284** (1991) 98.

[116] D. Stehlik, I. Sieckman and A. van der Est. *Photosyn. Res.*, **34** (1992) 129.

[117] S. G. Zech. Personal Communication.

[118] J. Tang, L. M Utschig, O. Poluektov and M. Thurnauer. *J. Phys. Chem.*, **103** (1999) 5145.